UAB

Universitat Autònoma de Barcelona

Nanobiosensors for contaminants detection in water

José Francisco Bergua Canudo
Ph.D. Thesis
Ph.D. in Biotechnology

Directors

ICREA Prof. Dr. Arben Merkoçi

Dr. Ruslan Álvarez

The present work entitled "Nanobiosensors for contaminants detection in waters", presented by José Francisco Bergua Canudo to obtain the degree of doctor in biotechnology by Universitat Autònoma de Barcelona, was performed at the Nanobioelectronics and Biosensors Group at the Institut Catalá de Nanociencia i Nanotecnologia (ICN2), under the supervision of Prof. Arben Merkoçi, ICREA Professor and Group Leader, and Dr. Ruslan Álvarez.

The author

José Francisco Bergua Canudo

The Supervisors

Prof. Dr. Arben Merkoçi   **Dr. Ruslan Álvarez**

The present Thesis was performed also under the doctoral program studies "Doctorado en Biotecnología" at the Faculty of Biosciences, Universitat Autònoma de Barcelona, under the tutorship of Professor Jordi Joan Cairó.

The University Tutor

Prof. Jordi Joan Cairó Badillo

Bellaterra, July 2020

The research work accomplished during this thesis resulted three manuscripts that are submitted to international peer-reviewed scientific journals:

The state-of-the-art studies have resulted in a review publication under preparation:

"Water pollutants and their detection using optical biosensors". **José Francisco Bergua**, Ruslan Álvarez-Diduk, Arben Merkoçi. To be submitted in 2020.

The experimental work performed conducted to two articles not yet published, and one article in preparation:

"Improved *Aliivibrio fischeri* based-toxicity assay: graphene-oxide as a sensitivity booster with a mobile-phone application". **José Francisco Bergua**, Liming Hu, Celia Fuentes, Ruslan Álvarez-Diduk, Abdelrahim H.A. Hassan, Claudio Parolo, Arben Merkoçi. Submitted to *Analytical Chemistry* in 2020.

"Improved *Aliivibrio fischeri* based-toxicity assay: graphene-oxide as a sensitivity booster with a mobile-phone application". **José Francisco Bergua**, Ruslan Álvarez-Diduk, Liming Hu, Abdelrahim H.A. Hassan, Arben Merkoçi. Submitted to *Journal of Hazardous Materials* in 2020.

"Portable platform for optical biosensing applications". **José Francisco Bergua**, Ruslan Álvarez-Diduk, Liming Hu, Andrea Idili, Claudio Parolo, Arben Merkoçi. To be submitted in 2020.

PREFACE

Additionally, the collaborations performed within the Ph.D. thesis resulted in several other publications non-related to this thesis:

"Tutorial: Design and fabrication of nanoparticle-based lateral flow immunoassays". Claudio Parolo, Amadeo Sena-Torralba, **José Francisco Bergua**, Enric Calucho, Celia Fuentes-Chust, Liming Hu, Lourdes Rivas, Ruslan Álvarez-Diduk, Emily P. Nguyen, Stefano Cinti, Daniel Quesada-González, Arben Merkoçi. *Nature Protocols*. Recently accepted in 2020.

"Lateral flow assay modified with time-delay wax barriers as a sensitivity and signal enhancement strategy". Amadeo Sena-Torralba, Duy Ba Ngo, Claudio Parolo, Liming Hu, Ruslan Álvarez-Diduk, **José Francisco Bergua**, Giulio Rosati, Werasak Surareungchai, Arben Merkoçi. *Biosensors & Bioelectronics*. Submitted in 2020.

"Validity of a single antibody-based lateral flow immunoassay depending on graphene oxide for highly sensitive determination of *E. coli* O157:H7 in minced beef and river water". Abdel-Rahim H. A. Hassan, **José Francisco Bergua**, Eden Morales-Narváez, Arben Merkoçi. *Food Chemistry*, 2019, 297 (124965), 1-10.

"Low-cost strategy for the development of a rapid electrochemical assay for bacteria detection based on AuAg Nanoshells". Lorenzo Russo, Juan Leva Bueno, **José Francisco Bergua**, Monica Constantini, Marco Giannetto, Víctor Puntes, Alfredo de la Escosura Muñiz, Arben Merkoçi. *ACS Omega*, 2018, 3 (12), 18849-18856.

"Straightforward immunosensing platform based on graphene oxide-decorated nanopaper: a highly sensitive and fast biosensing approach". Nopchulee Cheeveewattanagul, Eden Morales-Narváez, Abdel-Rahin H. A. Hassan, **José Francisco Bergua**, Arben Merkoçi. *Advanced Functional Materials*, 2017, 27 (1702741), 1-8.

En esta sección, me gustaría agradecer el apoyo a toda la gente que ha sido importante para mí durante la tesis, y que de una forma u otra han ayudado a que hoy esté escribiendo estas palabras.

Primero, me gustaría agradecer a mi familia todo el apoyo recibido durante estos cuatro años. Por estar siempre al pie del cañón en los buenos momentos y en los más duros, y por todo el cariño y la fuerza que siempre me habéis dado. Gracias papá por las horas interminables de teléfono escuchando experimentos que ni siquiera entendías. Gracias mamá por la energía positiva, los abrazos y los besos infinitos al volver a casa cada mes. Gracias Virgi por cuidarme, por todos los consejos desde la distancia, y por aportar siempre esa visión más realista que tu hermano a menudo necesita. Gracias yaya, gracias simplemente por estar allí, porque lo que más me motivaba para volver a Huesca cada mes era verte la sonrisa dibujada en la cara al verme aparecer en la residencia. Gracias también a mi tía Ana Salas por todos los ánimos, los consejos y la fuerza prestada, sobre todo durante el confinamiento y la escritura de la tesis. Tampoco me quiero olvidar de mi tía Elena y de mi prima Andrea, siempre dispuestas a reírse conmigo sea cual sea la situación a la que nos enfrentemos. Finalmente, gracias al resto de tíos y primos, que de alguna forma también me han ayudado a conseguir este objetivo.

Segundo, me gustaría agradecer a toda la gente que forma o ha formado parte del grupo Nanobioelectronics & Biosensors (NB2) y con la que he trabajado estos años. Como directores de mi tesis, me gustaría también agradecerles el apoyo y la supervisión a Arben Merkoçi y a Ruslan Álvarez. Gracias Arben, por aceptarme en el grupo para realizar el trabajo de fin de máster, más tarde por ofrecerme hacer el doctorado en el grupo, y finalmente por todas las oportunidades y los consejos prestados durante estos cinco años en el grupo. Gracias Ruslan, porque tú mejor que nadie sabes que si he llegado hasta aquí y he conseguido acabar esta tesis, en gran parte, es gracias a ti. Me llevo muy buenos momentos, muchas risas y aprendizajes, alguna bronca y, además, me llevo a un buen amigo también.

Como supervisores y personas de gran ayuda durante mi estancia en el ICN2, me gustaría nombrar a algunas personas. Daniel Quesada, gracias por ser como un padre para mí desde que entré en el grupo a realizar el TFM. Por las horas interminables de laboratorio que hemos pasado juntos, por todos los viajes y actividades que hemos realizado, y en general por tu apoyo, tu

ACKNOWLEDGMENTS

comprensión y tu amistad todos estos años. Para mí has sido un referente durante la tesis. Me gustaría también agradecer a Anna Puig todas las risas y la paciencia mostradas todo este tiempo, porque gracias a ella también hoy puedo depositar esta tesis. Por otro lado, quiero agradecer a Alfredo de la Escosura todo el apoyo y los consejos prestados durante el tiempo que coincidimos en el grupo. Y por supuesto, también por organizar los partidos de fútbol en el SAF y por los divertidos piques futbolísticos entre Huesca y Oviedo.

A continuación, me gustaría agradecer a los grandes amigos que he hecho en el grupo NB2 durante el doctorado. Amadeo Sena, gracias por estos cinco años que hemos vivido juntos, codo con codo. Porque hemos seguido caminos paralelos y nosotros mejor que nadie podemos entender el esfuerzo que hemos realizado. Me llevo a un grandísimo amigo, un muy buen compañero de laboratorio, y un más que aceptable goleador en los partidillos de fútbol que jugábamos. Quiero destacar la estancia que disfrutamos en Taiwán durante dos de los mejores meses de mi vida, todo el apoyo mutuo y las risas y risas que hemos compartido durante todo este tiempo. Enric Calucho, gracias también por tu amistad y tus ganas de ayudar siempre, dentro y fuera del laboratorio. Hemos compartido muchas y muy buenas experiencias, destacando algunos conciertos, incluyendo al mejor: Bob Dylan. Celia Fuentes, gracias por todo. Porque si ha habido alguien que me ha entendido y ha estado al pie del cañón desde que llegó al ICN2, has sido tú. Gracias por ser tan buena alumna, tan buena amiga, y por la alegría que siempre transmites cuando trabajamos juntos. Por otro lado, una parte de mí se ha enamorado de China, su lengua y su cultura durante el doctorado, y eso es en gran medida gracias a Liming, Qiuyue y Lei. Gracias por los buenísimos momentos disfrutados en la oficina y en las actividades que realizábamos fuera del trabajo. En especial, gracias a Liming por trabajar tan estrechamente y por enseñarme tantas cosas desde que aterrizó en el grupo.

También hay otros miembros del grupo a los que me gustaría mostrar mi agradecimiento. Claudio Parolo, gracias por el buen rollo, todo el trabajo, y los consejos durante este tiempo. Andrea Idili, gracias también por tus consejos y por el enorme apoyo y toda la fuerza mostrada para sacar adelante cualquier proyecto que se nos pusiera por delante. Lourdes Rivas, gracias por tu apoyo, tus recomendaciones, y todas tus ganas de ayudar durante el doctorado. Por último,

gracias también al resto de miembros del grupo NB2, algunos de los cuales también me han ayudado mucho, pero a los que no puedo nombrar uno por uno.

Siguiente, me gustaría también recordar a algunos antiguos miembros del grupo que me han marcado enormemente durante el doctorado. Gracias a Liu Jie (Emma), Nopchulee y Hassan por los grandes momentos que hemos compartido y por todas vuestras enseñanzas durante los primeros años de mi doctorado. También me gustaría acordarme de Marc Balsells, compañero inseparable de piscina y gran apoyo durante su estancia en el grupo. Además, no puedo olvidarme de Marc Botifoll, primer estudiante que tuve como supervisor. Gracias por tu esfuerzo, tus ganas de aprender, y en general por tu amistad y lo fácil que me pusiste tu supervisión. Gracias también a Xin Yi por toda tu alegría, y por los indescriptibles momentos embarazosos que vivimos en la oficina. En general, también me gustaría agradecer a los miembros del proyecto europeo INTCATCH la oportunidad de colaborar en un proyecto tan importante y todas las experiencias que me llevo al haber trabajado en numerosos países.

Tercero, me gustaría acordarme de otros grandes amigos que he hecho durante mi estancia en el ICN2, fuera del grupo NB2. Gracias a Javier Muro por su amistad, por todas las cosas que hemos vivido juntos y por siempre estar allí cuando lo he necesitado. Gracias especialmente a Alba Mingorance, por toda su alegría, sus abrazos, sus consejos, y, en definitiva, por todo su gran apoyo durante estos años. Gracias a Li Zhi por su enorme empatía y por sus ganas de disfrutar de la vida con una alegría de la que es imposible no contagiarse. Gracias a Cristina Peláez también por su alegría, las noches de cine, y los viajes y cenas que hemos compartido. Gracias a Pau Güell por su amistad y por todas las conversaciones que hemos compartido en el tren desde y hacia el ICN2 durante los últimos años de la tesis. Por último, gracias a José Cruz por todos los buenos momentos y las risas compartidas durante el doctorado.

No me quiero olvidar tampoco de mis compañeros del grupo de "Toxics" en la facultad de ingeniería, en especial de Teresa Vincent, y de otras personas del ICN2 que me han ayudado enormemente y han hecho mi estancia durante el doctorado mucho más agradable: Marcos Rosado y Belén Ballesteros del servicio de microscopía, Marta en recepción, y las siempre amables trabajadoras de la limpieza del ICN2.

ACKNOWLEDGMENTS

De forma rápida me gustaría acordarme también de los que considero mis mejores amigos fuera de Barcelona y de los que he recibido apoyo constante todos estos años. Gracias a la ya mencionada anteriormente Laura Paúl, pero también a Chema Navarro, a Inés Mármol, a Pedro Martínez, a Rubén López y a Javier Usón. Gracias a todos por acompañarme estos años desde la distancia y por vuestra amistad, que sin duda ha ayudado enormemente para poder terminar esta tesis.

Por último, gracias a una persona muy especial que conozco desde hace poco pero que sin duda ha supuesto un gran apoyo los últimos meses de la tesis. Gracias Marc por tu comprensión y por tu cariño constante, especialmente durante el periodo de confinamiento. Gracias por todo lo que me has dado estos meses y espero que me sigas dando en el futuro.

Gracias a ti, lector, a todos los partícipes de estos agradecimientos y a cualquier persona que de forma directa o indirecta me haya ayudado estos años. Gracias a todos.

ACKNOWLEDGMENTS

Water pollution is one of the major problems humankind is facing nowadays. On the one hand, the presence of chemicals (i.e. pesticides and heavy metals) coming from agriculture and industrial runoffs impairs the water quality. On the other hand, farming and urban areas produce huge quantities of dung and wastewaters that result in altered water microbiological status and may lead to waterborne outbreaks. In this regard, biosensing offers great opportunities for tracking in situ chemical and microbiological pollutants in water to prevent and reduce the associated environmental and health issues.

General aspects and experimental results are exposed in this thesis, starting from a general introduction that covers the description of a broad range of chemical and biological water pollutants, to a variety of biosensing techniques used to detect and quantify those pollutants. The experimental section focuses on the detection of *Escherichia coli* by a colorimetric lateral flow immunoassay (LFIA) as a fecal indicator and two environmentally persistent pesticides through a bioluminescent toxicity biosensor as chemical pollutants. Furthermore, a versatile and portable platform is thoroughly described to perform colorimetric, fluorescent, and bioluminescent assays for environmental and other applications.

As aforementioned, *E. coli* is considered the main fecal indicator for water quality assessment. Nowadays, standard *E. coli* detection methods are laboratory-based and time-consuming. For this reason, the development of a colorimetric AuNPs-based LFIA for general *E. coli* detection is reported in this thesis. The proposed system can detect three different strains of *E. coli*, while discerning from *Salmonella* spp, in tap, river, and sewage in 10 minutes. In addition, the implementation of a filtration system allows for preconcentrating *E. coli* and increasing the sensitivity in two orders of magnitude. Eventually, a gram-negative bacterium, similar in shape and size to *E. coli*, is used as a novel characterization system to study the microfluidics within different lateral flow materials.

Nowadays, pesticides are widely used worldwide mainly for agricultural applications. However, some pesticides are highly toxic to non-target organisms and remain for years in the soil and water. As two examples, tributyltin (TBT) and pentachlorophenol were broadly used in the EU for many years. For this reason, a toxicity biosensor based on the bioluminescent bacterium *Aliivibrio fischeri* is used to detect TBT and pentachlorophenol in water samples and is

SUMMARY

reported in this thesis. The proposed system relies on a standard 96-wells plate, an opaque box, and a smartphone to carry out the toxicity measurements. Besides, the addition of graphene-oxide as a growth enhancer allows for reducing the growing time of the bacteria and enhancing the sensitivity of the biosensor.

Third, a universal portable platform has been used to perform optical bioassays. This versatile platform allows for performing colorimetric, fluorescent, and bioluminescent assays. More in detail, the platform has been used to develop a colorimetric ELISA test to detect SARS-CoV-2 and human immunoglobulin G. Besides, it allows for studying the aggregation state of nanoparticles, which are critical elements in many optical bioassays. On the other hand, the detection of fluorophores such as quantum dots (QDs) and fluorescein is possible through the installation of a UV-led and a series of optical filters that allow for exciting the samples and filtering out the background signals for optimal imaging. In addition, bioluminescent assays can also be carried out for toxicity assessment of water samples by simply adjusting the smartphone camera settings and the dark conditions within the platform. Last, but not least, the platform allows for growing bacteria cultures under agitation and controlled temperature conditions, as well as monitoring bacterial growth through a new method to estimate turbidity changes within the media.

Finally, the general conclusions are exposed including some opinions and recommendations for further continuation of the research in the field

La contaminación del agua es uno de los principales problemas a los que la humanidad se enfrenta hoy en día. Por un lado, la presencia de productos químicos (ej. pesticidas y metales pesados) provenientes de la agricultura y de los vertidos industriales alteran la calidad del agua. Por otro lado, tanto la ganadería como las ciudades producen grandes cantidades de estiércol y aguas de desecho, lo que conlleva alteraciones del estado microbiológico del agua y puede provocar brotes de enfermedades infecciosas. En este sentido, los biosensores ofrecen grandes oportunidades para monitorizar in situ los contaminantes químicos y microbiológicos, lo que ayuda a prevenir y reducir los problemas medioambientales y de salud pública asociados.

En esta tesis se exponen los aspectos generales y resultados experimentales, comenzando por una introducción general que cubre la descripción de un amplio rango de contaminantes químicos y biológicos del agua, así como una gran variedad de biosensores utilizados para detectar y cuantificar dichos contaminantes. La sección experimental se centra en la detección de *Escherichia coli* como indicador fecal del agua a través de un inmunoensayo colorimétrico de tipo flujo lateral (*LFIA*, por sus siglas en inglés: "*lateral flow immunoassays*"). A su vez, se incluye la detección de dos pesticidas altamente persistentes en el medioambiente a través de un biosensor de toxicidad bioluminiscente. Además, se describe en profundidad una plataforma portátil y versátil que puede llevar a cabo ensayos colorimétricos, fluorescentes y bioluminiscentes orientados a aplicaciones medioambientales y de otros tipos.

Mencionado ya anteriormente, *E. coli* se considera el principal indicador de contaminación fecal del agua. Hoy en día, los métodos estándar de detección de *E. coli* en agua son extremadamente lentos y requieren de instalaciones especializadas para llevarse a cabo. Por esta razón, en esta tesis se expone el desarrollo de un biosensor de flujo lateral basado en nanopartículas de oro (AuNPs) para la detección de la especie *E. coli* como indicador fecal. El sistema propuesto es capaz de detectar hasta tres cepas diferentes de *E. coli*, discerniendo de *Salmonella* spp., en agua de grifo, de río y de una planta depuradora. Además, la implementación de un sistema de filtración adicional permite preconcentrar *E. coli*, y a su vez incrementar la sensibilidad del sensor en dos órdenes de magnitud. Finalmente, una bacteria gram-negativa, similar en forma y tamaño a *E. coli*, se usa como un sistema novedoso de caracterización para estudiar la microfluídica dentro de las diferentes partes del sensor de flujo lateral.

RESUMEN

Hoy en día, los pesticidas se usan de forma generalizada a través del mundo, principalmente en aplicaciones relacionadas con la agricultura. Sin embargo, algunos pesticidas son altamente tóxicos y no selectivos, permaneciendo durante años en el suelo y en las aguas. Como dos ejemplos, el tributilo de estaño (TBT) y el pentaclorofenol fueron ampliamente utilizados en la Unión Europea durante muchos años. Por esta razón, se expone en esta tesis el desarrollo de un biosensor basado en la bacteria bioluminescente *Aliivibrio fischeri* para detectar TBT y pentaclorofenol en muestras de agua. El sistema propuesto se basa en la combinación de una placa de 96 pocillos, una caja opaca, y un teléfono móvil para realizar las medidas de toxicidad. Además, la adición de óxido de grafeno (GO) actúa como un potenciador del crecimiento bacteriano, permitiendo reducir el tiempo de crecimiento de la bacteria e incrementando la sensibilidad del biosensor.

Tercero, se ha desarrollado una plataforma universal portátil para realizar bioensayos ópticos; en concreto, ensayos colorimétricos, fluorescentes y bioluminescentes. Más en detalle, la plataforma se ha utilizado para desarrollar test de ELISA colorimétricos para detectar SARS-CoV-2 y anticuerpos humanos isotipo G. Además, permite estudiar el estado de agregación de nanopartículas, que son elementos cruciales en la mayoría ensayos ópticos. Por otra parte, es posible detectar fluoróforos como quantum dots (QDs) y fluoresceína a través de la instalación de un led ultravioleta y una serie de filtros ópticos que permiten excitar las muestras y filtrar las señales de ruido de fondo para obtener imágenes de gran calidad. Asimismo, también se pueden llevar a cabo ensayos bioluminescentes para la evaluación de la toxicidad del agua, simplemente ajustado los parámetros de la cámara del teléfono móvil y las condiciones de oscuridad dentro de la plataforma. Por último, pero no menos importante, la plataforma permite crecer cultivos bacterianos en condiciones de agitación y temperatura controladas, así como monitorear el crecimiento bacteriano a través de un nuevo método que permite estimar cambios de turbidez en el medio de cultivo.

Por último, se exponen las conclusiones generales y futuras propuestas.

4-methylumbelliferyl-β-d-galactoside	MUGal
Acetylcholinesterase	AChE
Aliivibrio fischeri	AF
Butyrylcholinesterase	BChE
Dichlorodiphenyltrichloroethane	DDT
Deoxyribonucleic acid	DNA
Dissolved oxygen	DO
Enteroaggregative *E. coli*	EAggEC
European Food Safety Authority	EFSA
Enterohemorrhagic *E. coli*	EHEC
Enteroinvasive *E. coli*	EIEC
Enterotoxigenic *E. coli*	ETEC
Enterovirulent *E. coli*	EEC
European Environmental Agency	EEA
Enzyme-Linked Immunosorbent Assay	ELISA
European Union	EU
Food and Agriculture Organization of the United Nations	FAO
Förster resonance energy transfer	FRET
Gamma-Aminobutyric acid	GABA
Gas-Chromatography/Mass-Spectrometry	GC/MS
Glutamate-Chloride	GluCl
High-Performance Liquid Chromatography	HPLC
Hierarchical Cluster Analysis	HCA
Indoxyl β-D-glucuronide	IBDG

GLOSSARY OF TERMS, ACRONYMS AND ABBREVIATIONS

Indirect hemagglutination assay	IHA
Lateral Flow Immunoassay	LFIA
Limit of Detection	LOD
Limit of Quantification	LOQ
Matrix-Assisted Laser Desorption/Ionization	MALDI-TOF MS
Membrane filtration	MF
Metal-Organic Framework	MOF
Micro paper-based analytical device	(µPAD)
Molecular Imprinted Polymer	MIP
Most Probable Number	MPN
Multiple Tube Fermentation Method	MTFM
Monosodium methanearsonate	MSMA
Multi-Walled Carbon Nanotubes	MWNTs
Nanoparticles	NPs
Nicotinic acetylcholine receptors	nAChRs
Organochlorinated compounds	OCs
Organophosphorus compounds	OPs
Pentachlorophenol	PCP
Polymerase Chain Reaction	PCR
Quorum Sensing	QS
Rapid Enzyme Immunoassay	EIA
Reactive oxygen species	ROS
Ribosomal Ribonucleic Acid	rRNA
Scanning Electron Microscopy	SEM
Surface-enhanced Raman spectroscopy	SERS

Surface Plasmon Resonance	SPR
Shige toxin-producing *E. coli*	STEC
Transmission Electron Microscopy	TEM
Tributyltin	TBT
Upconverting Nanoparticles	UCNPs

Table of Contents

THESIS OVERVIEW

Water pollution threatens both environment and human health all over the world. The number and variety of water pollutants are huge, making their detection and water quality assessment though and complicated. Overall, chemical and microbiological pollution are the main cause of water pollution worldwide. Therefore, this thesis is focused on the development of portable platforms and biosensors for water quality monitoring, especially related to fecal contamination and chemical pollution.

General aspects and experimental results related to the present Ph.D. Thesis are divided into six chapters, including the introduction, thesis objectives, results and discussions, and general conclusions.

Chapter 1, entitled "*Introduction*", presents the description of chemical pollutants, mainly focused on pesticides but also including heavy metals and petroleum; as well as the description of waterborne pathogens, mainly focused on bacteria but also including viruses and other parasites. Next, a legal frame regarding water quality in the EU is presented, as well as more general aspects related to the regulations in other countries. In the following section, biosensors targeting pesticides are presented, from single compounds detection to a family of compounds, and more general toxicity biosensors. At last, biosensors targeting bacteria are presented, as well as the different bioreceptors and transducers employed in these biosensors.

Chapter 2, entitled "*Objectives of the thesis*", presents the different objectives of the Ph.D. Thesis. The main objective was to study and develop portable and easy-to-use platforms for chemical and microbiological analysis of water samples.

Chapter 3, entitled "*Escherichia coli detection as a fecal indicator*", reports the design, development, and optimization of a lateral flow biosensor for the detection of *E. coli* in water samples as a way to assess water fecal contamination. Besides, a new methodology is presented to characterize the microfluidics of bacteria cells within the lateral flow materials.

Chapter 4, entitled "*Water toxicity assessment*", reports the development and optimization of a bioluminescent toxicity biosensor based on the bacteria *Aliivibrio fischeri*. The quorum-sensing effect that triggers the bioluminescence is studied and characterized, and a new platform based on the growth of *A. fischeri* onto a solid substrate is presented as a strategy to enhance

bacterial bioluminescence. Besides, the use of graphene oxide (GO) as a biocompatible material to promote bacterial growth and enhance the system's sensitivity is described. Eventually, a smartphone is used to perform the toxicity measurements, enabling to move from the laboratory analysis to the field.

Chapter 5, entitled "*Portable platform for optical biosensing applications*", reports the design, fabrication, and use of a portable platform to perform colorimetric, fluorescent, bioluminescent, and turbidimetric assays. All the components of the platform have been installed to optimize the performance of a variety of bioassays that allow for biomarkers' and environmental monitoring. This chapter includes a detailed description of these bioassays, highlighting the performance with the portable platform and a smartphone and the envisaged real applications.

Concluding remarks of the present Thesis in addition to future perspectives regarding the results and research fields explored are enclosed in **Chapter 6**.

CHAPTER 1. INTRODUCTION

CHAPTER 1

Introduction

1.1. Water pollution

1.1.1. General Aspects

Water is the most essential resource for life. It covers 71% of the Earth's surface and it constitutes the fluids of most living organisms. These living organisms use water mainly for drinking, but for some of them, it is also their living media. Humans also use water for several other activities such as cooking, cultivating crops, farming, and washing.

Since the 19th century, with the arrival of the Industrial Revolution, new chemicals started to be produced and poured uncontrollably in water bodies. Moreover, new technological advances and improvements in sanitary conditions boosted life-expectancy, increasing the world population and the need for bigger cities and farming lands. Altogether, these circumstances have led to a dramatic increase in both water demand and pollution, threatening access to good-quality water all over the world. As an example, global water demand has raised almost 600% from 1900 to 2015 (Figure 1.1a)[1]. If water use keeps growing at this rate, it is estimated that around 50% of the world population will be living in water-stressed areas by 2050, with limited access to safe water sources[2]. Currently, most of the world water demand is due to agriculture and farming (≈ 70%), but there are important variations among different geographical areas (Figure 1.1b)[3]. The remaining global water consumption is carried out by the industries (≈ 20%), and by the urban areas (≈ 10%).

Water pollution arises when pollutants reach water bodies (i.e. rivers, lakes, seas, oceans and groundwater sources). Pollutants are substances introduced in the environment that cause adverse effects to specific living beings or the overall ecosystem. Water pollution can be chemical, biological, and physical. On the one hand, chemical pollution generally comes from the industrial and agricultural sectors and includes organic and inorganic substances such as pesticides and heavy metals. On the other hand, microbiological pollution is caused by microorganisms such as bacteria, viruses, and protozoa. Eventually, physical pollution arises as some physicochemical parameters of the water are impaired, such as temperature, pH, conductivity, and dissolved oxygen content.

INTRODUCTION

Main waste products produced by agriculture and farming are pesticides, dung, and other biological traces. These waste products may pollute the ecosystem through filtration in underground-water reservoirs or direct grooving to the rivers, lakes, seas, and oceans. Therefore, since agriculture and farming are human activities with the highest water demand worldwide, water quality is severely threatened by chemical and biological pollution. For example, in the European Union (EU), only 18% of the inner water bodies can be considered to have good or high quality (Figure 1.1c)[4]. On the other hand, almost 40% of the inner water bodies are considered to have poor or bad quality and are inappropriate for human consumption.

Consumption of unsafe water, polluted with chemicals and mainly with microorganisms, can lead to several diseases, some of which may be fatal, such as dysentery or cholera. More than 2 billion people in the world drink unsafe water contaminated with feces, and around 0.8 million people die every year as a consequence[5]. More than 98% of these deaths caused by waterborne outbreaks are produced in Africa and south-east Asia, being India and Nigeria the two countries with the highest number of deaths related to the consumption of unsafe water (Figure 1.1d)[6].

In summary, water pollution threatens water quality worldwide. Nowadays, agriculture and farming entail the highest pollution sources of water bodies. Since more than 2 billion people drink unsafe water causing almost 1 million deaths per year, it is crucial to know and detect the main pollutants found in water. Consequently, this control would allow for decreasing the personal and economical burdens associated with waterborne outbreaks and chronic related diseases.
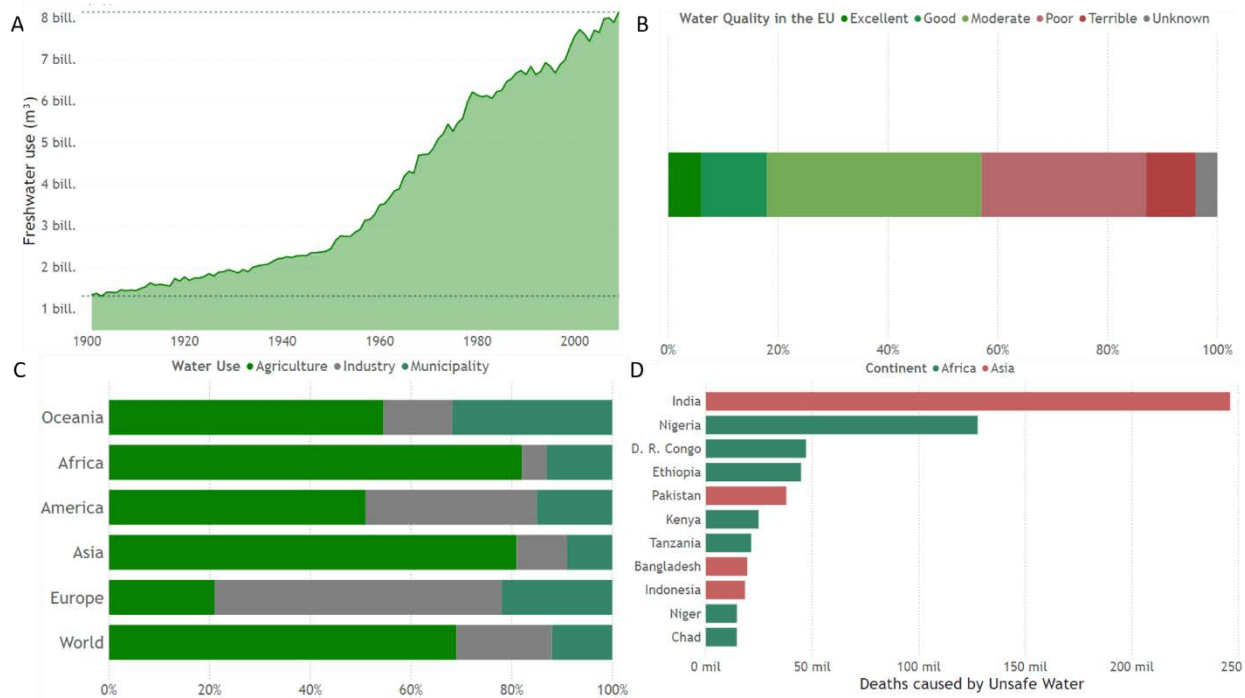
Figure 1.1. Water use, pollution, and related outbreaks. (A) Global water demand from 1900 to 2015 (Food and Agriculture Organization of the United Nations [FAO]). (B) Water use by sector (agriculture and farming, industry and urban areas) in the five continents and worldwide (2010, AQUASTAT). (C) Water quality of inner water bodies in the EU (2018, European Environmental Agency [EEA]). (D) Human deaths caused by waterborne diseases showing the top-ten countries with the highest mortality numbers (2016, AQUASTAT).

1.1.2. General Description of Pollutants

Water pollution occurs when wastewater bodies containing pollutants get in contact with cleaner water bodies. There exist many water pollutants that can be classified into seven major categories: organic compounds, inorganic compounds, pathogens, nutrients, and agriculture runoff, radioactive pollutants, thermal pollution and macroscopic pollutants[7] (Figure 1.2).

Organic and inorganic compounds can, in turn, be included in a larger category of chemical pollutants, whereas pathogens can be considered as biological pollutants. These two main categories are explained more in detail in the following sections. Besides, radioactive pollutants, thermal pollution, and macroscopic pollutants can be classified as physical pollutants. Some examples of macroscopic pollutants include plastics, large metallic pieces and other types of trash.
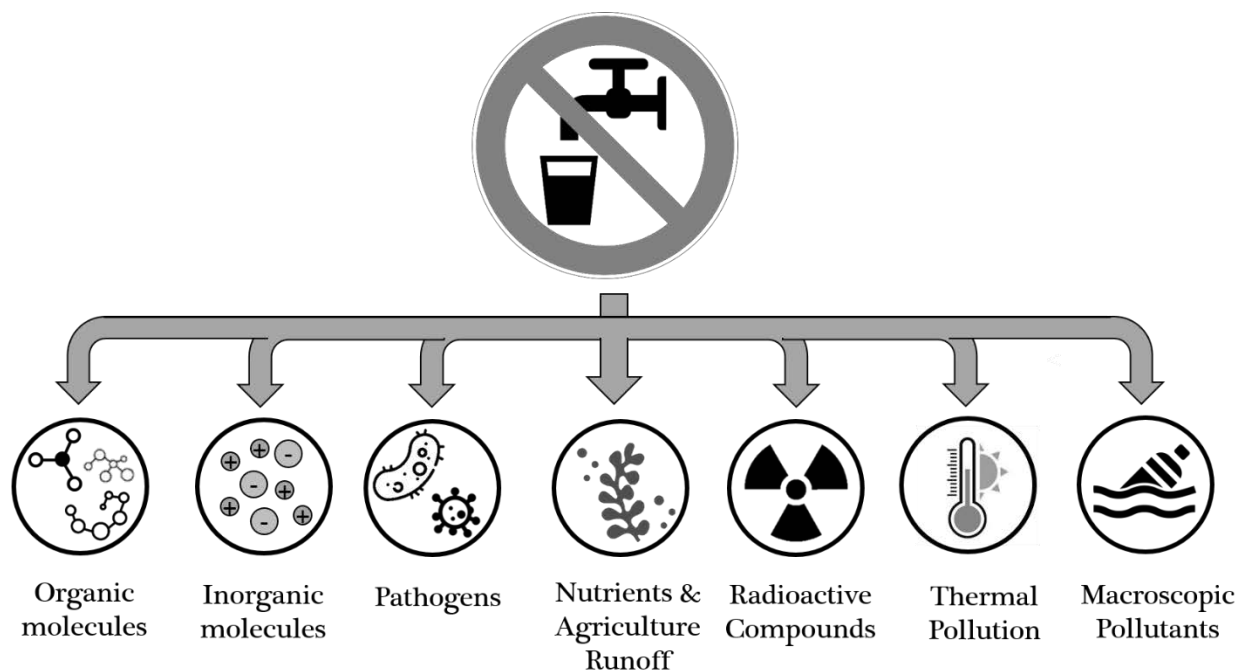
Figure 1.2. Water pollutants. The seven major classes of water pollutants found in water bodies.

These materials are further disintegrated into smaller particles, in the range of μm or nm, which can easily enter the food chain through small marine animals and plants. As an example, microplastics are pieces of plastic smaller than 5 mm in length[8,9] that come from larger manufactured products that are degraded within time by chemical processes. Microplastics include microfibers, microbeads and plastic pellets with an irregular shape. Thermal pollution of water comes from the discharges of thermal power plants and industries. An increase in the water temperature boosts bacterial metabolism, reducing the dissolved oxygen (DO) content present in water, thus altering the overall aquatic life[7]. Eventually, radioactive pollutants (i.e. cesium, plutonium, and uranium) emit harmful ionizing radiation that can damage the genome of living beings, inducing mutations in the DNA and ultimately provoking infertility[10] or serious diseases such as cancer[11].

1.1.3. Chemical Pollutants

One of the main sources of water pollution is chemical pollution. Chemical pollutants can be either organic or inorganic substances that are usually manufactured and purified by humans. Currently, there are more than 70,000 chemicals commercially available only in the USA, and

around 100 million registered worldwide[12,13]. Some examples of chemical pollutants are pesticides, petroleum and its derivatives, and heavy metals.

1.1.3.1. Pesticides
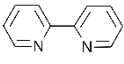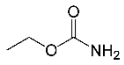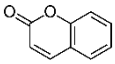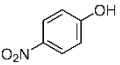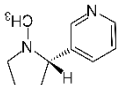
Pesticides are chemical compounds used to control pests (i.e. to prevent, contain, reduce or kill a harmful organism) in order to protect plants or animals from disease. Pesticides may be also used to keep water reserves, prevent epidemic and pandemic spreads, improve animal welfare, promote industrial processes and preserve home material. In any case, pesticides are toxic compounds intended to interfere with or modify fundamental physiological mechanisms on living organisms. In this regard, the major problem pesticides pose is the lack of selectivity against the target organisms[14–16]. For instance, broad-spectrum pesticides kill indiscriminately a great variety of organisms (i.e. insects), speeding up the ecosystem unbalance. Besides, several pesticide wastes can accumulate for years in soil and water, increasing the probability of contact with non-target animals, plants and, even humans. The first synthesized man-made pesticide was dichlorodiphenyltrichloroethane (DDT)[17], an insecticide synthesized in 1874 and which properties were elucidated in 1939. After the Second World War, the use of pesticides widespread all over the world, mainly due to the development of chemical industries and intensive farming.
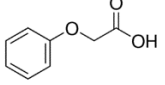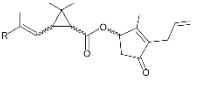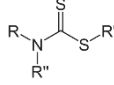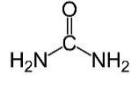
Pesticides can be classified according to different criteria, such as their specific target, physical state, danger level, intended use or chemical constitution. For example, pesticides may be used to control insects and mites (insecticides), fungi (fungicides), weeds (herbicides), bacteria (bactericides), rodents (rodenticides), worms (nematicides) and mollusks (molluscicides)[18]. Regarding the physical state, pesticides can be found in the form of gas, spray, powder, solid, liquid or tablets. Besides, the acute toxicity can be used to classify pesticides, from extremely dangerous to non-dangerous compounds, including three different intermediate categories (highly dangerous, dangerous and slightly dangerous)[18].

Pesticides can also be classified according to their final use. They are ubiquitous: agriculture uses up to 85% of the total pesticides produced worldwide, and up to 10% is used in public health to control vector-transmitted diseases (i.e. malaria) and eliminate illegal drug cultivations[17]. On the other hand, pesticides are useful to prevent weed growth in natural water reserves and to

avoid bacterial and fungi growth within the machines in the industry. Besides, home care pesticides are often used to control insects (i.e. ants and cockroaches). Nonetheless, for detection purposes, the most useful and widespread classification of pesticides is by their chemical structure and functional groups. Table 1.1 summarizes and updates the most important groups of pesticides used worldwide according to these criteria.

Chemical Class	Subgroups	Core Formula	Main Use	Mode of Action
Arsenic compounds	Inorganic, organic and arsenic gas		Fungicide, Herbicide, Insecticide, Rodenticide	Inhibition of pyruvate dehydrogenase
Bipyridylium compounds	Methyl-, alkane- & benzyl-derived		Herbicide	Interference with the photosystem I in plants
Carbamates	Aromatic & Non-aromatic		Insecticide	AChE reversible inhibition
Coumarin compounds	Simple coumarins & furanocoumarins		Bactericide, Fungicide, Rodenticide	Antagonists of vitamin K, inhibition of AChE & DNA fragmentation
Nitrophenols	Mono-, di- & tri-phenolic compounds		Fungicide, Herbicide, Insecticide	Oxidation and sulfonation of cytosolic molecules
Neonicotinoids	Nicotine-like molecules		Insecticide	Overstimulation of nicotinic-acetylcholine receptors (nAChRs)
Organochlorinated compounds	Chloroalkanes, Chlorinated alicyclic compounds & Chlorophenolic compounds	$-CH_2Cl$	Algaecide, Bactericide, Fungicide, Herbicide	Promoting *ROS* & epigenetic defects, alterations of the peripheral and central nervous systems & DNA damage
Organometallic compounds	Organotin, Organomercury, & Organocopper compounds	SnX, SnX_2, SnX_3, SnX_4 HgX, HgX_2 CuX, CuX_2	Acaricide, Bactericide, Fungicide, Herbicide, Miticide, Nematicide	Inhibition of mitochondrial enzymes (Sn), inhibition of thioredoxin reductase (Hg) & interference with the uptake of iron (Cu)

Organophosphorous compounds	Phosphate, Phosphonate & Phosphinate compounds	PO_4X_3, PO_3X_3, PO_2X_3	Herbicide, Insecticide, Parasiticide	AChE irreversible inhibition
Phenoxiacetic compounds	Alkyl-, Br-, Cl-, F- & I-derived phenoxyacetic acids		Herbicide	Hormonal disruptor in plants by mimicking auxins
Pyrethroids	1st & 2nd generation		Acaricide, Insecticide	Blockage of Na^+-channels in the neurons
Pyrazole compounds	Depending on the side chains connected to the pyrazole group		Insecticide	Blockage of GABA-gated chloride channels & GluCl-channels in the neurons
Thiocarbamates	O-isomeric & S-isomeric forms		Fungicide, Herbicide, Insecticide	Inhibition of nAch receptors and squalene epoxidase
Triazine compounds	Symmetrical & asymmetrical		Herbicide	Interference with photosystem II in plants
Triazole compounds	Symmetrical & asymmetrical		Fungicide	Inhibition of the synthesis of ergosterol
Urea compounds	Benzoylurea (BU) & Sulphonylurea (SU)		Herbicide, Insecticide	Inhibition of acetolactate synthase (BU) Inhibition of the synthesis of chitin (SU)

Table 1.1. Pesticides classification according to their chemical structure and functional groups.

Arsenic Compounds

Arsenic is a semi-metal element, which physical properties are intermediate between a metal and a non-metal. Arsenic compounds are classified into three main categories: inorganic arsenic compounds, organic arsenic compounds, and arsine gas[19]. Some examples of inorganic arsenic compounds are arsenic trioxide[20] (an anticancer drug) and arsenic pentoxide[21] (pesticide and wood preservative). Some examples of organic arsenic compounds are methylarsonic acid[22] (herbicide and fungicide) and cacodylic acid[23] (herbicide). Other uses of arsenic compounds include defoliation and cotton desiccation. Nonetheless, historically arsenic compounds have

mainly been used as pesticides for agricultural applications. Inorganic arsenic compounds were banned in the USA since 1993[24], and organic arsenic compounds were later on banned in 2009[25], except for monosodium methanearsonate (MSMA).

Arsenic compounds have been used as fungicides, herbicides, insecticides, and rodenticides. These compounds inhibit the enzyme pyruvate dehydrogenase[26] located in the matrix of the mitochondria, preventing the use of thiamine (vitamin B1), leading to the production of reactive oxygen species (*ROS*), and finally triggering cellular apoptosis[27]. Arsenic compounds are highly toxic for humans and the intake routes can be by inhalation and ingestion[24]. Acute toxicity induces vomiting, encephalopathy, and diarrhea[28]. Chronic exposure often leads to tumors, cancer, and heart disease[24].

Bipyridinium Compounds

Bipyridinium compounds are chemicals consisting of two pyridyl rings (C_5N_4H). Bipyridinium compounds are classified according to the regioisomery of the bipyridine group and the chemical groups connected to the pyridyl rings (i.e. methyl, formyl and cyano groups)[29]. The main use of bipyridinium compounds is as non-selective herbicides to kill grasses and weeds[30]. These herbicides interfere with the electron transfer process carried out by the iron-sulfur protein ferredoxin, located in the photosynthetic photosystem I of the plants, triggering the formation of *ROS*, causing lipid peroxidation and oxidative stress, and finally leading to cellular apoptosis[31]. Intoxication with bipyridinium compounds leads to liver, kidney and lungs damage[32]. Paraquat is the most widely used herbicide of this category. Bipyridinium compounds are also used as electrochemical labels and catalysts (i.e. 2,2'-Bipyridine)[33].

Carbamate Compounds

Carbamate compounds are organic compounds derived from carbamic acid (NH_2COOH). Carbamate compounds are classified as aromatic or non-aromatic carbamates[34]. The main use of carbamate compounds is as insecticides, but they are also used to synthesize polyurethane polymers. Carbamates inhibit reversibly the enzyme acetylcholinesterase (AChE), which catalyzes the breakdown of the acetylcholine neurotransmisor[35]. There are three main isoforms of AChE[36], which can be found both in invertebrate and vertebrate animals. In this regard, insects are the

main target of carbamate pesticides, but due to the presence of AChE also in the nerves and muscles of mammal animals and humans, poisoning and toxic effects are not rare to occur. Toxicity triggered by carbamate pesticides may lead to central nervous system alterations such as paralysis and asphyxiation in the most severe cases[37]. Carbaryl is one of the most commonly used carbamate insecticides worldwide since it is less toxic to humans than other carbamate pesticides such as carbofuran[38]. Regarding alternative uses, carbamate compounds are also used to develop anxiolytic and muscle relaxing drugs (i.e. pyridostigmine)[39].

Coumarin Compounds

Coumarin compounds are aromatic organic chemicals derived from coumarin ($C_9H_6O_2$). Coumarin compounds are classified as simple coumarins or furanocoumarins, as well as according to the chemical groups found on the side chains out of the coumarin aromatic rings[40]. Coumarin compounds have several applications, highlighting those related to the medicine (i.e. warfarin, anticoagulant)[41] and the control of pests (i.e. brodifacoum, rodenticide)[42]. As pesticides, coumarin compounds may behave as rodenticides, fungicides, and bactericides[43]. On the one hand, most coumarin compounds block the regeneration and recycling of vitamin K[44], leading to uncontrolled bleeding and hemorrhage in mice and rats. On the other hand, some coumarin compounds have also been reported to inhibit AChE and trigger DNA fragmentation[43]. Coumarin compounds are normally not toxic to humans at the concentrations used to kill rodents, but overexposure to higher doses may lead to hepatoxicity and internal hemorrhage in susceptible groups of human population[45].

Nitrophenol Derivatives

Nitrophenol derivatives are organic compounds derived from nitrophenol ($HOC_6H_{5-x}[NO_2]_x$). Nitrophenol has, in turn, three isomeric forms: *o*-nitrophenol, *m*-nitrophenol, and *p*-nitrophenol. The phenolic ring can also be connected to two or three NO_2 groups, yielding di- and tri-nitrophenols[46,47]. Nitrophenolic compounds can be directly used as herbicides, fungicides, and insecticides; or used as intermediates in the synthesis of more complex pesticides[48,49]. They trigger biological oxidations and cytosolic sulfonation of small molecules in the cytoplasm, leading to oxidative stress and cellular apoptosis[50]. Some nitrophenol derivatives are also used as pigments and chemicals for rubber and leather treatments[51]. Regarding the toxicological

effects on humans, nitrophenols are poisonous compounds that may cause eye, skin and respiratory tract irritation. In contact with internal organs, nitrophenol leads to the formation of methemoglobin and subsequent cyanosis, confusion, and unconsciousness[52,53].

Neonicotinoids

Neonicotinoids are structural analogs of nicotine. Nicotine is a bicyclic compound containing a pyridine cycle (5 C atoms and 1 N atom) and a pyrrolidine cycle (4 C atoms and 1 N atom). In this regard, neonicotinoids mimic nicotine biochemical activity by binding to the nicotinic acetylcholine receptors (nAChRs) and triggering their overstimulation[54]. While nAChRs' low activation causes nervous stimulation, excessive activation causes paralysis and ultimately death. Neonicotinoids are mainly used as insecticides because nAChRs are present in the central nervous system of insects[54,55]. These receptors can also be found in the central and peripheral nervous systems of mammals, whereby the selectivity of neonicotinoids lies in the structural differences of the nAChRs present in insects and mammals[56,57]. Nonetheless, neonicotinoids are highly toxic to a broad range of insects, including honeybees[55,58], having a dramatic impact on the ecosystem's biodiversity. Besides, side effects can also occur in humans, including infertility, hepatoxicity, neurotoxicity, and genotoxicity[55]. Some examples of neonicotinoids are acetamiprid, imidacloprid and thiamethoxam[59].

Organochlorinated Compounds

Organochlorinated compounds (OCs) are organic compounds containing at least one covalently bonded atom of chlorine. OCs are classified according to the chemical structure (chloroalkanes, chlorinated alicyclic compounds, and chlorophenolic compounds) and to the number of chlorine atoms present in the molecule (mono-, di-, tri-, tetra- and pentachlorophenol)[60]. OCs are used as algaecides, bactericides, fungicides, and herbicides[61,62]. Depending on their specific chemical structure, OCs cause a great variety of damages at the biochemical and cellular levels, inducing different toxic effects. For example, trichloroacetic compounds trigger epigenetic alterations in the DNA and oxidative stress[63]. On the other hand, DDT-like compounds (dichlorodiphenyltrichloroethane) cause hyperexcitability on the peripheral nervous system[64,65], whereas chlorinated cyclodienes trigger a widespread depression of the

nervous system[66,67]. Finally, chlorophenols directly damage DNA by inducing mutations and structural alterations of the DNA double strand[68].

OCs are also commonly used as disinfectants[68] (chlorophenolic compounds), electrical insulators and heat transfer agents[69] (polychlorinated biphenyls), flame retardants[70] (chloroalkanes) and substrates for the fabrication of plastics[71] (vinyl chloride). Some examples of organochlorinated pesticides include trichloroacetic acid[72] (herbicide), pentachlorophenol[61] (algaecide, fungicide, herbicide, and insecticide) and endosulfan[73] (chlorinated cyclodiene; acaricide and insecticide). OCs pose a risk for human health since some of them have proven to be carcinogenic and cause severe renal and neurological defects[61,74].

Organometallic Compounds

Organometallic compounds are organic compounds containing at least one covalently bonded atom of metal. In the case of organometallic pesticides, tin (Sn), mercury (Hg) and copper (Cu) are the most used metallic atoms. There exist a great variety of organometallic pesticides with different biological effects, including acaricides, bactericides, fungicides, herbicides, miticides and nematicides[75–78]. Tin-based organometallic compounds are classified as organotin halides, organotin hydrides, organotin oxides, organotin hydroxides, and stannanes[79]. Tributyltin (TBT) is an organotin compound commonly used as an anti-fouling paint and as an ingredient in some disinfectants[80,81]. Mercury-based organometallic compounds are classified as elemental mercury, inorganic mercury compounds, and organic mercury compounds[78,82]. Thiomersal (ethyl(2-mercaptobenzoato-(2-)-*O,S*) mercurate(1-)sodium, IUPAC name) is an organomercury compound formerly used as a bactericide[83]. Copper-based organometallic compounds include a pool of copper-based organic and inorganic compounds such as copper sulfate, copper oxide, and copper octanoate[84,85]. Copper sulfate is used as an algaecide and as an herbicide[84,86].

Tin-organometallic pesticides inhibit the ATPase activity and destroy the pH gradient in the mitochondria. Besides, they cause microtubule disassembly and disruption, and inhibition of several enzymes, including cytochrome P-450, leading to cellular apoptosis[87]. Mercury-organometallic pesticides inhibit selenoenzymes (i.e. thioredoxin reductase), leading to oxidative stress and cellular apoptosis[88]. Copper-organometallic pesticides interfere with the uptake of iron and other nutrients essential for the plants and fungi's metabolism, as well as induce

oxidative stress[77,89,90]. Other uses of organometallic compounds include catalysts (Sn-compounds)[91], sensing devices (Hg-compounds)[92] and coloring agents (Cu-compounds)[93]. Organometallic compounds are toxic to humans at different levels depending on their chemical structure and the intake route. The toxic effects might include bronchitis and endocrine disruption for Sn-compounds[94], central nervous system alterations (i.e. Minamata disease)[95] and kidney toxicity for Hg-compounds, and skin and respiratory irritation for Cu-compounds[96].

Organophosphorus Compounds

Organophosphorus compounds (OPs) are organic compounds containing at least one covalently bonded atom of phosphorus. OPs are classified according to the chemical valence of the phosphorus element: phosphorus (III) and phosphorus (V), as well as the chemical structure of the entire molecule (i.e. phosphates, phosphonates, phosphorothioates, phosphoramidites, etc.)[97]. OP pesticides are mainly used as anthelmintics, ectoparasiticides, herbicides, and insecticides[98]. OPs covalently bind to AChE and inhibit it irreversibly, behaving as neurotoxins that lead to muscle spasms and ultimately death[97,99]. Parathion, malathion, and diazinon are some examples of OP pesticides[100]. Other OPs are used as flame-retardants (i.e. triphenyl phosphate)[101]. OPs can be toxic for humans through inhalation, ingestion and dermal absorption, and toxic effects can be acute or chronic. In this regard, OPs have been classified as possible carcinogens[102], and acute toxicity leads to neurotoxic effects, even at low levels of exposure[97].

Phenoxiacetic Compounds

Phenoxiacetic compounds stem from phenoxiacetic acid. They are classified according to the functional groups bonded to the aromatic ring of the molecule, which can be alkyl and halogen groups (F, Cl, Br and I)[103]. Phenoxiacetic compounds are used as herbicides because they behave as hormonal disruptors in plants. More specifically, phenoxiacetic compounds mimic the structure of auxins, a class of plant hormones that play a critical role in plant growth and development[104,105]. These herbicides induce an unsustainable growth of the plants, finally leading to plants' death. An example could be 2,4-dichlorophenoxyacetic acid, a herbicide used to control weeds[106]. Other phenoxiacetic compounds are used as flavoring ingredients (i.e. phenoxiacetic acid)[107] and antidiabetic drugs (i.e. rosiglitazone)[108]. Phenoxiacetic compounds are safe for

humans at low doses, but high doses may produce acute toxic effects such as eye irritation[109], while chronic toxicity might lead to the formation of tumors and cancer development[106].

Pyrazole Compounds

Pyrazole compounds are organic compounds derived from pyrazole, a heterocycle containing three atoms of carbon and two atoms of nitrogen ($C_3H_4N_2$). Pyrazole compounds are classified according to the side chains connected to the pyrazole group (i.e. alkyl, phenyl). For example, fipronil is a pyrazole compound connected to four different chemical groups (amino, carbonitrile, halogenic phenol, and halogenic sulfinyl groups) that induces oxidative stress and widespread damage to lipids, DNA and intracellular proteins[110]. Pyrazole compounds are mainly used as insecticides, but some of them also have bactericide, fungicide, and herbicide activity[111]. Their insecticide activity comes from the blockage of the γ-aminobutyric acid-gated chloride (GABA) channels and glutamate-activated chloride (GluCl) channels present in insects[112]. Whereas GluCl channels are only present in protostome invertebrates[113] (i.e. arthropods, annelids, and mollusks), GABA-gated chloride channels are also in present in humans. Therefore, the selectivity of pyrazole insecticides arises from their more specific and stronger binding to the insect GABA-gated chloride channels. Other pyrazole compounds (i.e. chlorfenapyr and tebufenpyrad)[114,115] inhibit the complex I enzymes found in the mitochondria, disrupting the production of intracellular ATP, and finally leading to cellular death. Pyrazole insecticides may produce acute neurotoxic effects in humans (i.e. headache, tremors, and convulsions), and tumors and cancer upon chronic exposure[116]. Eventually, some pyrazole compounds are used as therapeutic drugs due to their analgesic and anti-inflammatory activity[111].

Pyrethroids

Pyrethroids are organic compounds analogs of pyrethrins, natural organic compounds produced by the plant *Tanacetum cinerariifolium*[117]. Pyrethroids consist of a molecule of chrysanthemic acid whose side chains can be alkyl, halogen, cycloalkyl and aromatic groups. Pyrethroids are classified according to their chemical nature, or the time they were synthesized (1st, 2nd, 3rd and 4th generation)[117]. They are mainly used as acaricides and insecticides. Bifenthrin is an example of a pyrethroid insecticide[118]. Pyrethroids behave as excitotoxins, preventing the closure of the voltage-gated sodium channels in the neurons[65]. Consequently, the nerves cannot

repolarize, paralyzing the organism and leading to death. The voltage-gated sodium channels are found both in insects and mammals, but most mammals can break down pyrethroid molecules at low doses[117]. However, cats are especially susceptible to pyrethroids since they lack the enzyme glucuronidase, which helps to detoxify the pyrethroids in the liver[119,120]. In this regard, pyrethroids have proven to be less toxic for humans than OPs and carbamate compounds, causing respiratory irritation if inhaled, but they are strongly toxic for honeybees and a wide range of aquatic organisms[28,117,119].

Thiocarbamates

Thiocarbamates are organic sulfur-compounds derived from carbamic acid. Thiocarbamates are classified according to the isomeric form of the thiocarbamate ester as O-isomers or S-isomers. Thiocarbamates are widely used in agriculture as fungicides, herbicides, and insecticides, but they are also used as biocides for household care products and several industrial applications. Some examples are tolnaftate (fungicide)[121], benthiocarb (herbicide)[122] and cartap (insecticide)[123]. On the one hand, fungicide thiocarbamates inhibit the enzyme squalene exposidase[121], hindering the synthesis of ergosterol, an essential compound in the fungal cellular membranes. On the other hand, herbicide thiocarbamates induce oxidative stress in plants through the formation of sulfoxide compounds[124]. Lastly, insecticide thiocarbamates are ion channel blockers of the nAChR[123]. Thiocarbamates show generally low toxicity to mammals, including humans, being skin and eyes irritation the most common side effects observed upon exposition. Nonetheless, some specific thiocarbamates might produce nausea, dizziness, ataxia and even convulsions[84].

Triazine and Triazole Compounds

Triazine and triazole compounds are nitrogen-containing organic heterocycles whose molecular formula is $C_3H_3N_3$ and $C_2H_3N_3$, respectively. Triazine and triazole compounds are classified according to the different isomeric and tautomeric forms of the heterocycles. While triazine compounds are fundamentally used as herbicides[125], triazole compounds are more commonly used as fungicides. Some examples of triazine compounds include atrazine and simazine[126], and some examples of triazole compounds include ketoconazole and tebuconazole[127,128]. On the one hand, triazine compounds interfere with the photosynthetic

system of the plants through the inhibition of the plastoquinone-binding protein of photosystem II, located on the thylakoid membrane of chloroplasts[84]. Consequently, the electron transport process is interrupted, resulting in the plant's death. On the other hand, triazole compounds inhibit the enzyme lanosterol 14α-demethylase, preventing the conversion of lanosterol to ergosterol[129], thereby harming the fungal cellular membrane integrity. Triazine compounds have generally low toxicity to mammals. However, some triazine compounds are skin irritators and might provoke irritability, anorexia, and hypothermia after ingestion, among other symptoms[84]. Additionally, triazole compounds may inhibit the enzyme aromatase[130], essential for the biosynthesis of estrogens, behaving as endocrinal disruptors. Regarding other uses, triazine compounds are often used as chemical reagents in organic synthesis[131], and triazole compounds are used as antifungal drugs to treat fungal infections.

Urea Compounds

Urea compounds are organic chemical compounds derived from urea ($CO[NH_2]_2$). Urea-based pesticides encompass three major categories known as benzoylureas, phenylureas, and sulfonylureas[132]. Benzoylureas are chemical derivatives of benzoylurea ($C_8H_8N_2O_2$) that act as insect growth regulators by inhibiting the biosynthesis of chitin[133], the primary component of insects' exoskeleton. Diflubenzuron is an example of benzoylurea insecticide[133]. Phenylureas are chemical derivatives of phenylurea ($C_8H_{10}N_2O$) that inhibit the plastoquinone-binding protein of the photosystem II in plants and algae, interrupting the electron transport chain, and finally leading to the plant's death[134]. Diuron is probably the most commonly used phenylurea worldwide[135]. Sulfonylureas are chemical derivatives of sulfonylurea (CH_2NO_3S) containing two additional side-chains composed of a variety of different chemical groups. They are classified as 1st, 2nd and 3rd generation sulfonylureas. Sulfonylureas are mainly used as herbicides due to their ability to inhibit the acetolactate synthase[136], an enzyme present in plants and some microorganisms involved in the biosynthesis of the amino acids valine, isoleucine and leucine. An example is flazasulfuron, a sulfonylurea herbicide used to prevent the growth of pre-emergent plants and kill post-emergent plants in a matter of days[137]. Some other sulfonylureas are used as antidiabetic drugs to treat diabetes mellitus type 2 (i.e. glimepiride) by stimulating the secretion
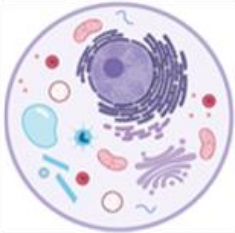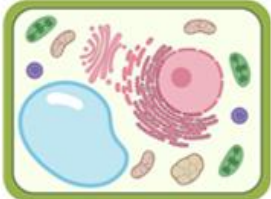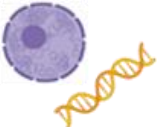
of insulin by the β-cells present in the pancreas[138]. Therefore, some toxic effects upon human exposure to herbicide sulfonylureas may include hypoglycemia and headache.

The following images summarize the cellular and synaptic targets of all the aforementioned classes of pesticides (Figure 1.3. and Figure 1.4.).

Enzyme / Receptor	Pesticide
AChE*	• Carbamates • Coumarin compounds • Organophosphates
Nicotinic-ACh Receptor	• Neonicotinoids • Thiocarbamates
Na⁺ Channels	• DDT-like compounds • Pyrethroids
Glutamate-activated Chloride Channel	• Pyrazoles
GABA Channels	• Chlorinated cyclodienes • Pyrazoles
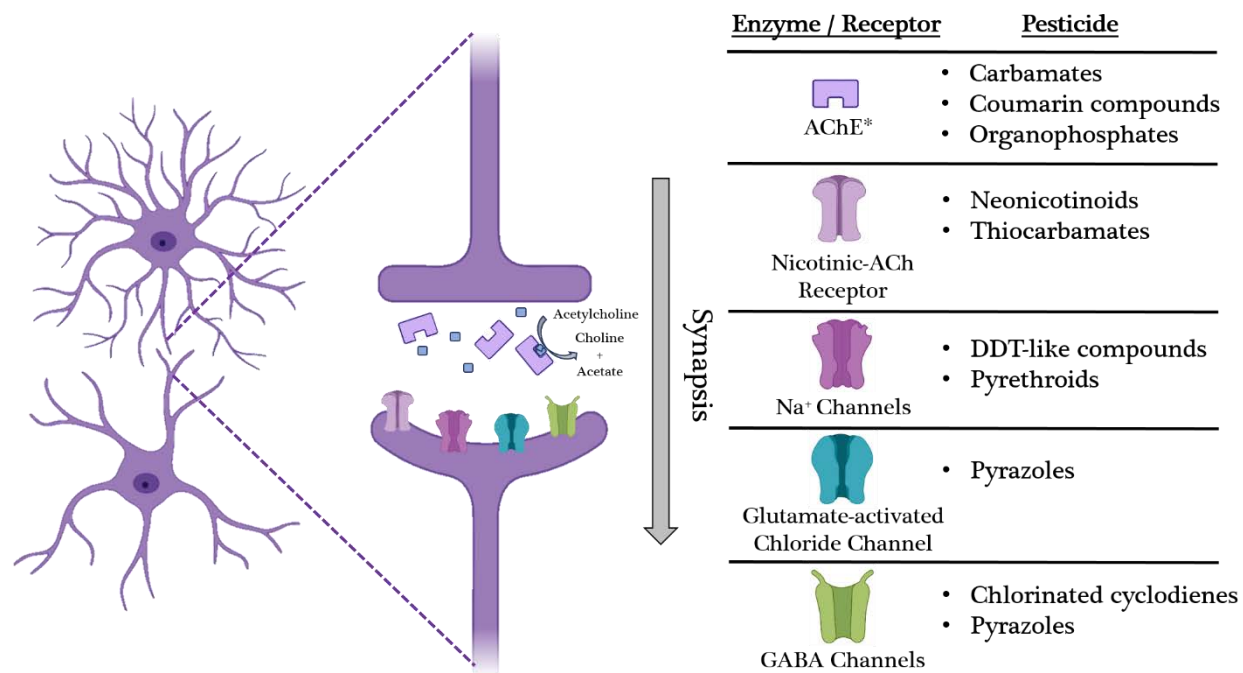
Figure 1.3. Pesticides and their synaptic targets. The diagram shows two neurons undergoing synapsis, the related enzymes and receptors, and the corresponding pesticides targeting these neuroreceptors and enzymes. (*) AChE = acetylcholinesterase.

Figure 1.4. Pesticides and their subcellular targets. The diagram shows the three main types of cells, different organelle and the corresponding families of pesticides targeting these subcellular locations.

1.1.3.2. Heavy Metals and Petroleum

Heavy Metals

Heavy metals are metallic elements with specific properties such as high density (3.5-7 g·cm^{-3}) and high atomic weight. Water pollution with heavy metals often arises from mining and other industrial activities. The most common heavy metals found in waters are arsenic (As), cadmium (Cd), chromium (Cr), copper (Cu), nickel (Ni), lead (Pb), mercury (Hg), thallium (Tl) and zinc (Zn)[139]. These heavy metals are not biodegradable, and though some of them are essential for humans' metabolism at low concentrations, higher concentrations often cause toxicity.

The following list summarizes the uses of these heavy metals, the pollution inputs of them into the water bodies, and their toxic effects on the environment and human's health:

- Arsenic: Arsenic compounds have historically been used as healing agents to treat several diseases such as leukemia and psoriasis[27]. More recently, roxarsone and arsanilic acid were still being used as feed additives for swine and poultry in some countries, including the US and Australia[24]. Pollution inputs often come from industrial processes and natural geological sources leaching into water bodies (i.e. aquifers)[27]. Arsenic pollution is a relevant issue in Bangladesh and West Bengal (India)[27]. Arsenic is not only a carcinogen but also a powerful poison, whose acute ingestion usually leads to death within one to four days.

- Cadmium: Cadmium is a habitual element found in paints, batteries and some plastics. Therefore, the main pollution inputs come from non-recycled batteries and industrial wastewaters. Cadmium is strongly toxic for humans, even at low concentrations[139]. Cadmium is considered a carcinogen since it can inhibit the enzymes involved in DNA reparation, as well as other *ROS* (Reactive Oxygen Species) detoxifying enzymes (i.e. catalase and superoxide dismutase)[140]. As an example, the *itai-itai* disease is a cadmium-poisoning related disease[141].

- Chromium: Chromium is used to produce stainless steel, manufacture paper, and tan leather cloths. It enters the ecosystem mainly through industrial wastewaters. Chromium inhibits the enzymes catalase and glutathione reductase, thereby increasing the

concentration of intracellular *ROS*, leading to lipid peroxidation and cell membrane's damage[140]. Chromium can produce irritation through inhalation, ingestion or even by skin contact, leading to more serious symptoms such as hemorrhagic gastroenteritis and acute renal deficiency[142].

- Copper: Copper is an essential element (micronutrient) that is required by most living beings (plants, animals and some microorganisms). It constitutes a key cofactor for some metalloenzymes and is involved in the formation of red blood cells[139,143]. Copper has been used since the prehistory for the construction of rudimentary tools, until nowadays for the production of wires and other electrical components[139]. Nonetheless, the intake of high concentrations of copper by drinking polluted waters leads to stomach and kidney problems in humans[139,144]. Furthermore, copper is extremely toxic to several aquatic organisms, even when found at low concentrations in water[139,145].

- Nickel: Nickel is a metallic element mainly found in volcanic rocks, and is used in diverse industrial applications such as the production of stainless steel, coins, and batteries[139,146]. Nickel is also necessary for the synthesis of red blood cells in humans, but it becomes toxic at high doses and longer exposure times[139]. It has been hypothesized that Ni atoms may replace Mg atoms in the double-strand DNA, enhancing chromatin condensation and triggering DNA methylation, resulting in important epigenetic modifications[63]. Nickel poisoning leads to liver toxicity, heart damage, and even cancer[139,146].

- Lead: Lead is used for the production of bullets, ship ballasts, and scuba diving weight belts. The plumbing pipes systems are the main sources of pollution of drinking water with lead, especially in old houses built in the first half of the 20th century. Lead atoms are highly toxic because they hinder the hemoglobin synthesis and disrupt the central nervous system[139]. Besides, lead also produces chlorosis and bleaching in plants exposed to Pb-polluted waters[139].

- Mercury: Mercury is used for the manufacture of thermometers, barometers, dental amalgams, and fluorescent lamps. Industrial wastewaters are the main mercury inputs in natural water bodies. Mercury can be inhaled or ingested, damaging severely the red blood cells by inducing *ROS* production[83]. Mercury is known to be mutagenic and cause

neurologic disabilities[78,139]. For example, Minamata disease is a neurological disorder caused by mercury poisoning[95].

- Thallium: Thallium is a rare metallic element used as an infrared optical material, as a photoresistor, and for nuclear medicine scanning. Thallium pollution of waters is not common. Upon ingestion, Tl^+ ions mimic K^+ ions, entering the cells through the potassium ionic channels. Once inside the cell, Tl^+ ions interact with sulfur ligands (i.e. cysteine), interfering with many cellular processes (i.e. regulation of oxidative stress and glutathione metabolism)[147]. The symptoms provoked by thallium poisoning are complex and nonspecific, including anxiety and delirium, which might lead to coma and death[148].

- Zinc: Zinc has several applications in the industry, highlighting the galvanization of steel and iron-made pieces and the fabrication of alloys such as bronze and brass. Zinc is also an essential micronutrient for plants and humans, which deficiency causes immunological depression, diarrhea, and psychological disorders[149,150]. In this regard, zinc is required for the correct working of many intracellular enzymes and transcription factors[149,151]. Nevertheless, high concentrations of zinc in water provoke phytotoxic effects and muscular disorders in humans after ingestion[139]. In this regard, several human activities such as mining, coal combustion, and steel processing might release traces of zinc into the soil and the rivers, rising the zinc concentration above the safety levels[152].

Petroleum

Petroleum is a natural hydrocarbon found beneath the Earth's surface that is used to produce a huge variety of products such as gasoline, plastics, asphalt, and kerosene. Therefore, it is primarily used as a source of energy for transport, heating, and lighting. Petroleum is formed after a large number of dead organisms are buried under sedimentary rocks undergoing intense heat and pressure[153].

Nowadays, humankind has a strong dependence on petroleum to produce energy and several manufactured products. However, petroleum sources underneath the Earth's surface are limited. Petroleum itself has limited toxicity on humans, mainly irritation after skin contact[154]. The ingestion of petroleum may lead to mild symptoms, such as nausea and diarrhea[154].

On the other hand, petroleum-derived oils pose a severe risk to marine life, and ultimately to humans as well[155]. Some oils derived from petroleum, together with some additives they contain, can reach the lungs by aspiration, leading to acute pneumonitis. Besides, a huge amount of petroleum-derived products and oils are transported by sea in freighter ships. When any of these ships break down, tons of a complex mixture of hydrocarbons together with additives (i.e. sulfur and nitrogen compounds), are released into the water[155]. Consequences are catastrophic. Some examples are Gulf War oil spill (the Persian Gulf, 1991, > $1.5 \cdot 10^6$ tons)[156], Ixtoc I oil spill (the Gulf of Mexico, 1979, > $4.5 \cdot 10^5$ tons)[157] and Atlantic Empress/Aegean Captain oil spill (the Caribbean Sea, 1979, > $2.5 \cdot 10^5$ tons)[158].

Several oil spills have also taken place around the Spanish coasts, being the Prestige oil spill occurred in November 2002, the most recent. The tank of the ship burst after a storm, releasing more than 63,000 tons of heavy fuel oil into de Atlantic sea, near the Galician coast. As a result, more than 1,000 km of coastline was covered by fuel, thousands of animals died, and environmental-related problems lasted for years[159].

1.1.4. Biological Pollutants

Pathogens are disease-causing microorganisms. Some of these microorganisms can be transmitted by water, producing waterborne outbreaks and serious diseases. Waterborne pathogens can be either bacteria, viruses, protozoa, algae or worms (Figure 1.5). Therefore, water disinfection is required to achieve drinkable water standards and the optimal treatment of wastewaters.

1.1.4.1. Bacteria

Bacteria are prokaryotic cells that can be free-living or interact with animals and humans either through symbiotic or parasitic relationships. Our own body has more bacteria cells than human cells, mainly living in the guts but also all over the skin, in our nose, mouth, throat, stomach, and genitals[160]. Water is also a common ecosystem for bacteria, and their presence is almost inevitable. Therefore, the parameter that indicates whether a specific source of water is drinkable or not, is not the presence of bacteria but their concentration (CFU/mL). Besides, many different bacteria species can be found in water, making the detection and quantification of all

of them nearly impossible. In this regard, only a few "indicator bacteria" are analyzed and quantified, which numbers suggest or not possible contamination with other pathogenic microorganisms[160].
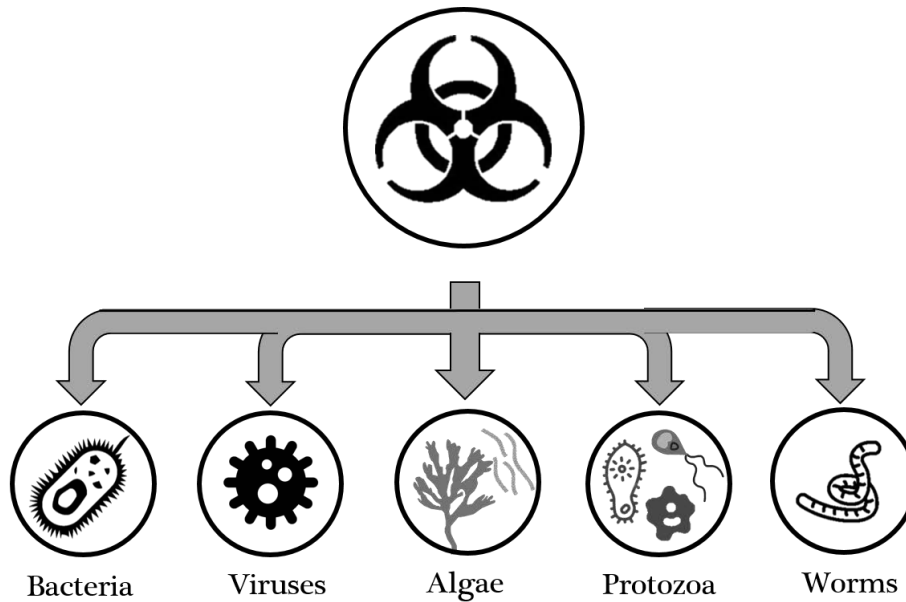
Figure 1.5. Biological pollutants. The five major classes of biological pollutants found in water bodies.

Coliforms are the main indicator of fecal pollution of waters. Most coliforms live inside the human and mammal guts and encompass a heterogeneous group of bacteria such as *Escherichia coli*, *Enterobacter* and *Klebsiella*. Generally, the presence of coliforms above a certain concentration (≥ 1 CFU per 100 mL in the US and EU countries), and more specifically *E. coli*, indicate fecal contamination of water, thereby unsuitable for human consumption[160]. The most common and important bacteria related to waterborne outbreaks are explained below.

Burkholderia pseudomallei

Burkholderia pseudomallei is a gram-negative, aerobic, motile, rod-shaped bacterium that can infect a wide range of animals and humans. *B. pseudomallei* is endemic from tropical and subtropical regions worldwide[161]. The infection intake route is mainly through the ingestion of contaminated water. In such cases, a disease named "melioidosis" is likely to happen, whose symptoms go from localized cutaneous manifestations in the milder cases to sepsis and death (40% of mortality in untreated cases)[161]. It is estimated that *B. pseudomallei* infects ≥ $1.5 \cdot 10^5$ people/year, killing approximately $9 \cdot 10^4$ people/year, mainly in southeast Asia[162], China[163],

Taiwan[164], and northern Australia[162]. Diagnosis and identification of *B. pseudomallei* can be carried out by culture on blood and MacConkey agar, 16S rRNA sequencing, PCR, serological diagnosis (i.e. IHA or ELISA), metabolic profiling, and more recently by MALDI-TOF MS[165].

Campylobacter jejuni & Campylobacter coli

Campylobacter spp. is a genus of gram-negative, microaerophilic, motile, rod and spiral-shaped bacteria that can be transmitted by ingestion of contaminated food and water, as well as by fecal-oral route from infected animals or people[166]. *Campylobacter jejuni* and *Campylobacter coli* are the two main pathogenic species of this genus of bacteria. *Campylobacter spp.* provokes around 2 million infections only in the US every year[166], and is considered to be the most frequent cause of gastroenteritis worldwide[167]. Campylobacteriosis causes high fever (≥ 40 ºC), nausea, stomachache, and bloody diarrhea. Most people overcome the disease after 7-10 days, but the infection reappears in around 25% of the cases[166]. Detection of *C. jejuni* is mainly made by immunological tests and bacterial growth on selective media[166].

Clostridium botulinum

Clostridium botulinum is a gram-positive, anaerobic, motile and rod-shaped bacterium. *C. botulinum* typically lives in water and can form endospores that enable the bacteria to survive at high temperatures and salinity conditions[168]. *C. botulinum* produces the botulinum neurotoxin, which can be ingested together with the bacteria through contaminated food and water, causing botulism. This neurotoxin blocks the release of acetylcholine, paralyzing the muscles, and consequently may lead to death because of respiratory failure[169]. The ingestion of only a few nanograms of the botulinum neurotoxin can kill a person[170]. Diagnosis of *C. botulinum* toxin is carried out by ELISA tests with digoxigenin-labeled antibodies, the so-called "mouse lethality bioassay", and quantitative PCR[171].

Escherichia coli

Escherichia coli is a gram-negative, facultative anaerobe, motile and rod-shaped bacterium. Most *E. coli* strains are considered normal microbiota in humans' and mammals' guts. However, there are specific strains of *E. coli* considered pathogenic, referred to as enterovirulent *E. coli* (EEC). For example, the strain O104:H4 belongs to a pathogenic group named Shiga toxin-

producing *E. coli* (STEC), which produces Shiga toxins that trigger inflammation in the intestines, followed by bloody diarrhea[172,173]. Other strains of *E. coli*, named enterotoxigenic *E. coli* (ETEC) cause the traveler's diarrhea. Infection occurs upon the ingestion of contaminated food or water. ETEC cells attach to the intestinal lining, secreting enterotoxins that cause watery diarrhea[174]. On the other hand, enterohemorrhagic *E. coli* (EHEC) strains cause hemolytic-uremic syndrome (i.e. O157:H7), characterized by acute kidney failure and low red blood cells and platelets levels[172]. Finally, enteroinvasive *E. coli* (EIEC) and enteroaggregative *E. coli* (EAggEC) invade the intestinal walls, causing either acute or chronic diarrhea, especially in children[172,175]. Diagnosis of EEC infections is carried out by bacteria culture and isolation on growing media, ELISA tests, and multiplex PCR[174,175].

Legionella spp.

Legionella spp. is a genus of gram-negative, aerobic, motile and rod-shaped bacteria. There exist around 50 species of *Legionella,* among which *L. pneumophila* is well known to cause legionellosis. Legionellosis can, in turn, appear as Legionnaire's disease (atypical pneumonia) or Pontiac fever (mild upper respiratory infection)[176]. There is no human to human transmission of these bacteria but through inhalation of water droplets from contaminated sources (water cooling towers, air-conditioning cooling systems, and fountains)[177]. Once inside the body, *Legionella* infects alveolar macrophages, in the lungs, usually leading to pneumonia[176]. Nonetheless, this disease tends to affect more immunocompromised hosts, thereby water quality monitoring inside hospitals is extremely important to prevent outbreaks. The mortality rate is less than 5% in healthy patients with antibiotics treatment but raises to 60% for nosocomial infections[178]. *Legionella* is detected by culture on buffered charcoal yeast extract agar since it requires cysteine and iron to grow[166,176]. The incubation process is slow and may take up to 10 days to have a definitive result[176], whereby immunological tests or even PCR are commonly used to speed up the process[179].

Non-tuberculous mycobacteria

Non-tuberculous *Mycobacteria* are those species of *Mycobacterium* that do not cause tuberculosis or leprosy. The bacteria belonging to this group are considered to be opportunistic pathogens, and often cause pulmonary diseases other than tuberculosis, but also lymphadenitis,

skin disease, and other affections[180]. *Mycobacterium* bacteria are ubiquitous and can be found in water, soil, and animals. Non-tuberculosis *Mycobacterium* can colonize indoor water systems, natural water sources, pools, and pipes. Therefore, these bacteria can be transmitted through contaminated water and droplets[180]. The overall mortality rate caused by non-tuberculosis *Mycobacteria* is around 10%[181]. Diagnosis is made by radiographic evidence of the lungs, culture growth on Löwenstein-Jensen medium (3-4 weeks) and 16S ribosomal RNA sequencing[182].

Pseudomonas aeruginosa

Pseudomonas aeruginosa is a gram-negative, facultative anaerobe, motile and rod-shaped bacterium. It is considered as an opportunistic pathogen for humans, meaning that *P. aeruginosa* usually causes disease when the host is immunocompromised, has an altered microbiota or the integumentary barriers are damaged. Therefore, most *P. aeruginosa* infections are nosocomial infections that can cause a variety of different symptoms depending on the intake route (i.e. folliculitis, otitis, pneumonia, and bacteremia)[183]. *P. aeruginosa* can be transmitted not only by contaminated water but also by contaminated tools, through skin contact, inhalation, and ingestion. It is a worldwide distributed bacteria that can broadly survive in non-optimal environments, including distilled water and soil[184]. Diagnosis includes culture growing on MacConkey agar, biochemical tests (oxidase +) and pigment production (pyocyanin)[185].

Salmonella spp.

Salmonella spp. is a genus of gram-negative, facultative anaerobe, motile and rod-shaped bacteria that encompass 3 different species: *S. enterica, S. bongori* and *S. subterranean*. *Salmonella enterica* is further divided into six subspecies and several serotypes according to three cellular surface antigens: O antigen (cellular wall), H antigen (flagella), and Vi antigens (bacterial capsule)[186]. Subspecies of *S. enterica* are enteropathogenic bacteria that cause salmonellosis (acute gastroenteritis). The transmission of *Salmonella* is produced by the ingestion of contaminated water and food (mainly raw meat and dairy products)[186]. After infection, *Salmonella* colonizes the small and large intestines, provoking diarrhea and stomach cramps. It is estimated that around 100 million cases of salmonellosis occur worldwide every year, causing more than 150,000 deaths per year[187]. *Salmonella spp.* detection is carried out by culturing bacteria in growth media containing ferrous sulfate and real-time PCR[188,189].

INTRODUCTION

Salmonella typhi

Salmonella typhi is a species of *Salmonella spp.* responsible for the disease called typhoid fever. The main symptoms after infection are headache, abdominal pain, and vomiting, whereas diarrhea is not common. Typhoid fever can be transmitted by eating or drinking contaminated food and water with feces of infected people[190]. Without appropriate treatment, typhoid fever has a mortality rate of 10-30%[191]. Diagnosis is made by culturing bacteria (i.e. bismuth sulfite agar), performing immunological tests (i.e. Widal test, Typhidot, and Tubex test)[192–194] or detecting bacteria's DNA in biological samples (i.e. blood and feces)[195].

Shigella spp.

Shigella spp. is a genus of gram-negative, facultative anaerobe, motile and rod-shaped bacteria. There are four species of *Shigella spp*: *S. dysenteriae, S. flexneri, S. boydii,* and *S. sonnei*. *Shigella*, in turn, classified into serotypes and serogroups[166]. Shigellosis is produced after the ingestion of water polluted with *Shigella spp*. In this case, bacterial cells invade the epithelium of the colon, inducing inflammation and killing the invaded cells[196]. As a result, diarrhea and dysentery (bloody diarrhea) are expected to occur. More specifically, *S. dysenteriae* strains secrete an enterotoxin that often leads to the hemolytic-uremic syndrome[196]. The mortality rate of shigellosis was around 10-15% at the end of the 20th century, but since then it is steadily decreasing[197]. Diagnosis and identification of *Shigella spp.* are made by agglutination tests using adsorbed rabbit antisera[196].

Vibrio cholerae

Vibrio cholerae is a gram-negative, facultative anaerobe, a halophilic, motile, comma-shaped bacterium that is typically transmitted due to the ingestion of contaminated water[160]. Cholera is the waterborne disease provoked by *V. cholerae*. It is an endemic disease in many developing countries in Africa, South America and Southeast Asia[160]. It is estimated that between 1.3 and 4 million cases of cholera occur every year worldwide[198]. In this regard, there are two strains of *V. cholerae* of special importance due to their virulence and widespread distribution: O1 (Indonesia) and O139 (India and Bangladesh)[160]. After the ingestion of contaminated water, *V. cholerae* attaches to the epithelial cells in the small intestine, thrives and secrete an

enterotoxin that causes strong diarrhea and dehydration (≥ 20 liters/day)[160]. Without the intake of liquids and the appropriate electrolytes, death is certain. The mortality rate is around 50-60% in the non-treated cases[199]. Diagnosis and detection of *V. cholerae* cells are normally made by microscopic observation of comma-shaped bacteria in the aqueous feces of sick people[160].

Yersinia enterocolitica

Yersinia enterocolitica is a gram-negative, facultative anaerobe, motile, rod-shaped bacterium that is transmitted by the ingestion of contaminated water and food. Pathogenicity of *Y. enterocolitica* relies on the virulence factors that the bacteria might express depending on certain chromosomal and plasmid genes[200]. Infection with *Y. enterocolitica* leads to yersiniosis, causing acute diarrhea and other digestive symptoms. The gravest condition of the infection by *Y. enterocolitica* is the enteric fever, a potentially lethal disease[166]. *Y. enterocolitica* provokes almost 90,000 infections per year only in the US[166]. Diagnosis and detection of *Y. enterocolitica* cells are made by imaging studies (i.e. computed tomography scan), ELISA tests (detection of human IgG, IgA, and IgM against *Yersinia*), PCR and immunofluorescence assays[201].

1.1.4.2. Viruses, Protozoa and other Parasites

Not only bacteria but also viruses, protozoa, algae, and helminths can cause waterborne outbreaks. Viruses are the smallest known parasites that can replicate inside their host cells. Protozoa are unicellular eukaryotic cells that can be either free-living or parasitic. Algae are photosynthetic eukaryotic organisms that can be either unicellular or pluricellular, some of which produce toxins. Finally, helminths, more commonly known as parasitic worms, are large macroparasites (> mm). The following list summarizes some of these microorganisms and parasites[202]:

- Enteroviruses: Enteroviruses are those viruses able to infect the human intestinal tract. Enteroviruses do not produce any symptoms in many cases, but mild intestinal symptoms are not rare. They represent almost 40% of all waterborne outbreaks produced by viruses in the US[202]. Enteroviruses can be detected using reverse transcriptase PCR (RT-PCR), serological methods (i.e. IgM and IgG detection by ELISA tests), and virus typing (genome sequencing)[203].

INTRODUCTION

- <u>Hepatitis A (HAV) and E (HEV) viruses:</u> These viruses can be transmitted by contaminated water and food with feces, infecting the liver and causing hepatitis. Their prevalence is very common in developing countries. The hepatitis A virus is resistant to inactivation by heat and has a worldwide distribution, whereas the hepatitis E virus is more common in tropical countries and is responsible for the highest number of cases of hepatitis[204]. Diagnosis of hepatitis A is made by serological testing of IgM, IgA and IgG anti-HAV since the symptoms may be similar to other hepatitis viruses[205], whereas the diagnosis of hepatitis E is made by detection of IgM and IgG anti-HEV and detection of HEV RNA[206].

- <u>Other viruses:</u> This group encompasses norovirus, rotavirus, astrovirus & adenovirus. Noroviruses were first discovered in the late 1960s in the US, and are known to cause vomiting and diarrhea[202]. Rotaviruses often cause gastroenteritis in children and elderly people, especially in developing countries, causing thousands of deaths in Africa, Latin America, and Asia. On the other hand, astroviruses are known to be the major cause of acute diarrhea in children[207]. Eventually, adenoviruses are transmitted by contaminated water and are resistant to adverse chemical and pH conditions. Among different infections, adenoviruses can cause ear infection, conjunctivitis, tonsillitis, bronchiolitis, and also gastroenteritis in some cases[208]. These viruses can be detected by rapid enzyme immunoassays (EIA), ELISA tests and immunochromatographic assays[209,210].

- *Giardia lamblia*: *Giardia lamblia* is a unicellular flagellated protozoan that causes enteritis. It can infect not only humans but also dogs, cats, cattle and other livestock. It is transmitted by the fecal-oral route through contaminated water in the form of cysts (an inactive and more resistant form of the parasite). *G. lamblia* causes around 280 million cases of enteritis worldwide, especially in developing countries, leading to diarrhea, bloating and abdominal pain. *G. lamblia* infections are diagnosed by microscopic identification, fluorescent immunoassays, and PCR[211].

- *Cryptosporidium*: *Cryptosporidium* is a parasitic protozoan that causes watery diarrhea in humans. Infection is produced by the intake of contaminated water and food sources. The related disease is particularly serious in immunocompromised hosts, which cases can be fatal. Currently, there are nine *Cryptosporidium* species known to be able to infect

humans[212]. This parasite undergoes a complex life cycle, in part of which it adheres to the cells in the intestinal epithelium and access to the host cell cytoplasm, feeding off its nutrients[212]. Diagnosis often includes seeking antigens or oocysts in stool samples by bright-field stain visualization, immunofluorescent assays, ELISA tests, and immunochromatographic assays[212].

- Other protozoa: This group encompasses *Naegleria fowleri*, *Entamoeba histolytica*, *Toxoplasma gondii* & *Cyclospora cayetanensis*. *Naegleria fowleri* is a free-living amoeba that can become pathogenic, causing a lethal brain infection called naegleriasis. The infection starts after the ingestion of contaminated water, mainly from hot springs, ponds, lakes and swimming pools[213]. *Entamoeba histolytica* is another amoeba that can be transmitted by sexual or fecal-oral routes, mainly in tropical and subtropical areas. Infection with *E. histolytica* might be asymptomatic or cause fulminant dysentery[214]. *Toxoplasma gondii* is a parasitic protozoan that undergoes a complex life cycle, first infecting cats, from which infects humans and other mammals afterward. Ingestion of contaminated food and water leads to toxoplasmosis, especially problematic for pregnant women. Typical symptoms of toxoplasmosis are fever, headache and muscle pain[215]. Eventually, *Cyclospora cayetanensis* is also a parasite that can infect humans, causing cyclosporiasis. Cyclosporiasis is an endemic disease in some tropical countries that causes nausea, fatigue, abdominal pain and diarrhea. Diagnosis of these protozoa involves cerebral spin fluid analysis by magnetic resonance imaging for *Naegleria*, and serological tests (i.e. ELISA tests), PCR and microscopic observation for *Entamoeba, Toxoplasma* and *Cyclospora*[213–216].

- *Microcystis*: *Microcystis spp.* is a genus of freshwater cyanobacteria. Among the different species of *Microcystis*, *M. aeruginosa* is responsible for the production of harmful algal blooms and several neurotoxins (lipopolysaccharides) and hepatotoxins (microcystins), thereby causing water contamination and health and economic burdens worldwide. Microcystins are not only produced by *M. aeruginosa* but alto by other cyanobacteria. These toxins are non-ribosomal cyclic heptapeptides that inhibit the intracellular Ser/Thr phosphatases in terrestrial mammals after drinking contaminated water[217]. Microcystins

detection is usually made by liquid chromatography coupled with tandem mass spectrometry, while the algae themselves can be tracked by PCR[218,219].

- *Anabaena*: *Anabaena spp.* is a genus of cyanobacteria that includes some species that produce some of the most toxic cyanotoxins (i.e. anatoxin-a). *Anabaena*'s cyanotoxins bind to nAchR by mimicking acetylcholine. These toxins typically cause acute neurotoxicity, leading to loss of coordination, convulsions, and death by respiratory paralysis. The intake route of cyanotoxins is through the ingestion of contaminated water[220]. Detection of cyanotoxins includes ELISA tests, protein phosphatase inhibition assays, HPLC combined with mass spectrometry, liquid chromatography, PCR, and microarrays[221].

- *Ascaris lumbricoides*: *A. lumbricoides* is a parasitic nematode that infects humans causing intestinal and respiratory problems[222]. It is estimated that worldwide more than 1.3 billion people are infected with *A. lumbricoides*, out of which around 15% develop symptoms. Female worms can produce over 200,000 eggs per day, many of which are excreted through the feces. Infection occurs after the ingestion of contaminated food and water with eggs[222]. Diagnosis is mainly carried out by the floatation concentration Faust method[222].

- Other helminths: This group encompasses *Trichuris trichiura, Necator americanus*, *Taenia spp.* and *Schistosoma mansoni*. *Trichuris trichiura* is a parasitic helminth that causes trichuriasis after the ingestion of contaminated food or water. As a consequence, the worm colonizes the large intestine, producing diarrhea and anemia[223]. *Necator americanus* is another parasitic helminth that can penetrate throughout the healthy skin, invading different organs until it settles down in the intestines, where it feeds off the host's blood. This infection causes iron-deficiency anemia, diarrhea, and abdominal pain. It is estimated that *N. americanus* infects around 10% of the world's population[224]. On the other hand, *Taenia spp.* is also a parasitic helminth that can infect humans, causing taeniasis. Two main species of Taenia infect humans: *T. saginata* and *T. solium*. Symptoms are not usually more serious than weight loss or abdominal pain. However, if the parasites reach the ventricles, heart problems may arise[225]. Finally, *Schistosoma mansoni* is a

trematode that is estimated to infect around 230 million people worldwide. *S. mansoni* is transmitted by drinking fresh water contaminated with the feces of infected people. The related infection is asymptomatic in many cases, but fever, myalgia, headache, and abdominal pain often occur on travelers or adults that are exposed to the worm for the first time. Diagnosis is performed by quantification of *S. mansoni* eggs in urine, DNA detection in stool, urine and serum, and serological tests[226].

Overall, waterborne diseases cause millions of deaths worldwide every year. The majority of these diseases are also associated with important economic burdens. Figure 1.6. outlines both the main waterborne diseases and their etiological agents.
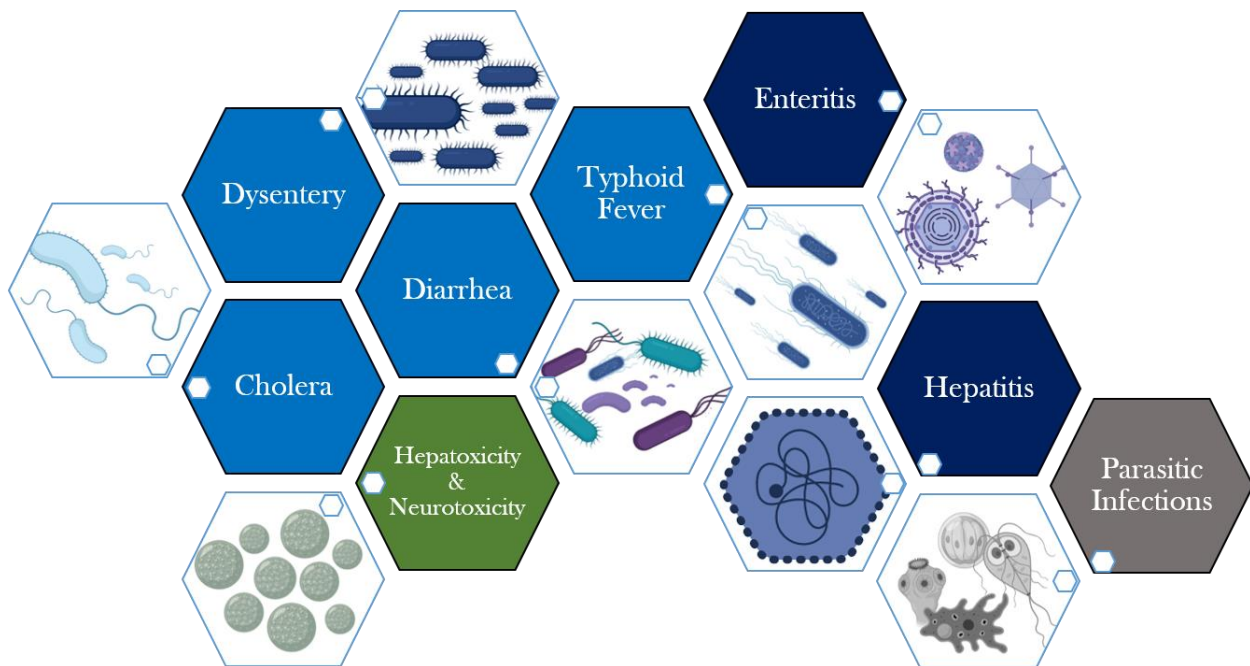
Figure 1.6. Waterborne diseases and etiological agents. List of the most common waterborne diseases and the associated microorganisms. The hexagons in blue highlight bacterial infections, those in dark blue highlight viral infections, the green hexagon highlights algae toxins outbreaks, and that one in gray highlights parasitic infections provoked by protozoa and worms.

1.1.5. European Union Regulation

European Union (EU) has launched several directives and regulations in the last years regarding the control of pollutants and contaminants in water. Directive 2013/39/EU states that "Chemical pollution of surface water poses a threat to the aquatic environment, […], and also poses a threat to human health. As a matter of priority, the causes of pollution should be identified […]".[227] Therefore, it is clear that legislation is required to limit and monitor water pollutants in drinking water.

The Drinking Water Directive was first established in the EU in 1998 and is regularly updated. Currently, all Member States are required to monitor a total of 48 parameters, divided into 2 microbiological parameters (*E. coli* and *Enterococci*), 26 chemical parameters (i.e. arsenic, lead, nickel, and some pesticides), and 20 indicator parameters to assess the organoleptic quality of the water (i.e. color and odor), physicochemical parameters (i.e. temperature and pH), and minimum required concentrations (i.e. alkalinity and hardness). The concentration thresholds of all these parameters are usually in compliance with the WHO guidelines[228,229].

The last update of this document was performed in 2018 and adds naturally present but harmful compounds to the list such as uranium; emerging contaminants such as perfluorinated compounds, and endocrine disruptors, such as bisphenol A and β-estradiol[228]. Besides, microplastics have been included as an issue of emerging concern, new microbiological parameters have been set to avoid the formation of bacterial biofilms, the uses of lead and chromium have been tightly restricted, and the limits for some emerging chemicals have been cut down.

Nowadays there still exist enormous challenges to achieve optimal water quality monitoring. First, new techniques to evaluate the toxicity of water are required in combination with the more traditional methods used to measure individual substances[81]. Second, the appearance of new chemical pollutants pushes the legislation to move forward faster to tackle their release into the water bodies. Third, more efforts are required to reduce both sewage pollution and industrial pollution of rivers and seas. Finally, securing sustainable management of water remains one of the key challenges in the EU[81].

In the EU, the good chemical status of water bodies is defined by setting limits on the concentration of certain pollutants named as priority substances. Good chemical status is achieved when none of these pollutants found in water exceed environmental quality standards. As an example, the pesticide atrazine, which used to control weeds, must be at lower concentrations than 2 µg/L in inland and other surface waters to comply with the environmental quality standards (EQS)[227]. Nonetheless, some chemicals have not only been restricted but also banned for further use in the EU. Tributyltin (TBT) was broadly used as an antifouling agent to protect the hull of the boats in the EU until 2008 when it was banned due to the adverse effects it causes on marine ecosystems[230]. On the other hand, pentachlorophenol (PCP) is a broad-spectrum pesticide used as an antimicrobial agent, wood preservative and detergent. It is highly persistent in the environment since it can persist in water from one to two decades[231]. The marketing and use of PCP were banned in the EU in 1991, except for restricted applications. From 2000, any substance containing more than 0.1% PCP (w/v) is prohibited within all the EU countries[232].

Regarding the presence of heavy metals in drinking water, there are slight differences in the legislation of the US, EU, and other countries (Table 1.2)[139,233].

	EPA (U.S.A.)	European Union	India
Arsenic (As) [mg·L^{-1}]	0.01	0.01	0.05
Cadmium (Cd) [mg·L^{-1}]	0.005	0.2	0.001
Chromium (Cr) [mg·L^{-1}]	0.1	0.5	0.1
Copper (Cu) [mg·L^{-1}]	1	3	0.01
Lead (Pb) [mg·L^{-1}]	0.1	0.5	0.1
Mercury (Hg) [mg·L^{-1}]	0.002	0.001	0.004
Nickel (Ni) [mg·L^{-1}]	0.1	0.1	0.1
Zinc (Zn) [mg·L^{-1}]	5	5	0.1

Table 1.2. Maximum allowed concentrations of heavy metals in the drinking water in the United States, European Union, and India.

INTRODUCTION

On the other hand, microbiological pollution often comes from the contamination of drinking water with sewage waters. In this regard, microbiological indicators ease the assessment of the water quality without the need for detecting and quantifying all the different pathogenic microorganisms that can be found in water. An ideal indicator should be universally present in the feces of humans and warm-blooded animals, easy to detect and enumerate, not able to grow in natural water bodies and be removed similarly to waterborne pathogens after water treatment to track the effectiveness of these water treatments[229]. In this regard, the EU Directive 80/778/EEC recommends fecal coliforms, total coliforms, and fecal streptococci as the microbiological indicators for water fecal pollution[229]:

- Coliforms are gram-negative, non-spore forming, oxidase negative, rod-shaped facultative anaerobic bacteria that can ferment lactose at 36 ºC within 24-48 h[229].
- Fecal coliforms are coliforms that can ferment lactose at 44.5 ºC within 24 hours[229].
- Fecal streptococci are gram-positive, catalase-negative cocci that possess the Lancefield group D antigen, and can grow on selective media for *Enterococcus* and bile aesculin agar at 45 ºC[229].

According to the EU directive 98/83/EC, *E.* coli and fecal streptococci are required to be absent in 100 mL of water to consider it as drinking water[234]. Nevertheless, it is estimated that up to 90% of the water samples contaminated with feces are overlooked because some pathogens do not correlate very well with coliform bacteria, some indicators might be stressed or injured during an inadequate water treatment thereby making them unable to grow and multiply in the laboratory, and some viruses and parasites are also more resistant to conventional water treatment methods than indicator bacteria[229]. For this reason, the legislation in the EU concerning the microbiological quality of drinking water added in 2018 *Clostridium perfringens* and somatic coliphages to the pre-existing list.

In this regard, European countries have achieved outstanding success in water treatment and sanitation, reducing waterborne outbreaks during the last decades. However, the European Food Safety Authority (EFSA) reported in 2013 more than 5,000 waterborne and foodborne outbreaks in the EU countries, including Iceland, Norway, Liechtenstein and Switzerland as well[235]. By analyzing the timeline between 2009 and 2013, there are significant differences in the trend

of some water- and foodborne diseases in this group of countries. Whereas the cases of salmonellosis and yersiniosis decreased, the cases of listeriosis and verotoxigenic *E. coli* (VTEC) increased[235]. In any case, salmonellosis still hogs the highest number of water- and foodborne outbreaks in the EU, involving more than 37% of the total cases, followed by bacterial toxins (25%), and viral infections (10%)[235].

1.2. Chemical Pollutants Detection

This section is mainly focused on the detection of pesticides as chemical pollutants, avoiding details on the detection systems harnessed to detect heavy metals and petroleum derivatives since they are not the main topic of this thesis.

Traditional methods used to detect pesticides are high-performance liquid chromatography (HPLC) and gas chromatography/mass spectrometry (GC/MS). Both methods usually offer high sensitivity, but at the cost of expensive and complex machines and facilities, requiring well-qualified personnel and the extraction of large volumes of water[28]. Therefore, due to the rising concern about the water quality worldwide, as well as the limited budget and resources that are available in many countries, governments and regulatory organizations need cheaper, faster, easier-to-use and standardized sensing platforms to detect and quantify a great number of chemical pollutants.

The research field for pesticides detection has stood out in recent years. Both new materials and nanomaterials, as well as novel recognition elements and detection devices, have been exploited to achieve higher specificity, selectivity, and simplicity. For example, for the first time, $NiCo_2S_4$ reticulated hollow spheres and PtPd nanoflowers have been used for the electrochemical detection of organophosphorus compounds with incredibly low detection limits (LOD around 10^{-14} g/mL)[236,237], taking the advantage of their favorable nanostructures and electroconductive properties. Besides, new optical detection approaches have also arisen for highly specific detection of different isomers of aromatic compounds using β-cyclodextrin-functionalized silver nanoparticles (AgNPs)[238]. However, not only new nanomaterials with better sensitivity and selectivity but also innovative detection systems have evolved for the last years. As an example, the use of pixelated dielectric metasurfaces for selective molecular barcode

imaging of several chemical compounds, including glyphosate, one of the most used pesticides worldwide[239]. Besides, new biosensors using carbon dots (CDs)[240,241], graphene-based devices[242,243], and Europium-based metal-organic frameworks (EuMOFs)[244] with improved properties have been recently reported. Finally, not only single nanomaterials but also combined nanomaterial-organic molecules sensing systems have been designed for detection purposes: Eu-allyl-3-carboxycoumarin[244] and rhodamine-Ag/Au bimetallic nanoparticles[245] are only two examples.

In recent years, smartphone-based techniques have also experienced a large development through their integration into sensing devices, enabling faster and more accurate in-situ detection methods[246,247]. Moreover, the use of aptamers has provided new tools to develop both new optical and electrochemical immunosensors, boosting pesticides detection sensitivity[248–251]. Eventually, new enzymes, with better properties (i.e. stability and sensitivity) have also been used as substitutes of the commonly used acetylcholinesterase (AChE) for organophosphorus and carbamates detection[252].

1.2.1. Single Compounds Detection

Overall, pesticides biosensors can be either classified by the recognition principle (i.e. immunoassay, enzymatic inhibition, non-specific chemical interactions, molecularly imprinted polymers [MIPs], etc.) or the (nano)materials used to construct the biosensor (AuNPs, QDs, CDs, bimetallic NPs, microwires, etc.). In particular, optical sensing systems aimed to detect pesticides can be classified according to the detection techniques as colorimetric, fluorescent, luminescent and surface-enhanced Raman spectroscopy (SERS) biosensors.

Nowadays, many colorimetric sensors rely on ratiometric changes that boost the dynamic range of measurements and reduce the errors caused by changes in the environment[253]. Ratiometric outputs can be achieved by combining different nanomaterials, such as infrared dyes, dual-metal nanoparticles, upconverting nanoparticles, bio-capped nanoparticles, and sensor arrays based on cross-responsive elements[246,250,254,255].

Weerathunge et al. employed tyrosine-capped silver nanoparticles as nanozymes, mimicking the enzymatic activity of peroxidase to detect the organophosphate (OP) pesticide

chlorpyrifos, yielding a detection limit of 11.3 µg/L[250]. Briefly, nanozymes are nanomaterials with enzymatic properties that provide stable catalytic behavior, lower cost-production, and easier surface modification than standard biological enzymes[244,256]. The present working principle is based on the non-covalent interaction of an aptamer specifically targeting chlorpyrifos with the Ag-nanozyme, and eventually with the target pesticide. Initially, an aptamer-nanoconjugate is formed after the incubation of the Ag-nanozyme with the aptamer. This process leads to the loss of the enzymatic activity of the Ag-nanozyme because of the passivation of the surface of the tyrosine-capped AgNPs. Next, the yellow chromogenic peroxidase substrate TMB (3,3',5,5'-tetramethylbenzidine) is added to the solution. Finally, the sample to be analyzed is added to the solution. On the one hand, exposure of the Ag-nanozyme-aptamer complex to chlorpyrifos traces leads to the dissociation of the complex, resulting in a color change from yellow to green. On the other hand, either the absence of chlorpyrifos or the exposure to other pesticides do not dissociate the aptamer from the Ag-nanozyme, hampering the color change from yellow to green (Figure 1.7a). This system has proven to be highly specific for chlorpyrifos detection, avoiding unspecific interactions with other organophosphate pesticides, and affording a detection time of 2 min with high recoveries (98-102%) in river samples.

Qiao et al. developed a simple colorimetric sensor array based on $KMnO_4$ and H_2SO_4 to recognize and quantify different pesticides through the combination of hierarchical clustering analysis (HCA) and the corresponding fitting curves[254]. The combination of these cross-responsive sensor elements produces unique responses, characteristic of particular analytes, avoiding the need for selective bioreceptors. Briefly, by using different concentrations and ratios of $KMnO_4$ and H_2SO_4, both a pattern recognition of different pesticides and a quantitative analysis based on the RGB change can be achieved (Figure 1.7b). In this regard, the authors tested 16 pesticides belonging to 5 different chemical families. A 30-dimensional vector was defined, and the data was classified by HCA to use the full dimensionality of the data, giving dendrograms based on the 30-dimensional RGB color changes. Overall, the colorimetric response of the sensor array is based on equilibrium reactions between the pesticides and the indicators. Detection limits vary among different pesticides, but all of them are in the range of $\approx$ 0.1 µg/L.

INTRODUCTION

Colorimetric sensors often provide the simplicity of use and easy interpretation by naked-eye detection, but at the cost of sensitivity in many cases. Therefore, the combination of a dual colorimetric and fluorescent output yields lower detection limits, usually broadening the detection range, while keeping the easy final interpretation[255,257]. In this regard, Tan et al. developed a lateral flow immunoassay (LFIA) using a monoclonal antibody against imidacloprid (neonicotinoid, insecticide) conjugated with AuNPs and time-resolved fluorescent nanobeads (TRFN) as colorimetric and fluorescent transducers, respectively[257]. As a result, the authors report a detection limit of 0.5 ng/g in food samples within 10-15 minutes. Nonetheless, the performance of the colorimetric and fluorescent assays showed similar sensitivity and LOD, meaning the use of fluorescent particles did not provide any additional advantage in that case.

On the other hand, Saleh et al. constructed an optical sensor film for the detection of metribuzin (triazine, herbicide) based on a dual colorimetric and fluorescent detection[255]. In this case, a near-infrared (NIR) dye and fluorescent upconverting nanoparticles (UCNPs) were used as the colorimetric and fluorescent reporter molecules, respectively. First, both reporters were immobilized over a polyvinyl-chloride (PVC) matrix deposited onto a polyester-support (Figure 1.7c). Next, metribuzin was added to the sensor, inducing a colorimetric change from green (806 nm) to blue (656 nm) of the NIR dye. Simultaneously, the UCNPs were quenched by the inner filter effect due to the overlapping of the absorption spectra of the blue NIR dye and the emission spectra of the fluorescent particles (659 nm). Besides, UCNPs provide an additional emission spectrum with a maximum emission peak at 545 nm, which persists uninfluenced by the presence of metribuzin, acting as a stable reference signal. Eventually, a detection limit of 68 nM was achieved by combining both colorimetric and fluorescent outputs with an assay time of 7 minutes. It is worth mentioning that these UCNPs are stimulated using an infrared laser diode at 980 nm, avoiding the interferences provoked by ultraviolet (UV) excitation wavelengths.
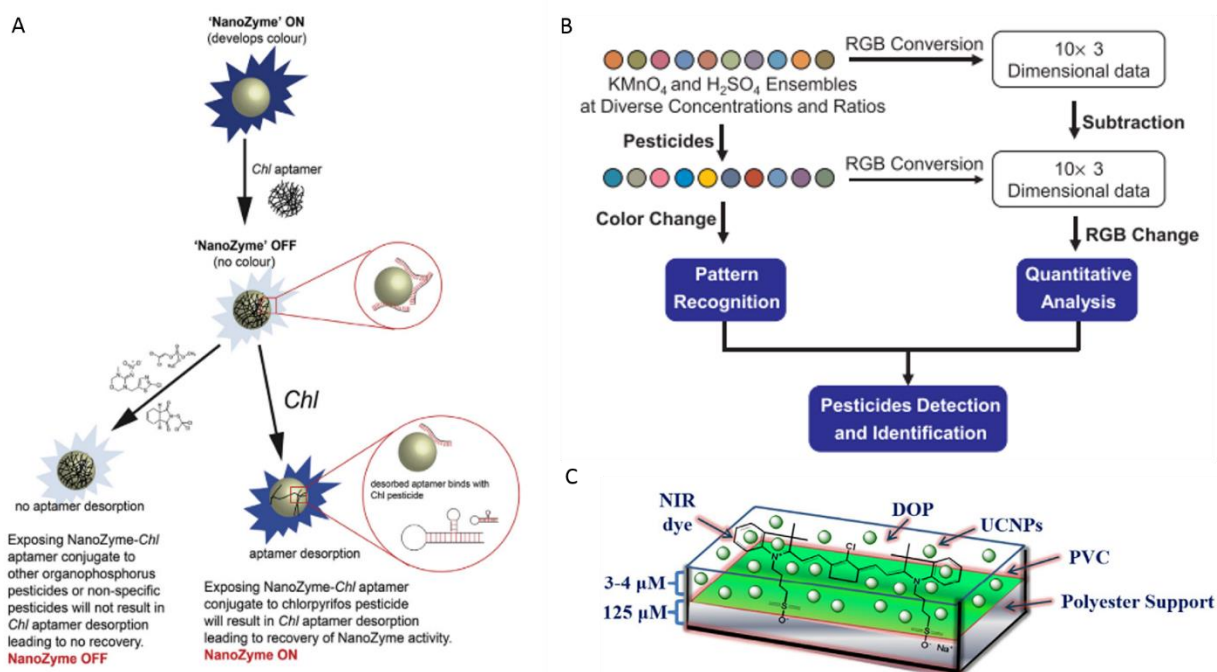
Figure 1.7. Specific optical detection methods of pesticides. (A) Working principle of the nanozyme based on AgNPs capped with tyrosine and functionalized with an aptamer against chlorpyrifos. This functionalization leads to the loss of the peroxidase activity of the nanozyme (OFF) and is kept upon the addition of other non-specific pesticides. On the other hand, the addition of chlorpyrifos triggers the dissociation of the aptamers, leading to a recovery of the peroxidase activity, and a color change in the presence of TMB and H_2O_2 (ON). (B) Working principle of the colorimetric dual system based on $KMnO_4$ and H_2SO_4 to detect pesticides based on the RGB conversion of the specific outputs generated by different pesticides. (C) Cross-section of the metribuzin sensor film composed of a thin layer of PVC deposited onto a thicker layer of polyester. On top of the sensor, the NIR-dye and UCNPs are put in contact with metribuzin, triggering a NIR-dye color change and UCNPs quenching, yielding both colorimetric and fluorescent outputs.

Recently reported fluorescent sensors aimed to detect pesticides rely on quantum dots (QDs)[258], carbon dots (CDs)[259], UCNPs[260], fluorochromes (i.e. rhodamine)[261], nanoparticles derived from conjugated organic polymers[262,263], and graphene quantum dots (GQDs)[264]. For example, Wang et al. developed an immunoassay based on CDs conjugated to antibodies (IgGs) aimed to detect glyphosate. Besides, magnetic beads (Fe_3O_4) conjugated to glyphosate were used to remove the excess of IgG-CDs[265]. The presence of glyphosate in the analyzed sample correlates to an increase in the fluorescence of the supernatant after a magnetic field is applied to retain the magnetic nanoparticles over the surface of the container. By using this simple method, the

authors report a detection limit of 8 µg/L in standard samples, and good recoveries between 87% and 104% in water, food and soil samples[265]. On the other hand, Tao et al. developed a pillared-layered entangled luminescent metal-organic framework (MOF) able to detect 2,6-dichloro-4-nitroaniline (DCN, fungicide), exhibiting strong fluorescent emission at 365 nm, together with a 99% quantum yield[266]. The detection principle is based on the aggregation-induced emission (AIE) that some molecules possess, being tetraphenylethene (TPE) the one utilized in this work. Then, a molecular-imprinted polymer is constructed by subsequent chemical modifications, yielding a TPE-based luminescent MOF (LMOF). Briefly, the luminescent emission of LMOF is quenched upon the addition of increasing concentrations of DCN due to the photoinduced electron-transfer (PET), yielding both a selective and a sensitive detection method with a LOD of 0.133 µg/L. Following the same direction, Xu et al. reported a luminescent and high surface-area MOF able to detect methyl-parathion (organophosphate, insecticide) in irrigation water[267]. The sensing mechanism is also based on the photoinduced electron-transfer, yielding a detection limit of 0.12 µg/L, the lowest LOD reported for methyl-parathion so far.

Another important group of optical sensing systems aimed to detect pesticides is based on surface-enhanced Raman spectroscopy (SERS). SERS is a surface-sensitive technique that analyzes the molecules adsorbed onto metal surfaces or nanostructures by enhancing the inelastic scattering of photons scattered by the irradiated material. In this regard, several research articles related to the detection of different pesticides based on SERS have been recently published [242,268–271]. As an example, Zhang et al. used flower-shaped AgNPs testing different pH and solvent type conditions in order to optimize the detection and quantification of ethion (organophosphate, acaricide)[270]. Flower-shaped AgNPs have abundant anisotropic protrusions, known as "hot spots", which enhance the system's sensitivity. In this work, the principal component analysis (PCA) was used to obtain the regression model that characterizes the pesticide's detection based on the intensity shift observed in the Raman spectra. As a result, the authors report a detection limit as low as 0.1 nM. On the other hand, Pham et al. reported a sensor based on optical fiber substrates with silver nano-dendrites structures using SERS to detect permethrin (pyrethroid, insecticide)[271]. The authors chose Ag nano-dendrites structures because of their great number of "hot spots"; that's to say, regions with a highly enhanced local

electromagnetic field. This system provides a detection limit of 3.5 ng/L of permethrin, yielding an RSD lower than 3%, supporting both their high sensitivity and reproducibility.

One of the advantages of SERS-based sensors is that different chemical compounds produce different SERS fingerprints due to the particular vibrational frequencies of different molecules. SERS systems allow not only to quantify the concentration of a concrete molecule because of the intensity changes in the Raman peaks but also to differentiate among different molecules because of the positional shifts observed in the Raman spectra. Following this direction, there exist several recent research articles in which SERS-based sensors are used to detect and quantify different pesticides within the same sample. For example, Kim et al. developed a sensor based on gold nanofingers to detect both chlorpyrifos and thiabendazole in food and water samples[269]. As another example, Ma et al. developed AgNPs/Graphene-oxide (GO) inks screen printed on to cellulose paper for SERS-based detection of thiram, thiabendazole and methyl-parathion in fruit samples, yielding detection limits in the range of ng/cm^2, lower than those required by the U.S. Environmental Protection Agency[243] (Figure 1.8).

1.2.2. Detection of a Family of Compounds

The detection of single compounds is only useful when a very specific chemical is known to be the major problem in a particular area. Nonetheless, the water quality status is usually affected by a pool of different chemicals in a real case scenario. As a consequence, the detection of single compounds becomes not only arduous but also meaningless in most of the cases[81]. In this regard, several methods have been developed to detect a specific family of compounds that encompasses a larger number of chemicals.

Enzymatic inhibition assays are probably the most broadly used sensing systems to detect particular families of pesticides. Unlike aptamers and antibodies, enzymes are generally less selective for the binding of specific molecules. In fact, most of the enzymes can bind to different molecules (substrates or inhibitors) with a stronger or a weaker affinity. As a general rule, the pool of molecules a particular enzyme can bind must be structurally and chemically related, since the enzymatic active site acts as a scaffold with a defined 3D conformation. As an example, acetylcholinesterase (AChE) is an enzyme found in the neuromuscular junctions, acting as a

controller of the synapsis transmission by breaking down the acetylcholine neurotransmisor[272]. Many pesticides belonging to the family of carbamates and organophosphates can bind to the AChE, provoking a conformational change on its active site, thereby blocking, either reversibly or irreversibly, the enzymatic activity[273]. AChE inhibition-based systems have been widely used to detect both carbamate and organophosphate pesticides for the last 50 years[274].
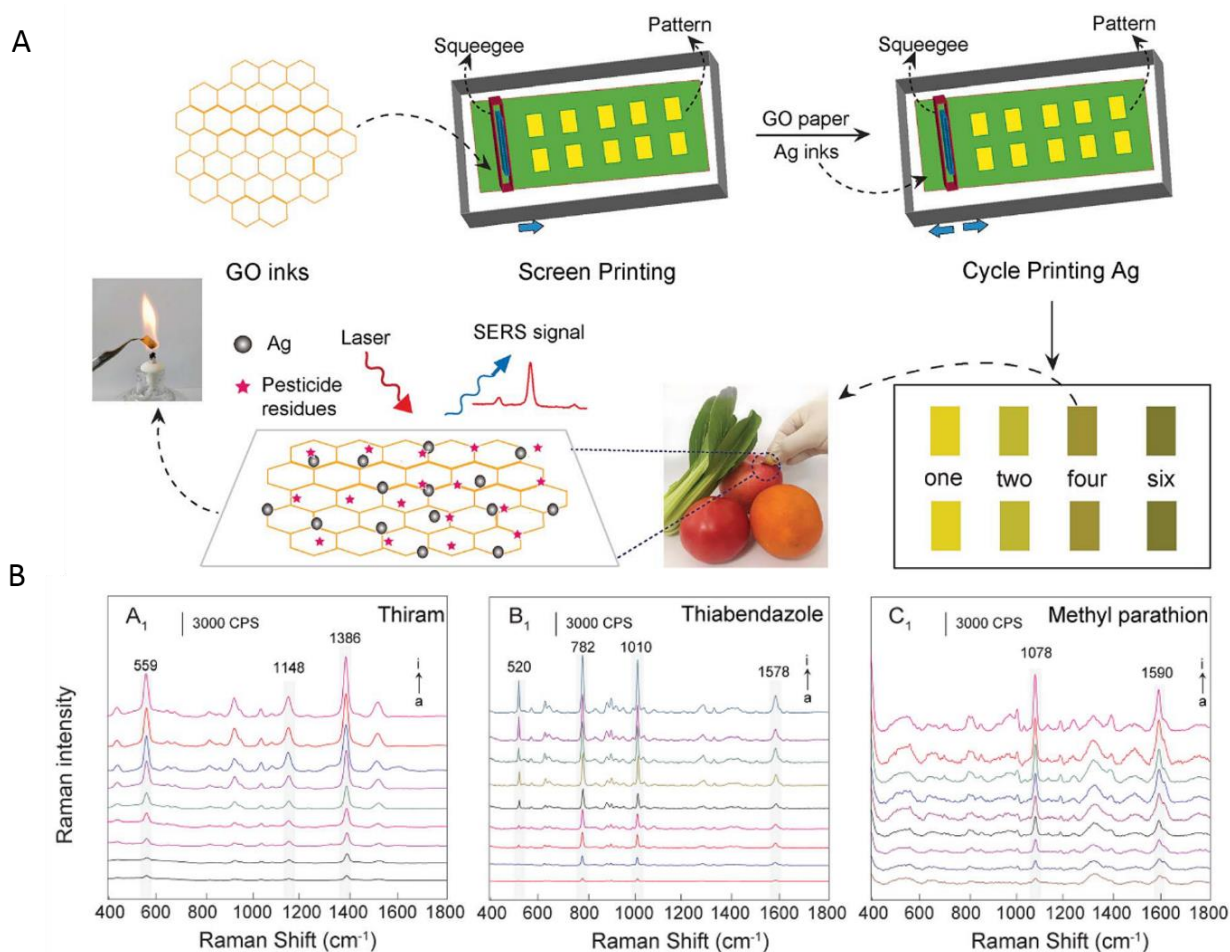
Figure 1.8. Detection of pesticides using Ag/GO screen printed inks onto cellulose paper. (A) Schematic representation of the fabrication of the fruit SERS swabs based on screen-printed GO and Ag inks onto cellulose paper. A different number of layers of Ag inks are applied for the fabrication of the swabs for further optimization, and those are rubbed for 3 seconds with fruit peels. Finally, the swabs are analyzed using a 780 nm laser with an integration time of 30 s. (B) Recorded SERS spectra for different concentrations of thiram (left), thiabendazole (center), and methyl-parathion (right). Both the peaks intensity and the peaks position change for different pesticide traces and concentrations.

Qing et al. developed a carbamate sensor based on rhodamine B (RB) modified AgNPs[261]. As aforementioned, carbamates can inhibit AChE, preventing the transformation of acetylcholine into thiocholine. In turn, thiocholine induces the aggregation of the yellow RB-AgNPs, generating a color change to gray, simultaneously unquenching the fluorescence of RB. Therefore, the presence of carbamates in the solution can be tracked both because of the stable yellow color and the fluorescence quenching of the rhodamine. By using this method, the authors report a LOD of 0.023 ng/L of carbaryl, one of the lowest values found in the literature so far. Besides, the sensor works properly with both food and water samples.

Not only AChE but also other similar enzymes are used to develop enzymatic inhibition-based pesticide sensors. Yan et al. created a fluorescent CDs-MnO_2 nanosheet sensing device able to detect organophosphates by Förster resonance energy transfer (FRET) (Figure 1.9a)[259]. Briefly, a solution of butyrylcholinesterase (BChE) is mixed with the sample to be analyzed for 30 minutes. Next, acetylcholine is added to the solution, followed by an incubation process of 20 minutes. Finally, MnO_2 nanosheets and CDs are also added to the solution, and the reaction is allowed to occur for 2 minutes. As a consequence, the fluorescence is quenched if the sample contains organophosphate pesticides because acetylcholine cannot be transformed into thiocholine, hindering MnO_2 nanosheets degradation, thereby leading to FRET (Figure 1.9b). Furthermore, if BChE is not inhibited, it transforms acetylcholine into thiocholine, triggering MnO_2 nanosheets degradation, and leading to the fluorescence recovery. Moreover, color changes are also observed from colorless to brown with increasing concentrations of paraoxon (organophosphate, insecticide) (Figure 1.9c). As a conclusion, the present biosensor can detect organophosphates at concentrations as low as 15 ng/L in food and water samples, discriminating from other classes of pesticides even when they are present at higher concentrations.

Following the same principle, Wang et al. used MnO_2-coated AuNPs supraparticles to detect organophosphates, achieving a LOD of 0.006 ng/L in river samples[275]. In this case, the absence of OPs triggers the etching of the supraparticles, provoking a color change from yellow to green. Conversely, the color remains yellow in the presence of OPs because AChE is inhibited and thiocholine is unable to etch the MnO_2 shell of the supraparticles.
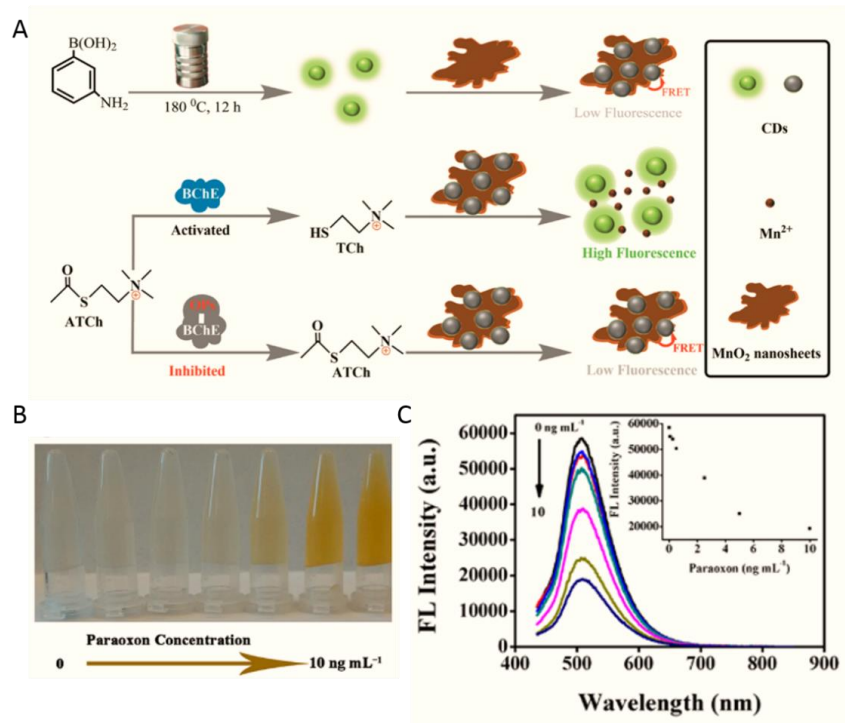
Figure 1.9. Detection of organophosphate pesticides using MnO₂ nanosheets and CDs. (A) Schematic representation of the OPs sensor based on the use of CDs as fluorescence reporters and MnO₂ nanosheets as fluorescence quenchers. The enzyme BChE is inhibited in the presence of OPs, hindering the formation of thiocholine and preventing MnO₂ nanosheets aggregation, leading to the quenching of the CDs emission. On the other hand, the absence of OPs triggers the enzymatic conversion of ACh into thiocholine, triggering MnO₂ degradation and a fluorescence recovery. (B) A colorimetric change of the sensing solution is also observed upon the addition of high concentrations of the OP pesticide paraoxon. (C) The fluorescence quenching is represented upon increasing concentrations of the OP pesticide paraoxon.

A more complex procedure was followed by Miao et al., who used an electrochemiluminescent sensor to detect organophosphates based on bi-metallic Pt-Au nanoparticles electrodeposited on to multi-walled carbon nanotubes (MWNTs)-modified glass carbon electrodes (Figure 1.10)[276]. The detection system is based on the bi-enzymatic reaction carried out by AChE and choline oxidase (ChOx), through which acetylcholine is finally transformed into H_2O_2. Reactive oxygen species (ROS) are known to enhance the electroluminescence signal due to the presence of unpaired valent shell electrons, thereby boosting the sensitivity of the sensor. In this regard, luminol is used as the electroluminescent substrate, whose light emission is boosted in the presence of H_2O_2. Besides, both bi-metallic Pt-Au nanoparticles and MWNTs are used because they are highly electroconductive, promoting the

whole electroluminescent signal of the luminol-H_2O_2 system. Overall, this innovative approach enables detecting OPs in the range of 0.08-0.16 nM for three different organophosphate pesticides, yielding good recoveries found between 78% and 108% in cabbage samples.
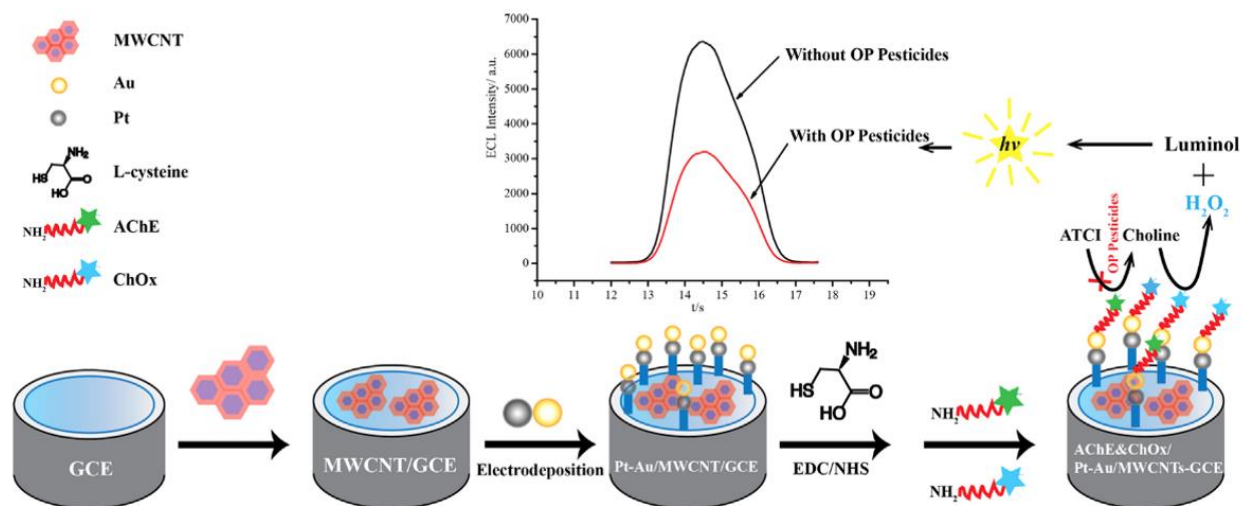
Figure 1.10. Detection of organophosphate pesticides based on an electroluminescent sensor. Schematic representation of the working principle and the generation of the electroluminescent output.

All aforementioned enzymatic inhibition-based sensors rely on AChE and BChE to detect OPs and carbamates. However, these enzymes are obtained from animal and insect tissues, involving complex extraction procedures. For this reason, Yang et al. studied the sensitivity and selectivity of a plant carboxylesterase enzyme present in the soybean, wheat, and rice, among other plants[252]. Their results suggest that the plant carboxylesterase can substitute both AChE and BChE for OPs and carbamates detection, reducing costs and paving the way for further improvement on the enzymatic inhibition-based pesticides detection assays.

Nevertheless, not only enzymatic inhibition assays but also other sensing systems are used to detect a variety of chemical compounds[238,239,241,261,264,277]. Remarkably, Tittl et al. developed a mid-infrared nanophotonic sensor based on dielectric metasurfaces to detect and differentiate absorption fingerprints of several molecules, including pesticides such as glyphosate[239]. As a summary, they implemented a 2D-array of high-quality metasurface pixels, matching the resonance positions of different chemical bonds to a specific pixel, creating a map in which there is a correlation between spectral and spatial information (Figure 1.11a). On the other hand, Chen

et al. fabricated a sensor based on CTAB-encapsulated copper nanoclusters (CuNCs) for the fluorescent and colorimetric detection of dithiocarbamates (DTCs) in fruit samples[277]. The sensing mechanism is based on the capability of DTCs to coordinate strongly with copper ions, to which they donate two sulfur atoms in the process. Briefly, the authors employed a micro paper-based analytical device (µPAD) to immobilize the copper nanoclusters, followed by the addition of the food samples. As a consequence, the presence of DTCs induces the reduction of Cu^{2+} to Cu^+ via ligand exchange, modifying the copper halide complex core, and leading to the aggregation of CuNCs. The overall process results in the quenching of the fluorescence signal. Surprisingly, this sensor shows good selectivity towards DTCs in comparison to carbamates, organophosphates and pyrethroids due to the selective interaction between DTCs and CuNCs.

Eventually, Xiao et al. developed a fluorescent ratiometric sensor using a molecularly imprinted polymers (MIP) integrated within a wearable glove to detect organophosphates (Figure 1.11b)[241]. This sensor is composed of CMC aerogel to provide a flexible scaffold, and Europium-based MOFs (EuMOFs) together with carbon dots (CDs) to provide the fluorescent signal. The presence of OPs is then determined by a fluorescent color change from red (negative) to blue (positive), due to the quenching of EuMOFs by absorption competition. On the other hand, CDs are used as the reference fluorescent centers. The presented detection system allows to detect traces of OPs by simply touching a vegetable sample with the tip of the index finger during 30 seconds. It is worth to mention that this system yields a LOD of 89 nM for OPs detection, without the need of AChE or other related enzymes. Nonetheless, the authors claim the detection of the whole organophosphate pesticides family, but they only tested the food samples spiked with chlorpyrifos, a specific OP pesticide. In this regard, the effectiveness and selectivity of the sensor are not studied with other OPs (i.e. malathion or methyl-parathion), and other non-related pesticides (i.e. carbamates or neonicotinoids), questioning the broad-spectrum detection range stated.
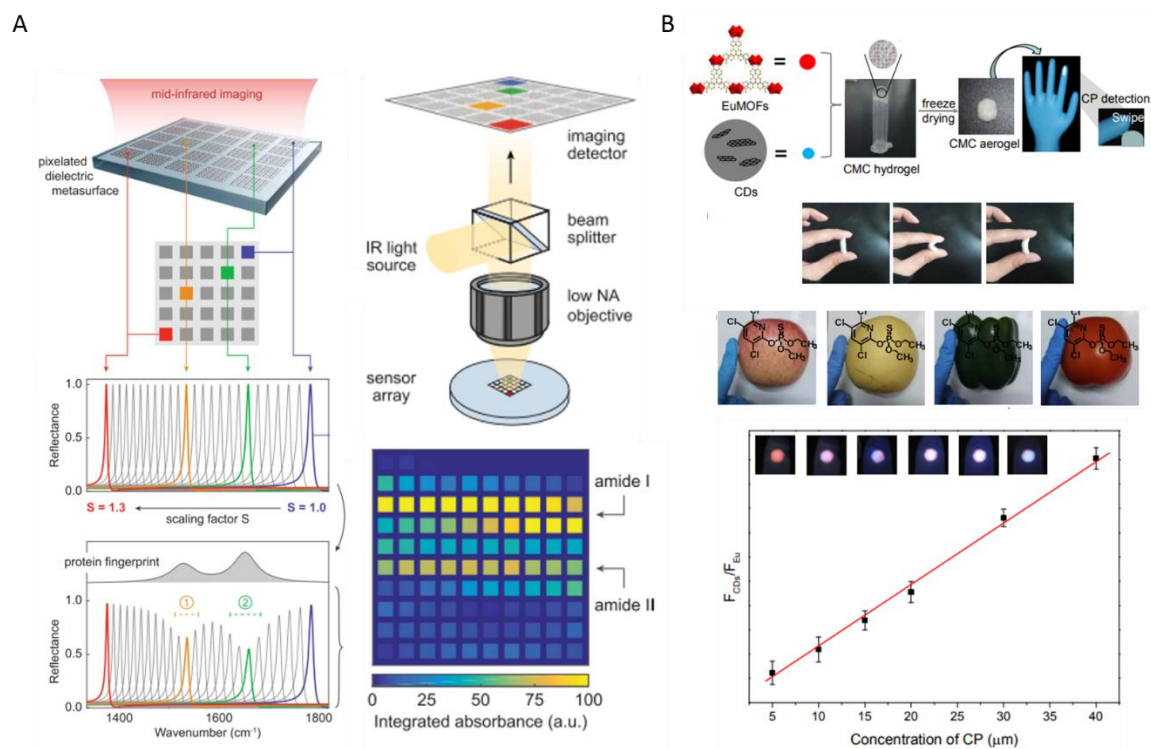
Figure 1.11. **Detection of different compounds without the need of enzymes**. (A) On the left, schematic representation of the working principle of the pixelated dielectric metasurfaces. On the left, a 2D-array is sampled with an unknown substance (i.e. glyphosate or a protein) and generates a molecular fingerprint based on the chemical bond resonances. On the top right, the infrared light is first filtered, then absorbed, and finally detected in the 2D array. On the bottom right, schematic representation of a chemical fingerprint. (B) On the top, schematic representation of the fabrication of the wearable glove-sensors made of CMC aerogel, EuMOFs, and CDs. In the middle, how to detect the pesticides on food residues for 30 seconds. On the bottom, the calibration curve for paraoxon detection in vegetables.

1.2.3. Toxicity Tests

Toxicity tests are biological assays that determine the extent to which a particular substance or a pool of substances harm a living organism. In this regard, toxicity tests enable to assess the overall water quality without considering the presence of single pesticides or even specific families of compounds, but the biological effect they provoke as a whole. More in detail, toxicity tests are inhibition-based methods that measure a metabolic parameter (i.e. growth rate or bioluminescence) to evaluate the toxicity of the water sample analyzed. Nowadays, toxicity tests are widely carried out in biotechnological and pharmaceutical companies[278,279], as well as in public health organizations[280].

INTRODUCTION

Common organisms used to detect and monitor pollutants in water are *Aliivibrio fischeri*, *Daphnia magna*, *Dreissena* mussels, zebrafish, and mammal cells[281,282]. On the one hand, Microtox ® is a well-known technology used to assess the toxicity of water samples by tracking the bioluminescence inhibition of the bacteria *Aliivibrio fischeri* in the presence of toxic compounds[283]. On the other hand, CellTiterGlo ® is a toxicity assay-based technology that quantifies the concentration of ATP, enabling to monitor the metabolic state of the cells[282]. Besides, other toxicity models based on animals such as rats and fish pose ethical issues on experimentation. Albeit these methods are well-standardized and worldwide employed, they are expensive, and often lack stability, robustness, and simplicity, involving several-step processes. For example, the commercially available Microtox 500 ® costs around 20,000 € and requires several preparation steps before testing the sample; whereas CellTiterGlo ® requires a lysing agent to extract the intracellular ATP, introducing several undesired components in the reaction, thus affecting the overall performance of the toxicity detection system[282,284].

In recent years, several researchers have been working on the development of simpler-to-use and sensitive toxicity-based biosensors for water quality assessment[282,285–287]. As an example, Pujol-Vila et al. used *E. coli* cells trapped within paper matrices to detect copper as a toxic agent[287]. The paper matrices (paper discs) serve themselves not only as carriers but also act as fluidic elements, avoiding the use of external pumps. Moreover, the authors claim to store the bacteria stable for at least 1 month at -20 ºC. Regarding the toxicity assays, ferricyanide is used as the substrate, whose reduction is determined by optical reflectometry, image analysis, and visual inspection. In the presence of copper, ferricyanide reduction capacity is hindered, thereby decreasing the gray color of the sample. Among all the aforementioned techniques, optical reflectometry (ΔAbs_{420}) yields the most sensitive results, with an EC50 value of 3.9 mg/L, similar to those previously reported in the literature.

One of the drawbacks most of the toxicity inhibition assays face is the stability of the organisms that, in turn, disrupt the reproducibility within different batches and shorten the working life of these sensing platforms. In this regard, Ben-Yoav et al. developed a bacterial biofilm-based sensor integrated within a microchip to stabilize and keep reproducibility while preserving simplicity (Figure 1.12a)[285]. Briefly, the authors use a genetically modified strain of *E.*

coli, tailored to respond to the presence of genotoxic compounds (i.e. nalidixic acid) by expressing the alkaline phosphatase as a reporter enzyme. This enzyme, in turn, produces p-nitrophenol (an electro-active species) that is finally detected by both colorimetric and chrono-amperometric outputs. On the one hand, the higher the concentration of genotoxic compounds, the higher the absorbance values at 405 nm. On the other hand, higher concentrations of genotoxic compounds yield higher electrical current per area on the surface of the electrodes. Although this system works better with biofilm-encapsulated cells than with planktonic cells, there are still some inherent limitations of the system, such as restricted penetration of the analyte into the biofilm, spatial heterogeneity within the biofilm, and quorum-sensing gradients, among others.

Another important issue of toxicity studies is that the toxic effects produced by different chemical compounds vary among different organisms (i.e. antibiotics, pesticides, and anticancer drugs). Therefore, by using mammal cells, and more in particular human cells, toxicity assays may correlate much better with a real case scenario for human beings. In this regard, Cevenini et al. developed a smartphone-based bioluminescent device using genetically modified human-embryonic-kidney cells (HEK cells) to evaluate the toxicity of water samples spiked with dimethylsulfoxide (DMSO) (Figure 1.12b)[282]. The genetically modified HEK cells express constitutively the green-emitting luciferase (GFP) whereby the bioluminescent output is kept more stable than with inducible promoters. Moreover, a smartphone readout is achieved by implementing a smartphone accessory with pre-loaded cartridges of immobilized cells whose bioluminescence is analyzed by an Android application. The aforementioned integrated system allows achieving quantitative and user-friendly outcomes classified as safe ($\geq$ 80%), harmful (79%-30%), or highly toxic ($\leq$ 29%). However, the calculated EC50 value for the presented sensor against DMSO is around 9% (v/v), higher than that EC50 reported by the CellTiterGlo kit ($\approx$ 6% [v/v]), thereby failing to achieve greater sensitivity than one of the gold standard methods. Besides, the system lacks enough simplicity, since it requires a tight control of the culture conditions (37 ºC, 5% CO_2 and 95% relative humidity), and up to 30 minutes to provide the definitive results.

Most of the toxicity assays rely on inhibitory effects provoked by toxic compounds. However, false-positive signals are common to occur due to the detrimental effects provoked by

uncontrolled environmental conditions such as temperature and pH changes, even in the absence of toxic compounds[282,285,288]. In this regard, other approaches rely on the stimulatory effects that some toxic compounds provoke on particular metabolic pathways. As an example, Woutersen et al. designed a genetically modified *E. coli* strain containing the *luxCDABE* genes from *A. fischeri* coupled to the *recA* promoter, which is activated upon DNA damage[281]. Consequently, bioluminescence is boosted in the presence of genotoxic compounds, such as mitomycin C and nalidixic acid (Figure 1.12c).

Nowadays, several research articles are reporting genetically-engineered microorganisms able to respond to the presence of different families of compounds. On the other hand, Khatun et al. developed a bacterial consortium-based sensing system relying on two *E. coli* strains that enable detecting organophosphates in food and soil samples with a LOD of 1 nM[289]. The first strain hydrolyzes organophosphates through the organophosphate hydrolase (OPH), yielding p-nitrophenol that, in turn, triggers the expression of β-galactosidase in the second strain, finally leading to the generation of a colorimetric output (Figure 1.12d). In another vein, other genetically modified microorganisms have been used to detect heavy metals through colorimetric and bioluminescent signals[290–292].

Ethical issues are important as well while performing toxicity tests, especially when using animals that may undergo detrimental chronic effects, such as infertility. In this regard, more than 1 million fish are used for experimental purposes in the EU every year[13]. More in detail, young animals are especially sensitive to toxic compounds, such as juvenile fish. Given these issues, Stadnicka-Michalak et al. developed a method to predict quantitatively the impact of chemical compounds on fish growth based on in vitro data[13]. The authors tested two widespread fungicides (cyproconazole and propiconazole) to carry out the toxicological experiments. To summarize, they propose that the inhibition of cell population growth under chemical stress can be used as an accurate alternative to real toxicity measurements. Indeed, their computational data support the in vitro measurements because of the almost perfect agreement between in vivo and in vitro results. Besides, this approach enables not only to reduce the experimental time from 90 days to 3 days but also to simplify the procedure, cut down associated costs and move towards more ethical experimental procedures. Overall, these results pave the way towards

alternative approaches to whole-organism toxicity testing through the combination of in vitro experiments with in silico modeling experiments in order to predict the impact of toxic compounds on whole-organisms.
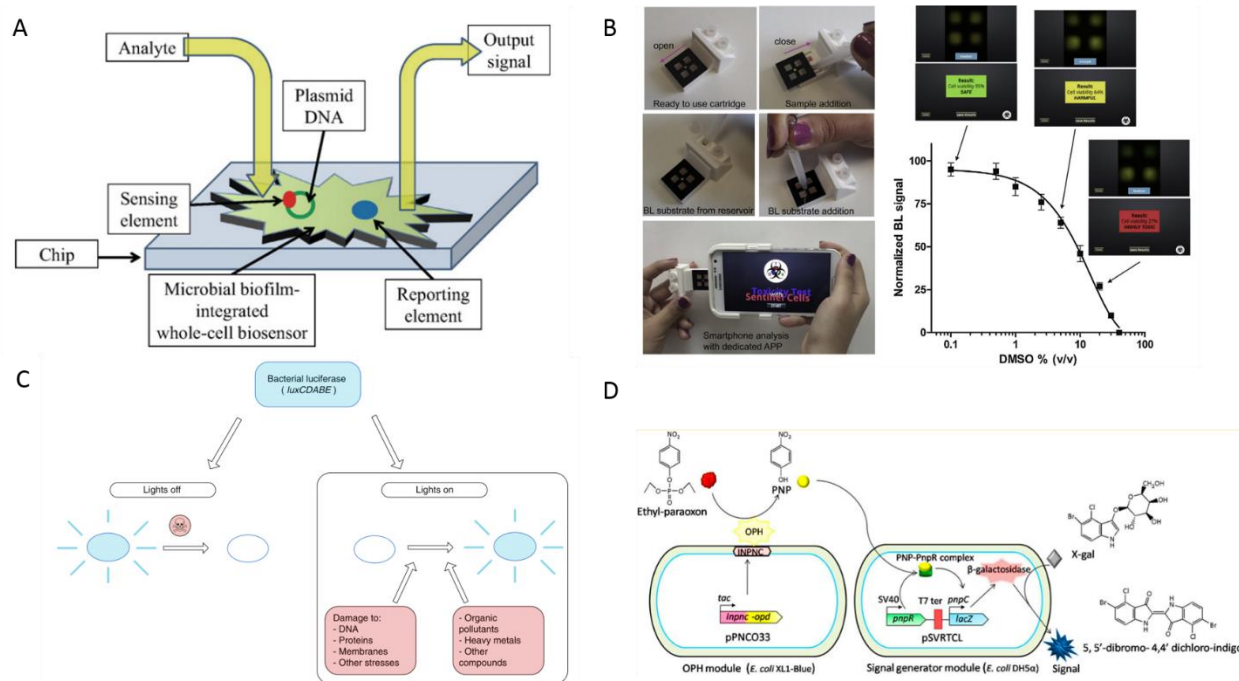
Figure 1.12. Different kinds of toxicity tests. (A) Schematic representation of a bacterial biofilm-based toxicity sensor. (B) Smartphone-based bioluminescent detection of DMSO using HEK cells. A smartphone app provides a visible output in green, yellow or red colors according to the degree of toxicity of the sample analyzed (C) Schematic representation of a toxicity sensor based on bioluminescence inhibition (left) and bioluminescence enhancement (right) upon exposure to toxic compounds (D) Schematic representation of a toxicity sensor based on two genetically-modified different strains of *E. coli* able to specifically trigger a colorimetric response in the presence of organophosphate pesticides.

Eventually, most of the aforementioned methods rely on acute or chronic toxic effects provoked by single compounds. Few other methods try to foresee the toxic effects provoked by a pool of chemicals at low concentrations that are realistically found in freshwater bodies. Besides, most of these methods are based on null additive models such as the concentration addition (CA), which considers that individual components provoke linear-additive toxic effects. The main drawback of CA and other related methods is that they usually ignore the "gray-zone" (10-20% below the individual toxicity threshold for each chemical), thereby underestimating the

overall toxicity in a real case scenario. Moreover, physical and other biological pollutants are not usually considered. For this reason, Rodea-Palomares et al. designed a dual system based on the computational global sensitivity analysis (GSA) and the experimental quantitative high-through screening (QHTS), named as GSA-QHTS (Figure 1.13)[293]. In this regard, GSA provides information about the outputs taking into account first-order inputs (direct effects) and higher-order inputs (interaction effects). On the other hand, QHTS uses *Anabaena sp.* (algae) to detect metabolic toxicity through a bioluminescent whole-cell sensor. Overall, this new approach enables screening pollutants at environmentally realistic low-dose mixtures, considering simultaneously other biotic and abiotic stressors that are often overlooked by other methods.
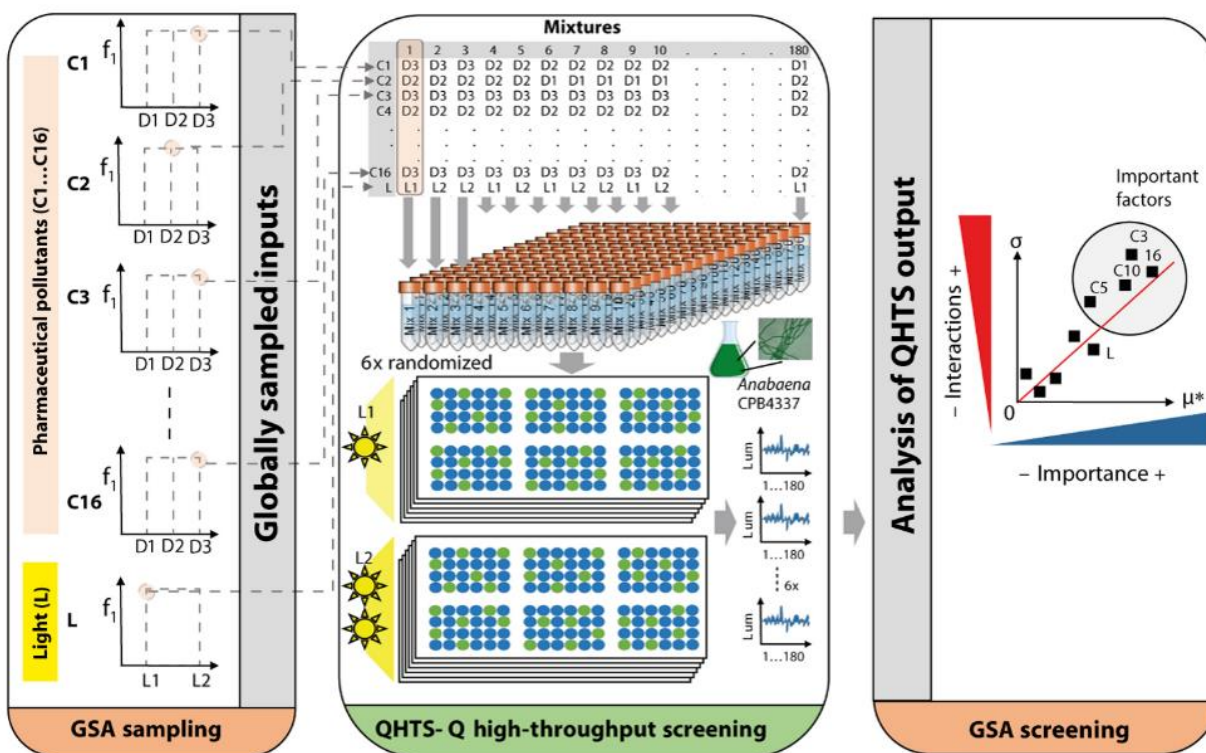
Figure 1.13. GSA-QHTS experimental framework for the analysis of water toxicity in a real case scenario. The authors tested mixtures of 16 different chemical compounds found at environmentally realistic concentrations in combination with different light intensities. On the left, GSA sampling allows generating an experimental design template. In the middle, QHTS relies on a genetically modified strain of the algae Anabaena to test the toxic effects of different mixtures of chemicals under different environmental conditions. On the right, GSA screening allows understanding the importance of the chemical compounds and their interactions on the overall biological response.

1.3. Biological Pollutants Detection

This section is mainly focused on the detection of bacteria as biological pollutants, avoiding details on the detection systems harnessed to detect viruses and other parasites since they are not the main topic of this thesis.

According to a recent study performed in 2020, fecal contamination of waters gets a foothold as the main source of water pollution in the EU (85% of polluting activity), followed by agriculture (70%), farm waste and oil tanks (50%), residential area (40%), and transport (35%)[294]. In this regard, water fecal contamination often leads to waterborne outbreaks caused by pathogenic microorganisms. However, pathogens' detection requires the analysis of large volumes of water since pathogens are usually present at low numbers within the water bodies. Therefore, as aforementioned, the detection of indicator microorganisms is not only preferred but also more practical when assessing water fecal contamination[295]. Coliform bacteria are the best indicator microorganisms (*Escherichia*, *Citrobacter*, *Enterobacter,* and *Klebsiella*). Among all these bacteria, *Escherichia coli* is the perfect indicator microorganism of water fecal contamination because it is always present in the guts of warm-blooded animals[166].

1.3.1. Traditional Methods

Currently, there are two universal methods used for the counting of *E. coli* in water samples: membrane filtration (MF) and multiple tube fermentation method (MTFM). On the one hand, MF uses a small pore-sized membrane to filter the water and trap the bacteria onto its surface. Next, the membrane is placed over an agar plate containing a selective growth media that only allows for coliforms' growth. However, this method is time-consuming and highly susceptible to the presence of other microorganisms. On the other hand, MTFM uses a mixture of bacterial growth media together with the water sample to be analyzed, in which bacteria are allowed to grow, normally within 16-24 hours, and detected by optical density (OD). This method does not require a filtration process but does require an enrichment process and a long incubation time to provide the definitive results. In this regard, the most probable number (MPN) analysis helps to narrow down the real concentration range of bacteria found in the water samples[295].

INTRODUCTION

Although not used as a gold standard to detect water fecal contamination, microscopy techniques also allow detecting and identifying bacteria and bigger pathogens. Several sorts of microscopy, including bright- and dark-field microscopy, phase contrast microscopy, differential contrast microscopy, fluorescence microscopy, laser scanning, transmission electron microscopy (TEM) and scanning electron microscopy (SEM) are used to identify and characterize bacteria according to their morphology and structural differences (i.e. Gram stain)[296]. Nonetheless, these techniques often ignore the presence of small pathogens and are not very specific.

More recently, new bacterial detection systems appeared, such as enzymatic assays (i.e. Colilert), immunological assays (i.e. ELISA and agglutination tests), and nucleic acid-based assays (i.e. PCR and loop-mediated isothermal amplification [LAMP]). On the one hand, enzymatic assays rely on the ability of specific bacteria to metabolize particular compounds: 4-methylumbelliferyl-β-d-galactoside (MUGal) for coliforms, and *indoxyl β-D-glucuronide (IBDG) specifically for E. coli.* However, they also require a long incubation time to provide definitive results (18-22 hours)[166]. On the other hand, immunological assays rely on antibodies that bind selectively to specific analytes. In this regard, ELISA tests are considered as a gold standard for clinical diagnosis and quantification of protein biomarkers and microorganisms. Nonetheless, ELISA tests are time-consuming, involving several steps (i.e. sample labeling with fluorescent reagents) and requiring well-trained personnel. Eventually, nucleic acid-based assays are usually more sensitive than enzymatic and immunological assays because of an additional amplification step that allows detecting few copies of specific genes found in particular bacteria. However, most of these methods often require an in-depth target selection, rely on expensive enzymes and devices (i.e. thermocyclers), and need several steps to perform the DNA amplification[296].

Overall, traditional methods for bacteria detection have several drawbacks: some techniques require specialized equipment and trained personnel, whereas in other cases the lack of sensitivity and specificity is the major problem. For instance, microscopy techniques are often quick but not specific. On the other hand, growth culture techniques require one to several days to be completed. Next, biochemical assays, such as the analytical profile index (API), detect the presence of particular enzymes due to colorimetric changes, giving a unique colorimetric profile for specific bacteria species, but also last one day to provide the definitive results. Finally, genetic

analysis may overlook mutant strains and still require a few hours to be performed and relatively expensive laboratory equipment. Therefore, there is a need for faster and simpler analytical devices that preserve at the same time the sensitivity and selectivity for specific bacteria detection.

1.3.2. Biosensors for Bacteria Detection

A biosensor is an analytical device that detects chemical or biological analytes. Biosensors are composed of two main parts: a bioreceptor that specifically recognizes the desired analyte, and a transducer that converts the bio-recognition event into measurable outputs. On the one hand, bioreceptors can be antibodies, enzymes, nucleic acids, viral particles, and other proteins (i.e. lectins) (Figure 1.14). On the other hand, transducers are usually nanoparticles because they provide a high-surface-area for bioreceptors conjugation and possess unique size- and shape-dependent optical and electrical properties[297]. Accordingly, transducing signals can be optical, electrochemical, electrical, mechanical, thermic and magnetic[298]. Eventually, a detector is required to read the generated output and display an interpretable outcome. In this regard, optical readers and potentiostats are normally used as detectors for optical and electrochemical biosensing, respectively[298]. More broadly speaking, biosensors can be either qualitative (ON-OFF response, i.e. pregnancy test) or quantitative by generating a measurable output that is proportional to the concentration of the detected analyte (i.e. glucose meter). Consequently, biosensors provide selectivity and specificity due to the bioreceptors, and enhanced sensitivity due to the transducers.

Surface plasmon resonance (SPR) sensors are a good choice for optical sensing because of their accuracy, low amount of sample required and versatility[296]. However, SPR sensors often yield poor sensitivity for bacteria detection due to the limited penetration of bacteria cells until the sensor's surface and to the similar refractive index of bacterial cytoplasm and the aqueous medium[299]. Nevertheless, localized surface plasmon resonance (LSPR) may help to overcome this limitation by using metal nanoparticles or nanorods deposited onto the transducer surface to enhance the sensitivity of the system. Besides, long-range SPR systems provide better performances for large analytes detection because of narrower resonance outputs and the

possibility to sense at higher distances from the metal surface[299]. As an example, Wang et al. developed an LSPR biosensor combined with magnetic nanoparticles for the detection of *E. coli* O157:H7 (Figure 1.15a) [300]. Overall, the combination of LSPR and magnetic nanoparticles enhances the biosensor's sensitivity by four orders of magnitude compared to the regular SPR-based sensors, yielding a LOD of 50 CFU/mL. In any case, SPR-based systems remain expensive and have not been implemented yet for point-of-care biosensors.
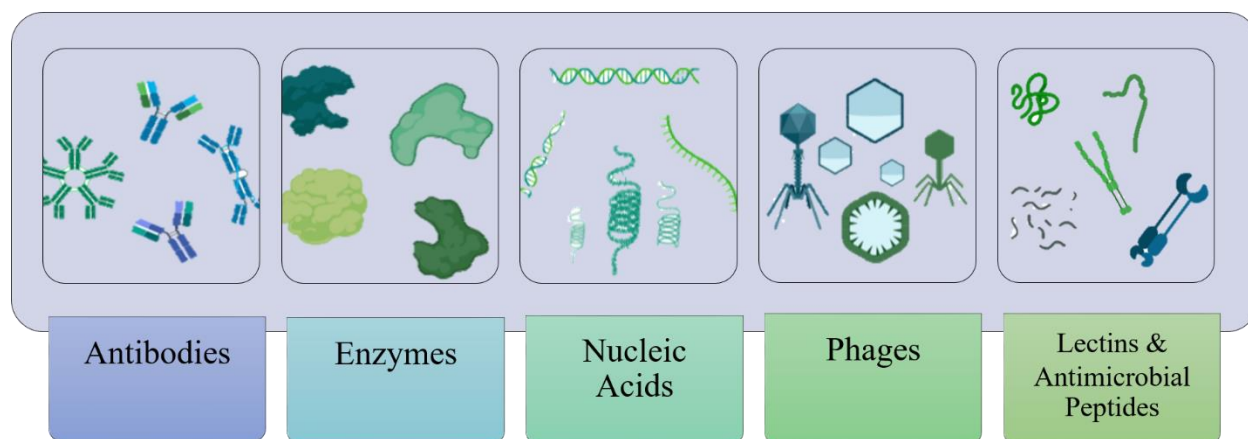
Figure 1.14. Bioreceptors used for the development of biosensors targeting bacteria. These include antibodies (IgG, IgA, IgM), nanobodies and isolated part of antibodies, many kinds of enzymes, DNA and RNA sequences, including aptamers, bacteriophages, and lectins and antimicrobial peptides.

Genosensors rely on bacterial DNA detection by employing miniaturized gene chips that are simpler and cheaper than other nucleic acid-based techniques (i.e. PCR)[296]. Genosensors also provide high sensitivity but do require primer sequences to perform the detection, as well as a DNA/RNA extraction step from the original samples. Among all nucleic acid possible targets, 16 rRNA is one of the most important since it simultaneously contains both highly conserved sequences that allow for general bacteria detection and hyper-variable sequences that allow for a very specific bacterial identification. As an example, Zeng et al. developed a genosensor targeting specific 16S rRNA sequences in order to detect *E. coli* and *S. aureus* simultaneously[301]. This sensor works as follows (Figure 1.15b): first, the bacteria are lysed and the 16S rRNA is amplified by reverse transcription PCR (RT-PCR). Next, half of the amplified DNA fragments are

conjugated to magnetic microbeads, whereas the other half of the amplified DNA fragments are hybridized with different fluorescent probes. As a result, the combination of magnetic microbeads, target DNA, and fluorescent probes yield a LOD of 180 CFU/mL after analyzing the samples by flow cytometry, enabling to differentiate among different bacterial species according to the particular fluorescence labels. On the one hand, this genosensor allows for multiplexing and very low detection limits. On the other hand, the overall process requires several working steps, as well as expensive devices and reagents.
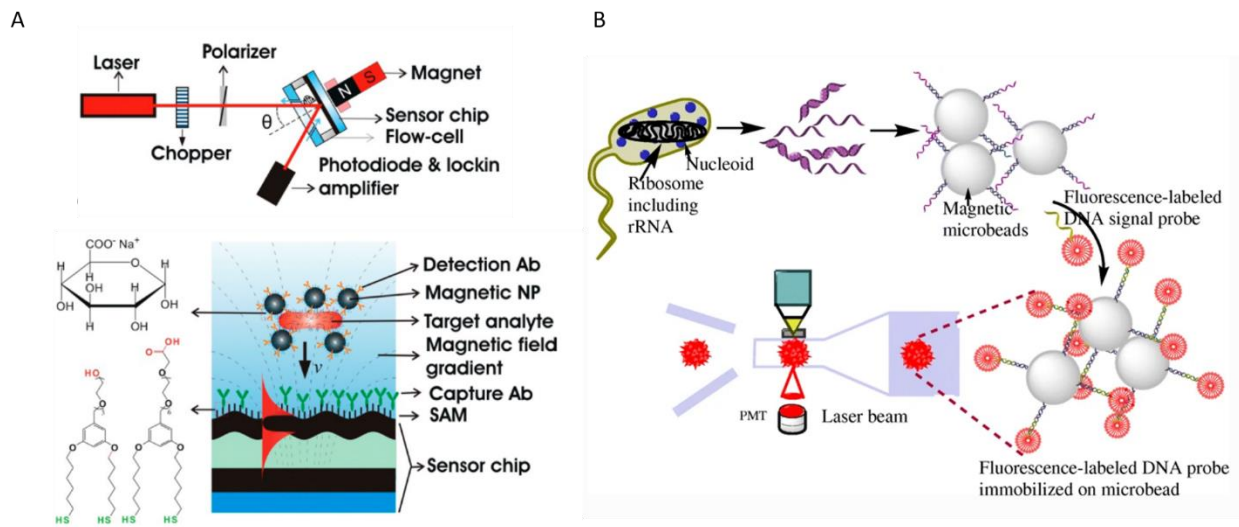
Figure 1.15. Surface plasmon resonance sensors and genosensors. (A) On the top, configuration of a grating-couple long-range surface plasmon (GC-LRSP) sensor. On the bottom, the detection mechanism of *E. coli* O157:H7 using magnetic nanoparticles coated with glucuronic acid and conjugated to polyclonal antibodies against *E. coli* O157:H7. The LRSP sensor's surface is coated with different polyclonal antibodies against *E. coli* O157:H7, which are attached to a thiol self-assembled monolayer deposited onto a gold surface. An additional gold monolayer is placed between the fluoropolymer and the glass substrate in order to increase the coupling efficiency. (B) The detection mechanism of a genosensor using 16 rRNA to detect *E. coli* and *S. aureus*. Following the arrows: 16 rRNA extraction and amplification by RT-PCR → conjugation to magnetic microbeads → conjugation to fluorescent labels → flow cytometry detection.

In general, genosensors require bacterial lysis to release the DNA/RNA contained within the cells. This additional step increases the difficulty and the overall time of the assays, thereby current biosensors should be focused on processing free-systems that target and detect whole-bacteria. In this regard, immunosensors rely on the formation of antigen-antibody complexes to

detect bacteria and other microorganisms. In most of the cases, antibodies target specific surface epitopes present on the cell wall of bacteria cells, mainly proteins, glycoproteins, lipopolysaccharides, and peptidoglycan[299]. On the one hand, surface epitope targeting avoids the need for bacteria lysis or any other additional steps that may interfere with the detection process. However, immunosensors are also more susceptible to nonspecific interactions due to the presence of many surface epitopes in any kind of microorganism. On the other hand, bacteria detection and quantification through immunosensors cannot be correlated to other standard techniques such a growth culture or PCR. While growth culture gives an idea of the number of viable bacteria cells present in the sample, PCR gives an idea of the number of specific DNA/RNA sequences found in a particular sample. In this regard, PCR might estimate both viable and dead bacteria cells by targeting genetic sequences whose presence is independent of the cellular metabolic state. These differences complicate immunosensors validation and the estimation of bacteria concentration since a single bacterium or even broken pieces of bacterial cell walls could yield multiple antigen-antibody interactions.

The sensitivity and selectivity of the immunosensors strongly depend on the bioreceptor used to capture the bacteria cells. For example, polyclonal antibodies enable to target a pool of different unknown epitopes, thereby broadening the detection range of the immunosensors. Conversely, monoclonal antibodies are more specific since they target single epitopes, yielding higher sensitivity but ramping up the overall cost. Furthermore, lectins target bacterial cell wall glycoproteins with high selectivity and often represent a valid alternative for whole-bacteria detection. Eventually, bacteriophages, also known as phages, have also been used to develop biosensors aimed to detect bacteria. Phages are viruses that infect and replicate within bacteria and archaea. The main advantages of bacteria-targeting biosensors based on phages are the high specificity and robustness, as well as the low reagent cost, and the possibility to tune the selection of phages for different bacterial species[296]. Besides, phages can also be used to kill non-target bacteria, allowing the growth and thereby the detection of only the target bacteria[302].

Lateral flow immunoassays (LFIA) are excellent immunosensors for in-situ bacteria detection since they are portable, stable in a wide range of conditions, commercially available and tunable to yield different degrees of sensitivity. LFIA started to be developed in the early

1980s and can be present in sandwich format or competitive format, being the latter mainly used for the detection of small molecules with one antigenic determinant. On the contrary, LFIA based on the sandwich format has been widely used for the detection of different bacteria (i.e. *Campylobacter*, *Clostridium*, *E. coli*, *Pseudomonas*, *Salmonella*, *Vibrio*, etc.)[303–308]. The majority of these LFIA aim to target pathogenic strains of *E. coli* (i.e. *E. coli* O157) and *Salmonella* in food samples[309].

Most LFIA targeting bacteria rely on the use of antibodies, but others rely on antimicrobial peptides or nucleic acids as bioreceptors. In this regard, nucleic acids can target oligonucleotides, protein surface antigens or even whole-bacteria[309]. Aptamers present several advantages over polyclonal antibodies: low immunogenicity, controllable selectivity, and better stability[310]. Besides, aptamers can be easily tagged with reporter fluorescent molecules. On the other hand, aptamers present short half-life, low specificity in some cases and are quickly exposed to serum degradation when testing biological samples.

Regarding the LFIA transducers, AuNPs, QDs, carbon NPs, fluorescent dyes, up-converting emitters, and magnetic beads have been used, among others[302]. On the one hand, AuNPs are easy and cheap to synthesize. Moreover, the versatility of AuNPs' synthesis allows for tunable size and shape, which yield size-dependent electronic and optical properties. AuNPs are also considered highly biocompatible. Besides, AuNPs possess quenching ability, useful to develop dual colorimetric-fluorescent assays. Eventually, AuNPs interact strongly with thiol groups that may be present in antibodies and SH-modified aptamers for an optimal bioconjugation[310]. On the other hand, QDs are fluorescent nanometric semiconductor particles with special optical and electronic properties. In general, QDs possess high quantum yield, with broad absorption spectra and narrow emission spectra. Moreover, QDs present low photobleaching and high resistance to harsh chemical degradation[310].

As an example, Schenk et al. developed an AuNPs-based LFIA for the detection of *Salmonella* lipopolysaccharides (LPS) by structuring four channels within a single LFS (Figure 1.16a)[311]. Interestingly, the authors can detect the LPS of two different species of *Salmonella* (*S. enteritidis* and *S.* Typhimurium), and avoid the well-known "Hook effect" by adding an intermediate spot of LPS between the test dots and the control dots in the nitrocellulose pad. In

another example, Wang et al. developed a fluorescent LFIA based on magnetic-core@dual quantum dot-shell nanoparticles (Fe_3O_4@DQDs) for the detection of *Streptococcus pneumonia* (Figure 1.16b)[312]. Their new synthesis of Fe_3O_4@DQDs through polyethyleneimine (PEI)-mediated layer-by-layer yields better fluorescent properties and more stability than the conventional synthesis methods. On the one hand, the QDs allows for a strong fluorescent signal upon excitation at 365 nm. On the other hand, the Fe_3O_4 particles allow for the separation and pre-concentration of the target bacteria. Eventually, the authors report a LOD of 8 CFU/mL, with good a detection range from 10 to 10^7 CFU/mL, yielding good specificity and selectivity in blood and serum samples.

The combination of more than one signal transducer often yields better sensitivity than the use of single nanoparticles within the LFIA. For example, Chen et al. developed an LFIA system based on two different sized AuNPs (28 and 45 nm) to detect *E. coli* O157:H7 (Figure 1.16c)[313]. This procedure requires a first step performed in solution, in which the bacteria are incubated with 28 nm AuNPs conjugated with monoclonal antibodies anti-*E. coli* O157:H7. Next, this solution is loaded onto the sample pad and flows across the conjugate pad, where 45 nm AuNPs are immobilized. The antibodies conjugated to the 45 nm AuNPs recognize and capture the antibodies conjugated to the 28 nm AuNPs, forming a bigger complex of bacteria-28 nm AuNPs-45 nm AuNPs. Eventually, the antibodies printed on the test line capture the bacteria and the two kinds of AuNPs, boosting the sensitivity of the overall system until $\approx 10^3$ CFU/mL, at least two to three orders of magnitude better than the standard colorimetric LFS targeting whole-bacteria[302,314].

Bu et al. developed an even simpler method based on colorimetric LFIA targeting *Salmonella enteritidis* using a single monoclonal antibody (Figure 1.16d)[315]. Briefly, the authors stain the bacteria cells in solution with crystal violet for 1 minute, which is one of the two main dyes used for the conventional Gram stain. Next, the stained samples are loaded onto the sample pad of the LFS and flow throughout the LFS until the bacteria reach the monoclonal antibodies immobilized within the test line (TL), generating a strong violet line in case of a positive signal. This system avoids the use of conjugate particles and the first-target antibody since the color generation comes from the bacteria stain, and all specificity relies on the monoclonal antibodies

immobilized within the TL. Besides, no control line (CL) antibodies are required because of the absence of bioreceptors in the conjugate pad. The authors claim to detect *S. enteritidis* with a LOD as low as 80 CFU/mL, with a total assay time of 11 minutes.
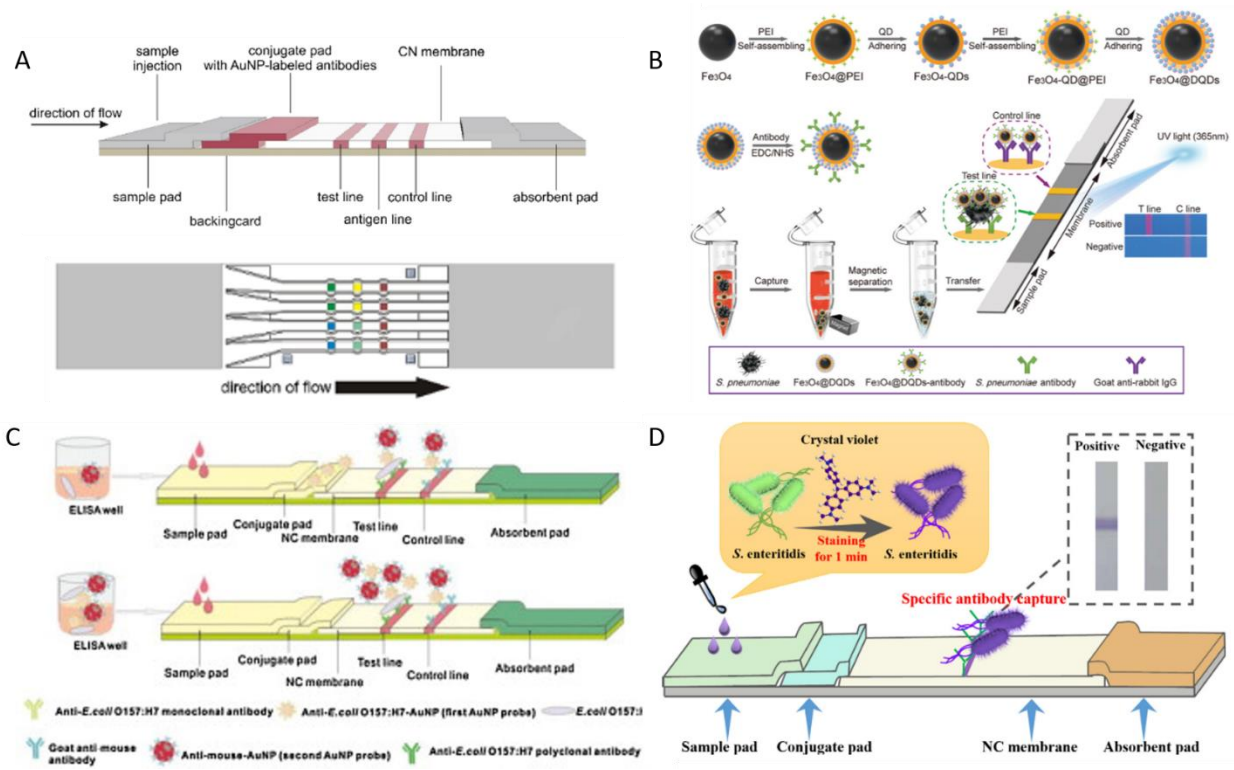
Figure 1.16. Lateral flow technology for bacteria detection. (A) Schematic representation of a multi-channel LFS for the detection of lipopolysaccharides of two different species of *Salmonella* using 20 nm AuNPs. (B) Schematic representation of a fluorescent LFIA system using Fe$_3$O$_4$@DQDs conjugated with monoclonal antibodies for the detection of *Streptococcus pneumonia*. (C) Schematic representation of two possible configurations of an AuNPs-based LFIA system for the detection of *E. coli* O157:H7 using two different sized AuNPs as a strategy for signal enhancement. (D) Schematic representation of an LFIA system for the detection of *Salmonella* Typhimurium using a single monoclonal antibody and crystal violet as a staining agent.

Not only LFIA but also different immunosensing platforms have recently been designed for bacteria detection. For example, Ruan et al. developed a fluorescent ELISA format-immunoassay (FLISA) to detect the bacteria *Delftia tsuruhatensis* by using CdTe:Zn/ZnS QDs (Figure 1.17a)[316]. With this system, the authors report a LOD close to 10^3 CFU/mL, at least two orders of magnitude lower than the standard ELISA. However, the true advantage of the FLISA is that it avoids the use of secondary antibodies, enzymes and fluorescent substrates due to the direct fluorescent output

produced by the antibodies conjugated to the CdTe:Zn/ZnS QDs. As a summary, this system yields not only better sensitivity than standard ELISA but also reduces two working steps and the need for additional expensive bioreceptors.

Silica nanoparticles (SiNPs) have also been used for bacteria detection through optical and electrochemical methods[317,318]. SiNPs have good biocompatibility and allow for an easy and cost-effective synthesis. Besides, SiNPs can easily undergo surface modification and possess hydrophilic properties. Last but not least, SiNPs sterically hinder nucleases, making them a powerful tool in combination with aptamers for biosensing[310]. Maldonado et al. used not SiNPs but silane-PEGylated-COOH surfaces to develop a dual aptamer-antibody biosensor for the simultaneous detection of *Pseudomonas aeruginosa* and methicillin-resistant *Staphylococcus aureus* (MRSA) (Figure 1.17b)[319]. Briefly, the silane-PEGylated-COOH surface is a repelling material highly resistant to bacteria attachment, avoiding non-specific interactions. The authors use polyclonal antibodies and aptamers to selectively capture *P. aeruginosa* and MRSA, respectively, to detect only the bacteria of interest. Next, a single-wavelength laser at 638 nm crosses the sensing surface. As a consequence, the presence of bacteria (*P. aeruginosa* and MRSA) attached to the surface is determined by changes in the refractive index (interferometry), yielding a theoretical LOD between 29 and 50 CFU/mL.
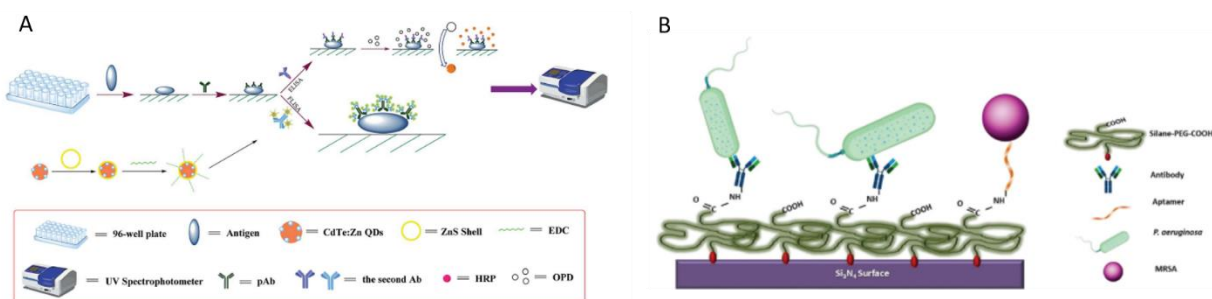
Figure 1.17. Surface plasmon resonance sensors and genosensors. (A) Schematic representation of a standard ELISA (top) and the novel fluorescent immunoassay (FLISA, bottom) for the detection of *Delftia tsuruhatensis*. (B) Schematic representation of an interferometric biosensor using PEGylated silane as a bacteria-repelling surface and antibodies and aptamers to detect specifically *Pseudomonas aeruginosa* and methicillin-resistant *Staphylococcus aureus* (MRSA), respectively.

Other approaches rely on detection systems performed in the liquid phase without the need for specific bioreceptors. For example, Huang et al. developed a liquid-phase colorimetric system to analyze the presence of bacteria in drinking water (Figure 1.18a) [320]. Briefly, the authors use 18 nm AuNPs (100 μL) functionalized with 4-mercaptophenylboronic acid (4-MPBA) in combination with bacteria samples (100 μL) within 96 micro-plate wells. After 15 min incubation, a solution of 1 M NaCl (10 μL) is added to the sample, and the color change is recorded and analyzed with a digital camera by RGB analysis. As a result, if bacteria are not present in the sample, AuNPs aggregate in the presence of NaCl, yielding a blue/purple color. On the other hand, if bacteria are present in the sample, 4-MPBA-AuNPs bind to the surface of the bacteria, thus preventing AuNPs aggregation in the presence of NaCl, yielding a red color. The authors tested five different bacterial species, including gram-positive and gram-negative bacteria, and report a linear detection range from 10^4 to 10^7 CFU/mL, with a mathematical LOD of $1.2 \cdot 10^3$ CFU/mL. Moreover, the presence of metal ions or a high concentration of NaCl does not interfere with the overall performance of the assay, showing potential applicability for the analysis of both salty and fresh water.

A different sensor developed by Wang et al. is based on a dual colorimetric and fluorescent detection system for *E. coli* in both liquid- and paper-based platforms (Figure 1.18b)[321]. This system relies on the ability of *E. coli* to reduce Cu^{2+} into Cu^+. Summarizing, the authors use *o*-phenylenediamine (OPD) as a substrate in a liquid solution, which is oxidized in the presence of Cu^{2+} ions, yielding orange-yellow fluorescence and visible yellow color. In the presence of *E. coli*, Cu^{2+} ions are reduced to Cu^+ ions, inhibiting the oxidation of OPD, thus quenching the fluorescence and hindering the color change. Besides, the authors use a filter paper impregnated with an OPD-Cu^{2+} solution under the UV lamp. In this case, the absence of *E. coli* yields a green fluorescent emission, whereas the presence of *E. coli* yields a dark-blue fluorescent emission under an excitation light of 302 nm. An integrated platform is set up by analyzing the color changes with a smartphone APP that estimates the bacterial concentration according to the fluorescent color change. Overall, this system yields a detection range from 10^2 to 10^6 CFU/mL, with a mathematical LOD between 44 CFU/mL (colorimetric assay) and 100 CFU/mL (fluorescent assay).
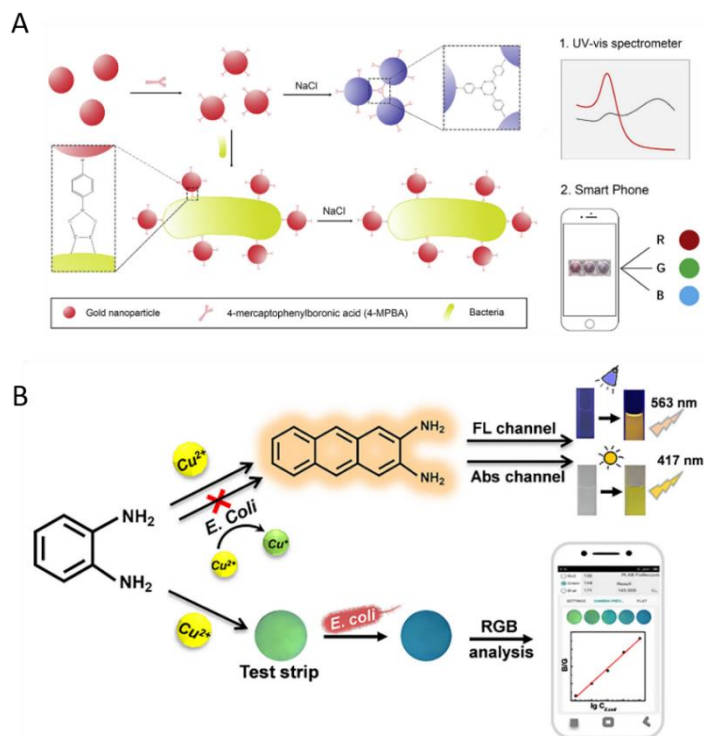
Figure 1.18. (A) Detection of *E. coli* by copper reduction. On the top, the presence of *E. coli* reduces Cu^{2+} to Cu$^+$, turning off the fluorescence emitted by *o*-phenylenediamine (OPD). On the bottom, the presence of *E. coli* hinders the colorimetric change of OPD (colorless) to the oxidized OPD (yellow) (B) Detection of total bacteria in water through a colorimetric test based on the aggregation of 4-mercaptophenylboronic acid (MPBA)-coated AuNPs in the presence of NaCl (1 M). On the one hand, the absence of bacteria induces the aggregation of the MPBA-AuNPs, switching the solution color from red to blue. On the other hand, the presence of bacteria prevents the aggregation of the MPBA-AuNPs because they bind to the surface of the bacterial cell wall, thereby the solution color remains red.

Furthermore, metal nanoclusters (NCs) are composed of few atoms of one or several metal elements with a total size smaller than 2 nm (i.e. AuNCs, AgNCs, CuNCs). As an example, AuNCs do not show the SPR properties that AuNPs do, but instead AuNCs show fluorescence and enhanced catalytic behavior. Metal NCs can be used for the detection of bacteria by label-free methods based on, for example, differential response to pH changes, agglomeration of NCs in the presence of bacteria, or fluorescence recovery of NCs upon Cu^{2+} reduction by bacteria[322]. On the other hand, metal NCs can also be used for bacteria detection through the recognition of molecular motifs by conjugation to small molecules, covering of bigger biomolecules such as enzymes, undergoing magnetic enrichment, or by FRET mechanism in the presence of

appropriate quenchers (i.e. AuNPs)[322]. Besides, the combination of metal NCs with particular proteins or antibiotics allows for the detection of different bacterial species by constructing sensing arrays. In this regard, metal NCs can attach to bacteria without the need for specific bioreceptors, but their modification allows for higher specificity. As a clear advantage, metal NCs do no need the covalent modification many fluorophores require and can be used for the detection of antibiotic-resistant bacteria when coupled to certain antibiotics.

Eventually, micromechanical sensors usually depend on an antigen-antibody interaction that causes a mass change upon bacteria's attachment. These sensors provide high sensitivity and fast response time without the need for sample processing. Quartz crystal microbalance (QCM) and microcantilever sensors are the two main examples of micromechanical sensors[296]. On the one hand, QCM sensors are label-free piezoelectric biosensors that can detect resonance frequency changes, yielding very low detection limits. On the other hand, microcantilever sensors rely on functionalized bioreceptors that oscillate at a particular resonance frequency after the analyte recognition. As a clear advantage, microcantilever sensors normally allow for label-free and real-time measurements. As an example, Salam et al. developed a QCM sensor coupled to a microfluidic system for the detection of *Salmonella* Typhimurium[323]. The authors use a gold sensor chip containing two antibodies immobilized onto its surface: a monoclonal antibody against *Salmonella* and an anti-mouse IgG antibody used as a controls spot. Therefore, the attachment of *Salmonella* cells alters the sensor frequency directly proportionally to the bacteria concentration. Importantly, this QCM sensor provides good selectivity against other bacteria because of the presence of monoclonal antibodies against *Salmonella*, as well as improved sensitivity when using a sandwich immunoassay with antibody conjugated AuNPs (LOD = 10-20 CFU/mL). Similarly, other authors have reported microcantilever sensors to detect whole-bacteria, such as *Bacillus anthracis*, *E. coli* O157:H7, and *Salmonella* Typhimurium[324].

1.4. Perspectives

Water pollution is one of the main challenges humankind is facing nowadays. In particular, agriculture and farming are the two main activities that introduce the highest quantities of wastewater into the environment worldwide. Consequently, as agriculture uses a myriad of pesticides to control pests and boost crops' growth, and farming generates large quantities of

dung, pesticides and fecal microorganisms are the most important water pollutants to be monitored.

In this regard, the detection of pesticides in water can be addressed through several perspectives, from specific compounds detection to the determination of the overall toxicity caused by a complex pool of different pesticides. The detection of specific compounds often yields high specificity and sensitivity through a wide variety of nanomaterials and approaches (i.e. MIPs and selective chemical reactions). On the other hand, the use of enzymes as bioreceptors allows detecting a family of structurally related pesticides that usually inhibit the catalytic activity of the enzyme. Eventually, toxicity biosensors allow for the evaluation of the overall toxicity of a water sample, without considering the identity and concentration of specific compounds. In a real case scenario, this last approach provides the most reliable information because water pollution often comprises different pollution inputs pouring a variety of pesticides in water that, in turn, are found at variable concentrations.

On the other hand, fecal contamination of water requires the detection of particular fecal indicators since the number of pathogens that can be found in wastewaters is large (i.e. bacteria, viruses, and parasites). So far, fecal coliforms, and more specifically *Escherichia coli*, are the best candidates as indicators of water fecal contamination. However, it is worth to mention that either the presence or absence of *E. coli* in water cannot completely foresee the presence of certain pathogens, such as some viruses and parasites.

Bacteria gold-standard detection methods have traditionally been growth culture, colony counting, and microscopy techniques. More recently, enzymatic assays, immunoassays, and PCR appeared, yielding better sensitivity and specificity but at the expense of cost and simplicity. In this context, biosensing has evolved as a promising alternative for bacteria detection, and especially for fecal bacteria detection in water. Genosensors, immunosensors, and enzymatic sensors are probably the most widely studied, each of them relying on nucleic acids, antibodies or aptamers, and enzymes as bioreceptors, respectively. A great variety of transducers is also used to boost the sensitivity of these biosensors, such as metal nanoparticles, nanoclusters, and quantum dots. Nowadays, lateral flow immunoassays (LFIA) represent one of the most appealing biosensing approaches because of their simplicity, portability, easy interpretation, and lack of

multiple and complex steps. Nonetheless, LFIA still has some drawbacks such as the lack of sensitivity, specificity and stability in certain cases due to the inherent characteristics of antibodies.

As a general conclusion, more efforts should be driven for the development of more sensitive, stable, and reliable toxicity biosensors, since they provide the broadest and most relevant information regarding the chemical pollution of waters. Besides, research should be focused on the development of inexpensive, small, easy-to-operate, and with little or no sample preparation bacterial biosensors, while boosting their sensitivity and stability for water fecal contamination determination.

1.5. References

1.   Ritchie H, Roser M. Water Use and Stress. Our World in Data. https://ourworldindata.org/water-use-stress. Published in 2015.

2.   Burek P, Satoh Y, Fischer G, et al. *Water Futures and Solution*.; 2016.

3.   Food and Agriculture Organization of the United Nations. AQUASTAT - FAO's Global Information System on Water and Agriculture. AQUASTAT. http://www.fao.org/aquastat/en/overview/methodology/water-use. Published in 2010.

4.   European Environmental Agency. *European Waters - Assessment of Status and Pressures*.; 2018. doi:10.4324/9780203938607

5.   World Health Organization. Drinking-water. https://www.who.int/news-room/fact-sheets/detail/drinking-water. Published in 2019.

6.   The global distribution of deaths from unsafe water. Our World in Data. https://ourworldindata.org/water-access#the-global-distribution-of-deaths-from-unsafe-water. Published in 2016.

7.   Ghangrekar MM, Chatterjee P. Water pollutants classification and its effects on the environment. In: *Carbon Nanotubes for Clean Water*. ; 2018:11-26. doi:10.1007/978-3-319-95603-9_2

8.   Eerkes-Medrano D, Thompson R. *Occurrence, Fate, and Effect of Microplastics in Freshwater Systems*. Elsevier Inc.; 2018. doi:10.1016/b978-0-12-813747-5.00004-7

9.   Ngo PL, Pramanik BK, Shah K, Roychand R. Pathway, classification and removal efficiency of microplastics in wastewater treatment plants. *Environ Pollut*. 2019;255:1-8. doi:10.1016/j.envpol.2019.113326

10.   Fuller N, Smith JT, Ford AT. Impacts of ionizing radiation on sperm quality, DNA integrity and post-fertilisation development in marine and freshwater crustaceans. *Ecotoxicol Environ Saf*. 2019;186(109764):1-9.

INTRODUCTION

doi:10.1016/j.ecoenv.2019.109764

11. Little JB. Principal Cellular and Tissue Effects of Radiation. In: *Cancer Medicine. 6th Edition.* 6th ed. ; 2003.

12. Environmental Protection Agency. Toxic Substances Control Act Inventory. https://www.epa.gov/tsca-inventory/how-access-tsca-inventory. Published in 2016.

13. Stadnicka-Michalak J, Schirmer K, Ashauer R. Toxicology across scales: Cell population growth in vitro predicts reduced fish growth. *Sci Adv*. 2015;1:1-8. doi:10.1126/sciadv.1500302

14. Hill MP, Macfadyen S, Nash MA. Broad spectrum pesticide application alters natural enemy communities and may facilitate secondary pest outbreaks. *PeerJ*. 2017;5:1-24. doi:10.7717/peerj.4179

15. Zeilinger AR, Olson DM, Andow DA. Competitive release and outbreaks of non-target pests associated with transgenic Bt cotton. *Ecol Appl*. 2016;26(4):1047-1054. doi:10.1890/15-1314

16. Collier R, Jukes A, Daniel C, Hommes M. Ecological selectivity of pesticides and pesticide application methods. *Integr Prot F Veg*. 2016;118:94-98.

17. Ramírez JA, Lacasaña M. Plaguicidas: clasificación, uso, toxicología y medición de la exposición. *Arch Prevención Riesgos Laborales*. 2001;4(2):67-75.

18. Bartual-Sánchez J, Berenguer-Subils MJ. *Pesticidas: Clasificación y Riesgos Principales*.; 1985.

19. World Health Organization. *Arsenic, Metals, Fibres and Dusts*. Vol 100.; 2012. https://www.iarc.fr/.

20. Davison K, Mann KK, Miller WH. Arsenic Trioxide: Mechanisms of Action. *Semin Hematol*. 2002;39(2):3-7. doi:10.1053/shem.2002.33610

21. National Center for Biotechnology Information. Arsenic pentoxide. PubChem Database,. https://pubchem.ncbi.nlm.nih.gov/compound/Arsenic-pentoxide. Published 2019.

22. National Center for Biotechnology Information. Methylarsonic acid. PubChem Database,. https://pubchem.ncbi.nlm.nih.gov/compound/Methylarsonic-acid. Published 2019.

23. National Center for Biotechnology Information. Cacodylic acid. PubChem Database,. https://pubchem.ncbi.nlm.nih.gov/compound/Cacodylic-acid. Published 2019.

24. World Health Organization. Arsenic, Metals, Fibres and Dusts. *IARC Monogr*. 2012;100(C):41-93.

25. Environmental Protection Agency. Organic Arsenicals: Product Cancellation Order and Amendments to Terminate Uses. *Fed Regist*. 2009;74(188):50187-50194. doi:10.1016/0196-335x(80)90058-8

26. Samikkannu T, Chen CH, Yih LH, et al. Reactive Oxygen Species Are Involved in Arsenic Trioxide Inhibition of Pyruvate Dehydrogenase Activity. *Chem Res Toxicol*. 2003;16(3):409-414. doi:10.1021/tx025615j

27. Ratnaike RN. Acute and chronic arsenic toxicity. *Postgrad Med J*. 2003;79:391-396. doi:10.1136/pmj.79.933.391

28. Aragay G, Pino F, Merkoçi A. Nanomaterials for Sensing and Destroying Pesticides. *Chem Rev*. 2012;112:5317-5338. doi:10.1021/cr300020c

29. Smith AP, Fraser CL. Bipyridine Ligands. In: *Comprehensive Coordination Chemistry II*. ; 2003:1-23. doi:10.1016/B0-08-043748-6/01103-8

30. Rao VS. *Transgenic Herbicide Resistance in Plants*. (Press C, ed.).; 2014.

31. Qian H, Chen W, Sun L, Jin Y, Liu W, Fu Z. Inhibitory effects of paraquat on photosynthesis and the response to oxidative stress in Chlorella vulgaris. *Ecotoxicology*. 2009;18:537-543. doi:10.1007/s10646-009-0311-8

32. Viales-López G. Intoxicación por Paraquat. *Med Leg Costa Rica*. 2014;31(2):1-7. https://www.scielo.sa.cr/scielo.php?script=sci_arttext&pid=S1409-00152014000200009%0Ahttp://www.scielo.sa.cr/pdf/mlcr/v31n2/art09v31n2.pdf.

33. Constable EC. *A Journey From Solution Self-Assembly to Designed Interfacial Assembly*. Vol 71. 1st ed. Elsevier Inc.; 2018. doi:10.1016/bs.adioch.2017.11.005

34. Ghosh AK, Brindisi M. Organic Carbamates in Drug Design and Medicinal Chemistry. *J Med Chem*. 2015;58:2895-2940. doi:10.1021/jm501371s

35. Fukuto TR. Mechanism of Action of Organophosphorus and Carbamate Insecticides. *Environ Health Perspect*. 1990;87:245-254. doi:10.1289/ehp.9087245

36. Schegg KM, Futamachi KJ, Peacock JH. Characterization of Acetylcholinesterase Isoforms in Septal and Hippocampal Cultures and Cocultures. *Dev Brain Res*. 1986;30:221-230. doi:10.1016/0165-3806(86)90112-4

37. Silberman J, Taylor A. *Carbamate Toxicity*.; 2019.

38. Mladenović M, Arsić BB, Stanković N, et al. The Targeted Pesticides as Acetylcholinesterase Inhibitors: Comprehensive Cross-Organism Molecular Modelling Studies Performed to Anticipate the Pharmacology of Harmfulness to Humans In Vitro. *Molecules*. 2018;23:1-37. doi:10.3390/molecules23092192

39. National Center for Biotechnology Information. Pyridostigmine. PubChem Database,. https://pubchem.ncbi.nlm.nih.gov/compound/Pyridostigmine. Published 2019.

40. Bruneton J. Principles of herbal pharmacology. In: *Principles and Practice of Phytotherapy*. ; 2013:17-82. doi:10.1016/b978-0-443-06992-5.00002-5

41. National Center for Biotechnology Information. Warfarin. PubChem Database,. https://pubchem.ncbi.nlm.nih.gov/compound/Warfarin. Published 2019.

42. National Center for Biotechnology Information. Brodifacoum. PubChem Database,. https://pubchem.ncbi.nlm.nih.gov/compound/54680676. Published 2019.

43. Poumale-Poumale HM, Hamm R, Zang Y, Shiono Y, Kuete V. *Coumarins and Related Compounds from the Medicinal Plants of Africa*.; 2013. doi:10.1016/B978-0-12-405927-6.00008-4

INTRODUCTION

44.   van Sittert NJ, Tuinman CP. Coumarin derivatives (rodenticides). *Toxicology*. 1994;91(10):71-76. doi:10.1016/0300-483X(94)90243-7

45.   Abraham K, Wöhrlin F, Lindtner O, Heinemeyer G, Lampen A. Toxicology and risk assessment of coumarin: Focus on human data. *Mol Nutr Food Res*. 2010;54:228-239. doi:10.1002/mnfr.200900281

46.   National Center for Biotechnology Information. Picric acid. PubChem Database,. https://pubchem.ncbi.nlm.nih.gov/compound/6954. Published 2019.

47.   Booth G. Nitro Compounds, Aromatic. In: *Ullmann's Encyclopedia of Industrial Chemistry*. Vol 24. ; 2006:301-349. doi:10.1002/14356007.a17

48.   Schwarzenbach RP, Stierli R, Folsom BR, Zeyer J. Compound Properties Relevant for Assessing the Environmental Partitioning of Nitrophenols. *Environ Sci Technol*. 1988;22:83-92. doi:10.1021/es00166a009

49.   National Center for Biotechnology Information. 2-nitrophenol. PubChem Database,. https://pubchem.ncbi.nlm.nih.gov/compound/2-Nitrophenol. Published 2019.

50.   National Center for Biotechnology Information. 4-Nitrophenol. PubChem Database,. https://pubchem.ncbi.nlm.nih.gov/compound/4-Nitrophenol. Published 2019.

51.   Koul B, Taak P. *Biotechnological Strategies for Effective Remediation of Polluted Soils*. Springer International Publishing; 2018.

52.   Sigma-Aldrich. *Ficha de Datos de Seguridad: 4-Nitrofenol*.; 2019.

53.   Lee CH, Kim SH, Kwon DH, Jang KH, Chung YH, Moon JD. Two Cases of Methemoglobinemia Induced by the Exposure to Nitrobenzene and Aniline. *Ann Occup Environ Med*. 2013;25(31):1-7. doi:10.1186/2052-4374-25-31

54.   Moffat C, Buckland ST, Samson AJ, et al. Neonicotinoids target distinct nicotinic acetylcholine receptors and neurons, leading to differential risks to bumblebees. *Sci Rep*. 2016;6:1-10. doi:10.1038/srep24764

55.   Han W, Tian Y, Shen X. Human exposure to neonicotinoid insecticides and the evaluation of their potential toxicity: An overview. *Chemosphere*. 2018;192:59-65. doi:10.1016/j.chemosphere.2017.10.149

56.   Taillebois E, Cartereau A, Jones AK, Thany SH. Neonicotinoid insecticides mode of action on insect nicotinic acetylcholine receptors using binding studies. *Pestic Biochem Physiol*. 2015;151:59-66.

57.   Cartereau A, Martin C, Thany SH. Neonicotinoid insecticides differently modulate acetycholine-induced currents on mammalian α7 nicotinic acetylcholine receptors. *Br J Pharmacol*. 2018;175:1987-1998. doi:10.1111/bph.14018

58.   Zhang E, Nieh JC. The neonicotinoid imidacloprid impairs honey bee aversive learning of simulated predation. *J Exp Biol*. 2015;218:3199-3205. doi:10.1242/jeb.127472

59.   Amirzade N, Izadi H, Jalali MA, Zohdi H. Evaluation of three neonicotinoid insecticides against the common

pistachio psylla, Agonoscena pistaciae, and its natural enemies. *J Insect Sci*. 2014;14(35):1-8. doi:10.1673/031.014.35

60.   Gribble GW. The Natural Production of Chlorinated Compounds. *Environ Sci Technol*. 1994;28(7):310-319. doi:10.1021/es00056a712

61.   Jayaraj R, Megha P, Sreedev P. Organochlorine pesticides, their toxic effects on living organisms and their fate in the environment. *Interdiscip Toxicol*. 2016;9(3-4):90-100. doi:10.1515/intox-2016-0012

62.   Ul'yanovskii N V., Kosyakov DS, Varsegov IS, Popov MS, Lebedev AT. Identification of novel disinfection byproducts in pool water: Chlorination of the algaecide benzalkonium chloride. *Chemosphere*. 2020;239:1-9. doi:10.1016/j.chemosphere.2019.124801

63.   Baccarelli A, Bollati V. Epigenetics and environmental chemicals. *Curr Opin Pediatr*. 2009;21(2):243-251. doi:10.1016/j.immuni.2010.12.017

64.   Van Wendel De Joode B, Wesseling C, Kromhout H, Monge P, García M, Mergler D. Chronic nervous-system effects of long-term occupational exposure to DDT. *Lancet*. 2001;357:1014-1016. doi:10.1016/S0140-6736(00)04249-5

65.   Raymond-Delpech V, Matsuda K, Sattelle BM, Rauh JJ, Sattelle DB. Ion channels: molecular targets of neuroactive insecticides. *Invertebr Neurosci*. 2005;5:119-133. doi:10.1007/s10158-005-0004-9

66.   Gant DB, Eldefrawi ME, Eldefrawi AT. Cyclodiene Insecticides Inhibit GABA Receptor-Regulated Chloride Transport. *Toxicol Appl Pharmacol*. 1987;88:313-321. doi:10.1016/0041-008X(87)90206-7

67.   Khan MAQ, Stanton RH, Sutherland DJ, Rosen JD, Maitra N. Toxicity-metabolism relationship of the photoisomers of certain chlorinated cyclodiene insecticide chemicals. *Arch Environ Contam Toxicol*. 1973;1(2):159-169.

68.   Igbinosa EO, Odjadjare EE, Chigor VN, et al. Toxicological Profile of Chlorophenols and Their Derivatives in the Environment: The Public Health Perspective. *Sci World J*. 2013;460215:1-11. doi:10.1084/jem.184.2.585

69.   Rossberg M& L, Wilhelm & Pfleiderer G, Tögel A, et al. *Chlorinated Hydrocarbons*.; 2006.

70.   de Boer J. Chlorinated Parafilms. In: *The Handbook of Environmental Chemistry*. ; 2010:1-198.

71.   Allsopp MW, Vianello G. Poly (Vinyl Chloride). In: *Ullmann's Encyclopedia of Industrial Chemistry*. ; 2012:411-467. doi:10.1002/14356007.a21

72.   International Agency for Research on Cancer. Trichloroethylene, tetrachloroethylene, and some other chlorinated agents. In: *IARC Monographs*. Vol 106. ; 2012:1-514.

73.   Alva S, Damodar D, D'Souza A, D'Souza UJA. Endosulfan induced early pathological changes in vital organs of rat: A biochemical approach. *Indian J Pharmacol*. 2012;44(4):512-516. doi:10.4103/0253-7613.99335

74.   Mclean D, Pearce N, Langseth H, et al. Cancer Mortality in Workers Exposed to Organochlorine Compounds

in the Pulp and Paper Industry: An International Collaborative Study. *Environ Health Perspect*. 2006;114(7):1007-1012. doi:10.1289/ehp.8588

75. Fickova M, Macho L, Brtko J. A comparison of the effects of tributyltin chloride and triphenyltinchloride on cell proliferation, proapoptotic p53, Bax, and antiapoptoticBcl-2 protein levels in human breast cancer MCF-7 cell line. *Toxicol Vitr*. 2015;29:727-731.

76. Dong-po X, Di-an F, Chang-sheng Z, Shu-lun J, Hao-yuan H. Effect of tributyltin chloride (TBT-Cl) exposure on expression of HSP90β1 in the river pufferfish (Takifugu obscurus): Evidences for its immunologicfunction involving in exploring process. *Gene*. 2018;666:9-17.

77. Lamichhane JR, Osdaghi E, Behlau F, Köhl J, Jones JB, Aubertot JN. Thirteen decades of antimicrobial copper compounds applied in agriculture. A review. *Agron Sustain Dev*. 2018;38(28):1-18. doi:10.1007/s13593-018-0503-9

78. Rosenfeld PE, Feng LGH. Mercury, BPA, and Pesticides in Food. In: *Risks of Hazardous Wastes*. ; 2011:223-235. doi:10.1016/b978-1-4377-7842-7.00017-9

79. Sigma-Aldrich. Organotin. Official Webpage of Merck. https://www.sigmaaldrich.com/chemistry/chemistry-products.html?TablePage=16246425. Published 2020.

80. Snoeij NJ, Penninks AH, Seinen W. Biological activity of organotin compounds-An overview. *Environ Res*. 1987;44:335-353. doi:10.1016/S0013-9351(87)80242-6

81. Whalley C, Mohaupt V. *Chemicals in European Waters*.; 2018. doi:10.2800/265080 European

82. Arrhenius E, Löfroth G, Ramel C. *Mercury Compounds*.; 2000. doi:10.1126/science.176.4039.1072

83. U.S. Department of Health and Human Services. *Toxicological Profile for Mercury*.; 1999. doi:10.1201/9781420061888_ch109

84. Gupta RC, Crissman JW. Agricultural Chemicals. In: *Haschek and Rousseaux's Handbook of Toxicologic Pathology*. Third Edit. Elsevier; 2013:1349-1372. doi:10.1016/B978-0-12-415759-0.00042-X

85. Abrahamian P, Jones JB, Vallad GE. Efficacy of copper and copper alternatives for management of bacterial spot on tomato under transplant and field production. *Crop Prot*. 2019;126:1-9. doi:10.1016/j.cropro.2019.104919

86. Wagner JL, Townsend AK, Velzis AE, Paul EA. Temperature and toxicity of the copper herbicide (NautiqueTM) to freshwater fish in field and laboratory trials. *Cogent Environ Sci*. 2017;3:1-12. doi:10.1080/23311843.2017.1339386

87. Doull J, Ecobichon D, Gammon D, Hodgson E, Reiter L, Ross J. Chapter 57: Pesticides Affecting Oxidative Phosphorylation. In: *Handbook of Pesticide Toxicology*. ; 2001:1214-1215.

88. Branco V, Godinho-Santos A, Gonçalves J, Lu J, Holmgren A, Carvalho C. Mitochondrial thioredoxin reductase

inhibition, selenium status,and Nrf-2 activation are determinant factors modulating the toxicityof mercury compounds. *Free Radic Biol Med*. 2014;73:95-105.

89.   Arnal N, Astiz M, de Alainz MJT, Marra CA. Clinical parameters and biomarkers of oxidative stress in agricultural workers who applied copper-based pesticides. *Ecotoxicol Environ Saf*. 2011;74:1779-1786.

90.   Husak V. Copper and Copper-Containing Pesticides: Metabolism, Toxicity and Oxidative Stress. *J Vasyl Stefanyk Precarpathian Natl Univ*. 2015;2(1):38-50. doi:10.15330/jpnu.2.1.38-50

91.   Ferreira AB, Lemos Cardoso A, da Silva MJ. Tin-Catalyzed Esterification and Transesterification Reactions: A Review. *ISRN Renew Energy*. 2012;2012:1-13. doi:10.5402/2012/142857

92.   Dakappa PH, Bhat GK, Bolumbu G, Rao SB, Adappa S, Mahabala C. Comparison of Conventional Mercury Thermometer and Continuous TherCom® Temperature Recording in Hospitalized Patients. *J Clin Diagnostic Res*. 2016;10(9):43-46. doi:10.7860/JCDR/2016/21617.8586

93.   Viera I, Pérez-Gálvez A, Roca M. Green natural colorants. *Molecules*. 2019;24(154):1-17. doi:10.3390/molecules24010154

94.   Nakanishi T. Endocrine disruption induced by organotin compounds; organotins function as a powerful agonist for nuclear receptors rather than an aromatase inhibitor. *J Toxicol Sci*. 2008;33(3):269-276. doi:10.2131/jts.33.269

95.   Harada M. Minamata Disease: Methylmercury Poisoning in Japan Caused by Environmental Pollution. *Crit Rev Toxicol*. 1995;25(1):1-24. doi:10.3109/10408449509089885

96.   Hostynek JJ, Maibach HI. Skin irritation potential of copper compounds. *Toxicol Mech Methods*. 2004;14:205-213. doi:10.1080/15376520490446365

97.   Gupta RC. Classification and Uses of Organophosphates and Carbamates. In: *Toxicology of Organophosphate and Carbamate Compounds*. ; 2006:5-24.

98.   Muhammad G, Rashid I, Firyal S. Practical Aspects of Treatment of Organophosphate and Carbamate Insecticide Poisoning in Animals. *Matrix Sci Pharma*. 2017;1(1):10-11. doi:10.26480/msp.01.2017.10.11

99.   Horsak RD, Bedient PB, Hamilton MC, Thomas F Ben. Pesticides. In: *Environmental Forensics*. ; 2005:144-163. doi:10.1016/B978-0-12-507751-4.50030-6

100. Videira RA, Antunes-Madeira MC, Lopes VICF, Madeira VMC. Changes induced by malathion, methylparathion and parathion on membrane lipid physicochemical properties correlate with their toxicity. *Biochim Biophys Acta*. 2001;1511:360-368.

101. Wade MG, Kawata A, Rigden M, Caldwell D, Holloway AC. Toxicity of Flame Retardant Isopropylated Triphenyl Phosphate: Liver, Adrenal, and Metabolic Effects. *Int J Toxicol*. 2019;38(4):279-290. doi:10.1177/1091581819851502

102. Lerro CC, Koutros S, Andreotti G, et al. Organophosphate insecticide use and cancer incidence among spouses of pesticide applicators in the Agricultural Health Study. *Environ Med*. 2015;72(10):736-744. doi:10.1136/oemed-2014-102798.Organophosphate

103. Wang X, Zhao T, Yang B, et al. Synthesis and biological evaluation of phenoxyacetic acid derivatives as novel free fatty aid receptor 1 agonists. *Bioorg Med Chem*. 2015;23:132-140.

104. Parry G, Delbarre A, Marchant A, et al. Novel auxin transport inhibitors phenocopy the auxin influx carrier mutation aux1. *Plant J*. 2001;25(4):399-406. doi:10.1046/j.1365-313X.2001.00970.x

105. Torii KU, Hagihara S, Uchida N, Takahashi K. Harnessing synthetic chemistry to probe and hijack auxin signaling. *New Phytol*. 2018;220:417-424. doi:10.1111/nph.15337

106. Benbrahim-Tallaa L, Voubard V, Brown R, et al. Carcinogenicity of lindane, DDT, and 2,4-dichlorophenoxyacetic acid. *Lancet Oncol*. 2015;16:891-892. doi:10.1016/S1470-2045(15)00081-9

107. National Center for Biotechnology Information. Phenoxyacetic Acid. PubChem Database,. https://pubchem.ncbi.nlm.nih.gov/compound/Phenoxyacetic-acid. Published 2020.

108. Morrow RL, Carney G, Wright JM, Bassett K, Sutherland J, Dormuth CR. Impact of rosiglitazone meta-analysis on use of glucose-lowering medications. *Open Med*. 2010;4(1):50-59.

109. Chemical Industry Press. Chapter 1: Introduction. In: *Analytical Methods for Food Safety by Mass Spectrometry*. ; 2018:1-9. doi:10.1016/B978-0-12-814167-0.00001-6

110. Wang X, Aránzazu-Martínez M, Wu Q, et al. Fipronil insecticide toxicology: oxidative stress and metabolism. *Crit Rev Toxicol*. 2016;46(10):876-899. doi:10.1080/10408444.2016.1223014

111. Venância Faria J, Fazolin Vegi P, Carvalho Miguita AG, Silva dos Santos M, Boechat N, Rolim Bernardino AM. Recently reported biological activities of pyrazole compounds. *Bioorganic Med Chem*. 2017;25:5891-5903. doi:10.1016/j.bmc.2017.09.035

112. Loretta CM, Nicholson RA, Casida JE. Action of Phenylpyrazole Insecticides at the GABA-Gated Chloride Channels. *Pestic Biochem Physiol*. 1993;46:47-54.

113. Wolstenholme AJ. Glutamate-gated chloride channels. *J Biol Chem*. 2012;287(48):40232-40238. doi:10.1074/jbc.R112.406280

114. Raghavendra K, Barik TK, Sharma P, et al. Chlorfenapyr: a new insecticide with novel mode of action can control pyrethroid resistant malaria vectors. *Malar J*. 2011;10(16):1-7. doi:10.1186/1475-2875-10-16

115. Sherer TB, Richardson JR, Testa CM, et al. Mechanism of toxicity of pesticides acting at complex I: relevance to environmental etiologies of Parkinson's disease. *J Neurochem*. 2007;100:1469-1479. doi:10.1111/j.1471-4159.2006.04333.x

116. Page SW. CHAPTER 10. Antiparasitic Drugs. In: *Small Animal Clinical Pharmacology*. Second Edi. Elsevier Ltd;

2013:228-229. doi:10.1039/9781849736862-00095

117. Pérez-Fernández V, García MÁ, Marina ML. Characteristics and enantiomeric analysis of chiral pyrethroids. *J Chromatogr A*. 2010;1217:968-989. doi:10.1016/j.chroma.2009.10.069

118. National Center for Biotechnology Information. Bifenthrin. PubChem Database,. https://pubchem.ncbi.nlm.nih.gov/compound/Bifenthrin. Published 2020.

119. Chrustek A, Hołyńska-Iwan I, Dziembowska I, et al. Current Research on the Safety of Pyrethroids Used as Insecticides. *Med*. 2018;54(61):1-15. doi:10.3390/medicina54040061

120. Fyfe JC, Kurzhals RL, Lassaline ME, et al. Molecular Basis of Feline β-Glucuronidase Deficiency: An Animal Model of Mucopolysaccharidosis VII. *Genomics*. 1999;58:121-128.

121. Ryder NS, Frank I, Dupont MC. Ergosterol Biosynthesis Inhibition by the Thiocarbamate Antifungal Agents Tolnaftate and Tolciclate. *Antimicrob Agents Chemother*. 1986;29(5):858-860. doi:10.1128/AAC.29.5.858

122. National Center for Biotechnology Information. Thiobencarb. PubChem Database,. https://pubchem.ncbi.nlm.nih.gov/compound/Thiobencarb. Published 2020.

123. Lee S-J, Caboni P, Tomizawa M, Casida JE. Cartap Hydrolysis Relative to Its Action at the Insect Nicotinic Channel. *J Agric Food Chem*. 2004;52:95-98. doi:10.1021/jf0306340

124. Xie J, Potter A, Xie W, Lync C, Seefeldt T. Evaluation of a dithiocarbamate derivative as a model of thiol oxidative stress in H9c2 rat cardiomyocites. *Free Radic Biol Med*. 2014;70:214-222.

125. LeBaron HM, McFarland JE, Burnside OC. Chapter 1. In: *The Triazine Herbicides: A Milestone in the Development of Weed Control Technology*. Elsevier B.V.; 2016:1-12. doi:10.1016/B978-044451167-6.50004-0

126. Barchanska H, Baranowska I. Procedures for Analysis of Atrazine and Simazine in Environmental Matrices. In: *Reviews of Environmental Contamination and Toxicology*. Vol 200. ; 2009:53-81. doi:10.1007/978-1-4419-0028-9

127. National Center for Biotechnology Information. Metconazole. PubChem Database,.

128. National Center for Biotechnology Information. Tebuconazole. PubChem Database,.

129. Sagatova AA, Keniya M V., Wilson RK, Monk BC, Tyndall JDA. Structural Insights into Binding of the Antifungal Drug Fluconazole to Saccharomyces cerevisiae Lanosterol 14α-Demethylase. *Antimicrob Agents Chemother*. 2015;59(8):4982-4989. doi:10.1128/AAC.00925-15

130. Iyer P, Makris S. Developmental and Reproductive Toxicology of Pesticides. In: *Hayes' Handbook of Pesticide Toxicology*. ; 2010:381-441. doi:10.1007/978-3-030-24436-1_17

131. Tappe H, Helmling W, Mischke P, et al. Reactive Dyes. In: *Ullmann's Encyclopedia of Industrial Chemistry*. ; 2012:277-289. doi:10.1002/14356007.a22

132. Morais S, Correia M, Domingues V, Delerue-Matos C. Urea Pesticides. In: *Pesticides - Strategies for Pesticides Analysis*. ; 2011:241-262. doi:10.5772/13126

133. Sun R, Liu C, Zhang H, Wang Q. Benzoylurea Chitin Synthesis Inhibitors. *J Agric Food Chem*. 2015;63:6847-6865. doi:10.1021/acs.jafc.5b02460

134. Bowyer J, Hilton M, Whitelegge J, et al. Molecular Modelling Studies on the Binding of Phenylurea Inhibitors to the D1 Protein of Photosystem II. *Zeitschrift fur Naturforsch - Sect C J Biosci*. 1990;45(c):379-387. doi:10.1515/znc-1990-0512

135. Kumar KS, Choo K-S, Yea SS, Seo Y, Han T. Effects of the Phenylurea Herbicide Diuron on the Physiology of Saccharina japonica Aresch. *Toxicol Environ Health Sci*. 2010;2(3):188-199. doi:10.1007/BF03216505

136. Pang SS, Guddat LW, Duggleby RG. Molecular Basis of Sulfonylurea Herbicide Inhibition of Acetohydroxyacid Synthase. *J Biol Chem*. 2003;278(9):7639-7644. doi:10.1074/jbc.M211648200

137. Magné C, Saladin G, Clément C. Transient effect of the herbicide flazasulfuron on carbohydrate physiology in Vitis vinifera L. *Chemosphere*. 2006;62:650-657.

138. Sola D, Rossi L, Schianca GPC, et al. Sulfonylureas and their use in clinical practice. *Arch Med Sci*. 2015;11(4):840-848. doi:10.5114/aoms.2015.53304

139. Gautam RK, Sharma SK, Mahiya S, Chattopadhyaya MC. Contamination of Heavy Metals in Aquatic Media: Transport, Toxicity and Technologies for Remediation. In: *Heavy Metals In Water*. ; 2014:1-24. doi:10.1039/9781782620174-00001

140. Gumpu MB, Sethuraman S, Krishnan UM, Rayappan JBB. A review on detection of heavy metal ions in water - An electrochemical approach. *Sensors Actuators, B Chem*. 2015;213:515-533. doi:10.1016/j.snb.2015.02.122

141. Nishijo M, Nakagawa H, Suwazono Y, Nogawa K, Kido T. Causes of death in patients with Itai-itai disease suffering from severe chronic cadmium poisoning: a nested case-control analysis of a follow-up study in Japan. *BMJ Open*. 2017;7:1-7. doi:10.1136/bmjopen-2016-015694

142. Baruthio F. Toxic Effects of Chromium and Its Compounds. *Biol Trace Elem Res*. 1992;32:145-153. doi:10.1007/BF02784599

143. SK Jain DW. Copper deficiency anemia: altered red blood cell lipids and viscosity in rats. *Am J Clin Nutr*. 1988;48(3):637-640.

144. Festa RA, Thiele DJ. Copper: an Essential Metal in Biology. *Curr Biol*. 2011;21:1-14. doi:10.1016/j.cub.2011.09.040.Copper

145. Nor YM. Ecotoxicity of copper to aquatic biota: A review. *Environ Res*. 1987;43:274-282. doi:10.1016/S0013-9351(87)80078-6

146. Das KK, Reddy RC, Bagoji IB, et al. Primary concept of nickel toxicity - an overview. *J Basic Clin Physiol Pharmacol*. 2019;30(2):141-152. doi:10.1515/jbcpp-2017-0171

147. Shyng S, Valiyaveetil F, Whorton M. *Thallium Flux Assay for Measuring the Activity of Monovalent Cation Channels and Transporters*.; 2017.

148. Cvjetko P, Cvjetko I, Pavlica M. Thallium toxicity in humans. *Arh Hig Rada Toksikol*. 2010;61:111-119. doi:10.2478/10004-1254-61-2010-1976

149. Sharma A, Patni B, Shankhdhar D, Shankhdhar SC. Zinc - An Indispensable Micronutrient. *Physiol Mol Biol Plants*. 2013;19(1):11-20. doi:10.1007/s12298-012-0139-1

150. Prasad AS. Discovery of Human Zinc Deficiency: Its Impact on Human Health and Disease. *Am Soc Nutr*. 2013;4:176-190. doi:10.3945/an.112.003210.176

151. Cherasse Y, Urade Y. Dietary Zinc Acts as a Sleep Modulator. *Int J Mol Sci*. 2017;18:1-12. doi:10.3390/ijms18112334

152. Lenntech. Zinc - Zn. Lenntech BV (website). https://www.lenntech.es/. Published 2020.

153. Cyprian Eneh O. A Review on Petroleum: Source, Uses, Processing, Products and the Environment. *J Appl Sci*. 2011;11(12):2084-2091.

154. Henry JA. Composition and toxicity of petroleum products and their additives. *Hum Exp Toxicol*. 1998;17:111-123. doi:10.1191/096032798678908350

155. The National Academies Press. *Oil in the Sea III: Inputs, Fates, and Effects*.; 2003.

156. Michel J. 1991 Gulf War Oil Spill (Chapter 37). In: *Oil Spill Science and Technollgy*. ; 2011:1127-1132.

157. Egawhary E. How big is the Deepwater Horizon oil spill? *BBC News*. http://news.bbc.co.uk/2/hi/uk_news/magazine/8664684.stm.

158. Chang SE, Stone J, Demes K, Piscitelli M. Consequences of oil spills: A review and framework for informing planning. *Ecol Soc*. 2014;19(2):1-25. doi:10.5751/ES-06406-190226

159. Penela-Arenaz M, Bellas J, Vázquez E. Effects of the prestige oil spill on the biota of NW Spain: 5 years of learning. *Adv Mar Biol*. 2010;56:365-396. doi:10.1016/S0065-2881(09)56005-1

160. Madigan MT, Martinko JM, Dunlap P V., Clark DP. Tratamiento de aguas residuales, potabilización de aguas y enfermedades microianas transmitidas por el agua. In: *Brock, Biología de Los Microorganismos*. 12th ed. ; 2009:1142-1160.

161. Joost Wiersinga W, Virk HS, Torres AG, et al. Melioidosis. *Nat Rev Dis Prim*. 2018;4:1-49. doi:10.1038/nrdp.2017.107

162. Cheng AC, Currie BJ. Melioidosis: Epidemiology, Pathophysiology, and Management. *Clin Microbiol Rev*. 2005;18(2):383-416. doi:10.1128/CMR.18.2.383

INTRODUCTION

163. Yang S. Melioidosis research in China. *Acta Trop*. 2000;77(2):157-165.

164. Chen YS, Lin HH, Mu JJ, et al. Distribution of Melioidosis Cases and Viable Burkholderia pseudomallei in Soil: Evidence for Emerging Melioidosis in Taiwan. *J Clin Microbiol*. 2010;48(4):1432-1434. doi:10.1128/JCM.01720-09

165. Lau SKP, Sridhar S, Ho CC, et al. Laboratory diagnosis of melioidosis: Past, present and future. *Exp Biol Med*. 2015;240:742-751. doi:10.1177/1535370215583801

166. Madigan M, Martinko J, Dunlap P, Clark D. Brock Biología de los Microorganismos. In: *Brock. Biología de Los Microorganismos*. 12th ed. Madrid, Spain; 2009:935-936.

167. World Health Organization. Campylobacter.

168. World Health Organization. Botulismo. https://www.who.int/es/news-room/fact-sheets/detail/botulism. Published 2018.

169. Carter AT, Peck MW. Genomes, neurotoxins and biology of Clostridium botulinum Group I and Group II. *Res Microbiol*. 2015;166:303-317. doi:10.1016/j.resmic.2014.10.010

170. Kumar Dhaked R, Kumar Singh M, Singh P, Gupta P. Botulinum toxin: Bioweapon & magic drug. *Indian J Med Res*. 2010;132(5):489-503.

171. Thirunavukkarasu N, Johnson E, Pillai S, et al. Botulinum Neurotoxin Detection Methods for Public Health Response and Surveillance. *Front Bioeng Biotechnol*. 2018;6(80):1-12. doi:10.3389/fbioe.2018.00080

172. Hunt JM. Shiga toxin-producing escherichia coli (STEC). *Clin Lab Med*. 2010;30(1):21-45. doi:10.1016/j.cll.2009.11.001

173. Navarro-Garcia F. Escherichia coli O104:H4 Pathogenesis: an Enteroaggregative E. coli/Shiga Toxin-Producing E. coli Explosive Cocktail of High Virulence. *Microbiol Spectr*. 2014;2(6):1-19. doi:10.1128/microbiolspec.ehec-0008-2013

174. Evans DJ, Evans DG. Chapter 25: Escherichia coli in Diarrheal Disease. In: *Medical Microbiology*. ; 1996.

175. Rich C, Alfidja A, Sirot J, Joly B, Forestier C. Identification of Human Enterovirulent Escherichia coli Strains by Multiplex PCR. *J Clin Lab Anal*. 2001;15:100-103. doi:10.1002/jcla.9

176. Wang C, Chuai X, Liang M. Legionella feeleii: pneumonia or Pontiac fever? Bacterial virulence traits and host immune response. *Med Microbiol Immunol*. 2019;208:25-32. doi:10.1007/s00430-018-0571-0

177. Crook B, Willerton L, Smith D, et al. Legionella risk in evaporative cooling systems and underlying causes of associated breaches in health and safety compliance. *Int J Hyg Environ Health*. 2020;224:1-7.

178. Marrie TJ, Haldane D, Bezanson G. Nosocomial Legionnaires' disease: Clinical and radiographic patterns. *Can J Infect Dis*. 1992;3(5):253-260. doi:10.1155/1992/582736

179. Avni T, Bieber A, Green H, Steinmetz T, Leibovici L, Paul M. Diagnostic Accuracy of PCR Alone and Compared

to Urinary Antigen Testing for Detection of Legionella spp.: A Systematic Review. *J Clin Microbiol*. 2016;54(2):401-411. doi:10.1128/JCM.02675-15

180. Pryangani Adikaram C. Chapter 13: Overview of Non Tuberculosis Mycobacterial Lung Diseases. In: *Mycobacterium - Research and Development*. ; 2018:258-286. doi:10.5772/intechopen.73542

181. Gommans EPAT, Even P, Linssen CFM, et al. Risk factors for mortality in patients with pulmonary infections with non-tuberculous mycobacteria: A retrospective cohort study. *Respir Med*. 2015;109:137-145. doi:10.1016/j.rmed.2014.10.013

182. Simon A, Onya O, Mazza-Stalder J, Nicod L, Gilbert G, Katia J. Added diagnostic value of 16S rRNA gene pan-mycobacterial PCR for nontuberculous mycobacterial infections: a 10-year retrospective study. *Eur J Clin Microbiol Infect Dis*. 2019;38:1873-1881. doi:10.1007/s10096-019-03621-z

183. Bush LM, Pérez MT. Pseudomonas and Related Infections. MSD Manual Professional Version.

184. Instituto Nacional de Seguridad e Higiene en el Trabajo. *Pseudomona Aeruginosa*.; 2016. doi:https://doi.org/10.1101/269001

185. Hall S, McDermott C, Anoopkumar-Dukie S, et al. Cellular effects of Pyocyanin, a Secreted Virulence Factor of Pseudomonas aeruginosa. *Toxins (Basel)*. 2016;8(236):1-14. doi:10.3390/toxins8080236

186. Bishop R, Erdman MM, Fields P, Fullerton K, Jackson K, Mahon B. National Enteric Disease Surveillance: Salmonella Surveillance Overview. *Centers Dis Control Prev*. 2011;(July):1-12.

187. The Center for Food Security & Public Health. *Salmonellosis*.; 2013.

188. Hoorfar J, Ahrens P, Radstrom P. Automated 5' nuclease PCR assay for identification of Salmonella enterica. *J Clin Microbiol*. 2000;38(9):3429-3435.

189. Cudjoe KS, Krona R, Crøn B, Olsen E. Use of ferrous sulphate and immunomagnetic separation to recover Salmonella enteritidis from raw eggs. *Int J Food Microbiol*. 1994;23:149-158.

190. Akullian A, Ng'eno E, Matheson A, et al. Environmental Transmission of Typhoid Fever in a Urban Slum. *PLoS Negl Trop Dis*. 2015;9(12):1-14.

191. Buckle GC, Walker CLF, Black RE. Typhoid fever and paratyphoid fever: Systematic review to estimate global morbidity and mortality for 2010. *J Glob Health*. 2012;2(1):1-9. doi:10.7189/jogh.02.010401

192. Mawazo A, Bwire GM, Matee MIN. Performance of Widal test and stool culture in the diagnosis of typhoid fever among suspected patients in Dar es Salaam, Tanzania. *BMC Res Notes*. 2019;12(319):1-5. doi:10.1186/s13104-019-4340-y

193. Krishna S, Desai S, Anjana V, Paranthaaman R. Typhidot (IgM) as a reliable and rapid diagnostic test for typhoid fever. *Ann Trop Med Public Heal*. 2011;4(1):42-44.

194. Bakr W, El Attar L, Ashour M, El Tokhy A. TUBEX Test Versus Widal Test In The Diagnosis Of Typhoid Fever in

Kafr El-Shekh, Egypt. *J Egypt Public Heal Assoc*. 2010;85(5-6):285-296.

195.   Goay YX, Chin KL, Tan CLL, et al. Identification of Five Novel Salmonella Typhi-Specific Genes as Markers for Diagnosis of Typhoid Fever Using Single-Gene Target PCR Assays. *Biomed Res Int*. 2016;2016:1-9. doi:10.1155/2016/8905675

196.   Hale TL, Keusch GT. Chapter 22: Shigella. In: *Medical Microbiology*. 4th ed. ; 1996.

197.   Bennish M, Wojtyniak B. Mortality due to shigellosis: community and hospital data. *Rev Infect Dis*. 1991;13(4):245-251.

198.   World Health Organization. Cholera.

199.   Todar K. Vibrio cholerae and Asiatic Cholera. Online Textbook of Bacteriology.

200.   Drummond N, Murphy BP, Ringwood T, Prentice MB, Buckley JF, Fanning S. Yersinia Enterocolitica: A Brief Review of the Issues Relating to the Zoonotic Pathogen, Public Health Challenges, and the Pork Production Chain. *Foodborne Pathog Dis*. 2012;9(3):179-191. doi:10.1089/fpd.2011.0938

201.   Aziz M, Waheed A. Yersinia Enterocolitica. StarPearls.

202.   Gerba CP, Pepper IL. Microbial Contaminants. In: *Environmental and Pollution Science*. 3rd ed. Elsevier Inc.; 2019:191-217. doi:10.1016/b978-0-12-814719-1.00013-6

203.   Harvala H, Broberg E, Benschop K, et al. Recommendations for enterovirus diagnostics and characterisation within and beyond Europe. *J Clin Virol*. 2018;101:11-17. doi:10.1016/j.jcv.2018.01.008

204.   Arora D, Jindal N, Shukla RK, Bansal R. Water Borne Hepatitis A and Hepatitis E in Malwa Region of Punjab, India. *J Clin Diagnostic Res*. 2013;7(10):2163-2166. doi:10.7860/JCDR/2013/5966.3459

205.   Nainan O V, Xia G, Vaughan G, Margolis HS. Diagnosis of Hepatitis A Virus Infection: a Molecular Approach. *Clin Microbiol Rev*. 2014;19(1):63-79. doi:10.1128/CMR.19.1.63

206.   Aggarwal R. Diagnosis of hepatitis E. *Nat Rev Gastroenterol Hepatol*. 2012;(January 2013):1-10. doi:10.1038/nrgastro.2012.187

207.   Jeong HS, Jeong A, Cheon DS. Epidemiology of astrovirus infection in children. *Korean J Pediatr*. 2012;55(3):77-82. doi:10.3345/kjp.2012.55.3.77

208.   Qiu F zhou, Shen X xin, Li G xia, et al. Adenovirus associated with acute diarrhea: a case-control study. *BMC Infect Dis*. 2018;18(450):1-7. doi:10.1186/s12879-018-3340-1

209.   Tran A, Talmud D, Lejeune B, et al. Prevalence of Rotavirus, Adenovirus, Norovirus, and Astrovirus Infections and Coinfections among Hospitalized Children in Northern France. *J Clin Microbiol*. 2010;48(5):1943-1946. doi:10.1128/JCM.02181-09

210.   CerTest Biotec. Rotavirus + Adenovirus + Astrovirus + Norovirus. https://www.certest.es/es/products/rotavirus-adenovirus-astrovirus-norovirus-2/. Published 2020.

211. Rumsey P, Waseem M. *Giardia Lamblia Enteritis*.; 2019.

212. Leitch GJ, He Q. Cryptosporidiosis-an overview. *J Biomed Res*. 2011;25(1):1-16. doi:10.1016/S1674-8301(11)60001-8

213. Grace E, Asbill S, Virga K. Naegleria fowleri: Pathogenesis, Diagnosis, and Treatment Options. *Antimicrob Agents Chemother*. 2015;59(11):6677-6681. doi:10.1080/21678707.2019.1571904

214. Showler AJ, Boggild AK. Entamoeba histolytica. *Can Med Assoc J*. 2013;185(12):1064. doi:10.1503/cmaj.121576

215. Montoya JG, Liesenfield O. Toxoplasmosis. *Lancet*. 2004;363:1965-1976.

216. Ortega YR, Sanchez R. Update on Cyclospora cayetanensis, a Food-Borne and Waterborne Parasite. *Clin Microbiol Rev*. 2010;23(1):218-234. doi:10.1128/CMR.00026-09

217. Qu J, Shen L, Zhao M, et al. Determination of the Role of Microcystis aeruginosa in Toxin Generation Based on Phosphoproteomic Profiles. *Toxins (Basel)*. 2018;10:1-14. doi:10.3390/toxins10070304

218. van der Merwe D, Sebbag L, Nietfeld JC, Aubel MT, Foss A, Carney E. Investigation of a Microcystis aeruginosa cyanobacterial freshwater harmful algal bloom associated with acute microcystin toxicosis in a dog. *J Vet Diagnostic Investig*. 2012;24(4):679-687. doi:10.1177/1040638712445768

219. Chiu YT, Chen YH, Wang TS, Yen HK, Lin TF. A qPCR-Based Tool to Diagnose the Presence of Harmful Cyanobacteria and Cyanotoxins in Drinking Water Sources. *Int J Environ Res Public Health*. 2017;14(547):1-17. doi:10.3390/ijerph14050547

220. Haddad SP, Jonathan BM, Taylor, Raegyn TB, et al. Determination of microcystins, nodularin, anatoxin-a, cylindrospermopsin, and saxitoxin in water and fish tissue using isotope dilution liquid chromatography tandem mass spectrometry. *J Chromatogr A*. 2019;1599:66-74.

221. United States Environmental Protection Agency. Detection Methods for Cyanotoxins. https://www.epa.gov/ground-water-and-drinking-water/detection-methods-cyanotoxins. Published 2017.

222. Hagel I, Giusti T. Ascaris lumbricoides: An Overview of Therapeutic Targets. *Infect Disord - Drug Targets*. 2010;10:349-367. doi:10.2174/187152610793180876

223. Manz KM, Clowes P, Kroidl I, et al. Trichuris trichiura infection and its relation to environmental factors in Mbeya region, Tanzania: A cross-sectional, population-based study. *PLoS One*. 2017;12(4):1-16. doi:10.1371/journal.pone.0175137

224. Chauhan VM, Scurr DJ, Christie T, Telford G, Aylott JW, Pritchard DI. The physicochemical fingerprint of Necator americanus. *PLoS Negl Trop Dis*. 2017;11(12):1-19. doi:10.1371/journal.pntd.0005971

225. Symeonidou I, Arsenopoulos K, Tzilves D, Soba B, Gabriël S, Papadopoulos E. Human taeniasis/cysticercosis: A potentially emerging parasitic disease in Europe. *Ann Gastroenterol*. 2018;31(4):406-412.

doi:10.20524/aog.2018.0260

226. Colley DG, Bustinduy AL, Evan Secor W, King CH. Human schistosomiasis. *Lancet*. 2014;383(9936):2253-2264. doi:10.19173/irrodl.v8i3.463

227. The European Parlament and the Council of the European Union. *Directive 2013/39/EU.*; 2013. doi:http://eur-lex.europa.eu/legal-content/EN/TXT/?uri=celex:32013L0039

228. Laaninen T. *Revision of the Drinking Water Directive*. Vol 625.; 2019.

229. Bernasconi C, Daverio E, Ghiani M. *Microbiology Dimension in EU Water Directives.*; 2003.

230. Gipperth L. The legal design of the international and European Union ban on tributyltin antifouling paint: Direct and indirect effects. *J Environ Manage*. 2009;90(SUPPL. 1):86-95. doi:10.1016/j.jenvman.2008.08.013

231. Bettinetti R, Kopp-Schneider A, Vignati DAL. The European water-based environmental quality standard for pentachlorophenol is NOT protective of benthic organisms. *Sci Total Environ*. 2018;613-614:39-45. doi:10.1016/j.scitotenv.2017.09.055

232. OSPAR Commission. *Pentachlorophenol.*; 2001.

233. Environmental Protection Agency (EPA). *Chemical Contaminant Rules.*; 2020. https://www.epa.gov/dwreginfo/chemical-contaminant-rules.

234. World Health Organization. *Drinking Water Parameter Cooperation Project.*; 2017. http://ec.europa.eu/environment/water/water-drink/pdf/20171215_EC_project_report_final_corrected.pdf.

235. Food Safety European Authority. The European Union summary report on trends and sources of zoonoses, zoonotic agents and food-borne outbreaks in 2013. 2015;13(1). doi:10.2903/j.efsa.2015.3991

236. Ma L, Zhou L, He Y, et al. Mesoporous Bimetallic PtPd Nanoflowers as a Platform to Enhance Electrocatalytic Activity of Acetylcholinesterase for Organophosphate Pesticide Detection. *Electroanalysis*. 2018;30(8):1801-1810. doi:10.1002/elan.201700845

237. Peng L, Dong S, Wei W, Yuan X, Huang T. Synthesis of reticulated hollow spheres structure NiCo2S4 and its application in organophosphate pesticides biosensor. *Biosens Bioelectron*. 2017;92:563-569. doi:10.1016/j.bios.2016.10.059

238. Chen X, Parker SG, Zou G, Su W, Zhang Q. β-Cyclodextrin-Functionalized Silver Nanoparticles for the Naked Eye Detection of Aromatic Isomers. *ACS Nano*. 2010;4(11):6387-6394. doi:10.1021/nn1016605

239. Tittl A, Leitis A, Liu M, et al. Imaging-based molecular barcoding with pixelated dielectric metasurfaces. *Science (80-)*. 2018;360:1105-1109. doi:10.1126/science.aas9768

240. Lin B, Yan Y, Guo M, et al. Modification-free carbon dots as turn-on fluorescence probe for detection of organophosphorus pesticides. *Food Chem*. 2018;245(378):1176-1182. doi:10.1016/j.foodchem.2017.11.038

241. Xu XY, Yan B, Lian X. Wearable glove sensor for non-invasive organophosphorus pesticide detection based on a double-signal fluorescence strategy. *Nanoscale*. 2018;10:13722-13729. doi:10.1039/c8nr03352h

242. Kant R. Surface plasmon resonance based fiber–optic nanosensor for the pesticide fenitrothion utilizing Ta2O5 nanostructures sequestered onto a reduced graphene oxide matrix. *Microchim Acta*. 2020;187(8):1-11. doi:10.1007/s00604-019-4002-8

243. Ma Y, Wang Y, Luo Y, et al. Rapid and sensitive on-site detection of pesticide residues in fruits and vegetables using screen-printed paper-based SERS swabs. *Anal Methods*. 2018;10:4655-4664. doi:10.1039/c8ay01698d

244. Azab HA, Khairy GM, Kamel RM. Time-resolved fluorescence sensing of pesticides chlorpyrifos, crotoxyphos and endosulfan by the luminescent Eu(III)-8-allyl-3-carboxycoumarin probe. *Spectrochim Acta - Part A Mol Biomol Spectrosc*. 2015;148:114-124. doi:10.1016/j.saa.2015.03.098

245. Luo Q, Lai J, Qiu P, Wang X. An ultrasensitive fluorescent sensor for organophosphorus pesticides detection based on RB-Ag/Au bimetallic nanoparticles. *Sensors Actuators, B Chem*. 2018;263:517-523. doi:10.1016/j.snb.2018.02.101

246. Guo J, Wong JXH, Cui C, Li X, Yu HZ. A smartphone-readable barcode assay for the detection and quantitation of pesticide residues. *Analyst*. 2015;140(16):5518-5525. doi:10.1039/c5an00874c

247. Zhao Y, Yang M, Fu Q, et al. A Nanozyme- and Ambient Light-Based Smartphone Platform for Simultaneous Detection of Dual Biomarkers from Exposure to Organophosphorus Pesticides. *Anal Chem*. 2018;90:7391-7398. doi:10.1021/acs.analchem.8b00837

248. Tang T, Deng J, Zhang M, Shi G, Zhou T. Quantum dot-DNA aptamer conjugates coupled with capillary electrophoresis: A universal strategy for ratiometric detection of organophosphorus pesticides. *Talanta*. 2016;146:55-61. doi:10.1016/j.talanta.2015.08.023

249. Wang J, Wu Y, Zhou P, et al. A novel fluorescent aptasensor for ultrasensitive and selective detection of acetamiprid pesticide based on the inner filter effect between gold nanoparticles and carbon dots. *Analyst*. 2018;143(21):5151-5160. doi:10.1039/c8an01166d

250. Weerathunge P, Behera BK, Zihara S, et al. Dynamic interactions between peroxidase-mimic silver NanoZymes and chlorpyrifos-specific aptamers enable highly-specific pesticide sensing in river water. *Anal Chim Acta*. 2019;1083:157-165. doi:10.1016/j.aca.2019.07.066

251. Pang S, Labuza TP, He L. Development of a single aptamer-based surface enhanced Raman scattering method for rapid detection of multiple pesticides. *Analyst*. 2014;139:1895-1901. doi:10.1039/c3an02263c

252. Yang X, Dai J, Zhao S, et al. Identification and characterization of a novel carboxylesterase from Phaseolus vulgaris for detection of organophosphate and carbamates pesticides. *J Sci Food Agric*. 2018;98:5095-5104. doi:10.1002/jsfa.9048

253. Tang X, Zhu Z, Liu R, Tang Y. A novel ratiometric and colorimetric fluorescent probe for hypochlorite based

on cyanobiphenyl and its applications. *Spectrochim Acta Part A Mol Biomol Spectrosc*. 2019;219:576-581.

254.   Qiao L, Qian S, Wang Y, Lin H. A colorimetric sensor array based on sulfuric acid assisted KMnO4 fading for the detection and identification of pesticides. *Talanta*. 2018;181:305-310. doi:10.1016/j.talanta.2018.01.029

255.   Saleh SM, Alminderej FM, Ali R, Abdallah OI. Optical sensor film for metribuzin pesticide detection. *Spectrochim Acta Part A Mol Biomol Spectrosc*. 2020;229(117971):1-9. doi:10.1016/j.saa.2019.117971

256.   Wang Q, Wei H, Zhang Z, Wang E, Dong S. Nanozyme: An emerging alternative to natural enzyme for biosensing and immunoassay. *rends Anal Chem*. 2018;105:218-224. doi:10.1016/j.trac.2018.05.012

257.   Tan G, Zhao Y, Wang M, Chen X, Wang B, Li QX. Ultrasensitive quantitation of imidacloprid in vegetables by colloidal gold and time-resolved fluorescent nanobead traced lateral flow immunoassays. *Food Chem*. 2020;311(126055):1-7. doi:10.1016/j.foodchem.2019.126055

258.   Nsibande SA, Forbes PBC. Development of a quantum dot molecularly imprinted polymer sensor for fluorescence detection of atrazine. *Luminescence*. 2019;34(5):480-488. doi:10.1002/bio.3620

259.   Yan X, Song Y, Zhu C, et al. MnO2 Nanosheet-Carbon Dots Sensing Platform for Sensitive Detection of Organophosphorus Pesticides. *Anal Chem*. 2018;90:2618-2624. doi:10.1021/acs.analchem.7b04193

260.   Wang P, Li H, Hassan MM, Guo Z, Zhang ZZ, Chen Q. Fabricating an Acetylcholinesterase Modulated UCNPs-Cu2+ Fluorescence Biosensor for Ultrasensitive Detection of Organophosphorus Pesticides-Diazinon in Food. *J Agric Food Chem*. 2019;67:4071-4079. doi:10.1021/acs.jafc.8b07201

261.   Luo QJ, Li YX, Zhang MQ, Qiu P, Deng YH. A highly sensitive, dual-signal assay based on rhodamine B covered silver nanoparticles for carbamate pesticides. *Chinese Chem Lett*. 2017;28(2):345-349. doi:10.1016/j.cclet.2016.10.024

262.   Talbert W, Jones D, Morimoto J, Levine M. Turn-on detection of pesticides: Via reversible fluorescence enhancement of conjugated polymer nanoparticles and thin films. *New J Chem*. 2016;40(9):7273-7277. doi:10.1039/c6nj00690f

263.   Azab HA, Khairy GM, Kamel RM. Time-resolved fluorescence sensing of pesticides chlorpyrifos, crotoxyphos and endosulfan by the luminescent Eu(III)-8-allyl-3-carboxycoumarin probe. *Spectrochim Acta Part A Mol Biomol Spectrosc*. 2015;148:114-124. doi:10.1016/j.saa.2015.03.098

264.   Gao L, Ju L, Cui H. Chemiluminescent and fluorescent dual-signal graphene quantum dots and their application in pesticide sensing arrays. *J Mater Chem C*. 2017;5(31):7753-7758. doi:10.1039/c7tc01658a

265.   Wang D, Lin B, Cao Y, Guo M, Yu Y. A Highly Selective and Sensitive Fluorescence Detection Method of Glyphosate Based on an Immune Reaction Strategy of Carbon Dot Labeled Antibody and Antigen Magnetic Beads. *J Agric Food Chem*. 2016;64:6042-6050. doi:10.1021/acs.jafc.6b01088

266.   Tao CL, Chen B, Liu XG, et al. A highly luminescent entangled metal-organic framework based on pyridine-substituted tetraphenylethene for efficient pesticide detection. *Chem Commun*. 2017;53:9975-9978. doi:10.1039/c7cc05031c

267.   Xu X, Guo Y, Wang X, et al. Sensitive detection of pesticides by a highly luminescent metal-organic framework. *Sensors Actuators, B Chem*. 2018;260:339-345. doi:10.1016/j.snb.2018.01.075

268.   Zhang Y, Wang Z, Wu L, Pei Y, Chen P, Cui Y. Rapid simultaneous detection of multi-pesticide residues on apple using SERS technique. *Analyst*. 2014;139(20):5148-5154. doi:10.1039/c4an00771a

269.   Kim A, Barcelo SJ, Li Z. SERS-based pesticide detection by using nanofinger sensors. *Nanotechnology*. 2015;26:1-7. doi:10.1088/0957-4484/26/1/015502

270.   Zhang D, Liang P, Yu Z, et al. The effect of solvent environment toward optimization of SERS sensors for pesticides detection from chemical enhancement aspects. *Sensors Actuators, B Chem*. 2018;256:721-728. doi:10.1016/j.snb.2017.09.209

271.   Pham TB, Hoang THC, Pham VH, et al. Detection of Permethrin pesticide using silver nano-dendrites SERS on optical fibre fabricated by laser-assisted photochemical method. *Sci Rep*. 2019;9(12590):1-10. doi:10.1038/s41598-019-49077-1

272.   Trang A, Khandhar PB. *Physiology. Acetylcholinesterase*.; 2019.

273.   Braitberg G. Acute Intoxication and Poisoning. In: *Critical Care Nephrology: Third Edition*. Third Edit. ; 2019:574-588. doi:10.1016/B978-0-323-44942-7.00098-4

274.   Abou-Donia MB, Menzel DB. Fish brain cholinesterase: Its inhibition by carbamates and automatic assay. *Comp Biochem Physiol*. 1967;21(1):99-104.

275.   Wang S, Ye Z, Wang X, Xiao L. Etching of Single-MnO2-Coated Gold Nanoparticles for the Colorimetric Detection of Organophosphorus Pesticides. *ACS Appl Nano Mater*. 2019;2:6646-6654. doi:10.1021/acsanm.9b01517

276.   Miao SS, Wu MS, Ma LY, He XJ, Yang H. Electrochemiluminescence biosensor for determination of organophosphorous pesticides based on bimetallic Pt-Au/multi-walled carbon nanotubes modified electrode. *Talanta*. 2016;158:142-151. doi:10.1016/j.talanta.2016.05.030

277.   Chen S, Wang Y, Feng L. Specific detection and discrimination of dithiocarbamates using CTAB-encapsulated fluorescent copper nanoclusters. *Talanta*. 2020;210(120627):1-7. doi:10.1016/j.talanta.2019.120627

278.   Pharmamar. Pharmamar. http://pharmamar.com/sobre-pharmamar/. Published 2020.

279.   Lovšin Barle E, Looser R, Černe M, Bechter R. The value of acute toxicity testing of pharmaceuticals for estimation of human response. *Regul Toxicol Pharmacol*. 2012;62:412-418. doi:10.1016/j.yrtph.2012.01.005

280.   Parasuraman S. Toxicological screening. *J Pharmacol Pharmacother*. 2011;2(2):74-79. doi:10.4103/0976-

500X.81895

281. Woutersen M, van Der Gaag B, Boakye AA, et al. Development and validation of an on-linewater toxicity sensor with immobilized luminescent bacteria for on-line surface water monitoring. *Sensors*. 2017;17:1-14. doi:10.3390/s17112682

282. Cevenini L, Calabretta MM, Tarantino G, Michelini E, Roda A. Smartphone-interfaced 3D printed toxicity biosensor integrating bioluminescent "sentinel cells." *Sensors Actuators, B Chem*. 2016;225:249-257. doi:10.1016/j.snb.2015.11.017

283. Bennet J, Cubbage J. *Review and Evaluation of MicrotoxTest for Freshwater Sediments*.; 1992. https://fortress.wa.gov/ecy/publications/publications/92e04.pdf.

284. Ponsoda NA. Diseño y puesta a punto de un método para la determinación de la toxicidad en efluentes líquidos. 2016.

285. Ben-Yoav H, Amzel T, Biran A, et al. Bacterial biofilm-based water toxicity sensor. *Sensors Actuators B Chem*. 2011;158:366-371. doi:10.1016/j.snb.2011.06.037

286. Liu J, Morales-Narváez E, Orozco J, Vincent T, Zhong G, Merkoçi A. Bioluminescent Nanopaper for the Fast Screening of Toxic Substances. *Nano Res*. 2017:1-19.

287. Pujol-Vila F, Vigués N, Guerrero-Navarro A, et al. Paper-based chromatic toxicity bioassay by analysis of bacterial ferricyanide reduction. *Anal Chim Acta*. 2016;910:60-67. doi:10.1016/j.aca.2016.01.006

288. Scheerer S, Gomez F, Lloyd D. Bioluminescence of Vibrio fischeri in continuous culture: Optimal conditions for stability and intensity of photoemission. *J Microbiol Methods*. 2006;67:321-329. doi:10.1016/j.mimet.2006.04.010

289. Khatun MA, Hoque MA, Zhang Y, et al. Bacterial Consortium-Based Sensing System for Detecting Organophosphorus Pesticides. *Anal Chem*. 2018;90:10577-10584. doi:10.1021/acs.analchem.8b02709

290. Sharma P, Asad S, Ali A. Bioluminescent bioreporter for assessment of arsenic contamination in water samples of India. *J Biosci*. 2013;38(2):251-258. doi:10.1007/s12038-013-9305-z

291. Joe MH, Lee KH, Lim SY, et al. Pigment-based whole-cell biosensor system for cadmium detection using genetically engineered Deinococcus radiodurans. *Bioprocess Biosyst Eng*. 2012;35:265-272. doi:10.1007/s00449-011-0610-3

292. de Mora K, Joshi N, Balint BL, Ward FB, Elfick A, French CE. A pH-based biosensor for detection of arsenic in drinking water. *Anal Bioanal Chem*. 2011;400(4):1031-1039. doi:10.1007/s00216-011-4815-8

293. Rodea-Palomares I, Gonzalez-Pleiter M, Gonzalo S, et al. Hidden drivers of low-dose pharmaceutical pollutant mixtures revealed by the novel GSA-QHTS screening method. *Sci Adv*. 2016;2:1-12. doi:10.1126/sciadv.1601272

294.   Gunnarsdottir MJ, Gardarsson SM, Figueras MJ, et al. Water safety plan enhancements with improved drinking water quality detection techniques. *Sci Total Environ*. 2020;698:1-11. doi:10.1016/j.scitotenv.2019.134185

295.   Bannister E. Evaluation of methodology for detection and quantification of coliform bacteria and their survival in soil and water. 2010.

296.   Mobed A, Baradaran B, de la Guardia M, et al. Advances in detection of fastidious bacteria: From microscopic observation to molecular biosensors. *Trends Anal Chem*. 2019;113:157-171. doi:10.1016/j.trac.2019.02.012

297.   Holzinger M, Le Goff A, Cosnier S. Nanomaterials for biosensing applications: a review. *Front Chem*. 2014;2:1-10. doi:10.3389/fchem.2014.00063

298.   Bhalla N, Jolly P, Formisano N, Estrela P. Introduction to biosensors. *Essays Biochem*. 2016;60:1-8. doi:10.1042/EBC20150001

299.   Ahmed A, Rushworth J V., Hirst NA, Millner PA. Biosensors for Whole-Cell Bacterial Detection. *Clin Microbiol Rev*. 2014;27(3):631-646. doi:10.1128/CMR.00120-13

300.   Wang Y, Knoll W, Dostalek J. Bacterial Pathogen Surface Plasmon Resonance Biosensor Advanced by Long Range Surface Plasmons and Magnetic Nanoparticle Assays. *Anal Chem*. 2012;84:8345-8350. doi:10.1021/ac301904x

301.   Zeng Y, Zhang D, Qi P. Combination of a flow cytometric bead system with 16S rRNA-targeted oligonucleotide probes for bacteria detection. *Anal Bioanal Chem*. 2019;411:2161-2168. doi:10.1007/s00216-019-01651-2

302.   Singh J, Sharma S, Nara S. Evaluation of gold nanoparticle based lateral flow assays for diagnosis of enterobacteriaceae members in food and water. *Food Chem*. 2015;170:470-483. doi:10.1016/j.foodchem.2014.08.092

303.   Song C, Liu J, Li J, Liu Q. Dual FITC lateral flow immunoassay for sensitive detection of Escherichia coli O157:H7 in food samples. *Biosens Bioelectron*. 2016;85:734-739. doi:10.1016/j.bios.2016.05.057

304.   Hwang J, Kwon D, Lee S, Jeon S. Detection of Salmonella bacteria in milk using gold-coated magnetic nanoparticle clusters and lateral flow filters. *RSC Adv*. 2016;6:48445-48448. doi:10.1039/c6ra05446c

305.   Zhao Y, Wang H, Zhang P, et al. Rapid multiplex detection of 10 foodborne pathogens with an up-converting phosphor technology-based 10-channel lateral flow assay. *Sci Rep*. 2016;6:1-8. doi:10.1038/srep21342

306.   Carroll KC, Mizusawa M. Laboratory Tests for the Diagnosis of Clostridium difficile. *Clin Colon Rectal Surg*. 2020;33(02):73-81.

307.   Poonlapdecha W, Seetang-Nun Y, Wonglumsom W, et al. Antibody-conjugated ferromagnetic nanoparticles with lateral flow test strip assay for rapid detection of Campylobacter jejuni in poultry samples. *Int J Food Microbiol*. 2018;286:6-14. doi:10.1016/j.ijfoodmicro.2018.07.009

308. Zhao F, Niu L, Nong J, et al. Rapid and sensitive detection of Pseudomonas aeruginosa using multiple cross displacement amplification and gold nanoparticle-based lateral flow biosensor visualization. *FEMS Microbiol Lett*. 2018;365:1-6. doi:10.1093/femsle/fny147

309. Shan S, Lai W, Xiong Y, Wei H, Xu H. Novel Strategies To Enhance Lateral Flow Immunoassay Sensitivity for Detecting Foodborne Pathogens. *J Agric Food Chem*. 2015;63:745-753. doi:10.1021/jf5046415

310. Jo H, Ban C. Aptamer-nanoparticle complexes as powerful diagnostic and therapeutic tools. *Exp Mol Med*. 2016;48(5):e230. doi:10.1038/emm.2016.44

311. Schenk F, Weber P, Vogler J, Hecht L, Dietzel A, Gauglitz G. Development of a paper-based lateral flow immunoassay for simultaneous detection of lipopolysaccharides of Salmonella serovars. *Anal Bioanal Chem*. 2018;410:863-868. doi:10.1007/s00216-017-0643-9

312. Wang C, Shen W, Rong Z, et al. Layer-by-layer assembly of magnetic-core dual quantum dot-shell nanocomposites for fluorescence lateral flow detection of bacteria. *Nanoscale*. 2020;12:795-807. doi:10.1039/c9nr08509b

313. Chen M, Yu Z, Liu D, et al. Dual gold nanoparticle lateflow immunoassay for sensitive detection of Escherichia coli O157:H7. *Anal Chim Acta*. 2015;876:71-76. doi:10.1016/j.aca.2015.03.023

314. Çam D, Öktem HA. Optimizations needed for lateral flow assay for rapid detection of pathogenic E. Coli. *Turkish J Biol*. 2017;41:954-968. doi:10.3906/biy-1705-50

315. Bu T, Huang Q, Yan L, et al. Applicability of biological dye tracer in strip biosensor for ultrasensitive detection of pathogenic bacteria. *Food Chem*. 2019;274:816-821. doi:10.1016/j.foodchem.2018.09.066

316. Ruan Y, Xu H, Yu J, Chen Q, Gu L, Guo A. A fluorescence immunoassay based on CdTe : Zn/ZnS quantum dots for the rapid detection of bacteria, taking: Delftia tsuruhatensis CM'13 as an example. *RSC Adv*. 2019;10:1042-1049. doi:10.1039/c9ra08651j

317. Bonnet R, Farre C, Valera L, et al. Highly labeled methylene blue-ds DNA silica nanoparticles for signal enhancement of immunoassays: application to the sensitive detection of bacteria in human platelet concentrates. *Analyst*. 2018;143:2293-2303.

318. Borsa BA, Guna BG, Hernandez FJ, et al. Staphylococcus aureus detection in blood samples by silica nanoparticle-oligonucleotides conjugates. *Biosens Bioelectron*. 2016;86(15):27-32.

319. Maldonado J, Estévez MC, Fernández-Gavela A, González-López JJ, González-Guerrero AB, Lechuga LM. Label-free detection of nosocomial bacteria using a nanophotonic interferometric biosensor. *Analyst*. 2020;145:497-506. doi:10.1039/c9an01485c

320. Huang J, Sun J, Warden AR, Ding X. Colorimetric and photographic detection of bacteria in drinking water by using 4-mercaptophenylboronic acid functionalized AuNPs. *Food Control*. 2020;108:1-7. doi:10.1016/j.foodcont.2019.106885

321.   Wang C, Gao X, Wang S, Liu Y. A smartphone-integrated paper sensing system for fluorescent and colorimetric dual-channel detection of foodborne pathogenic bacteria. *Anal Bioanal Chem*. 2020;412:611-620. doi:10.1007/s00216-019-02208-z

322.   Li D, Kumari B, Makabenta JM, Gupta A, Rotello V. Effective detection of bacteria using metal nanoclusters. *Nanoscale*. 2019;11:22172-22181. doi:10.1039/c9nr08510f

323.   Salam F, Uludag Y, Tothill I. Real-time and sensitive detection of Salmonella Typhimurium using an automated quartz crystal microbalance (QCM) instrument with nanoparticles amplification. *Talanta*. 2013;115:761-767.

324.   Buchapudi KR, Huang X, Yang X, Ji H-F, Thundat T. Microcantilever biosensors for chemicals and bioorganisms. *Analyst*. 2011;139:1539-1556.

CHAPTER 2

Thesis Objectives

The main objective of the present thesis is to develop portable biosensors for water quality monitoring. These sensors aim to tackle microbiological and chemical pollution through the detection of the bacterium *E. coli* as a fecal indicator and the pesticides pentachlorophenol and tributyltin (TBT). Besides, an innovative platform is presented as a sensing device for environmental and health-related applications.

More in detail, the objectives of the thesis can be summarized as follows:

-   The design, fabrication, characterization, and optimization of a colorimetric lateral flow biosensor for the detection of *E. coli* using gold nanoparticles (AuNPs) and antibodies for a fast, cheap, and simple determination of water fecal contamination.

-   The design, fabrication, characterization, and optimization of a bioluminescent toxicity-based biosensor for the assessment of water toxicity and the detection of two particular pesticides (TBT and pentachlorophenol).

-   The design, fabrication, and development of a new smartphone-based portable analytical device for optical biosensing (i.e. colorimetric, fluorescent and bioluminescent) of environmental pollution and other related applications.

CHAPTER 3. ESCHERICHIA COLI DETECTION AS A FECAL INDICATOR

CHAPTER 3

Escherichia coli detection as a fecal indicator

This chapter summarizes the design, construction, development, and optimization of a colorimetric lateral flow biosensor based on polyclonal antibodies conjugated to gold nanoparticles for the detection of the fecal indicator *Escherichia coli*. The chapter is divided into i) a short introduction to set out the topic and the current needs, as well as the presented proposal; ii) materials and methods; iii) the experimental results related to the optimization of the lateral flow biosensors; iv) the characterization of the sensitivity, selectivity, reproducibility, and working with real samples of the lateral flow biosensors; v) the conclusions of the chapter, and vi) the references.

3.1. Introduction

Water safety and quality are fundamental to human development and well-being. In recent years, water pollution has arisen as one of the main challenges humankind is facing globally. Drinking polluted water leads to waterborne illnesses that are connected to a substantial disease burden. Worldwide, about 2.2 billion people use drinking water sources polluted with feces, causing more than 800.000 deaths globally, according to the estimates of the World Health Organization (WHO)[1]. In this regard, the United Nations (UN) states as one major objective for 2030 "worldwide clean water and sanitation"[2]. Currently, it is well accepted that fecal bacteria coming from sewage treatment plants, farm effluents, and flooding are the main indicators of water microbial pollution[3]. Among all fecal indicators, *Escherichia coli* (*E. coli*) is the best indicator for water microbial pollution because of two main reasons: first, *E. coli* is the most abundant bacteria in mammal digestive systems; and second, *E. coli* is more easily detected than other waterborne pathogens[3].

In this regard, according to the EU standards, drinking water must contain less than 1 CFU of *E. coli* per 100 mL[4]. Nonetheless, sewage waters usually reach levels of thousands of fecal coliforms per 100 mL, thereby fecal contamination endangers water quality standards[5]. Currently, the gold standard techniques for *E. coli* detection in water are bacterial culturing (i.e. membrane filtration and defined substrate method) and DNA-based methods (i.e. qPCR)[6]. Nonetheless, these techniques suffer from important drawbacks, namely, they are time-consuming,

complicated, relatively expensive and require well-trained personnel and highly equipped laboratories.

Lateral flow strips (LFS) are paper-based sensors that enable a fast (from 5 to 15 minutes)[7] and easy interpretation of the results. Besides, LFS typically require low sample volumes, are one-step assay, have long shelf-life, and demand relatively short development time[8]. Most LFS rely on colorimetric reporters to indicate the presence of the analyte of interest in the analyzed sample[9–12]. Among all of these labels, gold nanoparticles (AuNPs) are usually chosen because of their easy and versatile synthesis, long shelf-life[13], intense red color, and easy conjugation to different biomolecules (i.e. antibodies, DNA and aptamers, etc.)[14–18] making them powerful transducers for optical biosensing. Other LFS rely on fluorescent (i.e. upconverting nanoparticles and quantum dots) and Raman reporters that boost sensitivity at the cost of simplicity and naked-eye detection[19–21]. Nowadays, several AuNPs-based LFS products to detect bacteria are already available in the market[22–25]. LFS specifically targeting bacteria usually rely on monoclonal antibodies (mAb) to boost the sensitivity and selectivity of the assays[26–29]. Typically, these mAb-AuNPs-based LFS present LOD between 10^5 and 10^6 CFU/mL[30–32]. Furthermore, most of these LFS aim to target pathogenic strains of *E. coli* and *Salmonella* in food samples, but few of them do it for water analysis[33]. In this regard, one of the main challenges in detecting fecal pollution of waters is the countless number of different *E. coli* strains possibly found depending on the sewage water pollution inputs (i.e. cities or farms). Consequently, the detection of certain *E. coli* strains using monoclonal antibodies would thus neglect the overall water microbial pollution. The required broader detection range needs the use of polyclonal antibodies (pAb) instead of monoclonal antibodies, usually at the cost of sensitivity and selectivity of the system. However, pAb are cheaper to produce and possess higher stability than mAb[34], making pAb more affordable for massive production and scaling worldwide.

Herein, we have developed AuNPs-pAb-based LFS with an easily interpretable colorimetric output to detect several strains of *E. coli* species. The optimization of the lateral flow materials, AuNPs, and antibodies allow detecting *E. coli* at 10^4 CFU/mL in 25 minutes in combination with a simple filtration system. More in detail, we present a novel bioluminescent characterization

method to study the microfluidics of bacteria within the lateral flow materials. Other parameters such as selectivity and reproducibility have also been studied. Eventually, the proposed system proves to work properly with river and sewage samples, yielding always recoveries above 80%.

3.2. Materials and methods

3.2.1. Materials

Polyclonal anti-*E. coli* antibody (PA1-7213, ThermoFisher) and polyclonal anti-rabbit antibody (ab6702 & ab6720, Abcam) were purchased. $HAuCl_4$, sodium citrate, bovine serum albumin (BSA), sodium dodecyl sulfate (SDS), sucrose, Tween-20, drying pearls, trizma salts, phosphate salts, borate salts, tryptic soy agar (TSA) and tryptic soy broth (TSB) were purchased from Sigma-Aldrich. Commercial 60 & 80 nm AuNPs were purchased from nanoComposix. Lateral flow strips were made of nitrocellulose (HF170, HF140, HF125 & SS40, from Advanced Microdevices; CN95 & CN150, from Sartorius), glass fiber (CN14 & CN17, GE Healthcare), cellulose (GE Healthcare) and laminated cards as a scaffold (Millipore). TEM grids (carbon film 300 MESH Copper grids CF300-CU) were purchased from Electron Microscopy Sciences. Lyophilized *E. coli* cells (strain B) were purchased from Sigma-Aldrich. Other *E. coli* strains (ATCC11775, ATCC11303, ATCC25922) *& Salmonella* Typhimurium (strain ATCC14028) were purchased from the ATCC collection and the company LGC.

3.2.2. Synthesis of gold nanoparticles

A 150 mL solution of 2.2 mM sodium citrate in MilliQ water was heated up to 135 ºC. After boiling, one mL of 25 mM $HAuCl_4$ was added to the solution, and the solution color changed to light red/dark pink after 10 minutes. Next, the temperature was lowered down to 90 ºC, and then one mL of 60 mM sodium citrate was added to the solution. After 2 minutes, one mL of 25 mM $HAuCl_4$ was added to the solution and the reaction was allowed to last for 30 minutes. These last two steps were repeated 2 times and 5 times to obtain 20 nm and 40 nm AuNPs, respectively. In the last step, either 20 nm or 40 nm AuNPs were cooled down and carefully stored at +4 ºC for further use.

3.2.3. Lateral flow strips construction

Glass fiber sample pad was used as the sample pad, which is soaked in 0.01 M PBS 0.5% BSA 0.05% Tween-20 buffer and dried overnight at room temperature. The conjugate pad was prepared using AuNPs conjugated to anti-*E. coli* polyclonal antibodies (pAb). Briefly, the AuNPs solution pH was first adjusted to pH 8. Then, pAb was added to the solution at a final concentration of 10 µg/mL, followed by an incubation at 550 rpm and 4 ºC for 2 hours. Afterward, a solution of 1% BSA was added to the solution and incubated at 550 rpm and 4 ºC for 30 minutes. A centrifugation step at 9,000 rpm was then performed, and the supernatant was discarded. The pellet was resuspended in one-fourth of the initial volume of TRIS buffer 10 mM (pH 8, 0.5% sucrose, 1% BSA & 0.5% Tween-20). Finally, the AuNPs-pAb solution was dispensed over a glass fiber conjugate pad (8 mm width) and dried up using a vacuum pump for 3 hours (model N938.50KN.18, KNF LAB). Detection pad, made of nitrocellulose, was prepared by dispensing two lines (Isoflow Flatbed Dispenser, Image Technology): test line (TL, anti-*E. coli* pAb) and control line (CL, anti-rabbit pAb) and then dried at 37 ºC overnight. The following day, the nitrocellulose pad was blocked using 2% BSA for 20 minutes, washed twice using PBS 0.01% SDS and then dried at 37 ºC for 4 hours. Once all components are completely dried, the conjugate pad was carefully assembled onto the detection pad, with an overlapping of 2 mm. In the next step, the sample pad was assembled onto the conjugate pad, with an overlapping of 6 mm. The absorbent pad was finally assembled on the upper-part of the laminated card (Figure 3.1). Eventually, LFS were cut with a 5 mm width and stored with drying pearls at room temperature for further use (Guillotine Strip Cutter, Shanghai Kinbio Tech. Co. Ltd, China).
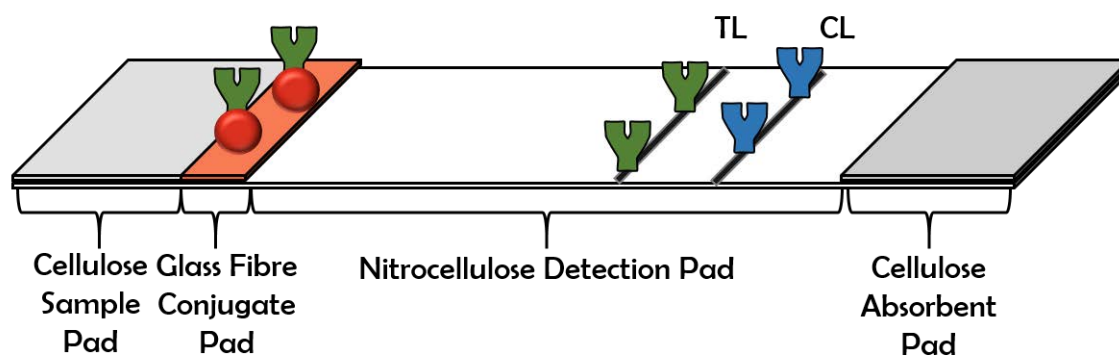
Figure 3.1. Lateral flow strip design for *Escherichia coli* detection

3.2.4. Bacteria samples preparation

Different concentrations of lyophilized *E. coli* were prepared in tap, river and sewage waters by adjusting OD600 to the reference values provided by Agilent Genomics. Whereas, for the other living strains of *E. coli* and *Salmonella*, bacterial cultures were first grown in TSB cultures. TSA plates were then incubated overnight at 37 ºC with 5 μL of the grown TSB cultures. Afterward, some colonies were picked up and added to filtered water. Optical density at 600 nm was measured, and bacterial solutions were diluted to obtain the closest OD600 value equivalent to 10^9 CFU/mL. Finally, bacteria were heat-killed at +65 ºC for 20 min before use on the strips.

3.2.5. Bacteria detection

Ten-fold decimal dilutions of different *E. coli* and *Salmonella* strains were prepared in various water samples from the original bacterial concentration. A volume of 150 μL of different *E. coli* concentrations was carefully dispensed on the sample pad of the LFS. After 10 minutes, one (CL) or two (TL & CL) lines appeared on the detection pad and the results were recorded with a lateral flow strips reader (SkanEasy, Skannex). The redder the TL, the greater the concentration of *E. coli* in the water sample. To perform the selectivity tests, the same volume and concentrations of different strains of *E. coli* and *Salmonella* were added to the LFS and the color intensity of both TL and CL was recorded after 10 minutes. The comparison was made using three different strains of *E. coli*, *Salmonella* and *E. coli* + *Salmonella* tested in the same batch of LFS. R-statistical program was used to evaluate the response of the LFS to different strains of *E. coli*[35]. Reproducibility tests were carried out using three different batches of LFS produced on different days. Inter-assay and intra-assay relative standard deviation (RSD) were calculated comparing the outputs of the three batches of LFS and testing triplicates of different concentrations of bacteria (10^6, 10^7, 10^8 CFU/mL). In another vein, filtration of water samples in the laboratory was carried out using a peristaltic pump and a microfluidic system using 0.25 μm pore-size filters (Perimax 12 SPETEC, GmbH). On the other hand, filtration in the river was performed with a portable boat that collected and filtered the water while sailing. In both cases, when the filtration was over, the filters were collected, immersed in a smaller amount of clean water (i.e. 1-2 mL),

and vortexed for 5 minutes to release the bacteria (autonomous boats, INTCATCH). These solutions were eventually used as water samples for further detection of *E. coli* on the LFS**.**

3.3. Optimization of the lateral flow biosensors

3.3.1. Characterization of AuNPs & conjugate particles

The physical and chemical properties of AuNPs are crucial to achieving the sensitivity, specificity, and reproducibility required by lateral flow immunoassays (LFIA). In this work, we chose 40 nm round-shaped AuNPs as colorimetric labels for the LFS development, based on previous LFS aimed at detecting whole-cell bacteria[36–38]. We synthesized the AuNPs by kinetically controlled seeded growth using sodium citrate as a stabilizer[39]. The UV-Vis characterization and the TEM images of AuNPs confirm the expected size as well as the homogenous size and shape distribution, which are essential features to achieve a robust performance of the LFS. In particular, the UV-Vis spectrum of 40 nm AuNPs gives a maximum absorbance peak at 526 nm, as reported in previous works (Figure 3.2a)[39,40], and TEM images show an average diameter of 39 ± 4 nm (Figure 3.2b & Figure 3.2c).

In the following step, we conjugated the AuNPs with antibodies for the construction of the LFS. We performed gold aggregation tests (GAT) to determine the most optimal pH and concentration of antibodies for the conjugation process. The conjugation performed at pH 8 using a final concentration of ≥ 10 µg/mL of antibody and $2.2 \cdot 10^{11}$ AuNPs/mL (0.36 nM) yielded the most stable conjugate particles. Next, we optimized the conjugation time to maximize the number of antibodies surrounding the AuNPs while preventing aggregation (Figure 3.2d). Two hours incubation is the most optimal conjugation time using 40 nm AuNPs and polyclonal antibodies. Shorter incubation periods often lead to incomplete coverings of the AuNPs, whereas too long incubation periods may lead to particle aggregation. Besides, we also characterized 40 nm AuNPs conjugated and unconjugated to antibodies by DLS and Z-potential to evaluate particle dispersion, conductivity, and Z-potential. Average diameters before (37.8 ± 0.1 nm) and after (104.0 ± 0.5 nm) conjugation with antibodies prove that AuNPs are indeed covered after the conjugation process. Conductivity (1.24 ± 0.05 mS/cm before and 0.048 ± 0.001 mS/cm after conjugation) and Z-potential (-32.9 ± 0.3 mV before and -39.5 ± 0.2 mV after conjugation) results

support the conjugation process. Unconjugated AuNPs are more conductive and tend to agglomerate more than those AuNPs conjugated to antibodies, in which the stability increases due to the covering with an insulating layer of biomolecules. Besides, particle dispersion is better before (polydispersity index [PDI] = 0.165) than after the conjugation of antibodies (PDI = 0.256) because not all AuNPs are equally covered by antibodies during the conjugation process. Overall, these results support the optimal conjugation of the antibodies to the AuNPs and the stability of the conjugate particles.
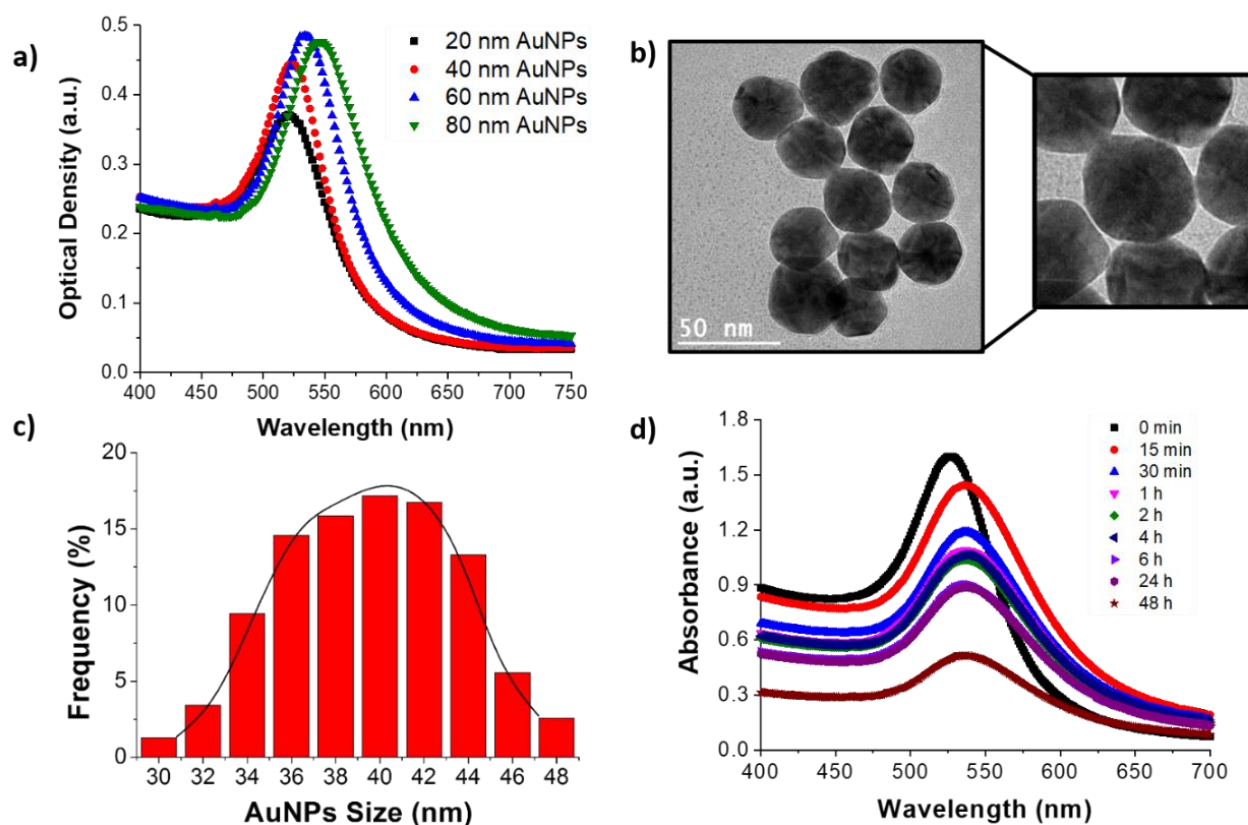
Figure 3.2. AuNPs characterization. (a) UV-Vis spectra of 20, 40, 60 and 80 nm AuNPs. (b) TEM images of 20 nm and 40 nm AuNPs. (c) Histogram representing the size distribution of AuNPs. (d) Influence of the conjugation time of 40 nm AuNPs with antibodies.

3.3.2. Characterization of the lateral flow materials

Several problems arise in the optimization of LFS regarding the flow properties of the materials that strongly influence the performance of the assay. Therefore, controlling the flow rate of big analytes within the LFS is extremely important to ensure an optimal flow throughout all the LF materials. Besides, the great difference between AuNPs size (around 40 nm) and of *E. coli* cells size (around 2 µm) often hinders an optimal control of the flow rate within the LFS. For this reason, we developed an innovative technique to characterize and evaluate simultaneously the microfluidics properties of several LF materials in 10 minutes. We exploited the bioluminescent capabilities of *Aliivibrio fischeri*, a gram-negative bacterium similar in size and shape to *E. coli*, to study the bacterial flow throughout different pads (Figure 3.3a). Briefly, *A. fischeri* was used as the analyte, dispensed on the sample pad of the LFS, and we employed a smartphone and a dark-opaque box to capture and track bioluminescence within time. By following this process, we were able to test different sample pad and detection pad materials, as well as several detection pad-blocking conditions (Figure 3.3b).
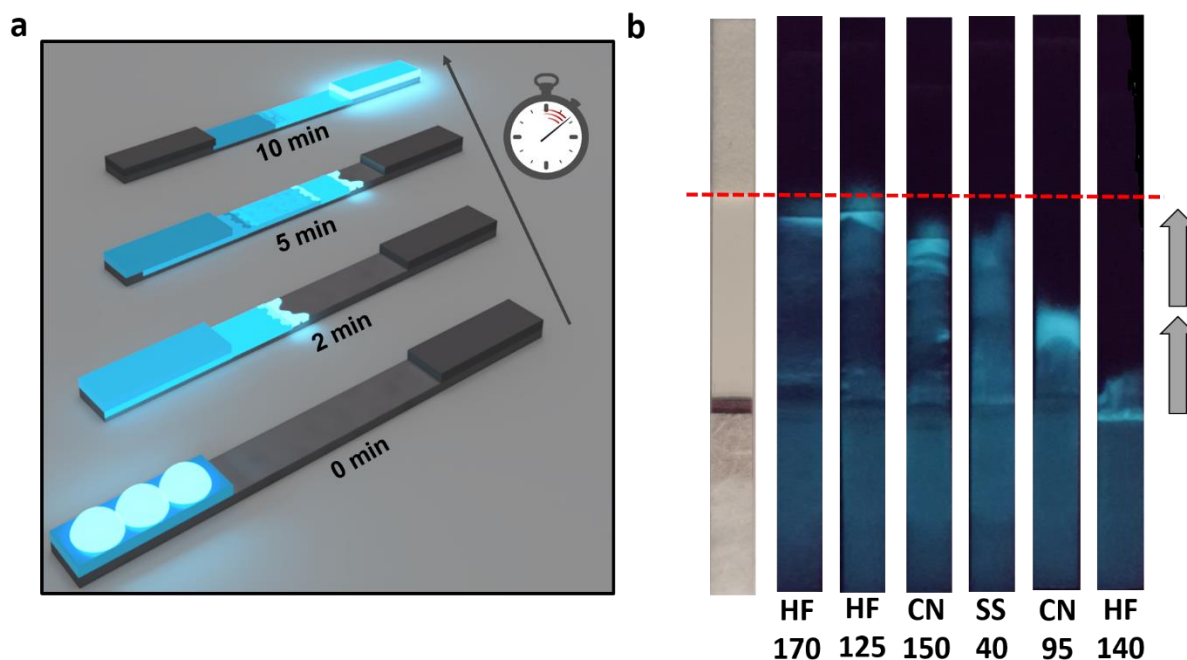
Figure 3.3. (a) Schematic representation of the new characterization method of the LFS materials using *Aliivibrio fischeri* to track the flow of rod-shaped bacteria (i.e. *E. coli*). (b) A real experiment testing the microfluidics properties of different nitrocellulose membranes as detection pads in LFS after 10 minutes using *A. fischeri*.

3.3.3. Lateral flow strips optimization

We optimized the LFS in terms of the selection of antibodies, the AuNPs size, the type of nitrocellulose membrane, the blocking of the nitrocellulose membrane, the concentration of antibody conjugated to AuNPs and the concentration of antibody immobilized on the test line by testing different *E. coli* concentrations in tap water. First, we tested four different antibodies within the conjugated pad and the test line, selecting those that provided the highest sensitivity (Figure 3.4a). Second, we analyzed the effect of AuNPs size as conjugate particles by using 20 and nm, 40 nm AuNPs, 60 nm, and 80 nm AuNPs conjugated to anti-*E. coli* antibodies (Figure 3.4b). We observed that 40 nm AuNPs provide higher sensitivity than the rest of the AuNPs. In fact, LOD improves from 10^7 CFU/mL to 10^6 CFU/mL when using 40 nm AuNPs instead of 20 nm, 60 nm, and 80 nm AuNPs. This LOD concords with other AuNPs-based LFS developed for whole-cell bacteria detection[10,30,41,42]. Besides, 40 nm AuNPs have stronger color than 20 nm AuNPs, while bigger AuNPs are less stable and may hinder antibody-antigen interactions[43].

Third and according to the previous results (Figure 3.3b), we selected the four-nitrocellulose pads that yielded an appropriate flow of bacteria to fabricate LFS and test LFIA performance (Figure 3.4c). Nitrocellulose HF170 provides the highest sensitivity, but also produces the strongest false-positive signals on the test line. Therefore, we studied different blocking conditions on the nitrocellulose pad HF170 to reduce this background signal. We selected BSA as the blocking agent to lessen the unspecific interaction of the antibodies conjugated to the 40 nm AuNPs and the antibodies immobilized within the TL. We tested different BSA concentrations, among which 2% BSA (w/v) yields the best performance, reducing the background signal while not affecting the overall sensitivity of the LFS (Figure 3.4d).

Next, we optimized the concentration of antibodies conjugated to the 40 nm AuNPs. We tested different anti-*E. coli* antibody concentrations (5, 10, 20 to 30 µg/mL) (Figure 3.4e) based on the previous gold aggregation test results. Using too low antibody concentration decreases the sensitivity of the LFS, whereas using too high antibody concentration increases the intensity of the false-positive signals. As a result, a concentration of 10 µg/mL of the antibody provides the bests results. Finally, we optimized the concentration of antibodies immobilized on the test line by comparing the sensitivity of the LFS using three different antibody concentrations (0.5, 1, 2

mg/mL) (Figure 3.4f). A concentration of 2 mg/mL provides the best results considering both the sensitivity of the assay and the intensity of the false-positive signals. Besides, this value is similar to those used in other AuNPs-based LFIA systems[32,43]. Nonetheless, we could not further test higher concentrations of antibodies due to the stock concentration of the commercially available antibody products.
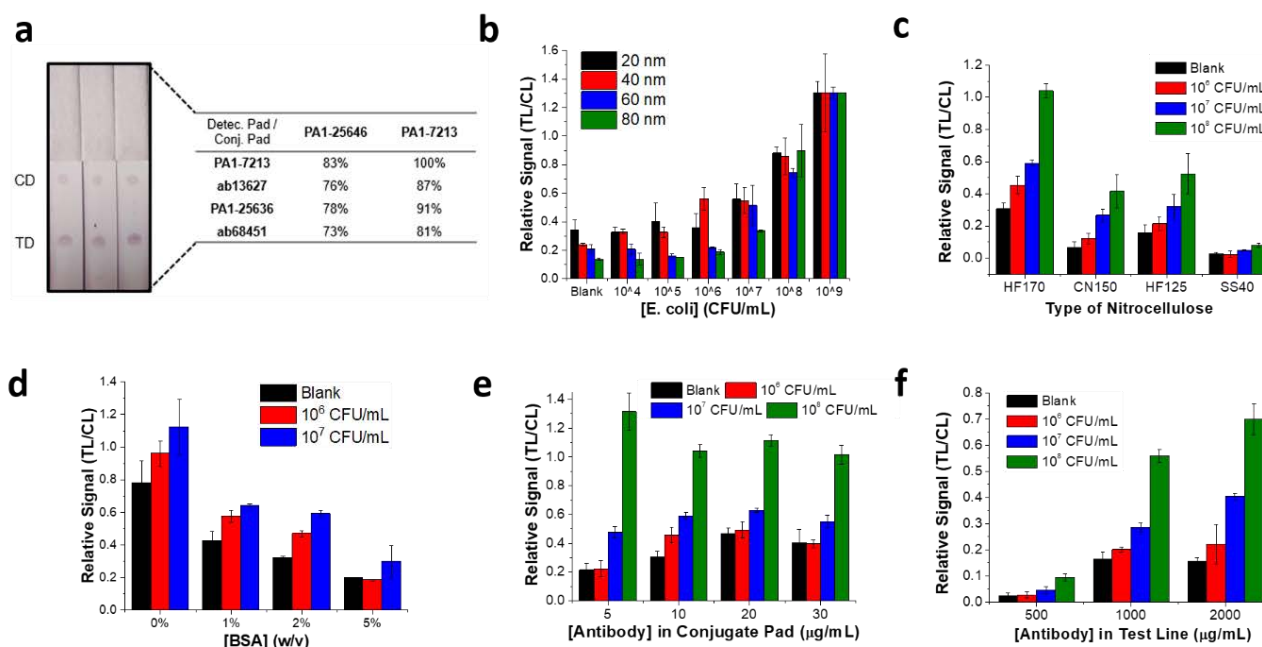
Figure 3.4. (a) Antibody selection based on the intensity color by testing different anti-*E. coli* antibodies in the conjugate pad and in the test line (test dot in this case). (b) AuNPs size selection based on the response of the LFS to variable concentrations of *E. coli* using different size AuNPs (20, 40, 60, and 80 nm). (c) Nitrocellulose selection for the detection pad based on the sensitivity of the LFS. (d) Selection of the most optimal % blocking BSA in the detection pad. (e) Selection of the most optimal concentration of antibody in the conjugate pad. (f) Selection of the most optimal concentration of antibody in the test line.

3.4. Characterization of the lateral flow biosensors

3.4.1. Sensitivity, selectivity and reproducibility

Our *E. coli* specific LFS shows the ability to quantify various strains of *E. coli* in tap water samples from 10^6 to 10^9 CFU/mL in 10 minutes, showing good sensitivity with a logarithmic slope within this working range. Optical detection limit (10^6 CFU/mL, Figure 3.5a) and mathematical

detection limit (1.2·10^6 CFU/mL)[44] correlate very well. In this regard, mathematical detection limit is calculated as:

$$x = e^{\frac{(Blank+3\cdot SD_{Blank}-b)}{a}} \quad : \quad \text{Equation 3.1}$$

Obtained LOD is similar to previous reported LOD values found in the literature for AuNPs-based LFS developed for bacterial detection[9,30,41,45]. Besides, in order to improve the LOD, we developed a filtration system using a small peristaltic pump and microfluidic tubes to pre-concentrate *E. coli* using 0.25 µm filters for further resuspension and testing on the LFS. First, 300 mL of tap water were filtered by the microfluidic system through the filter paper for 15 minutes (20 mL/min). Afterward, the filter was collected and immersed into 3 mL of clean water (without bacteria) for 5 minutes. In this regard, *E. coli* cells that were trapped on the surface of the filter are easily released into the solution. By following this method, LOD is quickly improved to 10^4 CFU/mL (Figure 3.5b). Overall, this process is more than 50 times faster than the *E. coli* traditional detection methods (i.e. culturing and colony counting on agar plates).

In order to prove the broad-range detection of several *E. coli* strains, we tested by triplicate three different strains of *E. coli* (ATCC11775, ATCC25922, and ATCC11303) in tap water on the LFS, showing good detection with similar sensitivity and LOD in all cases (Figure 3.5c). In this regard, Kruskal-Wallis statistical test (non-parametric) was performed to address significant differences among the three *E. coli* strains. At 95% confidence level the resulted p-value was 0.9543, meaning there are not significant differences among these strains. These findings confirm the ability of our LFS to detect *E. coli* as a fecal pollution indicator. Furthermore, we selected a different bacterial species from the same family (*Enterobacteriaceae*), namely *Salmonella* Typhimurium (ATCC 14028), as a negative control for the selectivity tests (Figure 3.5d). Indeed, LFS are able, not only to detect different strains of *E. coli*, but also to discriminate from *Salmonella*, providing a broad *E. coli* detection range, and meanwhile good selectivity.

Additionally, we assessed the reproducibility of the LFS within the same batch and within different batches through testing three different bacterial concentrations (10^8, 10^7 and 10^6 CFU/mL) by triplicate in tap water, and using three different batches of LFS. Relative standard

deviation (RSD) intra-assay is in all cases below 8%, while RSD inter-assay is always below 15%. These results highlight the good reproducibility achieved and support the robustness of the *E. coli* specific LFS.
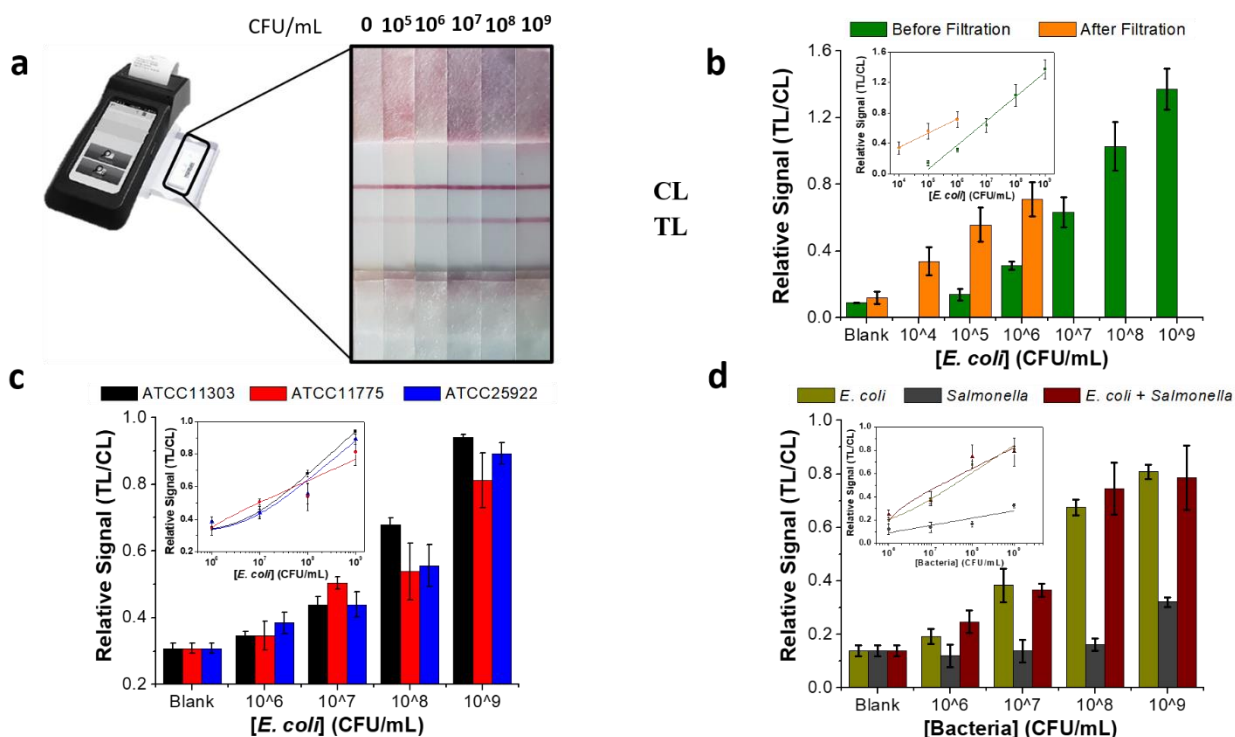
Figure 3.5. (a) LFS detecting different concentrations of *E. coli* in water and analyzed by a portable LF reader. (b) Sensitivity enhancement for the detection of *E. coli* achieved with the filtration system. (c) Performance of the LFS using three different testing three different strains of *E. coli*. (d) Performance of the LFS using *Salmonella* Typhimurium as a negative control.

3.4.2. Analysis with real samples

We investigated *E. coli* specific LFS with tap, river and sewage waters spiked with *E. coli* (Figure 3.6a, 3.6b and 3.6c). Consequently, we calculated the sensitivity, LOD and % recovery for all these water samples. Without pre-concentration, LOD remains 10^6 CFU/mL for tap, river, and outlet sewage waters; while it gets closer to 10^7 CFU/mL for the inlet and middle parts of the sewage treatment plant. % recoveries are 90% for river water and ≥ 80% in all sewage waters (Table 3.1).

These results indicate that sewage waters have a slightly detrimental effect on the LFS, probably because of the matrix effect provoked by the presence of several pollutants that may interfere with the antibody's functionality. Furthermore, flow cytometry was used as a gold

standard technique to evaluate the accuracy of our LFS after spiking *E. coli* in filtered river water, showing very good correlation (Figure 3.7).

Water Sample	Calibration Curve	Mathematical LOD (CFU/mL)	% Recovery for 10^9 CFU/mL
Tap water	y = 0.10·ln(x) - 1.23	$1.22 \cdot 10^6$	100%
River water	y = 0.08·ln(x) - 1.01	$1.93 \cdot 10^6$	90%
Inlet Sewage water	y = 0.07·ln(x) - 0.84	$2.01 \cdot 10^6$	84%
Middle Sewage water	y = 0.08·ln(x) - 0.97	$8.34 \cdot 10^6$	80%
Outlet Sewage water	y = 0.07·ln(x) - 0.72	$1.65 \cdot 10^6$	88%

Table 3.1. Sensitivity, detection limit and % recovery of different water samples spiked with *E. coli* and tested with specific anti-*E. coli* LFS.

Additionally, in another independent experiment, we collected river water samples directly from the river (river Ter, Spain), filtered them with a portable boat within the river, and tested them in the field. At this point, we tested LFS with non-spiked river samples, in order to estimate the filtration factor needed to observe a change in the signal of the LFS. We thereby applied different pre-concentration factors: x0, x20, x100, x200 and x500. Only the pre-concentration factor x500 yielded a positive signal with a relative TL/CL ratio of 0.4, indicating an approximate concentration of 10^6 CFU/mL after the filtration, and around 10^3 CFU/mL in the real sample (Figure 3.6d). In fact, this *E. coli* concentration was expectable considering these water samples were collected from the end of a collector pipe in an urban area[46,47]. In this regard, the boat took 1 hour to sail across the river area, collecting and filtering 1 L of water. Afterward, the filter was collected from the boat and immersed into 2 mL of clean water. Next, we loaded the resuspended solution onto the LFS. Altogether, the findings of real samples analysis (either spiked or non-unspiked ones) support the applicability of these *E. coli* specific LFS to determine fecal pollution in water samples.
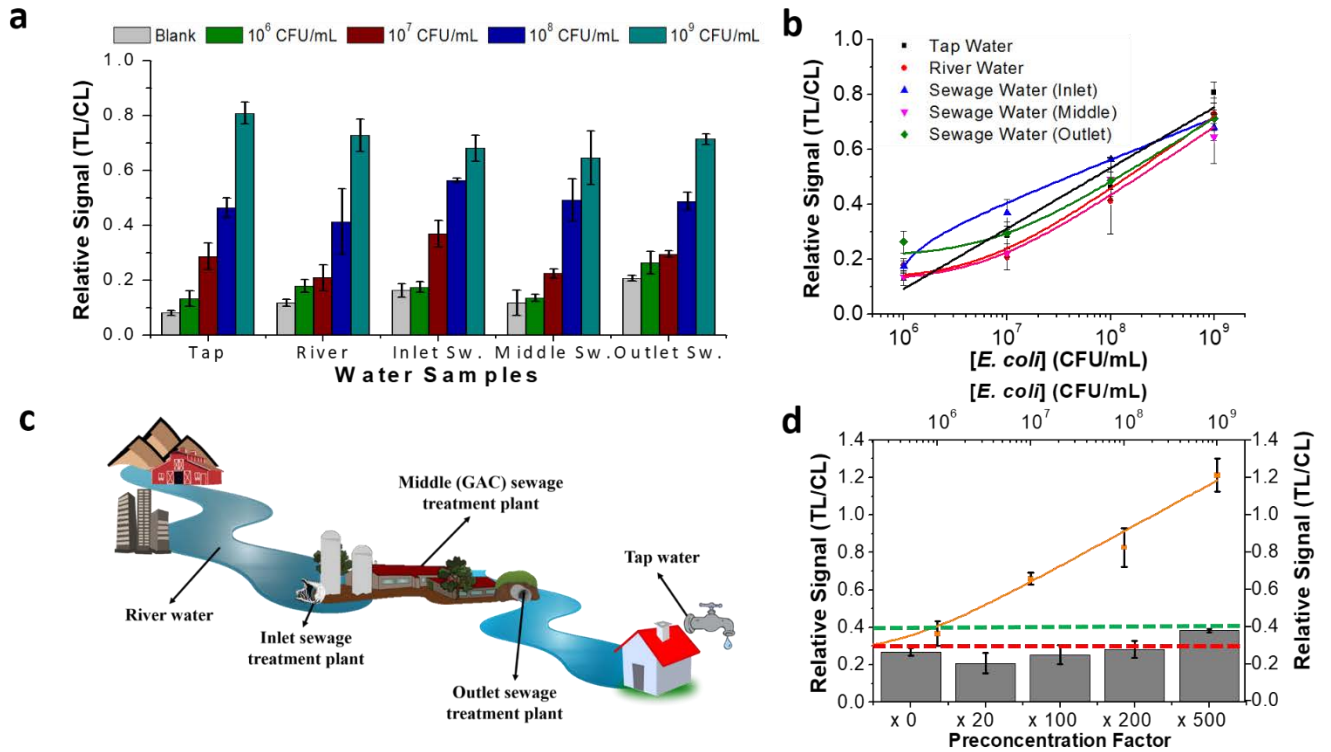
Figure 3.6. (a) Bar chart obtained for the detection of *E. coli* in spiked tap, river and sewage water samples. (b) Calibration curves obtained for the detection of *E. coli* in spiked tap, river and sewage water samples. (c) Schematic of the different water samples collected and analyzed in Figure 3.6a. (d). Pre-concentration factor required to detect *E. coli* in unspiked river samples (below X-axis) and the relative signal (TL/CL) obtained in all cases (left Y-axis). Besides, the calibration curve for *E. coli* detection in river water: *E. coli* concentration (top X-axis) vs. the relative signal (TL/CL) (right Y-axis). The red dashed line indicates the relative TL/CL threshold to consider a negative sample (upper limit of the SD bar of the blank at TL/CL = 0.35; [*E. coli*] below LOD), and the green-dashed line indicates the relative TL/CL signal obtained after pre-concentrating the water sample x500 times, giving an approximate *E. coli* concentration of 10^6 CFU/mL (TL/CL = 0.40; see the match between the bar corresponding to x500 and the orange dot corresponding to 10^6 CFU/mL).
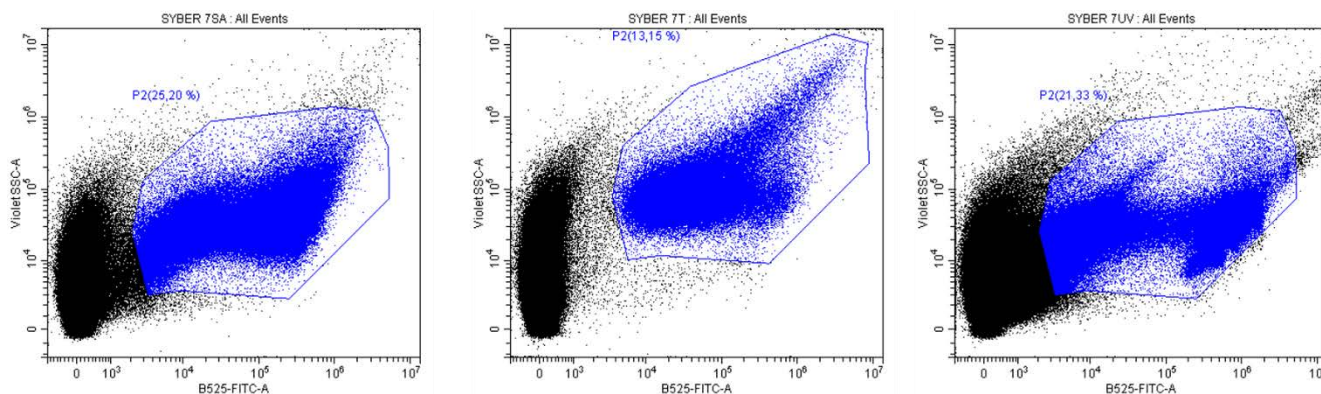
Figure 3.7. Flow cytometry results that confirm the accurate concentration estimated by our LFS in river water (10^7 CFU/mL). We tested three different river samples spiked with E. coli in our LFS, estimating a concentration of 10^7 CFU/mL for all of them. These results match very well with those obtained by flow cytometry.

3.5. Conclusions

We have tackled two fundamental problems for the development of lateral flow strips (LFS) aimed at detecting bacteria. First, we have discovered a novel characterization technique based on bioluminescent bacteria (*A. fischeri*) to evaluate the microfluidics of rod-shaped bacteria throughout LFS with the help of a smartphone in just 10 minutes. Second, we have developed a colorimetric lateral flow biosensor for the detection of any serotype of *Escherichia coli* species, as a fecal indicator, instead of a single strain that most of the LF-based systems do.

Additionally, by combining a filtration system before the lateral flow immunoassay (LFIA), the assay sensitivity improves by about two orders of magnitude compared with the sensitivity achieved with standard AuNPs-based LFS systems. Selectivity of the LFS shows no cross-reactivity with *Salmonella* Typhimurium and the reproducibility tests show RSD lower than 10% intra-assay and 15% inter-assay.

Eventually, the testing of spiked tap, river and sewage waters with our LFS provides good sensitivity and % recoveries. Furthermore, our results show that a pre-concentration factor of x500 of real river water was enough for the in-situ detection of *E. coli* species as a fecal pollution indicator.

3.6. References

1.   World Health Organization. Drinking-water. https://www.who.int/news-room/fact-sheets/detail/drinking-water. Published 2019.

2.   Garcia-Armisen T, Prats J, Servais P. Comparison of culturable fecal coliforms and Escherichia coli enumeration in freshwaters. *Can J Microbiol*. 2007;53(6):798-801. doi:10.1139/W07-033

3.   Environmental Protection Agency (EPA). Recreational Water Quality Criteria. 2011:1-63.

4.   Bernasconi C, Daverio E, Ghiani M. *Microbiology Dimension in EU Water Directives*.; 2003.

5.   Hendricks R, Pool EJ. The effectiveness of sewage treatment processes to remove faecal pathogens and antibiotic residues. *J Environ Sci Heal Part A*. 2012;47:289-297. doi:10.1080/10934529.2012.637432

6.   Hassan AHA, Bergua JF, Morales-Narváez E, Merkoçi A. Validity of a single antibody-based lateral flow immunoassay depending on graphene oxide for highly sensitive determination of E. coli O157:H7 in minced beef and river water. *Food Chem*. 2019;297(124965):1-10. doi:10.1016/j.foodchem.2019.124965

7.   Koczula KM, Gallotta A. Lateral flow assays. *Essays Biochem*. 2016;60:111-120. doi:10.1042/EBC20150012

8.   Quesada-González D, Merkoçi A. Nanoparticle-based lateral flow biosensors. *Biosens Bioelectron*. 2015;73:47-63. doi:10.1016/j.bios.2015.05.050

9.   Song C, Liu C, Wu S, et al. Development of a lateral flow colloidal gold immunoassay strip for the simultaneous detection of Shigella boydii and Escherichia coli O157: H7 in bread, milk and jelly samples. *Food Control*. 2016;59:345-351. doi:10.1016/j.foodcont.2015.06.012

10.   Bu T, Huang Q, Yan L, et al. Applicability of biological dye tracer in strip biosensor for ultrasensitive detection of pathogenic bacteria. *Food Chem*. 2019;274:816-821. doi:10.1016/j.foodchem.2018.09.066

11.   Quesada-González D, Sena-Torralba A, Wicaksono WP, de la Escosura-Muñiz A, Ivandini TA, Merkoçi A. Iridium oxide (IV) nanoparticle-based lateral flow immunoassay. *Biosens Bioelectron*. 2019;132:132-135. doi:10.1016/j.bios.2019.02.049

12.   Gupta A, Moyano DF, Parnsubsakul A, et al. Ultra-stable and Biofunctionalizable Gold Nanoparticles. *ACS Appl Mater Interfaces*. 2018;8(22):14096-14101. doi:10.1021/acsami.6b02548.

13.   Ciaurriz P, Fernández F, Tellechea E, Moran JF, Asensio AC. Comparison of four functionalization methods of gold nanoparticles for enhancing the enzyme-linked immunosorbent assay (ELISA). *Beilstein J Nanotechnol*. 2017;8:244-253. doi:10.3762/bjnano.8.27

14.   Jazayeri MH, Amani H, Pourfatollah AA, Pazoki-Toroudi H, Sedighimoghaddam B. Various methods of gold nanoparticles (GNPs) conjugation to antibodies. *Sens Bio-Sensing Res*. 2016;9:17-22. doi:10.1016/j.sbsr.2016.04.002

15. Gan H, Wu J, Ju H. Proximity hybridization-induced on particle DNA walker for ultrasensitive protein detection. *Anal Chim Acta*. 2019;1074:142-149. doi:10.1016/j.aca.2019.05.013

16. Quesada-González D, Jairo GA, Blake RC, Blake DA, Merkoçi A. Uranium (VI) detection in groundwater using a gold nanoparticle/paper-based lateral flow device. *Sci Rep*. 2018;8(16157):1-8. doi:10.1038/s41598-018-34610-5

17. Shayesteh OH, Ghavami R. Two colorimetric ampicillin sensing schemes based on the interaction of aptamers with gold nanoparticles. *Microchim Acta*. 2019;186(485):1-10. doi:10.1007/s00604-019-3524-4

18. Zhu L, Li S, Shao X, et al. Colorimetric detection and typing of E. coli lipopolysaccharides based on a dual aptamer-functionalized gold nanoparticle probe. *Microchim Acta*. 2019;186(111):1-6. doi:10.1007/s00604-018-3212-9

19. Morales-Narváez E, Naghdi T, Zor E, Merkoçi A. Photoluminescent Lateral-Flow Immunoassay Revealed by Graphene Oxide: Highly Sensitive Paper-Based Pathogen Detection. *Anal Chem*. 2015;87(16):8573-8577. doi:10.1021/acs.analchem.5b02383

20. Gong Y, Zheng Y, Jin B, et al. A portable and universal upconversion nanoparticle-based lateral flow assay platform for point-of-care testing. *Talanta*. 2019;201:126-133. doi:10.1016/j.talanta.2019.03.105

21. Wang R, Kim K, Choi N, et al. Highly sensitive detection of high-risk bacterial pathogens using SERS-based lateral flow assay strips. *Sensors Actuators, B Chem*. 2018;270:72-79. doi:10.1016/j.snb.2018.04.162

22. Romer Labs C. RapidChek. https://www.romerlabs.com/shop/inter_en/test-kits/lateral-flow-devices/.

23. Merk Millipore C. Singlepath. http://www.merckmillipore.com/ES/es/search/singlepath/.

24. Noack Group C. Reveal 2.0. https://www.noackgroup.com/product/reveal-2-0-for-e-coli-o157h7-lateral-flow-strip-test/.

25. BioControl C. VIP Gold. http://www.biocontrolsys.com/assets/uploads/14050855166-vip-gold-ehec-dfu-rev-01.pdf.

26. Hnasko R, Lin A V., McGarvey JA. Rapid Detection of Staphylococcal Enterotoxin-B by Lateral Flow Assay. *Monoclon Antib Immunodiagn Immunother*. 2019;38(5):209-212. doi:10.1089/mab.2019.0028

27. Wang J, Zhou J, Chen Y, et al. Rapid one-step enzyme immunoassay and lateral flow immunochromatographic assay for colistin in animal feed and food. *J Anim Sci Biotechnol*. 2019;10(82):1-10. doi:10.1186/s40104-019-0389-7

28. Khlebtsov BN, Bratashov DN, Byzova NA, Dzantiev BB, Khlebtsov NG. SERS-based lateral flow immunoassay of troponin I by using gap-enhanced Raman tags. *Nano Res*. 2019;12(2):413-420. doi:10.1007/s12274-018-2232-4

29. Bu T, Jia P, Liu J, et al. Diversely positive-charged gold nanoparticles based biosensor: A label-free and

sensitive tool for foodborne pathogen detection. *Food Chem X*. 2019;3(100052):1-8. doi:10.1016/j.fochx.2019.100052

30.   Moongkarndi P, Rodpai E, Kanarat S. Evaluation of an immunochromatographic assay for rapid detection of Salmonella enterica serovars Typhimurium and Enteritidis. *J Vet Diagnostic Investig*. 2011;23(4):797-801. doi:10.1177/1040638711408063

31.   Qi H, Zhong Z, Zhou H-X, et al. A rapid and highly sensitive protocol for the detection of Escherichia coli O157:H7 based on immunochromatography assay combined with the enrichment technique of immunomagnetic nanoparticles. *Int J Nanomedicine*. 2011;6:3033-3039. doi:10.2147/ijn.s25684

32.   Wang J, Katani R, Li L, et al. Rapid detection of Escherichia coli O157 and shiga toxins by lateral flow immunoassays. *Toxins (Basel)*. 2016;8(92):1-10. doi:10.3390/toxins8040092

33.   Singh J, Sharma S, Nara S. Evaluation of gold nanoparticle based lateral flow assays for diagnosis of enterobacteriaceae members in food and water. *Food Chem*. 2015;170:470-483.

34.   Pacific Immunology C. Polyclonal vs. Monoclonal Antibodies. https://www.pacificimmunology.com/resources/antibody-introduction/polyclonal-vs-monoclonal-antibodies/. Published 2019.

35.   R Foundation for Statistical Computing. R Core Team: A language and environment for statistical computing. 2017. https://www.r-project.org/.

36.   Chen W, Zhang J, Lu G, et al. Development of an immunochromatographic lateral flow device for rapid diagnosis of Vibrio cholerae O1 serotype Ogawa. *Clin Biochem*. 2014;47:448-454. doi:10.1016/j.clinbiochem.2013.12.022

37.   Yee C, Yong G, Lim A, et al. Dry-reagent gold nanoparticle-based lateral flow biosensor for the simultaneous detection of Vibrio cholerae serogroups O1 and O139. *J Microbiol Methods*. 2011;86(3):277-282. doi:10.1016/j.mimet.2011.04.020

38.   Liu C, Yeung C, Chen P, Yeh M, Hou S. Salmonella detection using 16S ribosomal DNA / RNA probe-gold nanoparticles and lateral flow immunoassay. *Food Chem*. 2013;141(3):2526-2532. doi:10.1016/j.foodchem.2013.05.089

39.   Bast NG, Comenge J, Puntes V. Kinetically Controlled Seeded Growth Synthesis of Citrate-Stabilized Gold Nanoparticles of up to 200 nm: Size Focusing versus Ostwald Ripening. *Langmuir*. 2011;27:11098-11105.

40.   Bald I. Effect of Adsorption Kinetics on Dissociation of DNA-Nucleobases on Gold Nanoparticles under Pulsed Laser Illumination Effect of adsorption kinetics on dissociation of. *Phys Chem Chem Phys*. 2017;19:10796-10803. doi:10.1039/C6CP08433H

41.   Preechakasedkit P, Pinwattana K, Dungchai W, et al. Development of a one-step immunochromatographic strip test using gold nanoparticles for the rapid detection of Salmonella typhi in human serum. *Biosens*

Bioelectron. 2012;31(1):562-566. doi:10.1016/j.bios.2011.10.031

42.   Wang W, Liu L, Song S, et al. Identification and quantification of eight Listeria monocytogene serotypes from Listeria spp. using a gold nanoparticle-based lateral flow assay. *Microchim Acta*. 2017;184:715-724. doi:10.1007/s00604-016-2028-8

43.   Gong Y, Hu J, Choi JR, et al. Improved LFIAs for highly sensitive detection of BNP at point-of-care. *Int J Nanomedicine*. 2017;12:4455-4466. doi:10.2147/IJN.S135735

44.   Armbruster DA, Pry T. Limit of Blank, Limit of Detection and Limit of Quantitation. *Clin Biochem*. 2008;29:S49-S52. http://www.ncbi.nlm.nih.gov/pubmed/18852857%0Ahttp://www.pubmedcentral.nih.gov/articlerender.fcgi?artid=PMC2556583.

45.   Park J, Shin JH, Park J. Pressed Paper-Based Dipstick for Detection of Foodborne Pathogens with Multistep Reactions. *Anal Biochem*. 2016;88:3781-3788. doi:10.1021/acs.analchem.5b04743

46.   Ofred JM, Robinson HM, Lughano JMK, Anita F, Anders D. Removal of Escherichia coli in treated wastewater used for food production in Morogoro, Tanzania. *African J Microbiol Res*. 2016;10(33):1344-1350. doi:10.5897/ajmr2016.8156

47.   Cirelli GL, Consoli S, Juanicó M. Modelling Escherichia coli concentration in a wastewater reservoir using an operational parameter MRT%FE and first order kinetics. *J Environ Manage*. 2009;90:604-614. doi:10.1016/j.jenvman.2007.12.015

CHAPTER 4. WATER TOXICITY ASSESSMENT

CHAPTER 4

Water Toxicity Assessment

This chapter summarizes the development and optimization of a bioluminescent biosensor based on *Aliivibrio fischeri* for water toxicity assessment. The chapter is divided into i) a short introduction to set out the topic and the current needs, as well as the presented proposal; ii) materials and methods; iii) the experimental results related to the bioluminescence enhancement, study of stability, and quorum sensing characterization; iv) the performance of the toxicity assays and the sensitivity enhancement using graphene-oxide; v) the conclusions of the chapter, and vi) the references.

4.1. Introduction

Aliivibrio fischeri (*A. fischeri*) is a bioluminescent bacterium found in marine waters around the world. Its bioluminescence relies on a biochemical reaction in which light is produced by the enzymatic oxidation of long-chain aldehydes, carried out by the luciferase enzyme[1–3]. Genetic expression of *A. fischeri* bioluminescent luciferase is triggered by the quorum-sensing system[4,5], which switches on/off genetic expression according to the cellular density[6–8]. Quorum sensing can be considered as a chemical-based inter-cellular communication system, where the bioluminescence production is an indicator of the health state of the bacterial population. On the other hand, many toxic compounds are known to interfere with different enzymatic processes in living organisms[9–12]. Since any enzymatic inhibition will decrease cellular fitness and bioluminescence is directly related to *A. fischeri* metabolic activity, any toxic compounds to the bacteria present in the media will unleash bioluminescence reduction. Therefore, the presence of toxic compounds in water samples can be analyzed according to the bioluminescence output of *A. fischeri*[13–18].

In this regard, both enzymatic and microbial luciferase-based toxicity sensors have been developed[19–22]. Nonetheless, there are important differences between enzymatic and microbial sensors: while enzymatic sensors generally provide higher sensitivity and shorter detection time[19,20], microbial sensors are often much cheaper, more resistant to pH and temperature changes, self-renewable and do not require extraction and purification steps[21–24]. An important constraint of enzymatic luciferase-based sensors is that they only rely on those compounds able to inhibit the luciferase activity[25]. However, *A. fischeri*-based sensors rely on any compounds able to interfere with any important metabolic pathway of the

bacteria, broadening the number of possible compounds to be detected. The first commercialized microbial-based toxicity-test-kit, called Microtox, was developed by Azur Environmental in 1979[26]. Since then, several products based on the bioluminescent *A. fischeri* system have been launched to the market[27–29]. However, sensitivity and stability are often two major problems of these technologies[30,31]. In addition, most microbial bioluminescent-based sensors require long-response times and provide limited bioluminescent outputs, often hindering real usefulness for in-situ analysis[18,22,32].

To overcome some of these limitations, researchers have been trying to enhance bioluminescence and bacterial growth in quorum sensing-based systems. In this regard, bacterial growth and the bioluminescent output can be enhanced by using molecular biology tools and relying on very sensitive devices to capture the emitted light[20,32–37]. For example, bacterial growth can be promoted by adding immiscible oxygenated oils[38], organic chemical compounds[39], graphene-oxide[40] (GO), and nanopaper[41] to the media. In fact, GO has been reported to be either a biocompatible[40,42,43] or an antimicrobial/cytotoxic nanomaterial[44–48]. On the one hand, some authors reported that GO behaves as a bacterial growth enhancer by promoting cell attachment and proliferation[40,49]. On the other hand, other authors reported GO toxicity, triggering the generation of reactive oxygen species (*ROS*) and the subsequent cellular death[45,50]. Nonetheless, in most of these cases, one or a few bacterial species are tested with an uncertain GO purity and a limited concentration range[40].

There is thereby a need to enhance the sensitivity, provide greater stability, and move to a more cost-effective approach for in-situ water toxicity analysis. Herein we study and characterize *A. fischeri*'s quorum-sensing system, and boost their bioluminescence and stability by growing the bacteria on solid media. Besides, we achieve more sensitive detection of toxic compounds by combining *A. fischeri* with graphene oxide in a liquid medium. Finally, we were able to demonstrate applicability for in the field analysis by using a smartphone camera to detect and analyze the bioluminescence outputs.

4.2. Materials and methods

4.2.1. Materials

Aliivibrio fischeri (ATCC® 700601™) was purchased from the ATCC Collection (Manassas, VA, USA). Ethanol (>99%), acetone (>99%), acetonitrile (>99%), tributyltin (TBT), pentachlorophenol, sodium chloride, tryptone, yeast extract, glycerol for molecular biology, agar, sucrose, and casein hydrolysate were purchased from Sigma-Aldrich. Cellulose nanofiber (nanopaper) was purchased from Nano Novin Polymer Co. Graphene-oxide (10 mg/mL) was purchased from Angstrom Materials.

4.2.2. Bacteria culture and storage

A stock culture of *Aliivibrio fischeri* frozen at -80 ºC was thawed at room temperature for 10 minutes. Then, 2.5 µL of this stock culture were put together with 25 mL of marine broth (MB medium), and the culture was allowed to grow at 25 ºC and 135 rpm (orbital shaking) for 24 h (SSM1 mini-orbital shaker from Stuart). If the culture had to be renewed, 2.5 µL of a 24 h bacterial culture was added again to 25 mL of MB medium and the process was repeated. To grow *A. fischeri* in nanopaper (NP), nanopaper scraps (4 mm diameter) were added to the bacterial culture (2.5 µL bacteria + 25 mL MB) under the same shaking conditions. In order to grow *A. fischeri* on solid media, 200 µL of marine agar medium (MA) were put in a 96-wells plate and let cool down to room temperature. After that, 30 µL of a 24 h bacterial culture was put on top of the solidified MA and grown at 25 ºC without shaking for 24 h.

A. fischeri was also grown in the presence of graphene oxide (GO). For this purpose, the stock solution of GO (10 mg/mL) was diluted as required in sterile MB medium in order to obtain different final GO concentrations (i.e. 100 µg/mL GO = 25 mL MB + 250 µL of stock GO). In the case of MA medium, GO was added at the desired concentration to the medium before thorough mixing, followed by autoclavation (121 ºC, 25 min). GO samples were characterized by UV-Vis spectra (200-800 nm), conductivity, and XPS (X-ray photoelectron spectroscopy).

For storage, *A. fischeri* could be frozen (-80 ºC) or lyophilized (-20 ºC). For freezing, 150 µL of a 24 h bacterial culture was put together with 50 µL of R18 medium in 500 µL Eppendorf tubes and immediately transferred to a -80 ºC freezer. For freeze-drying (lyophilizing), 1 mL of

bioluminescent bacteria was centrifuged at 5.000 rpm for 10 min. Then, the supernatant was removed, and the bacteria pellet was resuspended in 0.5 mL of R18 medium. 250 μL of the newly resuspended bacteria were transferred to glass vials, and after that, sealed with parafilm. Glass vials were straightforwardly frozen at -80 ºC for at least 2 hours. After complete freezing, glass vials were placed in a lyophilizing jar for 24 h at -53 ºC and < 2 mbar (CRYODOS 50 lyophilizer from Telstar). Finally, glass vials were vacuum-sealed in plastic bags (< 0.05 bar) and kept at -20 ºC in the freezer for further use.

4.2.3. Toxicity assays

For convenience, toxicity assays were performed in 96-wells plates as follows: 50 μL of bioluminescent *A. fischeri* (18-24 h cultivation) was put together with 200 μL of water sample in the wells. After 5 min of incubation time, bioluminescence was captured using either the spectrophotometer (5000 ms of integration time; SpectraMax iD3 from Molecular Devices) or the smartphone (ISO 400, 10 s of shutter speed; Samsung Galaxy S7 Edge). Data were subsequently analyzed either directly from the spectrophotometer or using the software ImageJ from the pictures captured with the smartphone. Data were plotted using the OriginPro 8 software, being the concentration of pesticide as the X-axis (log scale) and the relative bioluminescence intensity as the Y-axis (= absolute light produced with any water sample divided by the absolute light produced with a blank [clean] sample). All concentrations were analyzed at least by triplicate every time. Finally, EC50 value (concentration range) was estimated by the software adjusting a sigmoidal function to all the bioluminescence outputs produced for each different pesticide concentration tested in the toxicity assay.

4.3. Bioluminescence enhancement, stability, and quorum sensing characterization

4.3.1. Bioluminescence enhancement using agar media

We grew *A. fischeri* into liquid (marine broth), semi-solid (marine broth + nanopaper), and solid media (marine agar), after what we measured and characterized the bioluminescent output (Figure 4.1a). As reported in a previous article of our group[41], bioluminescence is slightly enhanced when *A. fischeri* is grown into nanopaper instead of in liquid media. Surprisingly, in our study, the bioluminescence is greatly enhanced when *A. fischeri* grows in agar medium, up to 20 times (x 2000%), compared to both, broth and nanopaper media.

Moreover, the stability of the bioluminescence increases from 8 h in the liquid medium to 12 h in the agar medium (RDS < 10%). This bioluminescence enhancement can be attributed to the denser bacterial populations formed when *A. fischeri* grows onto colonies (agar media) than in liquid media (broth media). Considering the previous results, we also evaluated the effect of different agar % in the media, from 1.5% (the gold standard in microbiology) to 0.25% (semi-solid media). Among all the media containing different % agar, the medium containing 1.5% agar yields the highest bioluminescence (Figure 4.1b). As a comparison, media containing 1% and 0.25% agar only yield 40% and 3% of the bioluminescence obtained with 1.5% agar, respectively. Since agar is not a nutrient itself for *A. fischeri*, we strongly believe that a higher agar % enables the bacteria to proliferate and form denser populations after the attachment to the solid media, boosting bioluminescence production because of the quorum sensing system.
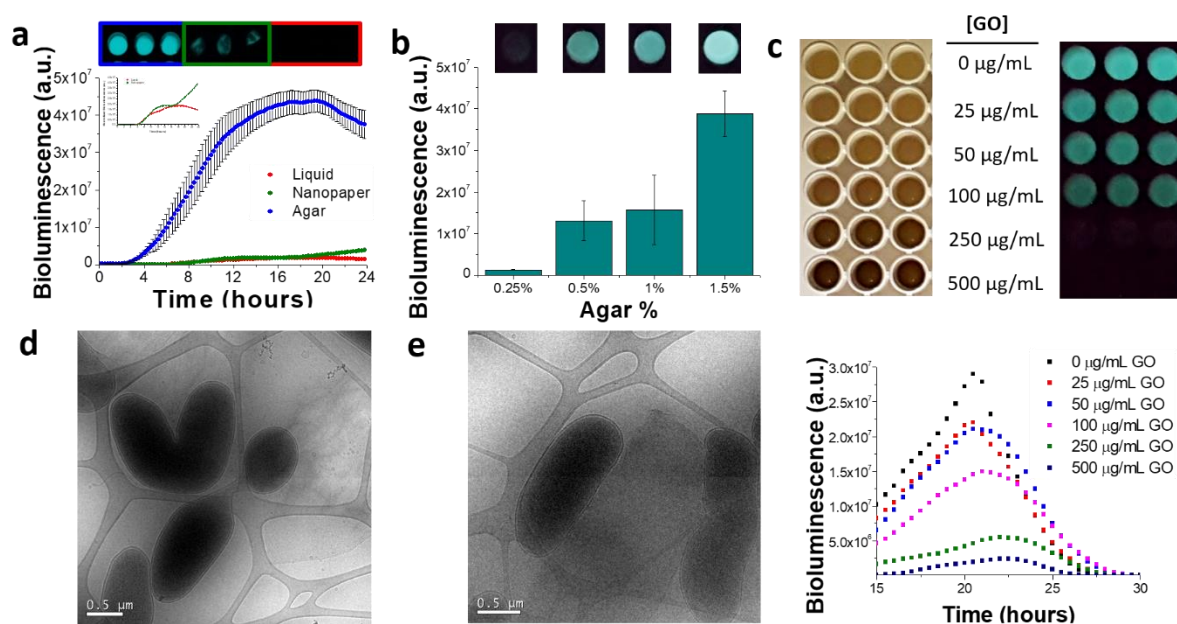
Figure 4.1. (a) Bacterial bioluminescence in liquid, nanopaper, and agar media. (b) Bacterial bioluminescence in marine media containing from 0.25% to 1.5% agar. (c) Bacterial bioluminescence in liquid media containing different concentrations of GO: above, the pictures with the "lights on" (left), and "lights off" (right); below, the graphic representing the recorded bioluminescence within time. (d) *A. fischeri* cells undergoing cellular division onto a GO flake. (e) *A. fischeri* showing standard morphology and good cell wall integrity upon direct contact with GO flakes.

4.3.2. Bioluminescence enhancement using graphene-oxide

We hypothesized that graphene-oxide (GO) could behave as a non-specific bacterial growth enhancer, thereby boosting bioluminescence via the quorum sensing system, based on previously reported scientific evidences[40]. Therefore, we grew *A. fischeri* in marine broth using different GO concentrations, ranging from 25 µg/mL to 500 µg/mL to determine the effect of GO on the bacterial growth and the bioluminescence. However, our results show a decrease in the bioluminescence intensity as the concentration of GO increases, suggesting that GO could be toxic to *A. fischeri* at these conditions (Figure 4.1c: above the picture, below the graphic). Furthermore, we studied the growth of *A.* fischeri in the presence of GO in liquid media (Figures 4.1d and 4.1e), as bioluminescence is an indirect response triggered by cellular growth. In this regard, cryo-TEM images show bacteria undergoing cellular division in direct contact with GO flakes. Besides, bacterial morphology and cell wall integrity are intact, questioning GO toxicity to *A. fischeri*.

In order to clarify whether GO promotes bacterial growth and bioluminescence, we also grew *A. fischeri* onto agar media containing different GO concentrations and tracked the emitted bioluminescence. First, we inoculated a constant volume of an *A. fischeri* broth culture onto marine agar plates with 25 µg/mL and 100 µg/mL of GO. Next, we counted the number of colonies after 24 h of incubation at room temperature. Bacteria grown onto marine agar without GO yielded 42 ± 2 CFU/plate, while bacteria grown onto marine agar with 25 µg/mL and 100 µg/mL GO yielded 226 ± 25 and 220 ± 39 CFU/plate, respectively.

We also evaluated the bioluminescence intensity of these colonies, which increased 35% in the agar plates with 100 µg/mL GO in comparison with those cultures grown on agar plates with 25 µg/mL GO and without GO (Figure 4.2a). On the one hand, the evident decrease in the bioluminescent output produced in the liquid media cultures can be attributed to the brownish color of the GO, which absorbs the light produced by the bacteria (Figure 4.2b). On the other hand, any optical interferences due to the media are eliminated in the agar media, since the light is directly captured from above, driving out any interferences from the media components. These results suggest overall that GO promotes *A. fischeri* growth, and consequently the bioluminescence through the quorum-sensing system.
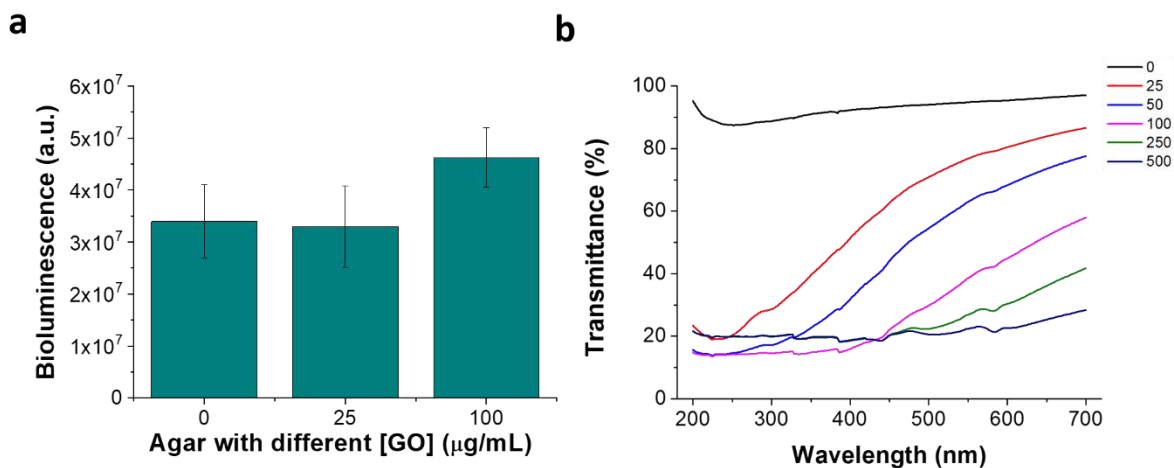
Figure 4.2. (a) Bacterial bioluminescence using different GO concentrations in marine agar media. (b) Transmittance of GO solutions from 200 nm to 700 nm at different concentrations (µg/mL) using quartz cuvettes.

4.3.3. Stability enhancement by lyophilization

Standard storage procedure consists of fast freezing *A. fischeri* cells giving the highest possible bioluminescence (in the late logarithmic phase, after 18-24 h of incubation) at -80 ºC using R18 medium, composed of several cryoprotectants. However, such high-demanding storage usually hinders the transport of bacteria, narrowing down the number of possible applications. Therefore, we studied the freeze-drying process, well known as lyophilization, to ease this demanding storage for *A. fischeri*. First, we optimized the R18 medium in terms of cryopreservatives composition and way of preparation. R18 medium contains a great amount of casein hydrolysate, which is adsorbed over the bacterial cell walls creating a viscous surface that prevents the formation of big ice crystals that could puncture the bacteria and destroy the cell integrity. Since casein is a temperature-sensitive protein, autoclaving is not an appropriate method to sterilize the R18 medium. In this way, filtration using 0.25 µm pore size filters allows for preparing a better quality lyophilization media.

We also studied the effect of GO during the lyophilization process. Briefly, we lyophilized *A. fischeri* using R18 medium without and with 2.5 and 10 µg/mL GO. Next, we stored the bacteria for one week, after what we grew them for 20 hours and then measured the bioluminescence intensity (Figure 4.3a). Bacterial cultures lyophilized using 10 µg/mL GO provided x2 times more bioluminescence than those cultures lyophilized with 2.5 µg/mL GO and without GO. However,

137

control cultures to which we also added 2.5 and 10 µg/mL GO after the lyophilization for bacterial growth provided a similar response. Then, we concluded that GO has not a strong influence on bacterial survival rate during the lyophilization process but only acts as a growth enhancer after rehydration.

Besides, we evaluated the influence of the storage temperature. In this regard, we compared the bioluminescence of bacterial cultures previously frozen at -80 ºC and those lyophilized cultures stored for one month at -20 ºC, +4ºC and +25ºC. As a result, *A. fischeri* cultures stored at -20 ºC with R18 medium and 10 µg/mL GO provided as much bioluminescence as those stored at -80 ºC by just freezing (Figure 4.3b). Nevertheless, bacterial cultures stored at +4 ºC and +25 ºC were not viable in any of the aforementioned cases, despite we successfully achieved milder storage with an absolute difference of 60 ºC by simply freeze-drying *A. fischeri* cultures in filtered modified R18 medium containing 10 μg/mL of GO.
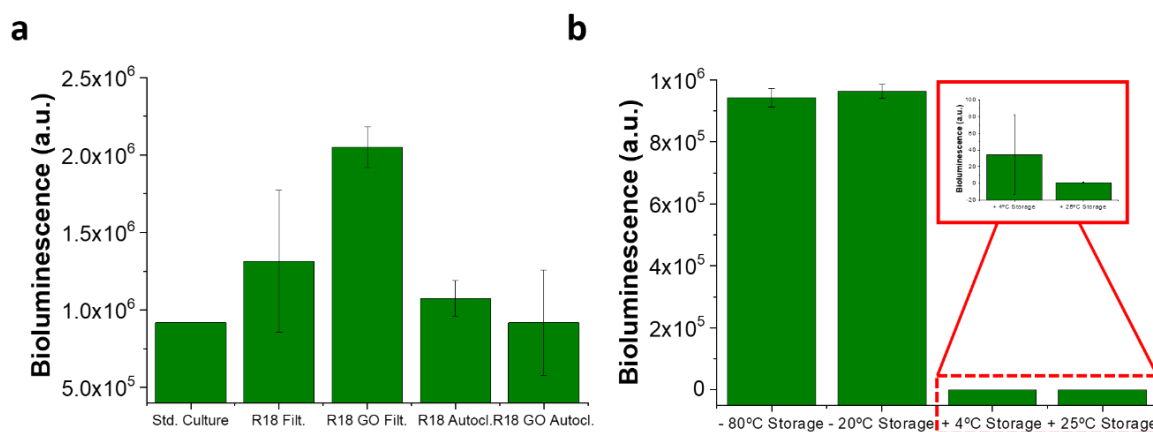
Figure 4.3. (a) Bacterial bioluminescence after lyophilization, rehydration and growth for 20 hours by using R18 medium prepared by either autoclavation or filtration, and either containing (10 µg/mL) or not GO. (b) Bacterial bioluminescence after storage, rehydration, and growth for 20 hours by using fast freezing (-80 ºC) or lyophilization (-20 ºC, +4 ºC, and +25 ºC).

4.3.4. Characterization of the quorum-sensing system

We evaluated the bioluminescence trend in time in a batch culture of *A. fischeri* incubated at 25 ºC (room temperature) and 135 rpm (orbital shaking) (Figure 4.4a). Maximum bioluminescence is achieved in the timeframe between 18 h and 24 h of cultivation; after this

period, waste products produced by bacteria overpopulation are accumulated in the media, leading to bacterial death and loss in light emission. We also measured the bioluminescence emission spectrum of *A. fischeri*, obtaining the maximum emission peak at 490 nm (Figure 4.4b).

Next, we characterized the quorum sensing system as the correspondence between bacterial growth and bioluminescence emission (Figure 4.5a, 4.5b, and 4.5c). Our results show that there is a latent phase for bioluminescence when *A. fischeri* starts to grow up to 10^5 CFU/mL. From this point, bioluminescence is greatly enhanced when the bacterial population grows from 10^5 CFU/mL to 10^9 CFU/mL. Interestingly, bioluminescence to cellular density ratio decreases when bacterial concentration is above 10^8 CFU/mL, indicating that the quorum-sensing system is slightly lessened at very high bacterial concentrations (Figures 4.5c and 4.5d).
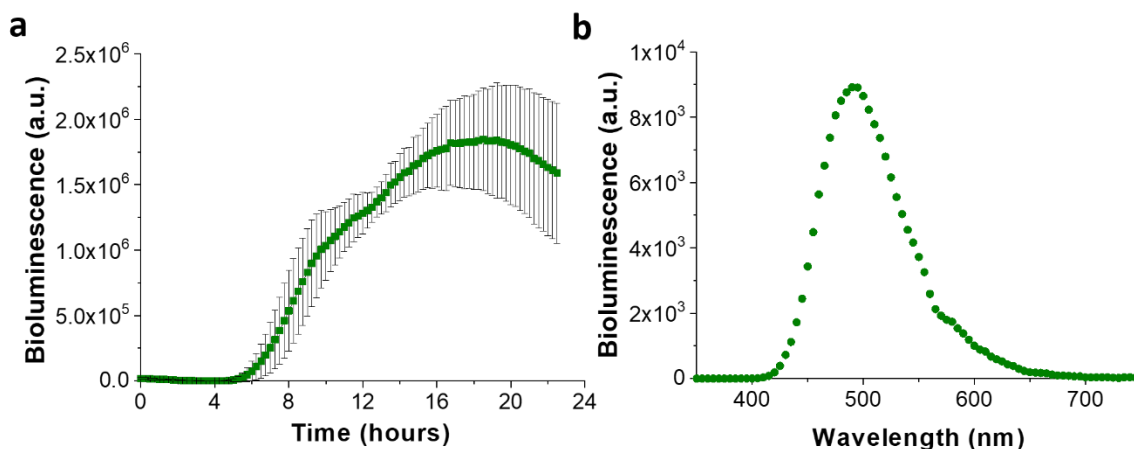
Figure 4.4. (a) Bioluminescence intensity of *A. fischeri* in liquid media within growth time. (b) Bioluminescence spectra of *A. fischeri*.

In this regard, bacterial overgrowth induces the synthesis of certain proteins that switch on the expression of metabolic pathways to manage more effectively the remaining nutrients in the media. The biochemical reaction producing the bacterial bioluminescence is summarized in Figure 4.5e. Simultaneously, non-vital cellular processes, such as bioluminescence may be switched down. Finally, we optimized the volume and relative ratio of bacteria to the water sample to be used for the toxicity assays within 96 wells-plates with a total volume of 400 μL. Therefore, we selected a ratio of 1 to 4 of *A. fischeri* to water sample by using 50 μL of bacteria and 200 μL of the water sample.

Eventually, we tracked and optimized several parameters such as oxygen concentration, agitation, and temperature in order to achieve good reproducibility upon bacterial growth. For this reason, we set a closed system (100 mL erlenmeyer) in which the air phase is 4.5 times larger than the liquid phase. As oxygen % in standard conditions is 21%, the system contains the same volume of liquid media and oxygen at the beginning of the bacterial culture. In addition, since *A. fischeri* is an aerobic bacterium, agitation is highly required to ensure optimal contact between the air and the liquid phases of the system. In this regard, different agitation conditions lead to different dissolved oxygen content in the media, thus to strong batch inter-variability. Eventually, we set 135 rpm to perform the bacterial culture. For convenience, we also controlled and set the temperature at 26 ºC, as *A. fischeri* growth's most optimal temperature is 26-28 ºC[51].
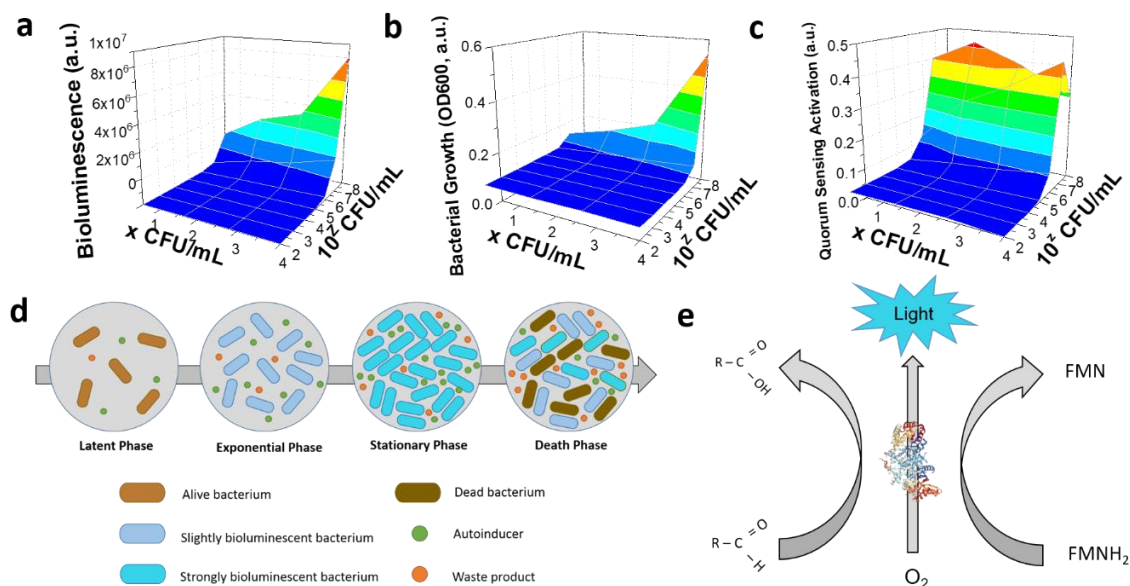
Figure 4.5. (a) Bacterial bioluminescence at different cellular densities. (b) Bacterial growth (OD600) at different cellular densities. (c) Quorum sensing (QS) system activation at different cellular densities. (d) Bacterial growth, bioluminescence, and QS system activation at the different growing stages of *A. fischeri*: (*1*) in an initial latent phase few bacteria start to colonize and get used to the new media; (*2*) bacteria keep growing and the quorum sensing system is activated, therefore triggering slight bioluminescence; (*3*) bacteria population has reached its maximum concentration in the closed system, yielding as well the greatest bioluminescence; (*4*) accumulation of waste products leads to a decrease in cellular fitness and lastly to cellular death. (e) Enzymatic mechanism of bacterial luciferase in which FMNH$_2$ (reduced flavin mononucleotide) and a fatty aldehyde are oxidized to FMN (oxidized flavin mononucleotide) and an acid with the subsequent production of light (Image obtained from Protein Data Bank, reference: 3FGC).

4.4. Toxicity assays and sensitivity enhancement using graphene-oxide

4.4.1. Optimization of the toxicity assay conditions

We selected tributyltin (TBT) and pentachlorophenol as two model pesticides to evaluate the toxicity assays using *A. fischeri*. First, we determined experimentally the detection range of both pesticides with the help of previous scientific works. Next, due to the chemical structure of these compounds, they are slightly soluble in water and require a certain amount of an organic solvent for complete dissolution. In this regard, we tested three very common organic solvents as diluents to dissolve TBT and pentachlorophenol: ethanol, acetone, and acetonitrile. We then concluded that ethanol and acetone are the most suitable organic solvents to prepare TBT and pentachlorophenol solutions, respectively. Nevertheless, organic solvents may be toxic to *A. fischeri*.
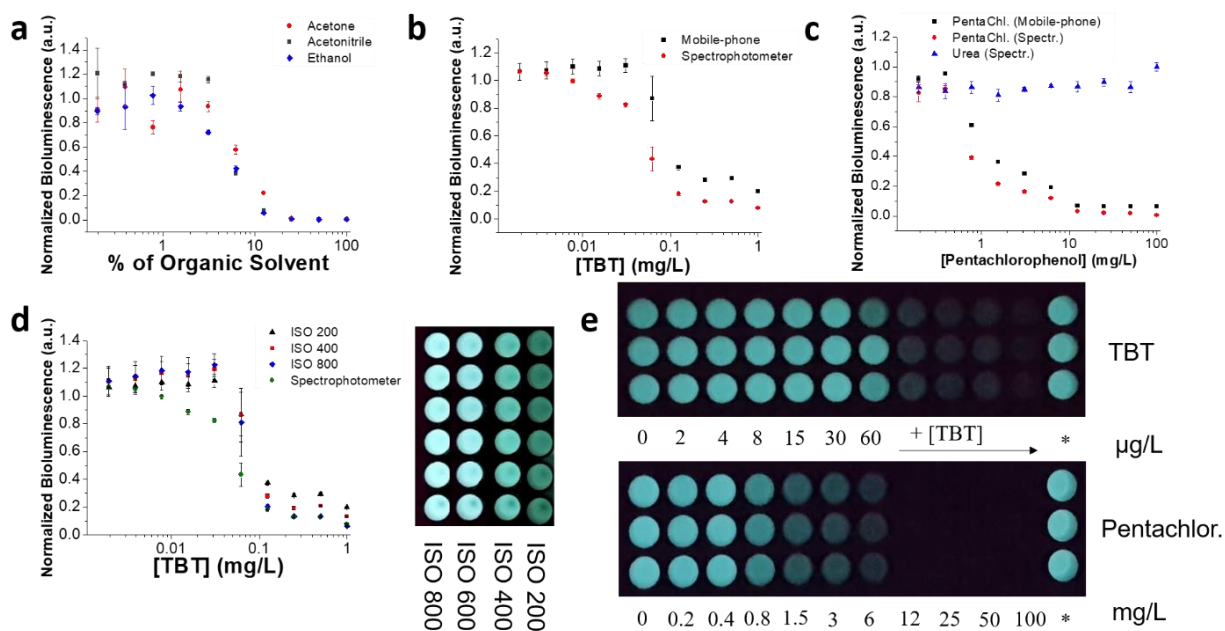
Figure 4.6. (a) Toxicity profiles of three organic solvents (ethanol, acetone, and acetonitrile) to *A. fischeri* at different % ranging from 0.2% to 100%. (b) Toxicity assay performed with TBT in the range from 1 mg/L to 2 µg/L using both the spectrophotometer and the smartphone. (c) Toxicity assay performed with pentachlorophenol and urea in the range from 100 mg/L to 0.2 mg/L using both the spectrophotometer and the smartphone. (d) On the left, toxicity assays performed by using different ISO parameters. On the right, bioluminescence capture by the smartphone by using different ISO parameters. (e) Bioluminescence inhibition profile captured with the smartphone after testing TBT and pentachlorophenol.

Therefore, there must be a commitment between pesticide solubility and organic solvent toxicity while performing the toxicity assays. Figure 4.6a displays the toxicity profiles of ethanol, acetone, and acetonitrile with concentrations ranging from 0.2% to 100% (v/v). In this regard, EC50 is the most important parameter regarding toxicity assays, which refers to the toxicity of a certain substance that induces a response halfway between the baseline and the maximum after a determined exposure time, 5 min in this case. EC50 values for these three organic solvents were 4.5 ± 1.1 % for ethanol, 4.8 ± 1.3 % for acetone, and 6.8 ± 1.4 % for acetonitrile. Importantly, all of them cause negligible toxicity at concentrations equal or below to 2%, whereby we prepared different TBT and pentachlorophenol concentrations by always keeping a constant 2% of ethanol and acetone in the solutions, respectively.

4.4.2. Smartphone-based toxicity assays

We performed the toxicity assay for TBT using a concentration range from 0.002 $\mathrm{mg/L}$ to 1 mg/L in 2% NaCl water, keeping a constant 2% ethanol[41]. Whereas we performed the toxicity assay for pentachlorophenol using a concentration range from 0.2 mg/L to 100 mg/L in 2% NaCl water, keeping a constant 2% acetone[52]. All the analyses were performed using both a spectrophotometer and a smartphone for TBT (Figure 4.6b and 4.6e) and pentachlorophenol (Figure 4.6c and 4.6e). In addition, we carried out a control test with urea, a non-toxic substance for humans, using the same concentrations as for pentachlorophenol. Indeed, urea does not trigger bioluminescence inhibition at any of the tested concentrations (Figure 4.6c). In order to assess the reproducibility of the toxicity assays, we performed six independent measurements by triplicate on different days. The data show that EC50 value for TBT is between 17 and 70 μg/L (Figure 4.7), while EC50 value for pentachlorophenol is between 0.16 and 21.06 mg/L (Figure 4.8). Therefore, *A. fischeri* enables to detect TBT in the range of ppb (μg/L)[41], and pentachlorophenol in the range of ppm (mg/L)[52].
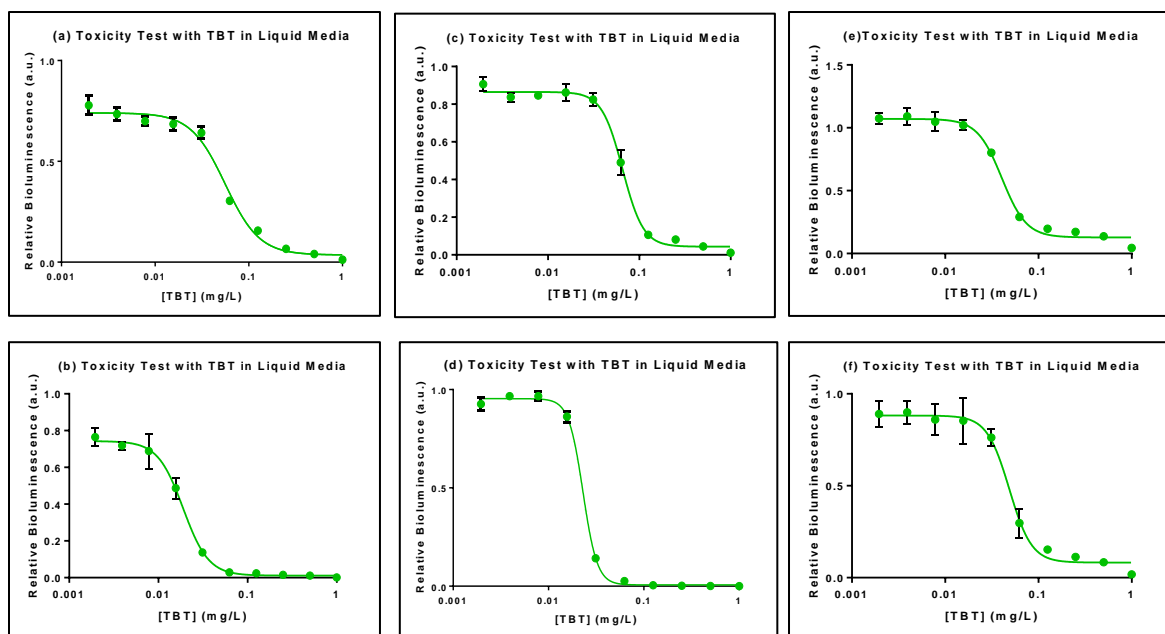
Figure 4.7. Bioluminescence inhibition trend of A. fischeri after 5 minutes of exposure to different concentrations of tributyltin (TBT). EC50 values: a) 0.050-0,062 mg/L; b) 0.017-0.021 mg/L; c) 0.062-0.070 mg/L; d) 0.022-0.024 mg/L; e) 0.037-0.044 mg/L; f) 0.043-0.054 *mg/L.*
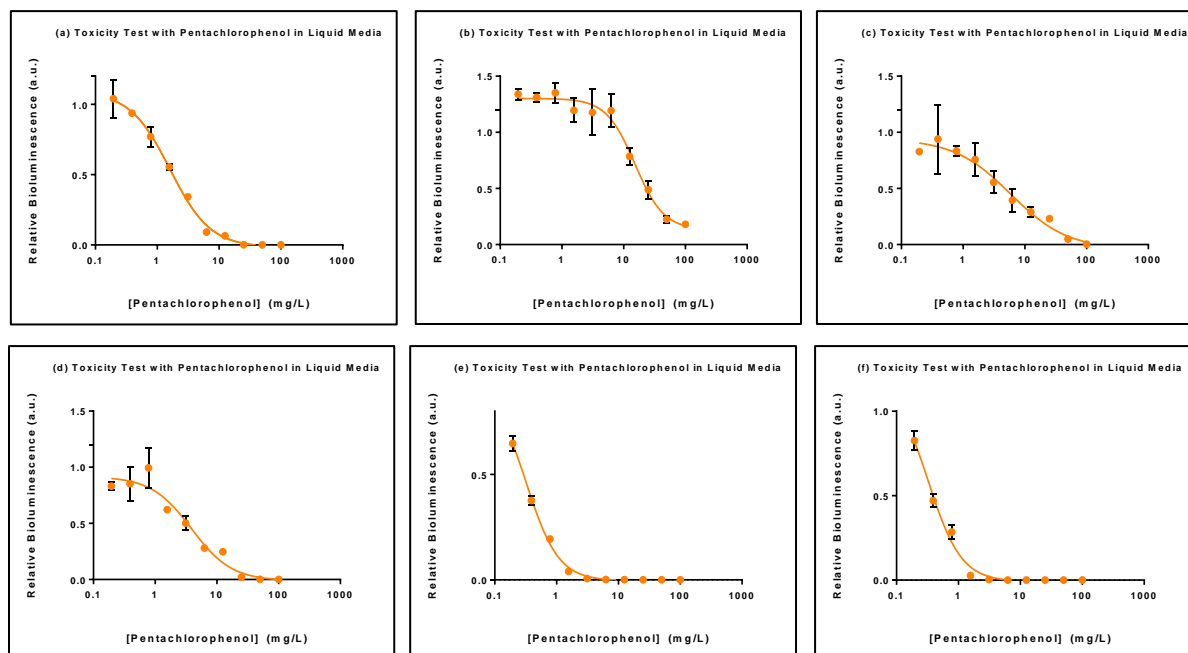
Figure 4.8. Bioluminescence inhibition trend of *A. fischeri* after 5 minutes of exposure to different concentrations of pentachlorophenol. EC50 values: a) 1.29-1,93 mg/L; b) 12.03-21.16 mg/L; c) 3.02-7.92 mg/L; d) 2.62-6.01 mg/L; e) 0.23-0.39 mg/L; f) 0.16-0.44 mg/L.

The detection system used to perform the measurements can strongly influence the sensitivity of the detection and quantification of both pesticides. In this regard, we analyzed and compared the sensitivity achieved by a spectrophotometer with a luminometer function and a smartphone using TBT as the model analyte. First, we performed the measurements with the spectrophotometer by setting 5 seconds of integration time and 1 mm of reading height. Second, we evaluated different smartphone ISO values to understand how this parameter could influence the sensitivity of the toxicity assays (Figure 4.6d). Then, we analyzed the pictures in raw image format (without processing) using the smartphone application Image J by setting the shutter speed as 10 seconds and the aperture like f/1.7. with manual focus.

The bioluminescence inhibition profiles show a lower EC50 value obtained with the spectrophotometer (0.047 mg/L) than those EC50 values obtained with the smartphone, no matter using which ISO values (0.112 mg/L for ISO 800, 0.106 mg/L for ISO 400 and 0.101 mg/L for ISO 200). We expected these results because spectrophotometers are highly sensitive devices, specifically designed to detect slight changes in an optical signal. Interestingly, there were not strong differences among the different ISO values studied, being ISO 200 the setting that provided the lowest EC50 value after the spectrophotometer. Again, we expected this result because lower ISO values allow for a lower amount of light captured by the smartphone. Nevertheless, we selected ISO 400 to perform the smartphone analysis for two main reasons. First, ISO 800 provides the brightest outputs but makes often difficult to discern between different low concentrations of pesticides due to the high amount of grain ("noise"); and second, ISO 200 provides the lowest EC50 value but the darkest pictures at the same time, with poor contrast, thus leading to a greater variability among different batches of the bioluminescent bacteria.

4.4.3. Sensitivity enhancement of the toxicity assays using graphene oxide (GO)

We studied the influence of GO on the toxicity assays sensitivity by adding different GO concentrations before the bacterial growth, and then we performed the toxicity assays with TBT and pentachlorophenol as stated in section 4.4.2. Figures 4.9a and 4.9d show the results obtained from three independent toxicity assays carried out with TBT and *A. fischeri* grown under different

GO concentrations. Besides, Table 4.1 summarizes the EC50 values obtained in this experiment, being the bacterial culture grown with 100 µg/mL GO the most sensitive one, followed by 25 µg/mL GO, and eventually by that bacterial culture without GO. This slight increase in the sensitivity could reflect a synergic toxic effect between the pesticides (TBT in the shown case) and GO, but it clashes with the fact that GO promotes *A. fischeri* growth. Furthermore, as aforementioned, GO shields bacterial bioluminescence in liquid media due to its blackness (Figure 4.2b).

[GO] (µg/mL)	EC50 before equalizing initial biolum. (mg/L)	EC50 after equalizing initial biolum. (mg/L)
0	0.18-0.62	0.06-0.12
25	0.08-0.18	0.08-0.18
100	0.05-0.12	0.04-0.10

Table 4.1. EC50 values for the toxicity assays carried out with TBT using different GO concentrations: 0, 25 and 100 µg/mL, before (left) and after (right) balancing the initial bioluminescence of the three bacterial cultures.

In the following experiment, we carried out the toxicity assays under similar conditions but diluting the most bioluminescent bacterial cultures with 2% NaCl to balance the initial bioluminescence (RSD < 10%) of those cultures grown with and without GO (Figure 4.9b). The results show this time that all three EC50 values are much more similar (Table 4.1). Therefore, GO has not a direct influence, neither positive nor negative, on the toxicity caused by either TBT or pentachlorophenol. Besides, since GO promotes the growth of *A. fischeri* at these concentrations, the greater sensitivity (lower EC50) obtained in those bacterial cultures grown with a higher concentration of GO can be indirectly attributed to the darker outputs produced by the bacterial cultures grown under these conditions (Figure 4.9c).
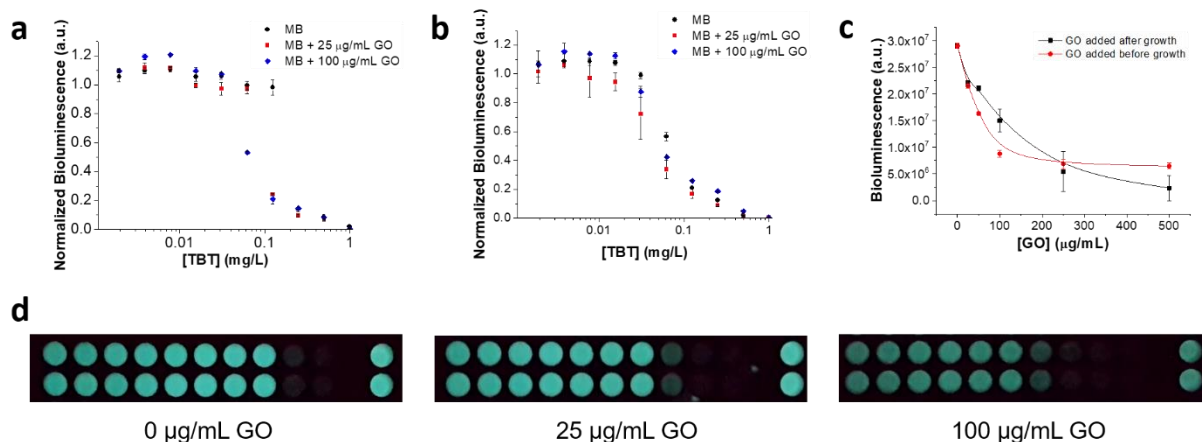
Figure 4.9. (a) Toxicity assays carried out with TBT and *A. fischeri* grown under three different GO concentrations: 0 (black dots), 25 (red squares) and 100 µg/mL GO (blue diamonds). (b) Toxicity assays carried out with balanced initial bioluminescence ("equalized") carried out with TBT and *A. fischeri* grown under three different GO concentrations: 0 (black dots), 25 (red squares) and 100 µg/mL GO (blue diamonds). (c) Bioluminescence produced by *A. fischeri* in liquid media with different GO concentrations added before (red dots) and after (black dots) the bacterial growth. (d) Pictures captured with the smartphone corresponding to the figure 4.9a.

4.5. Conclusions

We developed two strategies to enhance the growth and bioluminescence of *Aliivibrio fischeri*: a solid media platform based on marine agar that increases 20-fold the bioluminescence produced by *A. fischeri* and a GO-based platform that boosts both the bacterial growth and bioluminescence.

Besides, we developed a new platform based on *A. fischeri* for water toxicity monitoring, using a smartphone, a dark-box, and a 96-wells plate for the whole analysis. In this regard, we chose tributyltin (TBT) and pentachlorophenol as the model analytes to perform the toxicity assays. We also studied the reproducibility of the toxicity assays, as well as correspondence between the smartphone and spectrophotometer's outputs.

Eventually, we tested the influence of different GO concentrations on the sensitivity of the toxicity assays, yielding lower EC50 values with higher GO concentrations. Then, we proved this sensitivity enhancement is due to the blackness of the GO itself since GO promotes bacterial growth.

4.6. References

1.	Nunes-Halldorson VDS, Duran NL. Bioluminescent bacteria: *Lux* genes as environmental biosensors. *Brazilian J Microbiol*. 2003;34(2):91-96.

2.	Boettcher KJ, Ruby EG. Depressed Light Emission by symbiotic by *Vibrio fischeri* of the Sepiolid Squid *Euprymma scolopes*. *J Bacteriol*. 1990;172(7):3701–3706.

3.	Brooks JF, Gyllborg MC, Cronin DC, et al. Global discovery of colonization determinants in the squid symbiont *Vibrio fischeri*. *Proc Natl Acad Sci*. 2014;111(48):17284-17289.

4.	Visick KL, Foster J, Doino J, McFall-Ngai M, Ruby EG. *Vibrio fischeri lux* genes play an important role in colonization and development of the host light organ. *J Bacteriol*. 2000;182(16):4578-4586.

5.	Science B, Microbiology U, Lupp OAC, et al. The *Vibrio fischeri* quorum-sensing systems ain and lux sequentially induce luminescence gene expression and are important for persistence in the squid host. *Mol Microbiol*. 2003;50:319-331.

6.	Miyashiro T, Ruby EG. Shedding light on bioluminescence regulation in *Vibrio fischeri*. *Mol Microbiol*. 2013;84(5):795-806.

7.	Lupp C, Ruby EG. *Vibrio fischeri* Uses Two Quorum-Sensing Systems for the Regulation of Early and Late Colonization Factors. *J Bacteriol*. 2005;187(11):3620-3629.

8.	Ray VA, Visick KL. LuxU Connects Quorum Sensing to Biofilm Formation in *Vibrio fischeri*. *Mol Microbiol*. 2012;86(4):954-970.

9.	Khaled A, Pelkonen O. The inhibition of major human hepatic cytochrome P450 enzymes by 18 pesticides: Comparison of the N-in-one and single substrate approaches. *Toxicol Vitr*. 2012;27:1584-1588.

10.	Hodgson E, Wallace AD. Human Metabolic Interactions of Pesticides: Inhibition, Induction, and Activation. *ACS Symp Ser*. 2012;1099:115-132.

11.	Mesnage R, Seralini G-E. *Toxicity of Pesticides on Health and Environment*. Vol 6.; 2018.

12.	Singh S, Kumar V, Chauhan A, et al. Toxicity, degradation and analysis of the herbicide atrazine. *Environ Chem Lett*. 2018;16(1):211-237.

13.	Jarque S, Masner P, Klánová J, Prokeš R, Bláha L. Bioluminescent *Vibrio fischeri* Assays in the Assessment of Seasonal and Spatial Patterns in Toxicity of Contaminated River Sediments. *Front Microbiol*. 2016;7(NOV):1-11.

14.	Tingting X, Close D, Smartt A, Ripp S, Sayler G. Detection of Organic Compounds with Whole-Cell Bioluminescent Bioassays. *Adv Biochem Eng Biotechnol*. 2014:111-151.

15.	Mortimer M, Kasemets K, Heinlaan M, Kurvet I, Kahru A. High throughput kinetic *Vibrio fischeri*

bioluminescence inhibition assay for study of toxic effects of nanoparticles. *Toxicol Vitr*. 2008;22(5):1412-1417.

16.   Lopes I, Ribeiro R, Antunes FE, et al. Toxicity and genotoxicity of organic and inorganic nanoparticles to the bacteria *Vibrio fischeri* and Salmonella typhimurium. *Ecotoxicology*. 2012;21(3):637-648.

17.   Hernando MD, De Vettori S, Martínez Bueno MJ, Fernández-Alba AR. Toxicity evaluation with *Vibrio fischeri* test of organic chemicals used in aquaculture. *Chemosphere*. 2007;68:724-730.

18.   Menz J, Schneider M, Kümmerer K. Toxicity testing with luminescent bacteria - Characterization of an automated method for the combined assessment of acute and chronic effects. *Chemosphere*. 2013;93(6):990-996.

19.   Četkauskaite A, Pessala P, Södergren A. Elemental Sulfur: Toxicity In Vivo and In Vitro to Bacterial Luciferase, In Vitro Yeast Alcohol Dehydrogenase, and Bovine Liver Catalase. *Environ Toxicol*. 2004;19(4):372-386.

20.   Cevenini L, Calabretta MM, Lopreside A, et al. Exploiting NanoLuc luciferase for smartphone-based bioluminescence cell biosensor for (anti)-inflammatory activity and toxicity. *Anal Bioanal Chem*. 2016;408(30):8859-8868.

21.   van der Meer JR, Belkin S. Where microbiology meets microengineering: design and applications of reporter bacteria. *Nat Rev Microbiol*. 2010;8(7):511-522.

22.   van De Merwe JP, Leusch FDL. A sensitive and high throughput bacterial luminescence assay for assessing aquatic toxicity - The BLT-Screen. *Environ Sci Process Impacts*. 2015;17(5):947-955.

23.   Stoytcheva M. Enzyme vs. Bacterial Electrochemical Sensors for Organophosphorus Pesticides Quantification. In: *Intelligent and Biosensors*. Vol 11. ; 2016:218-230.

24.   Roda A, Cevenini L, Michelini E, Branchini BR. A portable bioluminescence engineered cell-based biosensor for on-site applications. *Biosens Bioelectron*. 2011;26(8):3647-3653.

25.   Leitão JMM, Esteves da Silva JCG. Firefly luciferase inhibition. *J Photochem Photobiol B Biol*. 2010;101(1):1-8.

26.   Bulich A. Use of Luminescent Bacteria for Determining Toxicity in Aquatic Environments. *Aquat Toxicol*. 1979:98-106.

27.   ModernWater. https://www.modernwater.com/contact.

28.   Orbit Technologies Pvt. Ltd. http://www.orbitindia.com/.

29.   AquaTox Research Inc. http://www.aquatoxresearch.com/contactmain.php.

30.   Munkittrick KR, Power EA, Sergy GA. The Relative Sensitivity of Microtox®, Daphnid, Rainbow Trout, and Fathead Minnow Acute Lethality Tests. *Environ Toxicol Water Qual*. 1991;6(1):35-62.

31.   Shen K, Shen C, Lu Y, et al. Hormesis response of marine and freshwater luminescent bacteria to metal

exposure. *Biol Res*. 2009;42(2):183-187.

32. Gregor C, Gwosch KC, Sahl SJ, Hell SW. Strongly enhanced bacterial bioluminescence with the ilux operon for single-cell imaging. *Proc Natl Acad Sci*. 2018;115(5):962-967.

33. Shimada T, Tanaka K. Use of a Bacterial Luciferase Monitoring System To Estimate Real-Time Dynamics of Intracellular Metabolism in *Escherichia coli*. *Appl Environ Microbiol*. 2016;82(19):5960-5968.

34. Álvarez-Diduk R, Orozco J, Merkoçi A. Paper strip-embedded graphene quantum dots: a screening device with a smartphone readout. *Sci Rep*. 2017;7(1):1-9.

35. Quesada-González D, Merkoçi A. Mobile phone-based biosensing: An emerging "diagnostic and communication" technology. *Biosens Bioelectron*. 2017;92:549-562.

36. Wang B, Barahona M, Buck M. Engineering modular and tunable genetic amplifiers for scaling transcriptional signals in cascaded gene networks. *Nucleic Acids Res*. 2014;42(14):9484-9492.

37. Wang B, Barahona M, Buck M. A modular cell-based biosensor using engineered genetic logic circuits to detect and integrate multiple environmental signals. *Biosens Bioelectron*. 2013;40(1):368-376.

38. Sklodowska K, Jakiela S. Enhancement of bacterial growth with the help of immiscible oxygenated oils. *RSC Adv*. 2017;7(65):40990-40995.

39. O'Donnell PM, Aviles H, Lyte M, Sonnenfeld G. Enhancement of In Vitro Growth of Pathogenic Bacteria by Norepinephrine: Importance of Inoculum Density and Role of Transferrin. *Appl Environ Microbiol*. 2006;72(7):5097-5099.

40. Ruiz ON, Fernando KAS, Wang B, et al. Graphene Oxide: A Nonspecific Enhancer of Cellular Growth. *ACS Nano*. 2011;5(10):8100-8107.

41. Liu J, Morales-Narváez E, Orozco J, Vincent T, Zhong G, Merkoçi A. Bioluminescent Nanopaper for the Fast Screening of Toxic Substances. *Nano Res*. 2017:1-19.

42. Jiao J, Cheng F, Zhang X, et al. Preparation of Graphene Oxide and Its Mechanism in Promoting Tomato Roots Growth. *J Nanosci Nanotechnol*. 2016;16(4):4216-4223.

43. Das MR, Sarma RK, Saikia R, Kale VS, Shelke M V., Sengupta P. Synthesis of silver nanoparticles in an aqueous suspension of graphene oxide sheets and its antimicrobial activity. *Colloids Surfaces B Biointerfaces*. 2011;83(1):16-22.

44. Wang K, Ruan J, Song H, et al. Biocompatibility of Graphene Oxide. *Nanoscale Res Lett*. 2011;6(1):1-8.

45. Gurunathan S, Han JW, Abdal Dayem A, Eppakayala V, Kim JH. Oxidative stress-mediated antibacterial activity of graphene oxide and reduced graphene oxide in Pseudomonas aeruginosa. *Int J Nanomedicine*. 2012;7:5901-5914.

46. Di Giulio M, Zappacosta R, Di Lodovico S, et al. Antimicrobial and Antibiofilm Efficacy of Graphene Oxide

against Chronic Wound Microorganisms. *Antimicrob Agents Chemother*. 2018;62(7):1-9.

47.   Chen J, Peng H, Wang X, Shao F, Yuan Z, Han H. Graphene oxide exhibits broad-spectrum antimicrobial activity against bacterial phytopathogens and fungal conidia by intertwining and membrane perturbation. *Nanoscale*. 2014;6(3):1879-1889.

48.   Mokkapati VRSS, Pandit S, Kim J, et al. Bacterial response to graphene oxide and reduced graphene oxide integrated in agar plates. *R Soc Open Sci*. 2018;5(11).

49.   Xue J, BinAhmed S, Wang Z, Karp NG, Stottrup BL, Romero-Vargas Castrillón S. Bacterial Adhesion to Graphene Oxide (GO)-Functionalized Interfaces Is Determined by Hydrophobicity and GO Sheet Spatial Orientation. *Environ Sci Technol Lett*. 2018;5(1):14-19.

50.   Pelin M, Fusco L, Martín C, et al. Graphene and graphene oxide induce ROS production in human HaCaT skin keratinocytes: the role of xanthine oxidase and NADH dehydrogenase. *Nanoscale*. 2018;10(25):11820-11830.

51.   Soto W, Gutierrez J, Remmenga MD, Nishiguchi MK. Salinity and Temperature Effects on Physiological Responses of *Vibrio fischeri* from Diverse Ecological Niches. *Microb Ecol*. 2009;57(1):1-21.

52.   Froehner K, Meyer W, Grimme LH. Time-dependent toxicity in the long-term inhibition assay with *Vibrio fischeri*. *Chemosphere*. 2002;46:987-997.

CHAPTER 5. PORTABLE PLATFORM FOR ENVIRONMENTAL APPLICATIONS

CHAPTER 5

Portable Platform for Environmental Applications

154

5.1. Introduction

The human population is growing exponentially worldwide and in 2030 is predicted to break the barrier of 8.5 billion people[1]. This rapid growth has a positive effect on industrialization and medicine development, but at the same time, it is opening a lot of concerns[2]. For example, the adoption of the current lifestyle by all these people will have a tremendous impact on the environment, affecting the social and healthcare systems[3–5]. Possible scenarios could be a shortage of food, an increase in environmental pollution, and rapid depletion of natural freshwater reservoirs[4]. Besides, the recent COVID-19 outbreak has highlighted the accelerated spread rate of infectious diseases in the form of epidemics and pandemics[6]. In these predicted scenarios, bioanalytical sciences could play an important role in tackling these issues. For example, the development of user-friendly, low-cost, portable-devices able to detect biologically, environmentally, and clinically relevant targets could facilitate the monitoring of environmental pollution, infectious diseases, and their transmission and diagnosis[7–9]. At the same time, these devices could open new perspectives for developing countries, which are the most exposed to these events and cannot prevent such issues using the classical laboratory-based methods (techniques which are very sensitive but highly-expensive, non-portable, and require to be used by specialized personnel inside laboratory facilities)[10,11]. Therefore, the development of integrated, low-cost, portable, and easier-to-use bioanalytical platforms able to be exploited for a broad number of applications is becoming an important topic in the analytical sciences[10,12].

An ideal bioanalytical platform should be lightweight, self-powered, and cost-effective, as well as allow for wireless communication and fast analysis while keeping the accuracy and sensitivity of the laboratory-based techniques[13]. In this regard, the main purpose of developing bioanalytical portable platforms is to substitute laboratory-based platforms that need to be used by trained personnel inside laboratory facilities, especially in developing countries with increasing population and limited access to sophisticated screening devices. Overall, portable platforms should display analytical performance comparable to the standard techniques used in the laboratories[14,15]. Inspired by these designing concepts, recently, several studies have demonstrated the development of portable sensing devices. For example, the smartwatches allow nowadays for the monitoring of a myriad of parameters, such as the heart-rate, the blood pressure, and the sleep cycle[16]. However, the bottleneck of these devices is that they can display a limited number of applications for relevant target monitoring.

In recent years, smartphone-based portable platforms have been developed for environmental monitoring, disease diagnosis, and forensic applications[9,13,17–19]. Besides portable

platforms, smartphones allow for imaging and data processing, making them powerful tools for optical sensing applications[20]. For instance, the development of a smartphone-microplate reader integrated within a 3D-printed optomechanical scaffold for diagnosis of viral diseases[13]. This platform relies on the colorimetric detection of the antibodies present in the serum of patients previously infected by herpes, mumps, and measles viruses. The authors use blue-emitting LEDs to illuminate the microplate wells and optical fibers to transmit the individual outputs from each well to an external lens. Eventually, a smartphone is used to capture an image integrating all the outputs transmitted by the optical fibers. Remarkably, this device allows for portability (small dimensions and self-powered by batteries) and fast monitoring (1 min to integrate the results). However, this system hinders alternative detection methods such as those based on fluorescence and bioluminescence. Besides, the optical fibers are used to maximize the number of wells read with a single photo, reducing the area per well that is read by the smartphone. Other researchers report the development of smartphone-spectrophotometer devices, for example, for the kinetics measurement of enzymatic reactions by attachment of a microcuvette to a self-made housing[21]. Furthermore, the development of a smartphone application allows for decomposing the pixels into RGB and hue values, which are further converted to the corresponding wavelengths by an algorithm, showing similar results to those provided by laboratory-based spectrophotometers[22]. On the other hand, other smartphone-based portable platforms rely on fluorescent detection of clinical biomarkers[23,24]. For instance, a 3D-designed scaffold attached to a smartphone to read lateral flow strips (LFS) used to detect hormones[24]. Eventually, other works report the detection of bacteria cells using smartphones and portable platforms[25,26]. For instance, the use of an enzyme-aptamer dual system allows for performing a dot-blot assay for assessment of *Mycobacterium tuberculosis* growth in 5 hours with a limit of quantification of 104 CFU/mL[25]. Despite these achievements, most of these smartphone-based platforms only allow for specific detection methods (i.e. either colorimetric or fluorescent) and constrained reaction chambers (i.e. specific microcuvette or LFS with controlled dimensions).

Herein, we report the design, construction, and testing of an automated portable platform, similar in size and shape to a shoebox, with integrated optical, mechanical, and electrical components that allow for optical sensing of environmental pollutants and disease biomarkers. In this regard, we have provided the portable platform with tools to perform colorimetric, fluorescent, bioluminescent, and turbidimetric assays. Besides, we have adapted the portable platform to measure ELISA plates since they are the most widely used analytical platforms nowadays. First, we have tested the colorimetric detection of disease biomarkers by

carrying out ELISA tests with the help of a light source and a smartphone to capture the images with the platform. We have also performed a gold aggregation test (GAT) with interest to evaluate the state of nanoparticles, which are the main components of many optical biosensors. Next, we have performed a bioluminescent assay to detect pesticides within the portable platform thanks to the opacity of the device and the professional mode of a smartphone camera. Besides, we have installed UV-LEDs and optical filters to perform fluorescent assays and allow the detection of different fluorophores, such as quantum dots (QDs) and fluorescein. Eventually, we have developed a new method to determine the turbidity of the media that converts the portable platform into a drug-screening device for the detection of antibiotic-resistance bacteria. Altogether, this work highlights the development of a versatile and automatized device controlled by a smartphone that allows for performing a variety of optical detection techniques with a myriad of sensing applications.

5.2. Materials & methods

5.2.1. Materials

Aliivibrio fischeri (ATCC® 700601™) was purchased from the ATCC Collection (Manassas, VA, USA). *E. coli* (ATCC11303, ATCC25922) were purchased from the ATCC collection and the company LGC. AuNPs of 40 nm size were synthesized by kinetic seed growth[27]. COVID-19 nucleoprotein and anti-COVID-19 nucleoprotein polyclonal antibody (anti-COVID-19 NP pAb) were purchased from Abyntek (Derio, Spain). Anti-COVID-19 NP monoclonal antibody (anti-COVID-19 NP mAb) was purchased from Fisher Scientific (Hampton, NH, USA). Human IgG, anti-human IgG, anti-human IgG-biotin, and tetramethylbenzidine (TMB) were purchased from Sigma-Aldrich (St. Luis, MO, USA). Streptavidin-horseradish peroxidase (HRP) and anti-mouse IgG-HRP were purchased from Abcam (Cambridge, UK). Red and green quantum dots (QDs) were purchased from Serviquimia (Tarragona, Spain). Blue carbon dots were synthesized by hydrothermal synthesis. Quantum dots conjugated to streptavidin were purchased from Fisher Scientific (Hampton, NH, USA). Fluorescein and pentachlorophenol were purchased from Sigma-Aldrich (St. Luis, MO, USA). Kanamycin, ampicillin, and amoxicillin were purchased from Sigma-Aldrich (St. Luis, MO, USA). White and black ELISA plates with transparent bottom wells were purchased from FisherScientific (Hampton, NH, USA). Transparent ELISA plates were purchased from FisherScientific (Hampton, NH, USA).

Optical lens (LA1540 and LA1576) and optical filters (bandpass 370nm FB370-10, longpass 400nm FEL0400) were purchased from Thorlabs (Newton, NJ, USA). White LED (C535A-WJN 5mm) and UV LED (KTDS-3534UV365B 1.95W 265nm) were purchased from Farnell as well as the Peltier module, heatsink, and fans (Leeds, UK). A smartphone Huawei P20 Lite was used to

perform the optical analysis with the platform. SpectraMax iD3 (San José, CA, USA) was used to perform additional optical measurements. Bacteria were cultivated either within the portable platform while performing optical measurements within SpectraMax iD3, or by using a 37 ºC microbiological incubator (Single 184L incubator, FisherScientific, MA, USA).

5.2.2. Colorimetric ELISA tests

ELISA wells were first coated with capture antibodies against the COVID-19 nucleoprotein and human-IgG (16 h, 4 ºC). Then, a washing step with washing buffer (PBST; 0.01 M PBS, pH 7.4, 0.05% Tween-20) was performed, followed by a blocking step with 3% BSA in PBS (2h, 37 ºC), and an additional washing step with PBST. Next, different concentrations of nucleoprotein (from 1 ng/mL to 1 µg/mL) and human-IgG (from 1 ng/mL to 1 µg/mL) were added (1 h, 25 ºC), the ELISA wells were washed with PBST, and the detection antibodies were added (1 h, 25 ºC), using the PBST to wash the microwells again. In the following step, anti-mouse IgG (HRP) or streptavidin-HRP were added for 1 h of incubation at 25 ºC. Eventually, the last washing step was performed, and the colorimetric revealing agent (tetramethylbenzidine, TMB) was added to yield the final results.

5.2.3. Gold aggregation tests (GAT)

40 nm AuNPs were blocked with a solution of BSA at different concentrations (0%, 0.005%, 0.05%, 0.1%, and 1%) for 20 min (550 rpm, 25 ºC). Then, 80 µL of these blocked AuNPs were added to the microplate wells together with 20 µL of 10% NaCl. The solutions were incubated for 3 minutes and the colorimetric outputs were recorded either with the spectrophotometer or with the smartphone within the portable platform by using white LEDs to illuminate the samples. Then, the pictures were analyzed with the software ImageJ and the results were compared with those obtained with the spectrophotometer to estimate the AuNPs aggregation state and the correlation between both detection methods.

5.2.4. Fluorescent assays

The concentration of different QDs (red, green, and blue) was first adjusted to obtain similar fluorescent output intensities. Next, different QDs were put together to obtain different fluorescent colors (i.e. cyan, yellow, and pink). The fluorescent emission spectra were recorded with the spectrophotometer and pictures were captured with the smartphone and the portable platform using a UV-LED to excite the QDs at 365 nm. Besides, red QDs were prepared at different concentrations from 300 nM to 0.001 nM in order to detect and quantify them with the spectrophotometer and the portable platform. Briefly, 50 µL of different concentrations of red QDs were added to 96-wells plates, and pictures were taken by using different smartphone

settings (from ISO 200 to ISO 3200, integration time from 1/30 s to 5 s). The pictures captured with the smartphone were afterward analyzed using the software ImageJ. Besides, fluorescein was also detected as another common fluorophore using the portable platform. Different concentrations of fluorescein were prepared and quantified using both the spectrophotometer and the portable platform. The same UV-LED was used to excite the fluorescein (365 nm) and the outputs were recorded by the smartphone and afterward analyzed by ImageJ. The brighter the image, the higher concentration of fluorescein. Eventually, a fluorescent ELISA test was performed by immobilizing different concentrations of biotinylated-antibodies (100, 200, 500, and 2000 ng/mL) on the ELISA wells and using streptavidin-QDs as the revealing agents (10 nM, 5 nM, 2.5 nM, and 1 nM).

5.2.5. Bioluminescent assays

A. fischeri was grown in marine broth (MB) at 25 ºC for 20 hours. Bacteria concentration and bioluminescence were recorded and the experiments were only performed when cellular density was higher than 10^8 CFU/mL and bioluminescence was higher than 10^6 dimensionless units (spectrophotometer). Next, 50 µL of bacteria and 50 µL of the sample were put together within the microplate wells and incubated under agitation for 5 minutes. Eventually, individual pictures from each well were captured with the smartphone using ISO 1000 and different integration times. The pictures captured with the smartphone were afterward analyzed using the software ImageJ.

5.2.6. Elementary analysis with ImageJ

The pictures were uploaded to the software ImageJ and the optical outputs were selected with a circular shape that spans the whole microplate well. In this way, the analysis is not biased by a partial selection of the area of the well. The intensity of the optical output is then recorded, as well as the background signal within the same picture outside the microplate well. Next, the background signal is subtracted to the output obtained within the well. This process is repeated for the different samples analyzed during the same experiment. In the following step, all the numeric values are divided by the highest value (brightest output) in order to normalize the data (between 0 and 1). Finally, the data are graphically represented for an appropriate interpretation of the results.

5.2.7. Complex analysis with ImageJ

On the one hand, the intensity of the red color of the AuNPs was analyzed by ImageJ to estimate AuNPs' aggregation state. First, the pictures were uploaded to ImageJ. Then, the

following command was used to treat the images: Image → Color → Split Channels → Green Channel. As green color (540 nm) is complementary to red, and AuNPs yield red color, splitting the green channel allows for a B&W output in which the redder the original image, the blacker the processed image. In this regard, ImageJ can easily analyze the brightness of the picture according to the intensity of the red color in the original image, which is directly proportional to the blackness in the processed image.

On the other hand, the intensity of the yellow color yielded by the revealing reagent in the colorimetric ELISA tests is analyzed as follows: Image → Adjust → Color Threshold. At this point, three scrolling bars pop up that allows for a complex analysis of the uploaded images. First, the hue threshold must be framed between 35 and 45, which corresponds to the range in which the yellow color is found. Next, the saturation and brightness of the pictures must be adjusted in order to obtain the highest contrast between different color intensities. The overall process yields B&W images that can be easily analyzed by ImageJ, being the original yellowest pictures the blackest pictures after the images processing.

5.2.8. Bacteria culture and drug screening

A. fischeri was grown in marine broth (MB) at 25 ºC either in an orbital agitator or within the portable platform (20 h cultivation). The two strains of *E. coli* were cultured in tryptic soy broth (TSB) at 37 ºC either in an incubator or within the portable platform (18 h cultivation). Bacterial cultures were then adjusted to an OD_{600} = 0.2 (≈ $1.6 \cdot 10^8$ CFU/mL) by adding growth media and different concentrations of antibiotics. Next, 50 µL of antibiotics was added together with 50 µL of bacteria within the ELISA wells, followed by an incubation step performed at 25 ºC with shaking for *A. fischeri*, and at 37 ºC without shaking for *E. coli*. Eventually, bacterial growth was estimated and compared by using the spectrophotometer to measure the OD_{600} and the smartphone to analyze the turbidity of the media. In order to increase the contrast between the growth media and the media containing a high concentration of bacteria, a dark spot of wax printed over a white paper was placed centered below the ELISA wells. Briefly, this new method allows for increasing the contrast between those samples containing low concentrations of bacteria (darker spot, light not reflected) and high concentrations of bacteria (whiter spot, light reflected by the presence of particles [bacteria cells] within the media), boosting the sensitivity of the detection of bacterial growth within the portable platform.

5.3. Characterization of the optical system

Our portable platform consists of a physical scaffold that contains all the electronic, mechanical, and optical components required to perform the optical tests (Figures 5.1a and

5.1b). Specifically, the optical part is formed by a lens which is inserted on the lid of the portable platform, and it is located between the smartphone (used to acquire the images) and the ELISA plate (containing the different samples to be analyzed) and a LED as a light source. More specifically, 5 LEDs are installed within the portable platform: a UV LED with an excitation wavelength at 365 nm to perform fluorescent assays and 4 white LEDs to perform a variety of colorimetric assays. These LEDs are, in turn, combined with a series of two optical filters that enable the selection of the excitation wavelength (bandpass 370 nm) used to perform the fluorescent assays and to reduce the background signal (longpass filter 400 nm) observed in the pictures captures by the smartphone. We used a convergent lens to improve the focus of the smartphone camera since the physical distance between the smartphone and the ELISA plate is very short (17 mm), which limits the focus capability of the smartphone cameras[28]. By using the following formula:

$$\frac{1}{f} = \frac{1}{d} + \frac{1}{v} \quad : \quad \text{Equation 5.1}$$

where "f" is the desired focal length, "d" is the real distance between the smartphone camera and the surface of the liquid sample to be analyzed, and "v" is the real focal length of the smartphone, we estimated the focal length required by the lens to optimize the focus of the smartphone camera over the samples. By using this information, we selected five different smartphone brands and models (from Huawei, iPhone, Motorola, Samsung, and Xiaomi), out of which Huawei P20 Lite provided the shortest focal length ($\approx$ 30 mm). Moreover, considering the use of 100 µL of sample per well in the ELISA plate, the real distance between the smartphone camera and the sample is 17 mm. Therefore, the required focal length of the convergent lens is around 11 mm, providing an optimal focus and the best resolution of the images captured by the smartphone.

We integrated a set of different units into our platform to control the temperature and the shaking of the plates. Specifically, we have installed a temperature and a humidity sensor to monitor these parameters during the performing of the bioanalytical assays. Additionally, we integrated a Peltier module for heating and cooling the plates (for heating up to 37 ºC and cooling down to 4 ºC) to control precisely the temperature and, therefore, correct its fluctuation inside the device. Next, we installed a mechanical frame specifically designed to house ELISA plates within the platform and we connected it to a stepper motor to provide the device with shaking capabilities. In this regard, the activation of the motor allows the device to shake the plates, supporting all the incubation steps which are critical in standard ELISA tests and other immunoassays.

Finally, our device can be easily controlled and programmed through a smartphone making the overall bioanalytical process user-friendly. The portable platform is controlled by a dedicated app (Figure 5.1c) installed on the smartphone. By using this app is possible to monitor the temperature and humidity, adjust the temperature conditions, select the optical assay to perform (colorimetric, fluorescent or bioluminescent), move precisely and agitate the ELISA plate, turn on and off the UV LED and white LEDs, and to take pictures when necessary. To keep the cost of the device accessible, the whole system is managed by an Arduino board, a motor driver, and other electronic components that allow the control of the optical and mechanical parts through the smartphone app.
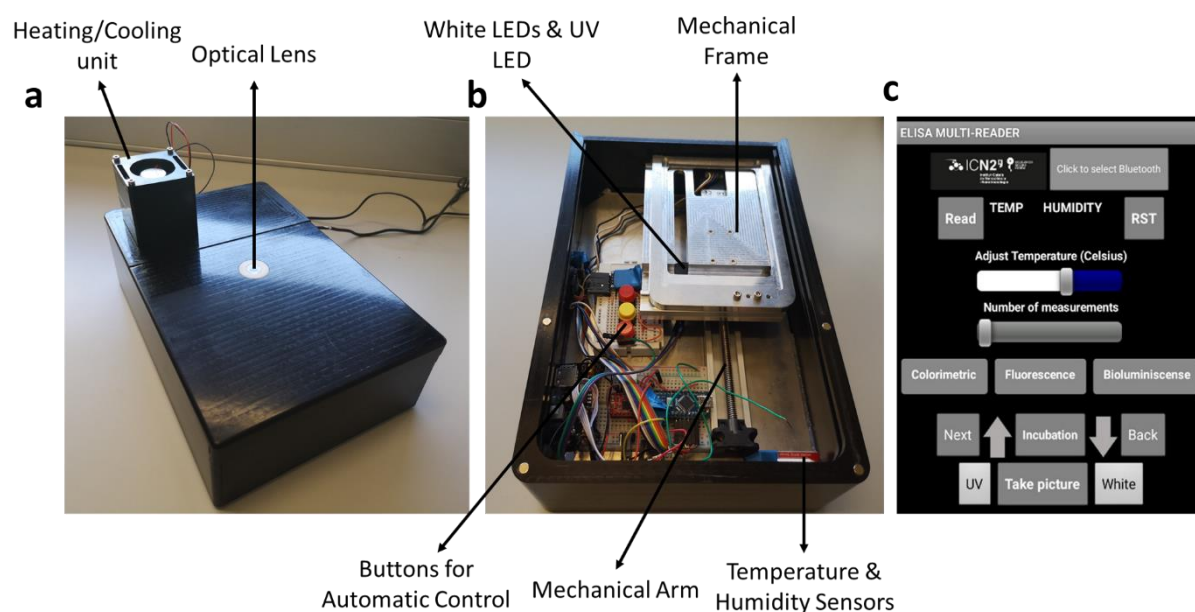
Figure 5.1. (a) Portable platform from the outside, with the lid and the heating/cooling unit. (b) Portable platform from the inside, with the different mechanical, optical and electrical components. (c) Dedicated smartphone app used to control the portable platform from the smartphone.

5.4. Colorimetric assays

5.4.1. Colorimetric ELISA test

To test the analytical performance of our portable platform, we selected ELISA tests as a testbed. ELISA tests are one of the most used bioanalytical assays to diagnose diseases and monitor the health of individuals[29,30]. Therefore, we developed two colorimetric ELISA tests for the detection of the nucleoprotein of SARS-CoV-2 and the total amount of human immunoglobulin G (human IgG) to understand the sensitivity of our platform concerning the colorimetric signal outputs. More in detail, these biomarkers are important to diagnose the infectious disease and to monitor the state of the host immunological system. We thereby used a sandwich assay to detect the nucleoprotein of SARS-CoV-2 and human IgG by the formation

of immunocomplexes, which are further detected by a third antibody conjugated with an enzyme. Eventually, the presence of the enzymatic substrate triggers the enzymatic reaction which leads to the formation of a colored product.

The selection of appropriate ELISA plates is crucial to achieving the most optimal performance of the assays. We thereby selected white ELISA plates with transparent bottom wells because white color avoids "light cross-contamination" from well-to-well but preserves an optimal illumination of all the samples. Based on our previous expertise, we tested a wide concentration range of the analytes, from 1 ng/mL to 1 µg/mL. Then, we placed the ELISA plates in the supporting frame and we closed the lid. At this point, we deposited the smartphone on the lid, which is well-aligned with the lens, to acquire the image of the well. Furthermore, by using a second smartphone, we can control the device moving the plate from well to well, allowing us to collect the signal outputs from all the wells of the plate.

The results yield a pale to yellow colorimetric output: the more yellow, the higher concentration of the analyte within the sample. These results were read and quantified with the spectrophotometer and the portable platform using the smartphone camera (Figure 5.2a). Nonetheless, whereas the spectrophotometer can select and specifically read the yellow optical signal of the wells, the smartphone camera only captures the images but cannot directly quantify their color intensity. We thereby used ImageJ as an optical software to analyze the pictures yielded after the ELISA tests. Briefly, precise control of the analysis conditions (see section 5.2.7) allows for transforming the yellow to pale gradient into a white to black gradient, which can be easily analyzed by ImageJ (Figure 5.2b). We then plotted and compared the results obtained by the spectrophotometer and the portable platform (Figures 5.2c and 5.2d). On the one hand, there is a clear correlation between the results obtained by both methods, with a better correlation for the detection of the SARS-CoV-2 nucleoprotein (optical LOD = 3 ng/mL for the spectrophotometer and 10 ng/mL for the portable platform). On the other hand, the RSD among the different replicates for the same concentration of the analytes are higher with the portable platform than with the spectrophotometer, especially at low concentrations of human-IgG. These results can be expected by considering slight changes in the illumination given for different wells within the portable platform. That's to say, these slight illumination variations amplify the real differences among the replicates due to the later analytical treatment performed with ImageJ. Nonetheless, the obtained results support that the portable platform can be used to perform and read colorimetric ELISA tests, showing great potential for other related applications.
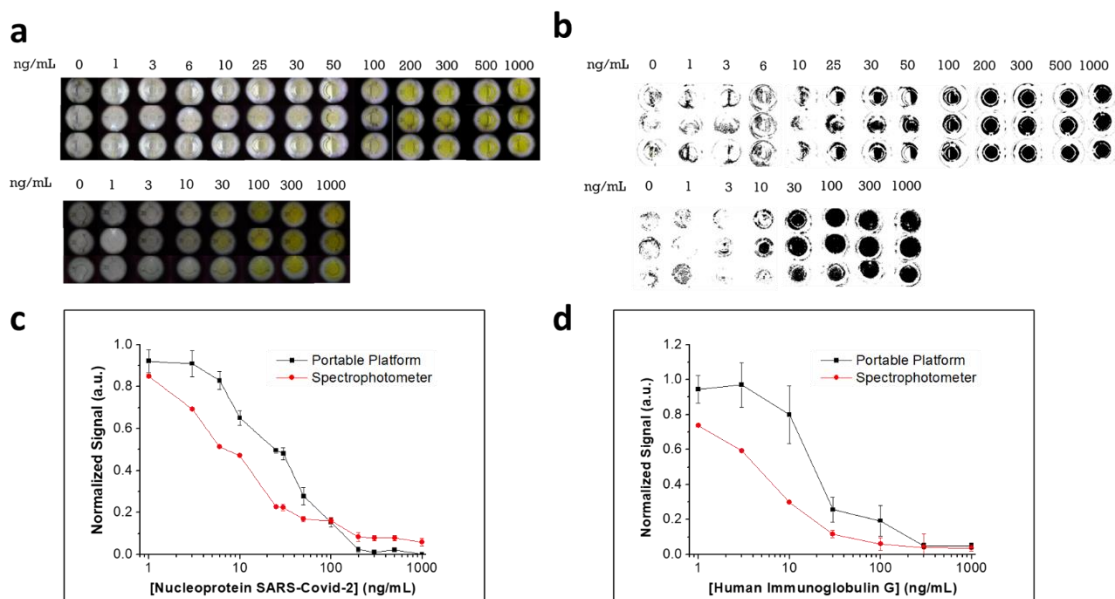
Figure 5.2. (a) Colorimetric outputs obtained after performing ELISA tests for SARS-CoV-2 nucleoprotein detection (top) and human IgG (bottom). (b) The corresponding processed images for an optimal analysis with ImageJ. (c) Calibration curves obtained for SARS-CoV-2 nucleoprotein detection with the spectrophotometer (red) and the portable platform (black). (d) Calibration curves obtained for human IgG detection with the spectrophotometer (red) and the portable platform (black).

5.4.2. Gold Aggregation Test

To further demonstrate the ability of our platform to collect a colorimetric signal output, we performed a gold aggregation test (GAT) to evaluate the stability of gold nanoparticles (AuNPs). AuNPs are optical transducers broadly used in rapid tests, such as lateral flow strips (LFS)[31,32]. In this regard, the size, concentration, and stability of AuNPs are critical parameters to optimize the performance of these sensors. We selected 40 nm AuNPs and we blocked them using different concentrations of bovine serum albumin (BSA), from 1% to 0.01% (w/v). Afterward, the stability of these blocked AuNPs was tested by adding a solution of 10% NaCl and we monitored the optical signal using a classic spectrophotometer and our portable platform. In this regard, the AuNPs become more resistant to the aggregation induced by a high concentration of salts when they are sufficiently covered by a blocking agent, such as BSA. The spectrophotometer enables to read the absorbance spectra of the AuNPs, showing the maximum absorbance peak around 540 nm. As expected, this absorbance peak declines when lower concentrations of BSA are used to block the AuNPs because of AuNPs aggregation (Figure 5.3a).

In the next step, to demonstrate the capability of our system to convert the image into a quantitative value, we evaluated the aggregation state of these AuNPs using the portable

platform by tuning the smartphone camera settings. We found that the most optimal conditions were ISO 640 and 1/40 s of integration time (Figure 5.3b). After the acquisition of the images, we performed the optical analysis with ImageJ. Specifically, we can precisely see AuNPs absorbance at the visible range by splitting up the color channels of the images, and filtering the green channel because green and red are complementary colors. The final output is a black and white (B&W) image that can be easily analyzed by ImageJ: the redder the original picture, the blacker the processed image (Figure 5.3b). Once we converted the images into quantitative values, we compared this set of data with those obtained with the spectrophotometer (Figure 5.3c). In this regard, we normalized the signals collected by the spectrophotometer and the analyzed images to better compare the data. Eventually, we found a good agreement between the two sets of data and a high-correlation at different AuNPs-blocking conditions. Overall, this portable platform allows for accurate analysis of the stability of AuNPs with clear applications in the development of LFS and other optical sensors.
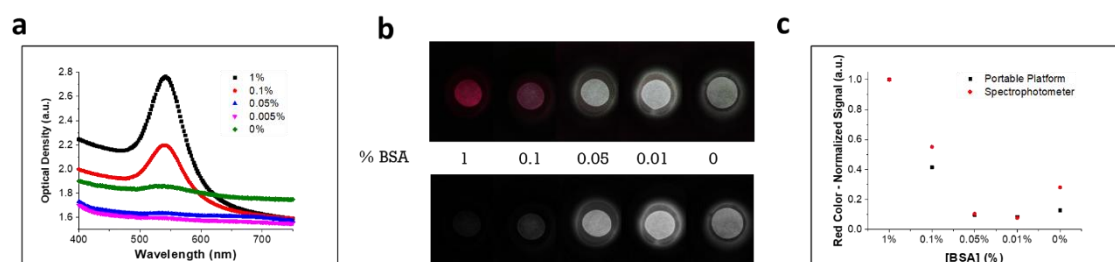
Figure 5.3. (a) AuNPs absorption spectra at different BSA blocking conditions, after the addition of 10% NaCl to induce nanoparticles aggregation. (b) Colorimetric outputs obtained after performing the GAT (top), and after processing the images with ImageJ (bottom). (c) Correlation between the results provided by the spectrophotometer (red) and the portable platform (black).

5.5. Bioluminescent assays

Our portable platform allows not only to perform colorimetric tests but also a variety of other optical tests such as bioluminescent assays. Bioluminescence is the production of light by a living organism, and has several applications, highlighting the performance of toxicity tests. A toxicity test is an assay that measures the physiological response of an organism to the presence of a specific chemical or a pool of substances[33]. As an example, the bacteria *Aliivibrio fischeri* is widely used to perform bioluminescence toxicity assays that determine the toxicity of polluted water samples, more specifically the concentration of certain pesticides found in these water samples.

The measurement of the bioluminescent signal requires an optimization of the optical setup. As mentioned before, bioluminescence is a phenomenon that does not require an

excitation wavelength since the light production is triggered by a chemical reaction within a living organism[34,35]. Therefore, the opacity of the portable platform and the darkness inside it are critical parameters to evaluate in order to ensure the highest sensitivity and prevent light contamination during the assays. For this reason, we selected white ELISA plates with opaque wells to avoid light cross-contamination among different wells and, at the same time, to prevent light absorption by the plate. Next, we optimized the volume of sample per ELISA well to obtain the best focus and resolution during the bioluminescent assays. We observed that lower volumes allow for a better focus of the images (because of the higher distance between the sample and the smartphone camera), whereas higher volumes lead to avoid the light contamination produced by the reflection of the bioluminescence on the walls of the ELISA wells (Figure 5.4a). Accordingly, we selected 100 μL as the most optimal volume for the bioluminescent assays, representing a good compromise in terms of reagents amount and optimal focus.

Besides, the intensity of the bioluminescence and the quality of the pictures captured by the smartphone camera represent two important parameters. We can adjust the image acquisition using the smartphone by selecting different ISO values and integration times. To optimize these parameters, we created a matrix of images by selecting 5 different ISO values (400, 640, 800, 1000, and 1600) and 5 different integration times (4 s, 6 s, 8 s, 10 s, 15 s) using the same batch of bioluminescent bacteria (Figure 5.4b). On the one hand, low ISO values and integration times provide low reflection and light contamination of the final output, but at the expense of very low intensity and contrast of the bioluminescence captured by the smartphone. On the other hand, high ISO values and integration times provide bright images, but the overexposure times often lead to burn the images, which are difficult to analyze. Hence, a commitment must be achieved among bioluminescence intensity, light reflection, and optimal contrast among the different bioluminescent outputs yielded during a toxicity test.

In order to find a real application, we performed a toxicity test using pentachlorophenol (PCP), a broad-spectrum pesticide, as the chemical whose toxicity would be tested with *A. fischeri*. We thereby tested 6 different concentrations of PCP in the range of mg/L with the bioluminescent bacteria (proportion 1:1) and incubated the samples for 5 minutes at room temperature. Next, we analyzed the toxicity profiles with the spectrophotometer and the portable platform using different ISO values and integration times (Figure 5.4c). As expected, the bioluminescence spectra do not change the emission wavelength distribution but the bioluminescence intensity upon increasing concentrations of PCP (Figure 5.4d). Afterward, we compared the toxicity profiles provided by the spectrophotometer and the different camera

settings tested with the portable platform (Figure 5.4e). The analysis of the images captured by the smartphone was performed with ImageJ without any further image treatment. In this regard, ISO 400 and 4 s of integration time yield better sensitivity than the spectrophotometer, whereas increasing ISO values and integration times allow for brighter images but lower sensitivity. Overall, the toxicity tests performed with the portable platform give reliable results, comparable to those obtained with the spectrophotometer, and enable to tune the detection range of PCP by selecting the most appropriate smartphone camera settings.
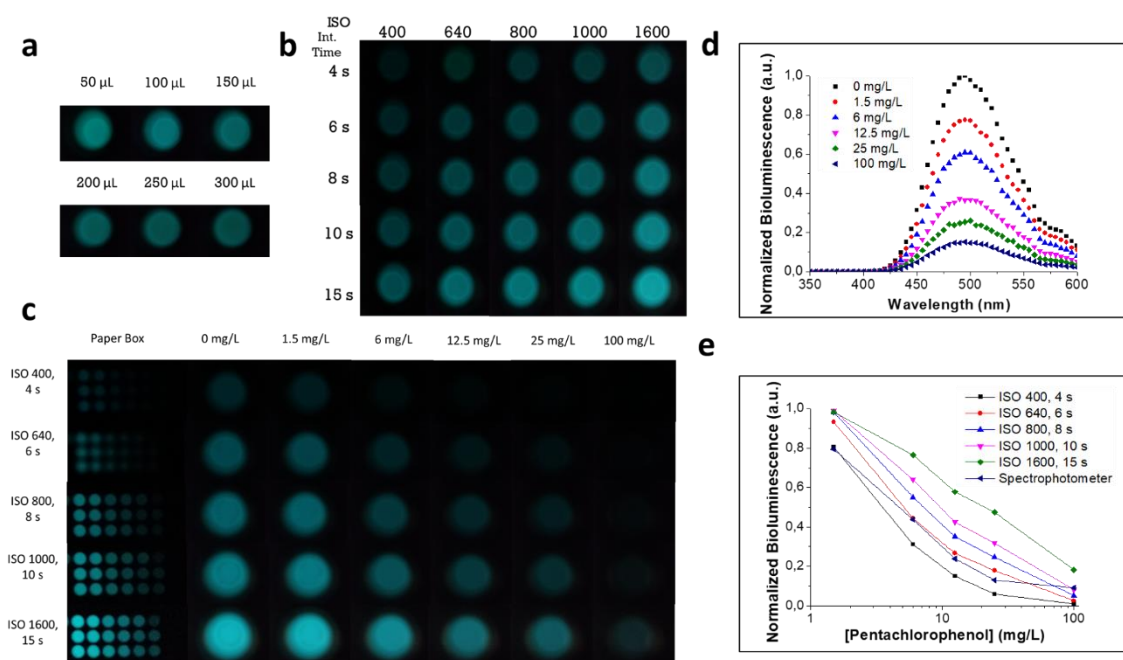
Figure 5.4. (a) Different volumes of bioluminescent bacteria tested within the portable platform. (b) Different smartphone parameters tested to capture the bioluminescence of *A. fischeri* within the portable platform. (c) Different smartphone parameters tested to analyze the toxicity profile of pentachlorophenol with *A. fischeri* within the portable platform. (d) Bioluminescence spectra of *A. fischeri* upon increasing concentrations of PCP. (e) Toxicity profiles of PCP with *A. fischeri* by using the spectrophotometer and different smartphone settings within the portable platform.

5.6. Fluorescent assays

5.6.1. Fluorophores characterization

To further demonstrate the versatility of the platform, we performed fluorescent assays with several fluorophores broadly used for biosensing applications (i.e. quantum dots [QDs] and fluorescein)[36–39]. As previously described, we installed a UV led that emits at 365 nm to excite the fluorophores used for the fluorescent assays and an appropriate filter to reduce the signal background produced by the excitation source. In this case, the opacity within the portable

platform is important to prevent light contamination and signal noise. We employed black ELISA plates with transparent bottom wells since the samples are excited from below and the images are captured from above. The black ELISA plates hinder cross-contamination among different wells and help to screen any interferences provoked by the UV led in the final images. We followed the same optimization performed with the bioluminescent assays, considering the volume of sample and smartphone camera parameters. Again, 100 µL provides the best quality images in terms of fluorescent intensity and optical focus (Figure 5.5a). Next, we selected 3 different color-emitting quantum dots (red, blue, and green) and we adjusted their concentration in order to display the same raw fluorescent signal (Figure 5.5b). Then, we tested them alone and together to obtain different fluorescent colors through their combination (ISO 400, ½ s). We recorded the emission spectra of all the possible combinations, and we captured the corresponding images with the smartphone camera and the portable platform (Figures 5.5b and 5.5c). The quality of the images obtained highlight the versatility of the portable platform since different color emitting QDs can be detected, demonstrating that the platform can support multiplexing measurements.
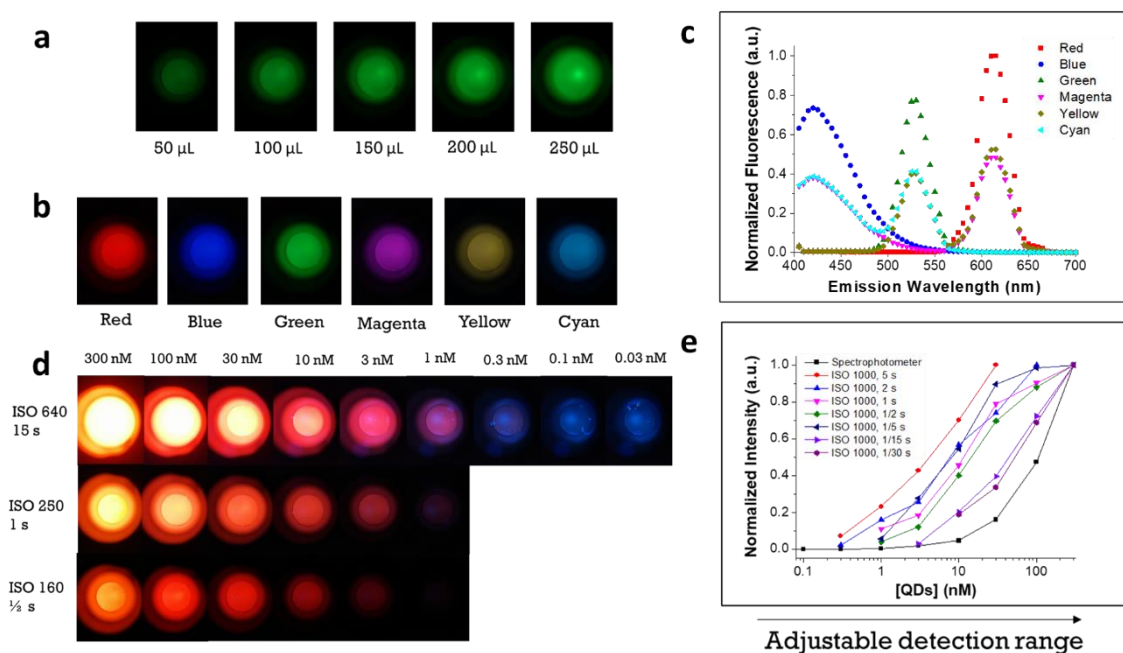
Figure 5.5. (a) Different volumes of green QDs tested within the portable platform. (b) Different color QDs (red, blue, and green) and their combinations tested within the portable platform. (c) Emission spectra of different color QDs read by the spectrophotometer. (d) Images of different concentrations of red QDs captured by using different smartphone camera settings. (e) Calibration curve of the detection of red QDs by using the spectrophotometer and different smartphone camera settings within the portable platform.

In a further step, we selected the red QDs and we created an array of images using the corresponding calibration curves (Figures 5.5d and 5.5e). The purpose of this experiment is to find the optimal parameters required to detect different concentrations of QDs. Whereas high integration times lead to detect low concentrations of QDs (in the range of nM or lower), low integration times lead to detect higher concentrations of QDs with better sensitivity, avoiding the "burn-effect". This optimization step is crucial to improve the sensitivity and detection limit of the device. Furthermore, we followed the same procedure used for QDs using fluorescein, a commonly used fluorophore in microscopy, serological tests, and biomolecules labeling[36,37,40]. We thereby detected different concentrations of fluorescein under different smartphone camera settings, and we observed different detection ranges depending on the settings employed. In this regard, we could detect down to 3.5 µM of fluorescein by using ISO 400 and 4 s of integration time (Figures 5.6a and 5.6b). Conversely, we could not detect lower concentrations by using higher ISO values or integration times. Of note, fluorescein displays the maximum excitation wavelength at 494 nm and our light source (UV LED) emits at 365 nm. Therefore, the sensitivity of fluorescein detection could be improved by simply installing a different UV LED exciting at a higher wavelength.
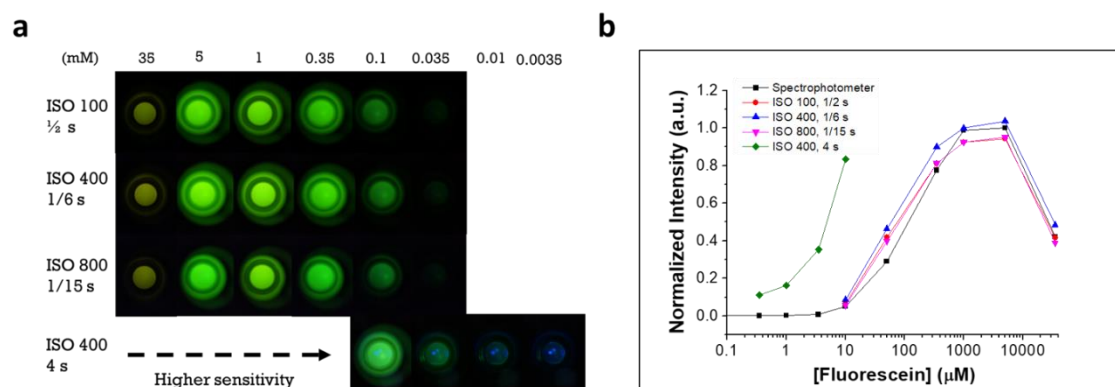
Figure 5.6. (a) Detection of different concentrations of fluorescein by using different smartphone camera settings and the portable platform. (b) The corresponding calibration curves obtained after plotting the results shown in Figure 5.6a and the measurements carried out by the spectrophotometer.

5.6.2. Fluorescent ELISA test

To demonstrate the ability of our device to exploit a fluorescent signal as an analytical readout, we performed a fluorescent test to mimic the experimental conditions used in a classical ELISA test. We coated a black ELISA plate with biotinylated antibodies (100, 200, 500, and 1000 ng/mL) and used streptavidin-QDs (10, 5, 2.5, and 1 nM) as the tagged analytes. We recorded the fluorescence of the samples before and after washing the ELISA plate containing the samples with the spectrophotometer and the portable platform (Figures 5.7a and 5.7b). By

following this approach, we could detect streptavidin-QDs with the portable platform before the washing step, but only with the spectrophotometer after the washing step. Then, we plotted a calibration curve of the fluorescence signal of the streptavidin-QDs depending on their concentration (Figure 5.7c), showing that the final concentration of streptavidin-QDs after the washing step was in the range of pM, which cannot be detected by the smartphone camera. Nonetheless, we can improve the readout of the fluorescent ELISA with the portable platform by increasing the initial concentration of streptavidin-QDs, reducing the concentration of biotinylated-Abs coated in the ELISA wells (see Figure 5.7b), or further optimizing the washing/blocking steps. In any case, the portable platform allows for detecting different fluorophores with very little signal noise in the range of nM, showing great potential for a myriad of fluorescent assays.
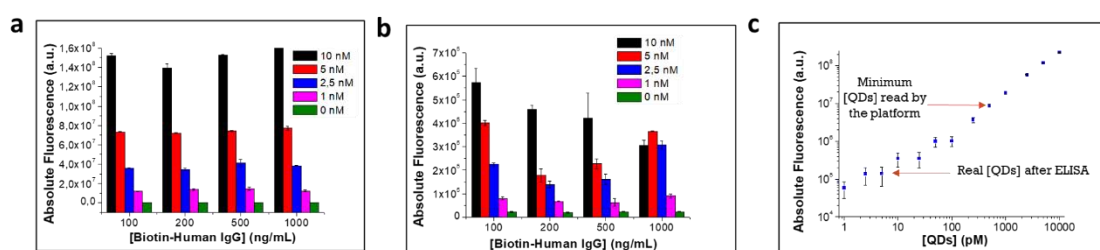
Figure 5.7. (a) The fluorescence signal of streptavidin-QDs within the ELISA plate before the washing step (10^7-10^8 a.u.). (b) The fluorescence signal of streptavidin-QDs within the ELISA plate after the washing step (10^5 a.u.). (c) Calibration curve of streptavidin-QDs carried out by the spectrophotometer, showing the real concentration of streptavidin-QDs after the washing step and the minimum concentration of streptavidin-QDs that can be detected using the smartphone and the portable platform.

5.7. Bacterial growth & drug screening

5.7.1. Bacterial growth & turbidity measurements

Finally, to highlight the advantage of the design of our portable platform, we demonstrate the possibility to grow bacteria for biosensing applications. Briefly, we used the mechanical frame designed to hold the ELISA plates to agitate a vial containing 5 mL of marine broth media (MB) and an inoculum of *A. fischeri* under controlled temperature conditions (25 ºC). In parallel, to estimate the efficiency of the new approach, we also grew the bacteria in a microbiological incubator under orbital shaking (135 rpm) at 25 ºC. After a period of incubation of 20 hours, we checked the bacterial growth and bioluminescence for both approaches (Figure 5.8a). *A. fischeri* grew 45% and yielded 57% of the bioluminescence in the portable platform compared to the culture grown in the microbiological incubator. These differences could be explained because of the lower agitation capability of the portable platform since *A. fischeri* is an aerobic bacterium

that requires powerful agitation to boost bacterial growth and bioluminescence. However, these results also support that the portable platform can be used to grow bacteria under agitation and controlled temperature conditions and could be improved by increasing the agitation power of the device.

Having this in mind, we also used the portable platform to determine bacterial growth through the analysis of the turbidity of the media. However, turbidity changes are very difficult to observe in comparison with color changes, especially for smartphone images. For this reason, we created an innovative system that is based on the introduction of a background contrast in the well. Specifically, this contrast allows us to calculate turbidity changes using a simple smartphone camera. Briefly, we printed standard paper sheets with a pattern of black wax circles which are smaller in size than the ELISA wells. After that, we stuck them to the bottom of the wells of an ELISA plate and we tested the signal output with media without bacterial growth. Accordingly, we observed the blackness of the wax circle remained unchanged. Then, we added media with bacterial growth and we observed the wax circle becomes whiter due to the presence of bacterial cells, which increase the light reflection within the wells. Accordingly, in the presence of a higher concentration of bacteria, we observe a whiter wax circle in the smartphone images. Furthermore, by optimizing this system, we can increase the sensitivity of the detection of bacterial growth within the platform. Therefore, we optimized this system in terms of the number of paper sheets stuck to the ELISA plate and the smartphone camera settings (Figure 5.8b). The best results are obtained by using a single sheet of paper, the maximum ISO value (3200), and 1/8 s of integration time with the smartphone camera, providing a relative change of 42% between the media without bacteria (MB) and the media with bacteria ($\approx 10^9$ CFU/mL).
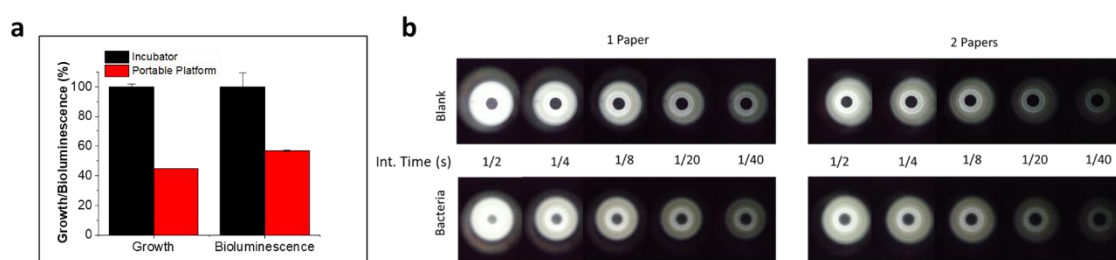
Figure 5.8. (a) Bacterial growth and bioluminescence of *A. fischeri* by carrying out the bacterial cultures in a microbiological incubator (black) and the portable platform (red). (b) Turbidity measurements using paper sheets printed with wax circles and different smartphone camera settings.

5.7.2. Drug screening

Finally, we envisaged a direct application for these turbidity measurements. Since antibiotic resistance has become one of the major problems the health care systems are facing nowadays[41], the use of the portable platform to detect bacterial resistance to antibiotics provides a powerful functionality as a screening device. In this regard, we tested 3 different strains of bacteria (*A. fischeri*, *E. coli* ATCC11303, and *E. coli* ATCC25922) with different concentrations of 3 antibiotics (kanamycin, ampicillin, and amoxicillin). After 20 hours of growth (25 ºC for *A. fischeri*, and 37 ºC for *E. coli*), we evaluated the turbidity of the media (MB for *A. fischeri*, and TSB for *E. coli*) by using the spectrophotometer (OD600) and the portable platform (Figures 5.9a, 5.9b, 5.9c, and 5.9d). The results show a very good correlation between both methods, with a slighter higher sensitivity of the spectrophotometer in all the cases (all in the range of µg/mL). Nevertheless, the newly developed system allows for direct visual detection of bacterial growth, with an easier interpretation of the results than with the spectrophotometer. Besides, the turbidity measurements could be used to monitor the bacterial growth kinetics by recording a video or to determine the formation of biofilms and other bacterial structures by simply adjusting the smartphone camera settings and the temperature and shaking conditions within the portable platform.
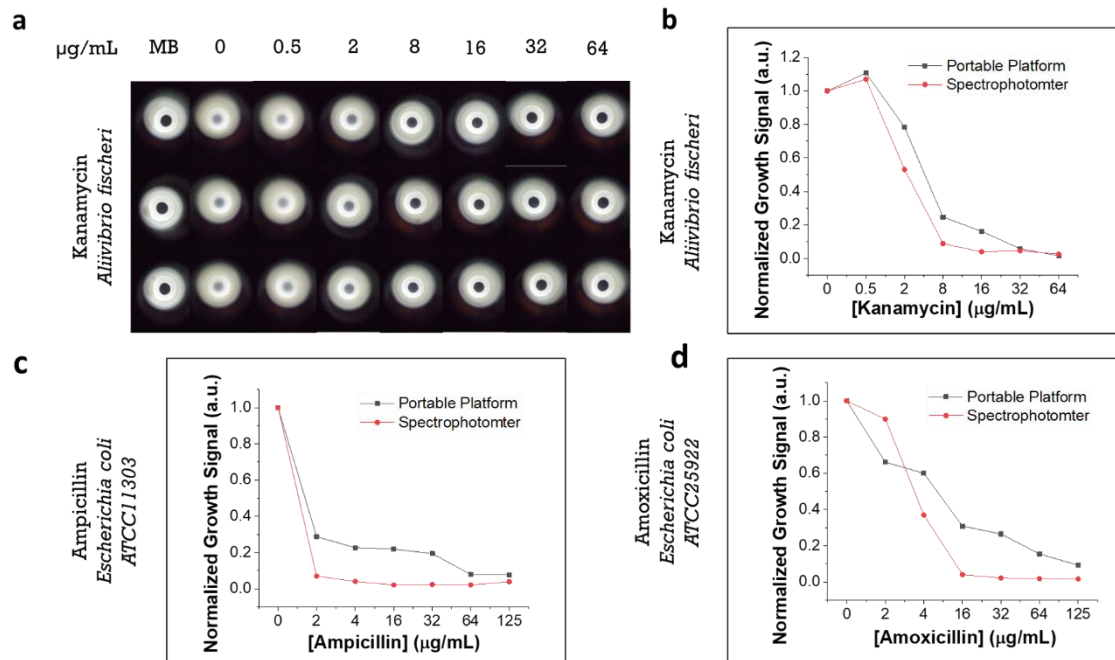
Figure 5.9. (a) Turbidity measurements performed with kanamycin and *A. fischeri* within the portable platform. (b) Drug screening performed with kanamycin and *A. fischeri* by the spectrophotometer and the portable platform. (c) Drug screening performed with ampicillin and *E. coli* ATCC11303 by the spectrophotometer and the portable platform. (d) Drug screening performed with amoxicillin and *E. coli* ATCC25922 by the spectrophotometer and the portable platform.

5.5. Conclusions

In this work, we have developed a portable platform able to perform a myriad of biosensing applications. First, an optical lens, UV and visible light sources, and optical filters have been installed to optimize the sensing capabilities of the device. Second, a Peltier module with heating and cooling capabilities have been installed to allow for a wide range of temperature conditions to carry out bioassays and bacterial cultures. Besides, the control of the temperature and humidity conditions is performed by two sensors set within the platform. On the other hand, the portable platform can also agitate the samples due to a motile mechanical arm. At last, an Arduino allows for controlling all these components from a dedicated app in your smartphone, creating a powerful tool for biosensing applications. In the next step, we tested the portable platform through the colorimetric detection of biomarkers by ELISA tests and the control of nanoparticle aggregation state. The careful design and total opacity of the platform also allow for performing bioluminescent assays with interest in environmental applications such as water toxicity assessment. In addition, a wide range of fluorescent assays can be performed thanks to the optimal detection of a variety of fluorophores, including different classes of quantum dots and fluorescein. Eventually, a new optical method has been developed to perform turbidity measurements, which shows great potential to characterize bacterial growth and can be used as a drug screening tool to determine antibiotic-resistant bacteria. Overall, the combination of this portable platform and personal smartphone yields a versatile, cost-effective, and user-friendly tool for a variety of optical biosensing applications.

5.6. References

1.   United Nations. *World Population Prospects 2019.*; 2019.

2.   Uniyal S, Paliwal R, Kaphaliya B, Sharma RK. Human Overpopulation. In: *Megacities and Rapid Urbanization*. IGI Global; 2020:20-30. doi:10.4018/978-1-5225-9276-1.ch002

3.   Sandu Z-S, Sukiasyan N. Overpopulation of India: Factors, Implications and Recommendations. *Int J Humanit Art Soc Stud*. 2018;3(2):1-8.

4.   Singh R, Srivastava P, Singh P, Upadhyay S, Raghubanshi AS. Human Overpopulation and Food Security. In: *Urban Agriculture and Food Systems*. IGI Global; 2019:439-467. doi:10.4018/978-1-5225-8063-8.ch022

5.   Baus D. Overpopulation and the Impact on the Environment. *City Universtity New York Acad Work*. 2017.

6.   Liu Y-C, Kuo R-L, Shih S-R. COVID-19: The first documented coronavirus pandemic in history. *Biomed J*. May 2020:1-6. doi:10.1016/j.bj.2020.04.007

7.   Yang X, Sun M, Wang T, Wong MW, Huang D. A smartphone-based portable analytical system for on-site quantification of hypochlorite and its scavenging capacity of antioxidants. *Sensors Actuators, B Chem*. 2019:524-531. doi:10.1016/j.snb.2018.11.131

8.   Bilal M, Iqbal HMN. Microbial-derived biosensors for monitoring environmental contaminants: Recent advances and future outlook. *Process Saf Environ Prot*. 2019;124:8-17. doi:10.1016/j.psep.2019.01.032

9.   Brown K, Secco EL, Nagar AK. A Low-Cost Portable Health Platform for Monitoring of Human Physiological Signals. *Lect Notes Electr Eng*. 2019;532:211-224. doi:10.1007/978-3-030-02242-6_16

10.   Zamora-Sequeira R, Starbird-Pérez R, Rojas-Carillo O, Vargas-Villalobos S. What are the Main Sensor Methods for Quantifying Pesticides in Agricultural Activities? A Review. *Molecules*. 2019;24:1-26. doi:10.3390/molecules24142659

11.   De Bruyne S, Speeckaert MM, Delanghe JR. Applications of mid-infrared spectroscopy in the clinical laboratory setting. *Crit Rev Clin Lab Sci*. 2018;55(1):1-20. doi:10.1080/10408363.2017.1414142

12.   Kim Y, Radoias V. Screening, diagnosis, and long-term health outcomes in developing countries — The case of hypertension. Morrissey K, ed. *PLoS One*. 2018;13(12):1-10. doi:10.1371/journal.pone.0208466

13.   Berg B, Cortazar B, Tseng D, et al. Cellphone-Based Hand-Held Microplate Reader for Point-of-Care Testing of Enzyme-Linked Immunosorbent Assays. *ACS Nano*. 2015;9(8):7857-7866. doi:10.1021/acsnano.5b03203

14.   Wu K, Klein T, Krishna VD, Su D, Perez AM, Wang JP. Portable GMR Handheld Platform for the Detection of Influenza A Virus. *ACS Sensors*. 2017;2:1594-1601. doi:10.1021/acssensors.7b00432

15.   Orth A, Wilson ER, Thompson JG, Gibson BC. A dual-mode mobile phone microscope using the onboard camera flash and ambient light. *Sci Rep*. 2018;8(1):1-8. doi:10.1038/s41598-018-21543-2

16. Perez-Pozuelo I, Zhai B, Palotti J, et al. The future of sleep health: a data-driven revolution in sleep science and medicine. *npj Digit Med*. 2020;42:1-15. doi:10.1038/s41746-020-0244-4

17. de Haan K, Ceylan Koydemir H, Rivenson Y, et al. Automated screening of sickle cells using a smartphone-based microscope and deep learning. *npj Digit Med*. 2020;3(76):1-9. doi:10.1038/s41746-020-0282-y

18. Long F, Li W, Song D, et al. Portable and automated fluorescence microarray biosensing platform for on-site parallel detection and early-warning of multiple pollutants. *Talanta*. 2020;210:1-10. doi:10.1016/j.talanta.2019.120650

19. Shin J, Choi S, Yang J-S, Song J, Choi J-S, Jung H-I. Smart Forensic Phone: Colorimetric analysis of a bloodstain for age estimation using a smartphone. *Sensors Actuators B Chem*. 2017;243:221-225. doi:10.1016/j.snb.2016.11.142

20. Kanchi S, Sabela MI, Mdluli PS, Inamuddin, Bisetty K. Smartphone based bioanalytical and diagnosis applications: A review. *Biosens Bioelectron*. 2018;102:136-149. doi:10.1016/j.bios.2017.11.021

21. Schäfer M, Bräuler V, Ulber R. Bio-sensing of metal ions by a novel 3D-printable smartphone spectrometer. *Sensors Actuators, B Chem*. 2018;255:1902-1910. doi:10.1016/j.snb.2017.08.207

22. de Oliveira HJS, de Almeida PL, Sampaio BA, et al. A handheld smartphone-controlled spectrophotometer based on hue to wavelength conversion for molecular absorption and emission measurements. *Sensors Actuators B Chem*. 2017;238:1084-1091. doi:10.1016/j.snb.2016.07.149

23. Zhang C, Kim JP, Creer M, Yang J, Liu Z. A smartphone-based chloridometer for point-of-care diagnostics of cystic fibrosis. *Biosens Bioelectron*. 2017;97:164-168. doi:10.1016/j.bios.2017.05.048

24. Paterson AS, Raja B, Mandadi V, et al. A Low-Cost Smartphone-Based Platform for Highly Sensitive Point-of-Care Testing with Persistent Luminescent Phosphors. *Lab Chip*. 2017;176(6):1051-1059. doi:10.1016/j.physbeh.2017.03.040

25. Li L, Liu Z, Zhang H, Yue W, Li C-W, Yi C. A point-of-need enzyme linked aptamer assay for Mycobacterium tuberculosis detection using a smartphone. *Sensors Actuators B Chem*. 2018;254:337-346. doi:10.1016/j.snb.2017.07.074

26. Gopinath SCB, Tang TH, Chen Y, Citartan M, Lakshmipriya T. Bacterial detection: From microscope to smartphone. *Biosens Bioelectron*. 2014;60:332-342. doi:10.1016/j.bios.2014.04.014

27. Bast NG, Comenge J, Puntes V. Kinetically Controlled Seeded Growth Synthesis of Citrate-Stabilized Gold Nanoparticles of up to 200 nm: Size Focusing versus Ostwald Ripening. *Langmuir*. 2011;27:11098-11105.

28. Shahjalal MD, Khalid Hasan M, Chowdhury MZ, Jang YM. Smartphone Camera-Based Optical Wireless Communication System: Requirements and Implementation Challenges. *Electronics*. 2019;8(913):1-17. doi:10.3390/electronics8080913

29. ThermoFisher Scientific. ELISA (Enzyme-Linked Immunosorbent Assay). https://www.thermofisher.com/es/es/home/life-science/protein-biology/protein-assays-analysis/elisa.html. Published 2020.

30. Zhdanov A, Keefe J, Franco-Waite L, Konnaiyan KR, Pyayt A. Mobile phone based ELISA (MELISA). *Biosens Bioelectron*. 2018;103:138-142. doi:10.1016/j.bios.2017.12.033

31. Quesada-González D, Merkoçi A. Nanomaterial-based devices for point-of-care diagnostic applications. *Chem Soc Rev*. 2018;47(13):4697-4709. doi:10.1039/c7cs00837f

32. Quesada-González D, Merkoçi A. Nanoparticle-based lateral flow biosensors. *Biosens Bioelectron*. 2015;73:47-63. doi:10.1016/j.bios.2015.05.050

33. Kress N. Actual Impacts of Seawater Desalination on the Marine Environment Reported Since 2001. In: *Marine Impacts of Seawater Desalination*. ; 2019:81-133.

34. Strack R. Harnessing fungal bioluminescence. *Nat Methods*. 2019;16(2):140. doi:10.1038/s41592-019-0311-4

35. Miyashiro T, Ruby EG. Shedding light on bioluminescence regulation in Vibrio fischeri. *Mol Microbiol*. 2013;84(5):795-806.

36. Zhao X, Lu C, Yang S, Zhang J. Bioconjugation of aptamer to fluorescent trimethyl chitosan nanoparticles for bacterial detection. *Mater Lett*. 2020;264:1-3. doi:10.1016/j.matlet.2020.127330

37. Luka G, Samiei E, Dehghani S, Johnson T, Najjaran H, Hoorfar M. Label-free Capacitive Biosensor for Detection of Cryptosporidium. *Sensors*. 2019;19(258):1-9. doi:10.3390/s19020258

38. Sheng E, Lu Y, Tan Y, Xiao Y, Li Z, Dai Z. Ratiometric Fluorescent Quantum Dot-Based Biosensor for Chlorothalonil Detection via an Inner-Filter Effect. *Anal Chem*. 2020;92:4364-4370. doi:10.1021/acs.analchem.9b05199

39. Ma F, Jiang S, Zhang C yang. SiRNA-directed self-assembled quantum dot biosensor for simultaneous detection of multiple microRNAs at the single-particle level. *Biosens Bioelectron*. 2020;157:1-7. doi:10.1016/j.bios.2020.112177

40. Shen J, Li Y, Gu H, Xia F, Zuo X. Recent development of sandwich assay based on the nanobiotechnologies for proteins, nucleic acids, small molecules, and ions. *Chem Rev*. 2014;114(15):7631-7677. doi:10.1021/cr300248x

41. World Health Organization. Antibiotic resistance. https://www.who.int/news-room/fact-sheets/detail/antibiotic-resistance. Published 2020.

CHAPTER 6

Concluding Remarks

The study of different optical approaches (colorimetric, fluorescent, and bioluminescent) implemented into portable sensing devices for the detection of chemical and microbial analytes related to water pollution has been achieved within this work.

Considering the objectives previously described in Chapter 2, along with the obtained results presented from Chapter 3 to Chapter 5, the following specific conclusions on this Ph.D. Thesis can be given:

6.1. *Escherichia coli* detection as a fecal indicator

Lateral flow strips (LFS) have been designed to capture *E. coli* through polyclonal antibodies conjugated to 40 nm-AuNPs in a direct assay. First, lateral flow materials have been tested and optimized for the optimal flow of bacteria based on the flow of *A. fischeri*, a gram-negative bioluminescent bacterium similar in size and shape to *E. coli*. This approach is new and has not been previously reported in the literature. Second, AuNPs have been carefully synthesized and characterized to achieve an optimal size distribution (UV-Vis spectroscopy, TEM, DLS, and Z-potential). Third, LFS have been optimized in terms of the selection of antibodies, different size AuNPs, different concentration of antibodies both in the conjugate pad and in the test line, detection pad materials, and blocking conditions of the detection pad. Fourth, the optimized LFS can detect different strains of *E. coli* and neglect the presence of other related bacteria such as *Salmonella*, showing great potential for the determination of fecal contamination. Fifth, a filtration system allows for improving the sensitivity of the LFS by two orders of magnitude in just 15 minutes. Last, these LFS show great reproducibility and good performance with real samples (i.e. river and sewage waters), yielding recoveries always above 80%.

Briefly, the presented platform can detect *E. coli* species in different water samples at concentrations $\leq 10^4$ CFU/mL within 25 minutes. Besides, the sensitivity of the system can be further improved by incrementing both the filtration time and the amount of water filtered. Nonetheless, these values are still far from those recommended by WHO regarding drinking quality standards (≤ 0 CFU *E. coli*/100 mL). On the other hand, the system has proven to detect *E. coli* in a real case scenario at concentrations between 10^3-10^4 CFU/mL at the end of an urban area drainpipe, showing potential for use in particular locations subjected to continuous sewage discharges.

6.2. Water toxicity assessment

A bioluminescent toxicity biosensor based on the bacterium *Aliivibrio fischeri* has been developed for water toxicity assessment. This system relies on the well-known and commercially available Microtox technology. *A. fischeri* produces bioluminescence according to the number of bacteria alive present in the media, a regulation metabolic mechanism known as quorum sensing. First, bioluminescence has been boosted by growing the bacteria into a specific liquid medium that allows capturing the light with a standard smartphone and a 96-wells plate. Second, bioluminescence can be further improved by growing the bacteria onto agar medium, but the formation of biofilms avoids an appropriate performance of the toxicity assays. Third, two pesticides (tributyltin [TBT] and pentachlorophenol) have been spiked at different concentrations and successfully detected with the smartphone, showing a good correlation with those results obtained with a more sensitive luminometer. Fourth, graphene oxide (GO) was used as a non-specific growth enhancer to reduce the growing time of *A. fischeri* and speed up the whole process. This biocompatibility has been proven by cryo-TEM images that allow watching bacteria thriving in direct contact with GO flakes. Besides, GO can improve the system's sensitivity by screening bioluminescence at a particular concentration range. Overall, the system delves into the quorum-sensing mechanism to boost the bioluminescence of *A. fischeri* and also enhances the sensitivity of the water toxicity biosensor.

Briefly, the sensitivity achieved with *A. fischeri* is still low to detect the maximum allowable concentrations of TBT and pentachlorophenol in water samples according to the EU directives. Nonetheless, toxicity biosensors are useful to assess the overall water toxicity; that's to say, the presence of different chemical products at variable concentrations. In this regard, it is difficult to evaluate the usefulness of this system to assess water toxicity. In any case, Microtox technology, based on lyophilized *A. fischeri* and an ultra-sensitive luminometer, is widely used worldwide, supporting the applicability of our approach. Further improvements should be focused on improving the stability of the bacteria when stored and transported, and the stability of the bioluminescence within time and from batch-to-batch to achieve more reproducible results.

6.3. Portable platform for environmental applications

A portable platform has been developed in combination with a smartphone to perform a variety of different optical assays with several applications in the environmental and health-related fields. The portable platform consists of several components divided into optical, mechanical, and electrical categories. First, an optical lens allows for an optimal focus of the smartphone camera over the samples to be analyzed. Besides, UV and visible light LEDs allow for performing fluorescent and colorimetric assays, respectively. The use of optical filters enables to filter out any background signal produced by the LEDs in the final images. Second, a temperature controlling unit allows for heating and cooling down the samples from 4 ºC to 37 ºC according to the specific needs of the assay. Besides, temperature and humidity sensors have been installed to monitor the conditions within the platform. A mechanical arm has also been installed for agitation of the samples, boosting the capabilities of the platform. Third, all the components are electrically connected within the platform and controlled by an Arduino that is led by a dedicated smartphone app. In this regard, all the components of the portable platform are controlled from your smartphone. Fourth, the integration of all these components allows for performing a great variety of optical assays with several biosensing applications.

Briefly, colorimetric, bioluminescent, fluorescent, and turbidimetric assays have been performed within the portable platform. Two kinds of colorimetric assays have been tested, ELISA tests for the detection of the nucleoprotein of SARS-CoV-2 and human immunoglobulin G and gold aggregation tests for the determination of the nanoparticle aggregation state. These assays can be performed within the platform, the measurements are carried out by the smartphone and the optical analysis is made by the software ImageJ, after careful optimization of the curing of the images. Next, a bioluminescent assay is performed within the platform for the determination of the toxicity of the pesticide pentachlorophenol within water samples. The total opacity of the platform and the tuning of the smartphone camera parameters allow for very sensitive detection of the bioluminescence, comparable to that obtained with the spectrophotometer. In the next step, the detection of fluorescence particles (quantum dots and fluorescein) is carried out in the range from µM to nM thanks to the UV LED and the optical filters installed within the platform. In this regard, the portable platform allows for visualizing different fluorescent colors and

detecting different concentration range by controlling the smartphone camera settings. We also envisaged an application for the detection of these fluorophores by developing a fluorescent ELISA test. However, the final concentration of QDs after the ELISA test was in the range of pM and could only be detected by the spectrophotometer. On the other hand, we took advantage of the shaking capabilities of the portable platform to grow aerobic bacteria within the device. Eventually, a new method to determine turbidimetric changes was developed to evaluate bacterial growth, with applications in the detection of antibiotic-resistant bacteria. Different bacterial strains and species were tested with different antibiotics and the growth inhibition profiles were generated with the smartphone and the portable platform, showing great correlation with the spectrophotometer measurements.

ANNEXES

As annexes are attached the 2 following published articles:

"Validity of a single antibody-based lateral flow immunoassay depending on graphene oxide for highly sensitive determination of *E. coli* O157:H7 in minced beef and river water". Abdel-Rahim H. A. Hassan, **José Francisco Bergua**, Eden Morales-Narváez, Arben Merkoçi. *Food Chemistry*, 2019, 297 (124965), 1-10.

"Low-cost strategy for the development of a rapid electrochemical assay for bacteria detection based on AuAg Nanoshells". Lorenzo Russo, Juan Leva Bueno, **José Francisco Bergua**, Monica Constantini, Marco Giannetto, Víctor Puntes, Alfredo de la Escosura Muñiz, Arben Merkoçi. *ACS Omega*, 2018, 3 (12), 18849-18856.

"Straightforward immunosensing platform based on graphene oxide-decorated nanopaper: a highly sensitive and fast biosensing approach". Nopchulee Cheeveewattanagul, Eden Morales-Narváez, Abdel-Rahin H. A. Hassan, **José Francisco Bergua**, Arben Merkoçi. *Advanced Functional Materials*, 2017, 27 (1702741), 1-8.

Also, the following posters presented at different congresses:

Jie Liu, **José Francisco Bergua**, Eden Morales-Narváez, Jahir Orozco, Ruslan Álvarez-Diduk, Teresa Vincent, Guohua Zhong, Arben Merkoçi. "Fast Screening of Toxic sSbstances using Bioluminescent Nanopaper" – Presented at Globaqua, Barcelona (2017), and also at *International Congress of Analytical Nanoscience and Nanotechnology (IX NyNA)* (2019).

José Francisco Bergua, Chun-Jen Huang. "Improvement of Lateral Flow Strips Performance for Bacteria Detection" – Presented at Ministry of Science and Technology of Taiwan (MOST) (2018).
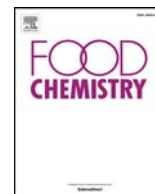
Validity of a single antibody-based lateral flow immunoassay depending on graphene oxide for highly sensitive determination of *E. coli* O157:H7 in minced beef and river water

Abdelrahim Hussein Abdelazeem Hassan[a,b], José Francisco Bergua[a], Eden Morales-Narváez[c], Arben Mekoçi[a,d,*]

[a] *Nanobioelectronics & Biosensors Group, Catalan Institute of Nanoscience and Nanotechnology (ICN2), CSIC and BIST, Campus UAB, Bellaterra, 08193 Barcelona, Spain*
[b] *Department of Food Hygiene and Control, Faculty of Veterinary Medicine, Beni-Suef University, Beni-Suef 62511, Egypt*
[c] *Biophotonic Nanosensors Laboratory, Centro de Investigaciones en Óptica A. C, Loma del Bosque 115, Lomas del Campestre León, Guanajuato 37150, Mexico*
[d] *ICREA, Institució Catalana de Recerca i Estudis Avançats, Pg. Lluís Companys 23, 08010 Barcelona, Spain*

ARTICLE INFO

ABSTRACT

Considering the health risks of *E. coli* O157:H7 presence in food and water, an affordable and highly sensitive detection method is crucial. Herein, we report the first use of a single antibody-based fluorescent lateral flow immunoassay (FLFIA) depending on non-radiative energy transfer between graphene oxide and quantum dots for determination of *E. coli* O157:H7 in beef and river water. FLFIA showed a high sensitivity rate thousand-fold better than the conventional lateral flow (LF). In inoculated minced beef and river water samples, the limits of detection were 178 and 133 CFU g^{-1} or mL^{-1}, respectively. Besides, it presented a high selectivity in the presence of other possible interfering bacteria. The single antibody approach reduced the assay cost to 60% less than the conventional LF. Alongside, the results could be read by portable LF readers or smartphones. These advantages offer FLFIA as a promising technology for pathogen detection in food and water.

1. Introduction

Foodborne and waterborne pathogens, mostly bacteria, may get into our bodies through contaminated food and water leading to several health disorders varying from mild diarrhoea to death, and great losses in productivity as well. *E. coli* O157:H7 is the most frequently reported serotype of Shiga toxins-producing *E. coli* (STEC) in foodborne-linked hospitalizations and deaths in the United States (Scallan et al., 2011). Beef has been incriminated in most food infection outbreaks by *E. coli* O157:H7 (CDC, 2009). However other sources such as drinking water, dairy products and vegetables were previously reported as well (Islam, Doyle, Phatak, Millner, & Jiang, 2004; Lorusso et al., 2011; Olsen et al., 2002; Tsiraki et al., 2018). The health problems that could be induced by *E. coli* O157:H7 infection range from mild watery diarrhoea to life-threatening conditions such as haemolytic uremic syndrome and

haemorrhagic colitis especially in children and the elderly (Jay, 2000). Considering the health risks of *E. coli* O157:H7 and its impact on food safety, rapid, affordable and highly sensitive methods of detection are necessary to monitor food and water contamination to protect the consumers from the danger of that foodborne hazard.

The currently available methods of *E. coli* O157:H7 detection that depend on culturing and then biochemical and serological examination usually take a couple of days to be completed, while molecular biology-based techniques might be required for confirmation of the results. Nevertheless, such conventional methods are reliable and quite accurate, they are not user-friendly as they require well-trained technicians, and relatively sophisticated laboratory equipment, as well as their high costs (Johnson, Brooke, & Fritschel, 1998; Ngwa, Schop, Weir, León-Velarde, & Odumeru, 2013; Zhou et al., 2018). Immunoassays became one of the most popular approaches in analytical determination of
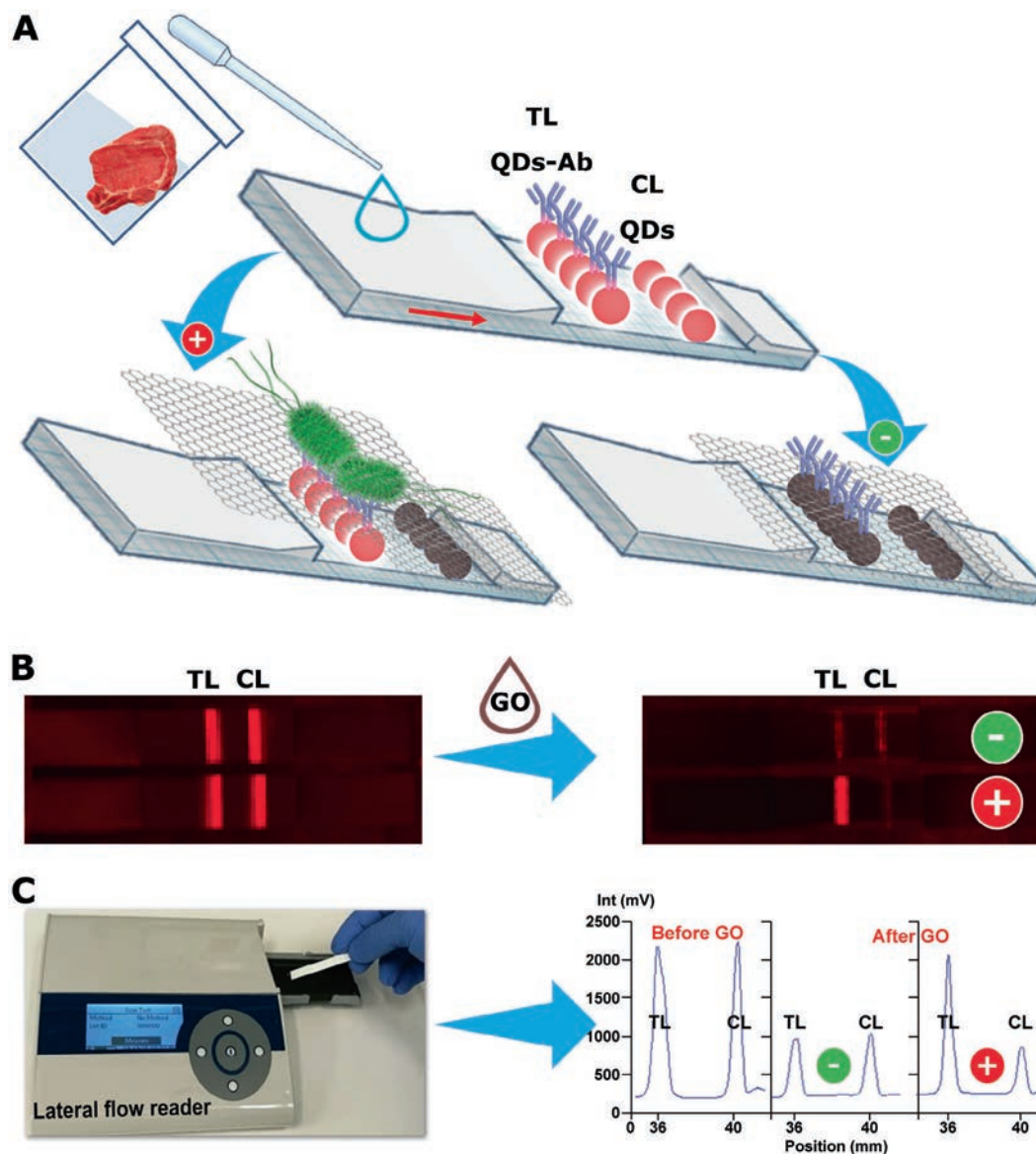
Fig. 1. Fluorescent lateral flow immunoassay (FLFIA) principle and reading. A) FLFIA strip is composed of a sample pad, detection part and an absorbent pad. The detection part of FLFIA strip is composed of a test line TL (Streptavidin-Quantum dots conjugated with biotinylated anti-*E. coli* O157:H7 antibody "QDs-Ab") and a control line CL (bare quantum dots "QDs"). When a beef extract or water sample is added to the sample pad of FLFIA strip, it flows by capillary force towards the absorbent pad. If the sample contains *E. coli* O157:H7, the bacteria will be captured by specific antibody-QDs conjugate on the TL. Afterwards, graphene oxide GO is added onto the sample pad. *E. coli* O157:H7 captured on the TL acts as a spacer between GO and QDs and interrupts the non-radiative energy transfer between them, and this keeps the fluorescence of QDs. On the other hand, the absence of the target bacteria allows the non-radiative energy transfer between GO and QDs on the TL and consequently, quenches the fluorescence of QDs. B) Scanned images with a fluorescence Typhoon reader of two FLFIA strips. Before addition of GO, both TL and CL are fluorescing in both strips. However, after addition of GO, both TL and CL are quenched in negative sample, while, TL of positive sample is still fluorescing. C) Another option of reading the assay is measuring TL and CL intensities by a portable fluorescence lateral flow reader. The measured fluorescence intensities (mV) of both TL and CL, before and after addition of GO to the strip clarify the difference between positive ($+$) and negative ($-$) samples.

countless kinds of pathogens in various samples, since they are moderately sensitive and selective. Nonetheless, immunoassays such as ELISA and microarrays are laboratory-based techniques that require multiple complex procedures to be done by well-trained operators, as well as they detect *E. coli* O157:H7 in food at a limit of detection (LOD) ranges from 10^5 to 10^6 colony forming units per mL or g (CFU mL^{-1} or g^{-1}) or even higher (Firstenberg-Eden & Sullivan, 1997; Arbault, Buecher, Poumerol, & Sorin, 2000; Shen et al., 2014; Zhaohui, Chunyang, Yingchun, & Yanbin, 2017; Kim, Jo, Mun, Noh, & Kim, 2018). Conversely, lateral flow (LF) immunoassays are one of the most important analytical tools nowadays, since they are simple, robust, portable, and rapid devices. Though, those conventional LF immunoassays-which based on gold nanoparticles, latex beads, or

quantum dots as labels-always need three antibodies; one for capturing the bacteria (conjugate pad antibody), a second one for detecting the bacteria (test line antibody), and a third one as a control line antibody, which means extra costs spent by such devices (Berg et al., 2015; Kim et al., 2018; Zhang et al., 2015). Moreover, their LOD of *E. coli* O157:H7 in water and minced beef is about 10^5 CFU mL^{-1} or g^{-1} (Hassan, de la Escosura-Muñiz, & Merkoçi, 2015). However, it has been assumed that exposure to < 100 cells of *E. coli* O157:H7 is enough to induce infection in humans. As the Food and Agriculture Organization of the United Nations and the World Health Organization (FAO/WHO, 2008) reported numerous food poisoning outbreaks by *E. coli* O157:H7 at doses as low as 5 CFU/g of food. So, they stated that the presence of *E. coli* O157:H7 at or above one CFU/25 g constitutes a risky food commodity.

Accordingly, the detection of this dangerous pathogen by conventional LF assays might result valueless in particularly demanding contexts. Consequently, the food and environment hygienists are in need to another simple, portable and rapid device that must be affordable, highly sensitive, and highly specific for rapid *in-situ* determination of *E. coli* O157:H7 in complex food matrices under the field conditions.

Our group has been studying the quenching capabilities of graphene oxide (GO) based on the fluorescence resonance energy transfer (FRET), and its interaction with photoexcited quantum dots (QDs) (Cheeveewattanagul et al., 2017; Morales-Nárvaez & Merkoçi, 2012; Morales-Nárvaez, Hassan, & Merkoçi, 2013; Morales-Nárvaez, Naghdi, Zor, & Merkoçi, 2015; Zamora-Gálvez, Morales-Nárvaez, Romero, & Merkoçi, 2018). We had previously patented a highly sensitive pathogen-detection device for the sensing of *E. coli* in a standard buffer (Merkoçi & Morales-Nárvaez, 2015; Morales-Nárvaez et al., 2013). However, using a traditional glass slide-based microarray system as a biosensing platform was quite expensive and not suitable for portability. Therefore, paper-based lateral-flow assay was another low-cost option in another study done by our group (Morales-Nárvaez et al., 2015). While, that study was limited to the detection of general *E. coli* in buffer and bottled water by using QDs/anti-*E. coli* antibody. Although, assessment of the validity of this GO-based LF immunoassay for detection of pathogenic *E. coli* O157:H7 in real samples of highly complex matrices such as minced beef and river water is another hot topic worthy to be investigated, since those samples are the main source of human infections by that pathogen.

Herein, we report the first exploit of FRET-based quenching properties of GO, and their interaction with QDs for development of a fluorescent lateral flow immunoassay (FLFIA) for determination of the highly pathogenic *E. coli* O157:H7 in minced beef and river water. The detection part of that strip has two lines; a test line (TL) which composed of CdSe@ZnS QDs/anti-*E. coli* O157:H7 antibody that works as a fluorescent probe and a control line (CL) that composed of only bare QDs. GO is added to the LF strip as a quencher for the fluorescent QDs after adding the sample to divulge the presence of bacteria. If the sample does not have *E. coli* O157:H7, the test line will be efficiently quenched when adding GO by FRET, since the distance between QDs/Abs (donor) and GO (acceptor) is few nanometres (Gaudreau et al., 2013; Lin et al., 2013). On the other hand, if the sample has *E. coli* O157:H7, it will be selectively captured by the specific QDs/Abs probe on the test line, then after adding GO, resonance energy transfer is hindered or minimally occurs since the distance between GO and QDs exceeds to more than 20 nm by the bacteria interference (Gaudreau et al., 2013; Lin et al., 2013). Consequently, the fluorescence of QDs on the test line is maintained, and its intensity is correlational to the concentration of the *E. coli* O157:H7 in the sample. Instead, the control line QDs will be always quenched by GO because this line has not any antibodies to the target pathogen. The principle and reading of FLFIA is fully illustrated in Fig. 1.

2. Materials and methods

2.1. Reagents and equipment

All commercial reagents were of analytical grade and they were handled according to the safety data sheets provided by the suppliers. Goat polyclonal Anti-*Escherichia coli* O157:H7 antibody (conjugated with biotin) (LS-C525826-100) was purchased from LifeSpan BioSciences (Seattle, WA, USA), and streptavidin-conjugated CdSe/ZnS quantum dots 655 (QDs) (Cat. No. Q10121MP) were obtained from Life Technologies (Carlsbad, CA, USA). Phosphate buffered saline (PBS) (PubChem CID: 24978514), bovine serum albumin (BSA), and Tween-20 (PubChem CID: 443314) were purchased from Sigma-Aldrich (Madrid, Spain). Graphene oxide (GO) was bought from Angstron Materials (Ohio, U.S.A.). *Escherichia* coli O157:H7 (CECT 4783, *E. coli* O157:H7) and *Salmonella* enterica subsp. enterica serovar Typhimurium

LT2 (CECT 722T, *S.* Typhimurium) strains were obtained from the Colección Española de Cultivos Tipo (CECT, Valencia, Spain). TS-100 Thermo-Shaker (Biosan, Riga, Latvia) was used as a stirrer for modification of QDs with antibodies. Laminated cards (HF000MC100), nitrocellulose membranes (SHF1800425), and cellulose fibre (CFSP001700) that were used for fabricating FLFIA strips were purchased from Millipore (Billerica, MA, USA). An IsoFlow reagent dispensing system (Imagene Technology, Hanover, NH, USA) was used for dispensing the TL and CL onto the nitrocellulose membrane. A Dahle 533 guillotine (Dahle, Peterborough, NH, USA) was used to cut the FLFIA strips into 6 mm width. JP Selecta 2000210 oven from JP selecta (Barcelona, Spain) was used to dry the strips. A portable ESEQuant lateral flow reader with its software LF-Studio Version 3.3.6 from Qiagen GmbH (Stockach, Germany) were used to measure the intensities of the TL and CL of FLFIA strips. As well as, fluorescent images of FLFIA strips were produced using a Typhoon 9410 Variable Mode Imager (GE, Freiburg, Germany). The intensities of the lines of those fluorescent images were measured using ImageJ 1.46r (Wayne Rasband, National Institutes of Health, Bethesda, MD, USA). PBS (10 mM, pH 7.4) with 0.5% (v/v) Tween-20 containing 1% of BSA fraction V (w/v) was employed as a standard buffer for preparation of bacterial inocula. While, PBS (10 mM, pH 7.4) with 0.05% (v/v) Tween-20 was used as a washing buffer. All aqueous solutions were freshly prepared in Milli-Q water produced using a Milli-Q system (> 18.2 MΩcm^{-1}) purchased from Millipore (Billerica, MA, USA). Scanning Electron Microscopy (SEM) images were obtained by a Magellan 400L High-Resolution SEM (FEI, Hillsboro, OR, USA).

2.2. Preparation of minced beef extract and bacterial inocula

Minced beef was purchased from a local retail market in Barcelona and analysed by the standard culturing method for the presence of *E.* coli O157 (ISO 4:1665, 2001). Only negative samples of beef and water were selected to be inoculated with bacteria. Twenty-five g of *E. coli* O157-free minced beef were homogenized in a sterile stomacher bag with 225 mL of sterile PBS (10 mM, pH 7.4) using a stomacher (Lab Blender 400, Seward, UK) for 3 min. Then the filtrate was used as a diluent for preparation of bacterial suspensions.

For preparation of bacterial inocula, freeze-dried cultures of *E. coli* O157:H7 and *Salmonella* Typhimurium were revived in a sterile tryptone soy broth (TSB, Oxoid Ltd., UK) and incubated at 37 °C for about 24 h, then transferred onto sterile tryptone soy agar (TSA, Oxoid Ltd., UK) plates for another 24 h at 37 °C. Stock cultures of both strains were kept on TSA slope tubes for future use. Bacterial cell suspensions were prepared directly from bacterial colonies of TSA plates, during the logarithmic phase, in sterile standard buffer and river water to obtain a bacterial load of 1.5×10^8 CFU mL^{-1} according to McFarland standards (McFarland, 1907) using Densimat densitometer (Biomerieux, Brazil). Afterwards, ten-fold decimal bacterial dilutions ($10–10^8$ CFU mL^{-1}) were prepared from the original one. Finally, heat killing of the bacteria was done by putting the bacterial suspension in tightly sealed tubes to be placed in a water bath at 80 °C for 15 min to stop bacterial replication. Regarding minced beef, a suitable volume of heat-killed bacterial suspension in a sterile standard buffer (1.5×10^8 CFU mL^{-1}) was used to prepare ten-fold decimal dilutions of *E. coli* O157:H7 in minced beef homogenate ($10–10^8$ CFU g^{-1}). The prepared bacterial dilutions were stored at 4 °C until being used for the assay within two weeks in case of standard buffer and river water. Whereas inoculated minced beef was used without delay to avoid sample deterioration.

2.3. Fabrication of FLFIA

The proposed lateral flow strips were prepared as follows: (a) assembling of the nitrocellulose membrane on the laminated card. (b) Dispensing the QDs/anti-*E. coli* O157:H7 as a TL and bare QDs as a CL using an IsoFlow reagent dispensing system on the nitrocellulose

membrane. For TL, we used a conjugate composed of 4 nM streptavidin-quantum dots 655 and 300 µg/mL biotinylated anti-*E. coli* O157:H7 polyclonal antibody in standard buffer. The conjugate was prepared through mixing them at 650 rpm/4 °C/30 min. Whereas for CL, we used only 4 nM of streptavidin-quantum dots 655. After line dispensing, the detection pad was kept overnight inside a tightly closed container in the fridge at 4 °C temperature. In the second day, the nitrocellulose membrane (2.5 × 20 cm) was homogenously treated with 5 mL of standard buffer, then kept in the fridge for 15 min before drying in the oven at 37 °C for about 3 h. (c) Some pieces of cellulose sample and absorbent pads (≈20 cm each) were saturated sequentially with Milli-Q water, and standard buffer, then they were kept in the oven at 37 °C for overnight until complete dryness. (d) Afterwards, assembling the sample and absorbent pads on the same laminated card. (e) Ultimately, cutting the assembled card using a clean guillotine into strips of 6 mm in width. The strips were kept in a tightly closed plastic container with some drying pearls in the fridge until use for bacteria determination.

2.4. Using FLFIA for E. coli O157:H7 detection in standard buffer

In order to use the prepared FLFIA strips for detection and quantification of *E. coli* O157:H7 in various samples, the initial photoluminescence intensities (I_1) of both TL and CL were measured using a portable lateral flow reader (Fig. 1C). Then 100 µL of previously prepared *E. coli* O157:H7 suspension of various concentrations in standard buffer was added onto the sample pad of the fabricated strip, the strips were left for about 15 min until complete flow of the sample to the absorbent pad. Afterwards, 100 µL of PBS with 0.05% tween 20 (v/v) was dispensed on the sample pad as a washing buffer, to remove any kind of intervention. Then, they were left at room temperature for around 10 min until complete flow of the washing buffer. Subsequently, 100 µL of aqueous solution of graphene oxide (GO) 150 µg mL^{-1} contains 0.1% Tween-20 (v/v) was dispensed on the sample pad, for revealing the presence of bacteria. A final step of dryness was done before reading the final photoluminescence intensities (I_2) of both lines using the LF reader. The ratio of the final intensity to the initial one (I_2/I_1) of the test line (R_{TL}) was used as an estimation for the concentration of the target bacteria in the sample.

2.5. Validation of FLFIA in real samples

To evaluate the overall performance of the proposed assay in real samples, artificially inoculated minced beef and river water with serial concentrations of *E. coli* O157:H7 (0, 50, 10^2, 10^3, 10^4, 10^5, and 10^6) CFU g^{-1}/mL^{-1} were used. The same abovementioned procedure used with standard buffer was conducted with real samples as well. Calibration curves were created for each sample type at decimal concentrations of bacteria. The linear regression and coefficient of determination (R^2) were calculated for both minced beef and river water.

Furthermore, spike and recovery experiment was conducted to distinguish how much the complex matrix of real sample could affect the performance of our FLFIA. Two concentrations of *E. coli* O157:H7 (10^3 and 10^4 CFU mL^{-1} or g^{-1}) were spiked in each of standard buffer, minced beef, and river water. At least 3 replicates were used in each concentration. The average R_{TL} of spiked minced beef and river water was compared to that of standard buffer at the same concentration to estimate the recovery percentage according to the following equation; recovery % = R_{TL} of real sample/R_{TL} of standard buffer.

As well as, the specificity of FLFIA against non-specific pathogen was tested. *Salmonella* enterica subsp. enterica serovar Typhimurium (*S.* Typhimurium), a Gram-negative pathogen from the same *Enterobacteriaceae* family of *E. coli* O157:H7, was used to conduct the specificity test. In this experiment, we evaluated the response of FLFIA to the presence of *S.* Typhimurium either alone or in a mixture with *E. coli* O157:H7, as well as it was compared with blank buffer. Blank (0 CFU mL^{-1}), single *S.* Typhimurium (10^4 CFU mL^{-1}), single *E. coli*

O157:H7 (10^2 and 10^4 CFU mL^{-1}), and two mixtures of both bacterial species (*E. coli* O157:H7 10^2 + *S.* Typhimurium 10^4 and *E. coli* O157:H7 10^4 + *S.* Typhimurium 10^2 CFU mL^{-1}) were prepared in standard buffer to conduct such experiment.

Additionally, the reproducibility of the assay was evaluated by estimating the variation coefficient through calculating the relative standard deviation (RSD %) along different batches of FLFIA strips used throughout the study.

3. Results and discussion

3.1. Optimization of fluorescence and quenching process

Since the currently available conventional LF immunoassays based on gold nanoparticles or latex beads used for *E. coli* O157:H7 detection in various food and water samples are of high costs (≈ 0.30 USD/test strip) and low sensitivity (≈10^5 CFU mL^{-1} or g^{-1}) (Han et al., 2018; Hassan et al., 2015; Karakus & Salih, 2013; Luo et al., 2017), the food and water monitoring may require another simple, portable, affordable and highly sensitive device. Herein, we designed a novel fluorescent lateral flow immunoassay based on the interaction between photo-excited molecules and quencher. We exploited streptavidin functionalized CdSe@ZnS QDs, of an approximate diameter of 14 ± 2 nm and a maximum emission wavelength at ≈665 nm, as donors of non-radiative energy that makes them a powerful fluorescence agent. As well as, we used GO sheets in the form of water-based dispersion of an average lateral dimension range of 500 nm, an average thickness of approximately 1.1 nm and C/O ratio of about one unit (according to manufacturer's data), as acceptors for the non-radiative energy leading to highly effectual quenching of fluorescence (Morales-Narváez et al., 2013). SEM images illustrated in Fig. 2C and C1 show GO sheets in water suspension surrounding to *E. coli* O157:H7 cells. In addition, Fig. 2C2 shows bare GO suspension of the same concentration. Since the distance between the QDs and GO is very crucial for non-radiative energy transfer between them as Lin et al. (2013) recorded that quenching is not strongly observable at distances greater than 20 nm, so here the target bacteria (≈0.5 × 2 µm size) acts as a spacer between the donor and the acceptor hindering the photons transfer and keeping the fluorescence of QDs. Fig. 2D shows a SEM micrograph of QDs-Ab conjugates are capturing to bacterial cells of *E coli* O157:H7.

To get the most suitable photoluminescence, different concentrations of QDs (1.5, 3, 4, 6, 8, 9, and 10 nM) were dispensed on nitrocellulose membranes and their intensities were measured by a portable LF reader (data not shown). The LF reader used in this study has an excitation wavelength of 365 nm, and an emission filter of about 670 nm. Hence, 4 nM was chosen as the appropriate concentration that gives about 80% of the dynamic range of the reader (Fig. 1C). Additionally, since the concentration of the acceptor molecules should affect the rate of photons transfer from the donor to the acceptor, so, different concentrations of GO suspension in Milli-Q water (60, 70, 80, 100, 150 and 200 µg mL^{-1}) with two concentrations of Tween-20 (0.05 and 0.1%) were investigated to optimize the most suitable quenching conditions. The presence of Tween-20 in the GO suspension aids the process of GO flow through the nitrocellulose. A hundred µL of each concentration was added onto a blank strip, the TL and CL intensities were measured before and after addition of GO. The degree of quenching (I_2/I_1) was calculated by dividing the final intensity (I_2) by the initial one (I_1). GO 150 and 200 µg mL^{-1} with 0.1% Tween-20 (v/v) achieved the highest quenching rates (I_2/I_1 ≈0.3–0.4) (Fig. 3A). However, GO 150 µg mL^{-1} with 0.1% Tween-20 (v/v) was preferred because it achieved the most reliable results afterwards, in terms of steady performance and error rate. In conclusion, 4 nM QDs and GO 150 µg mL^{-1} with Tween-20 (0.1% v/v) were the most appropriate condition for proper photoluminescence and quenching of blank strips.

Since bacterial cells are much bigger (≈0.5 × 2.0 µm, Fig. 2A) than other analytes like proteins, a nitrocellulose membrane with big pore
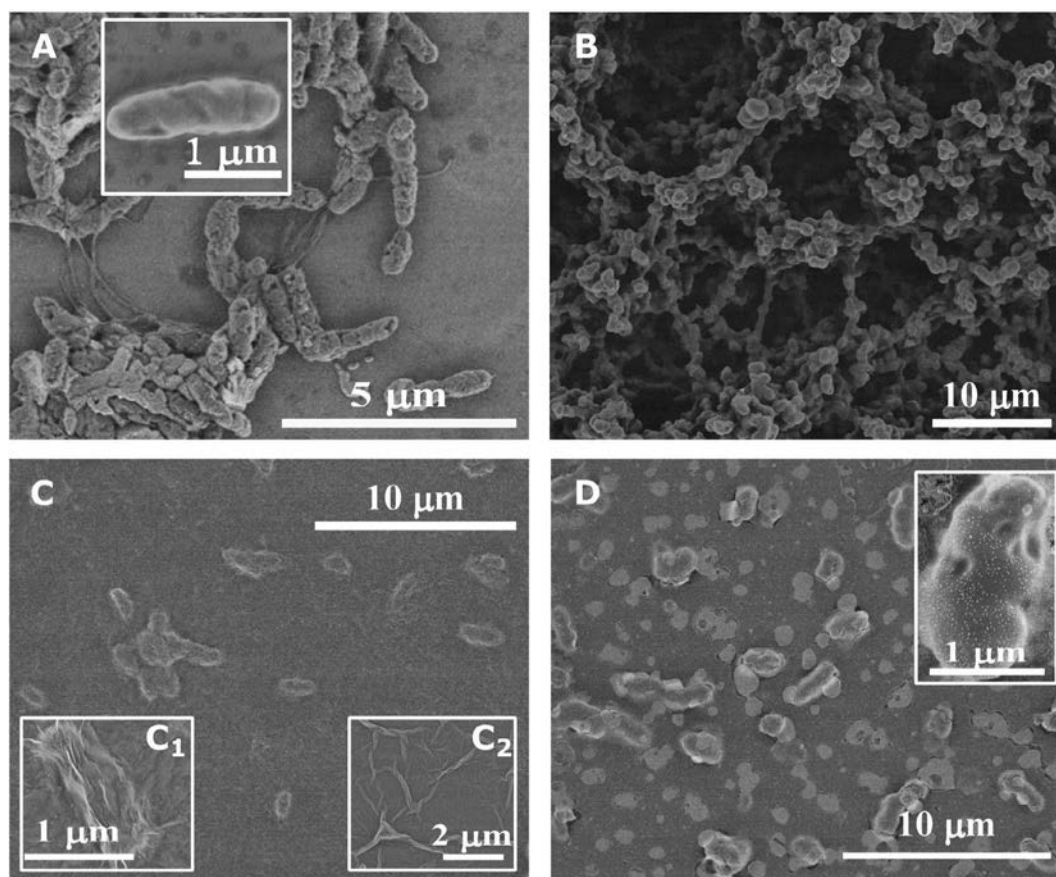
Fig. 2. Scanning electron micrographs. A) Heat-killed *E. coli* O157:H7 (10^5 CFU mL^{-1}) in standard buffer (10 mM PBS with 0.5% Tween-20 and 1% BSA). B) Bare nitrocellulose membrane (Hi-Flow 180, SHF1800425) used for development of detection part of strip. C) GO sheets (150 µg mL^{-1} with 0.1% Tween 20) suspended in Milli-Q water, coating *E. coli* O157:H7 cells. C$_1$) A magnified SEM image of *E. coli* O157:H7 cell is surrounded by GO sheets, C$_2$) Bare GO sheets. D) QDs-anti-*E. coli* O157:H7 antibody conjugates are capturing to heat-killed *E. coli* O157:H7 cells in standard buffer.

size (the diameter of the largest pore in the filtration direction) was essential for our proposed assay. Moreover, there is an inverse relationship between the flow rate and sensitivity of the assay, that means slow flow rate should give highly sensitive assays, because it allows longer time of interaction between the antibody and the target analyte, while fast flow rate reduces the sensitivity. Thus, to develop a highly sensitive assay for a big analyte like bacteria, Hi-Flow 180 nitrocellulose membrane (SHF1800425) of slow flow rate (≈ 180 s/4 cm) was chosen out of others to develop our assay. Fig. 2B demonstrates SEM image of HF 180 nitrocellulose membrane used in this study, it proves that the pore size (≈ 8–20 µm) is big enough to allow the proper flow of bacteria. Besides, it shows the difficulty of distinguishing between bacterial cells and nitrocellulose tissue by SEM. So, all SEM images of bacterial cells (Fig. 2A, C and D) were prepared on silicon discs not on nitrocellulose. The total cost of each strip of this fluorescent lateral flow assay was previously estimated to be ≈ 0.12 USD (Zamora-Gálvez et al., 2018), which is considered about 60% less than that of conventional lateral flow strip.

3.2. Optimization in standard buffer

To evaluate the overall performance of the proposed FLFIA, serial concentrations of *E. coli* O157:H7 (0, 10^2, 10^3, 10^4, 10^5 and 10^6 CFU mL^{-1}) in standard buffer were investigated. A hundred µL of each concentration was loaded onto the sample pad of FLFIA strips, then followed by 100 µL of GO 150 µg mL^{-1} with Tween 20 (0.1% v/v). A drying step of the strips for almost an hour in an oven at 35 °C before reading them using a portable lateral flow reader was essential because QDs have better photoluminescence capabilities in the solid phase than

the liquid one (Shi et al., 2010). Afterwards, the ratio of the final intensity of TL (I_2, after addition of GO) to the initial one (I_1, before addition of the sample) was calculated and used as an indicator to the presence or absence of *E. coli* O157:H7. We refer to it in this paper as $R_{TL} = I_2/I_1$ of TL. As high R_{TL} (close to one) indicates low quenching rate and high concentration of bacteria, whereas low R_{TL} (close to zero) indicates high quenching rate and low concentration or absence of bacteria. On the other hand, I_2/I_1 of CL = R_{CL} should be unchangeable with varying bacteria concentrations, since there are not any antibodies on the CL. However, CL is essential to prove the successful flow of GO along the strip. The obtained results showed an elevation in R_{TL} with increasing the concentration of bacteria in the standard buffer, which means that the target *E. coli* O157:H7 is captured by the specific antibody of TL (anti-*E. coli* O157:H7). However, a similar phenomenon was observed in R_{CL} as well. That indicates some bacterial cells halt over CL and act as a spacer between GO and QDs there, thus leading to nonspecific response of CL (Fig. 3B). Therefore, a washing step with 100 µL of PBS with 0.05% Tween 20 (v/v) by dispensing onto the sample pad after complete flow of the bacteria-containing buffer along the strip (approximately after 15 min) was suggested to remove any kind of nonspecific response before addition of GO.

Obviously, this washing step has improved greatly that issue of nonspecific response of CL, leading to almost constant R_{CL} with varying concentrations of *E. coli* O157:H7 in the buffer (Fig. 3C), while R_{TL} increased progressively with increasing the concentration of bacteria (from zero to 10^5 CFU mL^{-1}) and in a logarithmic manner from 50 to 10^5 CFU mL^{-1} with R^2 equals 0.9874. Then this response slightly decreased in concentrations higher than 10^5 CFU mL^{-1} (Fig. 4A, 4B). This decline behaviour in response could be attributed to blocking the
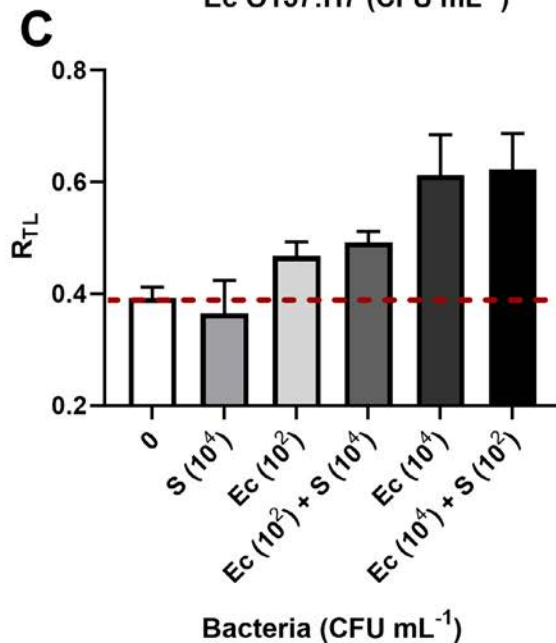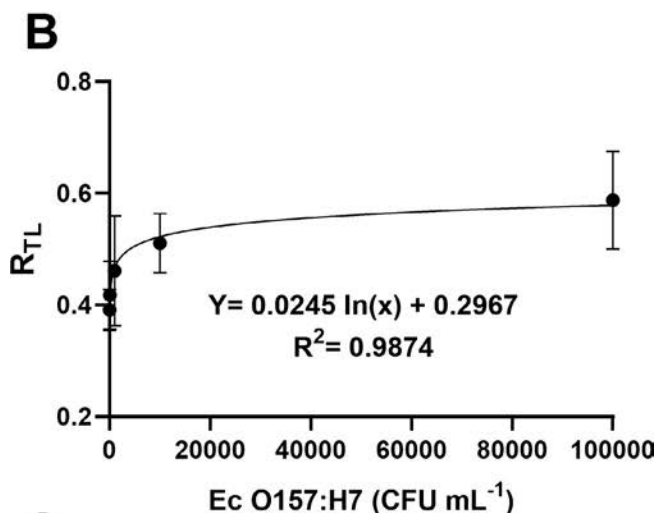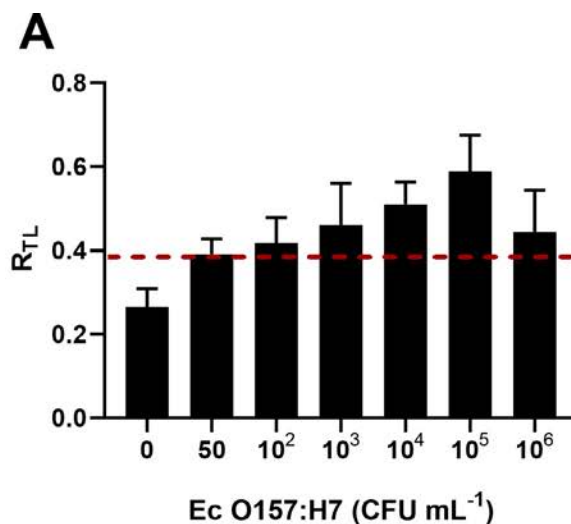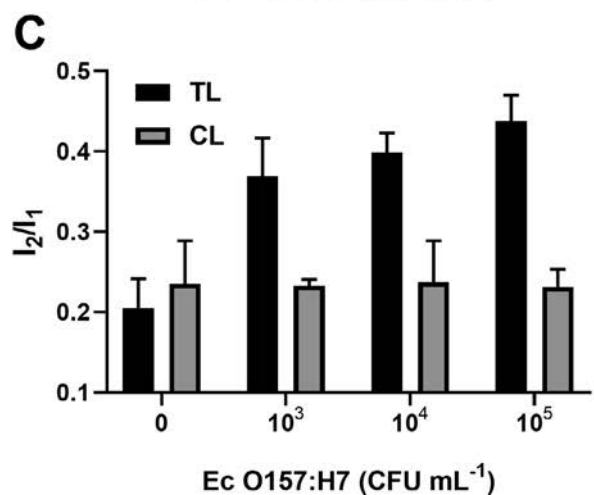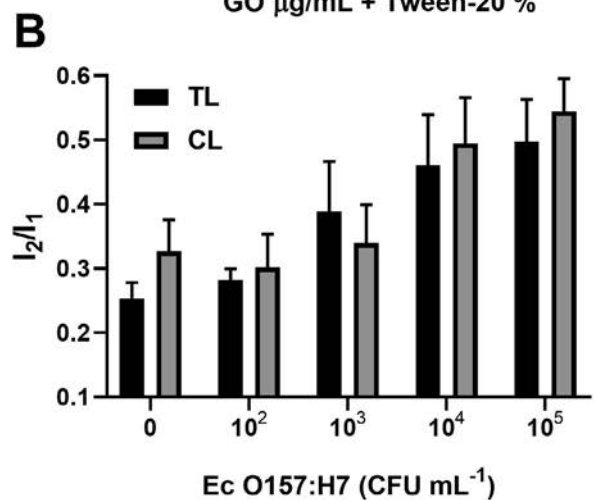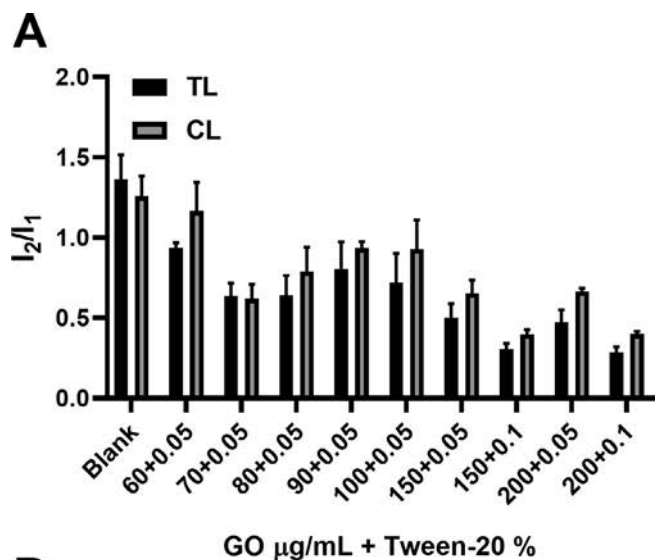
Fig. 3. A) Optimization of the quenching process of QDs. Different concentrations of graphene oxide (GO) suspension in Milli-Q water with Tween-20 were investigated to achieve the optimum quenching conditions of both test line (TL) and control line (CL) by measuring the ratio of the final intensity to the initial one (I_2/I_1) of lines. It shows that GO 150 and 200 $\mu g\,mL^{-1}$ with 0.1% Tween-20 are the most quenching conditions. B) and C) The significance of using a washing buffer after sample loading to remove nonspecific reaction. B) Without washing step, the initial optimization process exhibited a nonspecific accumulation of the bacterial cells on the CL. The I_2/I_1 of CL is increasing with bacterial concentration like the TL. C) Conversely, with a washing step, nearly constant I_2/I_1 of control lines were obtained regardless the bacterial concentrations in the sample. The error bars represent the standard deviation of at least 3

(caption on next page)

Fig. 4. A) Overall response of FLFIA to various concentrations of *E. coli* O157:H7 in standard buffer. Ratio of test line intensity (R_{TL}) = final intensity/ initial intensity of TL. B) Logarithmic response of FLFIA to *E. coli* O157:H7 (Ec O157:H7) concentrations from 50 to 10^5 CFU mL^{-1} in standard buffer. C) Specificity test against higher and lower concentrations of non-specific pathogen (*Salmonella* Typhimurium, S) either alone or in presence of the target pathogen, *E. coli* O157:H7 (Ec) were investigated. The dashed red lines (A and C) represent the limit of detection of *E. coli* O157:H7 in standard buffer by FLFIA ($\approx$ 57 CFU/mL), which was estimated as the mean value of blank buffer R_{TL} plus three times its SD. The error bars represent the standard deviation of at least 3 replicates.

nitrocellulose membrane by the enormous number of bacteria that lead to hindering the bacterial flow. A similar phenomenon was previously reported by some literatures such as Hassan et al. (2015) who reported a decline behavior in commercial gold nanoparticles-based lateral flow kits for *E. coli* O157:H7.

To estimate the sensitivity of FLFIA for detection of *E. coli* O157:H7 in standard buffer, the mean R_{TL} of blank samples plus 3 times its standard deviation (SD) was calculated and used to determine the limit of detection (LOD) of the assay. Fascinatingly, the estimated LOD of FLFIA was calculated to be 57 CFU mL^{-1} of *E. coli* O157:H7 in standard buffer (Fig. 4A). This achieved LOD by our assay was about thousand-fold better than the conventional lateral flow assays (LOD $\approx$ 10^5 CFU mL^{-1} or g^{-1}) that depend on a sandwich-type immunoassay on the TL and a third Ab on the CL (Han et al., 2018; Hassan et al., 2015; Karakus & Salih, 2013; Luo et al., 2017). However, the proposed FLFIA requires only one antibody on the TL and without any antibodies on the CL.

3.3. Specificity of FLFIA

The specificity of immunoassays is another crucial parameter of any innovative approach. The obtained results summarized in Fig. 4C showed that the average R_{TL} produced by *S.* Typhimurium (10^4 CFU mL^{-1}) was lower than the blank's one. Equally, the mixture of *E. coli* O157:H7 10^2 + *S.* Typhimurium 10^4 CFU mL^{-1} gave a response similar to *E. coli* O157:H7 10^2 CFU mL^{-1}. Likewise, *E. coli* O157:H7 10^4 + *S.* Typhimurium 10^2 CFU mL^{-1} and *E. coli* O157:H7 10^4 CFU mL^{-1}. That experiment proved the high selectivity of the proposed FLFIA to the target pathogen (*E. coli* O157:H7), without any interferences from non-specific bacteria present in the same medium.

3.4. Using FLFIA for determination of E. coli O157:H7 in real samples

Even though, investigation of the performance in standard buffer is quite important for the optimization process, the evaluation in complex matrices is vital for validation of new methods. The data illustrated in Fig. 5 summarize the performance in real samples. The obtained results in minced beef and river water showed a similar scenario to that of standard buffer. As R_{TL} elevated regularly in a logarithmic response in concentrations from 50 to 10^5 CFU g^{-1}/mL^{-1}, with R^2 equals 0.9592 and 0.9542 in minced beef and river water samples, respectively. Then the response slightly declined in concentrations higher than 10^5 CFU g^{-1}/mL^{-1} in both sample types, however, it is still within the positive range. The same decline behaviour in response to high concentrations happened with standard buffer, which confirms that this behaviour is due to the blockage of flow by the vast bacterial number in higher concentrations.

LOD of FLFIA in minced beef and river water was estimated by calculating the averages R_{TL} of FLFIA strips tested with at least 3 replicates of blank minced beef and blank river water plus 3 times their SD. The obtained LOD in minced beef samples was *ca.* 178 CFU g^{-1}, while it was *ca.* 133 CFU mL^{-1} in river water ones (Fig. 5A). The reduced sensitivity in minced beef and river water than standard buffer is attributed to the matrix effect of real samples. Similar effect of the sample matrix on immunoassays were previously reported by Aydin
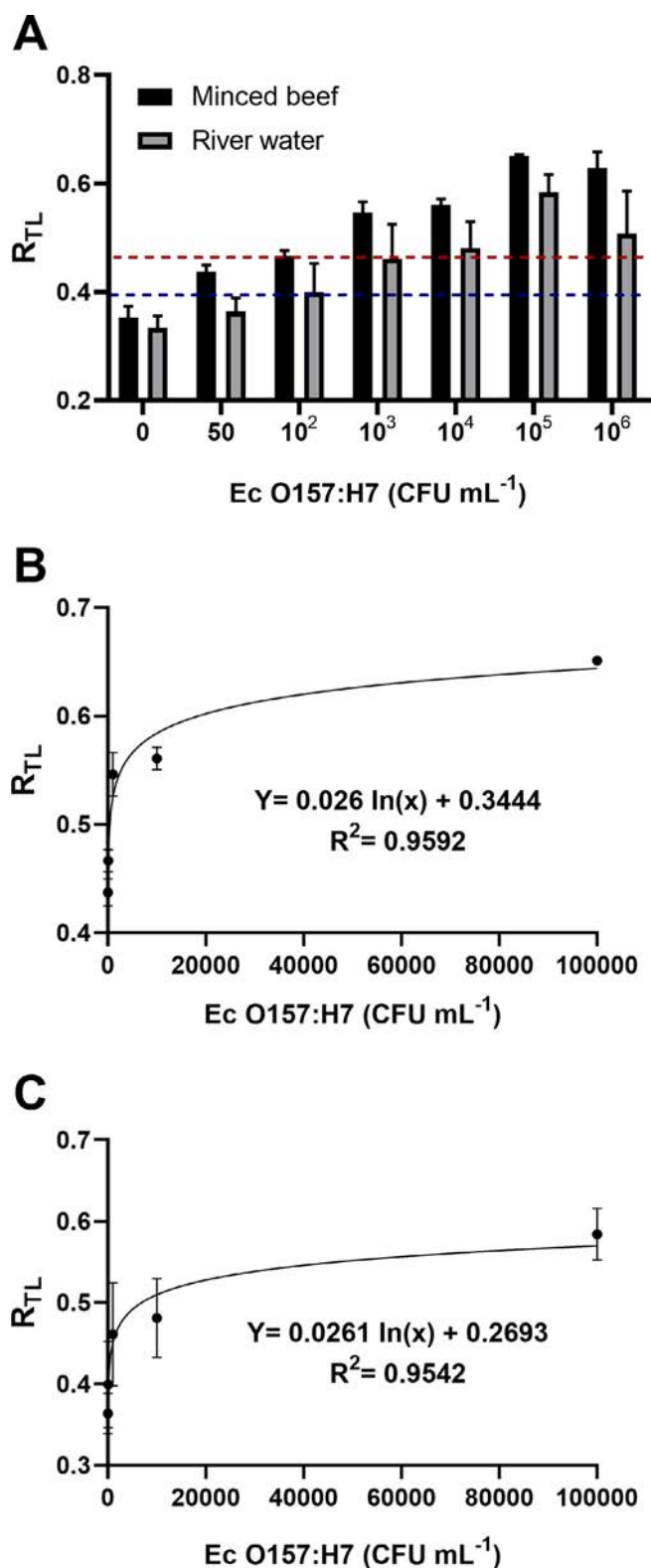
Fig. 5. A) Overall response of FLFIA strips to various concentrations of *E. coli* O157:H7 (Ec O157:H7) in minced beef and river water samples. The dashed lines represent the limit of detection of *E. coli* O157:H7 in minced beef (red) and water (blue) ($\approx$ 178 and 133 CFU g^{-1} or mL^{-1} respectively), which were calculated as the R_{TL} mean value of blank minced beef or river water plus three times their SD. B) Logarithmic response of FLFIA to *E. coli* O157:H7 concentrations from 50 to 10^5 CFU g^{-1} in minced beef. C) Logarithmic response of FLFIA to *E. coli* O157:H7 concentrations from 50 to 10^5 CFU g^{-1} in river water. The error bars represent the standard deviation of at least 3 replicates.

et al. (2014), Hassan et al. (2015), Luo et al. (2017), Han et al. (2018) and Kim et al. (2018). However, our achieved LODs in real samples do not affect the reliability of FLFIA and confirm its high sensitivity in comparing with conventional immunoassays. The ability to detect *E. coli* O157:H7 at such low concentrations without broth enrichment designates that FLFIA could be used to determine as low as one CFU g^{-1} or mL^{-1} of *E. coli* O157:H7 in minced beef and water samples after about 3 h of broth enrichment of the sample, since *E. coli* O157: H7 could duplicate by mitotic division every 15–20 min under favourable conditions (Buchanan & Klawitter, 1992).

By comparing FLFIA in terms of LOD with other reported rapid methods, which were depending on sandwich antibody formats, more complicated techniques and/or more expensive approaches for determination of *E. coli* O157:H7 in various food samples, we noticed the high sensitivity of our costless approach over those more complicated and expensive technologies. For instance, Aydin et al. (2014) reported 250 CFU g^{-1} as a LOD of *E. coli* O157:H7 in ground beef using magnetic bead–based immunoassay coupled with tyramide signal amplification after 3 h of enrichment. Hassan et al. (2015) reported *E. coli* O157:H7 LODs of 457 and 309 CFU g^{-1} or mL^{-1} in minced beef and tap water samples, respectively, through using gold nanoparticles-labelled antibody sandwich-based electrochemical detection. Additionally, Song, Li, Liu, and Liu (2016) reported an *E. coli* O157:H7 LOD of 10^5 CFU g^{-1} or mL^{-1} in bread, milk and jelly samples using Fluorescein isothiocyanate-based immunosensor. As well as, Luo et al. (2017) compared different immunochromatographic labels for lateral flow assays for *E. coli* O157:H7 determination in milk. In that study, they reported LODs accounted for 1×10^5, 2.5×10^4, 1×10^3, 5×10^2 CFU mL^{-1} using gold nanoparticles, quantum dots, fluorescent nanoparticles, and europium chelate nanoparticles as labels, respectively. Eventually, Han et al. (2018) mentioned that the sensitivity of the nanozyme-based LFA depending on a sandwich antibody format developed by them for *E. coli* O157:H7 was 900 CFU mL^{-1} in milk.

3.5. Spike and recovery test in real samples

The results of spike and recovery experiment are summarized in Table 1. The recovery percentages from minced beef ranged from 92.86 to 95.02%, while those of river water ranged from 95.11 to 97.98%. Obviously, the extreme complex matrix of beef affects the assay performance more than that of river water. However, it still performs in an admirable way, adequate for real application requirements. Accordingly, these recovery rates demonstrate that this novel approach is a promising device for determination of *E. coli* O157:H7 in food and water without any interferences from the complex food and water matrices nor other competing microorganisms.

3.6. Reproducibility

Another important parameter for evaluating new analytical technologies is the reproducibility. In this study, for executing all experiments mentioned above, we used different fabrication batches of FLFIA. Among the working range of bacterial concentrations, the FLFIA strips exhibited variation coefficients below 16% in minced beef and river water. This meets the validation criterion of reproducibility of new

immunoassays that was stated by Findlay et al. (2000), who recommended a RSD below 20% for acceptance of new procedure in terms of reproducibility.

3.7. Possibility of smartphone integration

To prove the possibility of integration of proposed FLFIA into smartphones without the need to a portable lateral flow reader, another device for reading the line intensities was tried. A fluorescence image Typhoon scanner was used to take pictures of the strips. Then those scanned pictures were analysed using ImageJ 1.46r software to determine line intensities (Fig. 1B). A similar procedure with smartphones could be used through a 3D-printed cassette containing an excitation LED for holding the FLIFA strip to enable smartphone camera to capture the fluorescence and then an ImageJ application (smartphone version) be used for analyzing the picture. This proof of concept makes it a highly promising device for automation, portability, and field applications without the need for a highly equipped laboratory.

3.8. FLFIA versus traditional methods for detecting E. coli O157 in random food samples

Herein, we summarize the whole procedure of using FLFIA to analyze a random unknown food sample for the presence of *E. coli* O157:H7, in comparing with the traditional method in terms of procedure and assay time. In case of FLFIA, firstly, 25 g or mL of the food sample is homogenized or mixed with 225 mL of a pre-warmed modified tryptone soya broth plus novobiocin (mTSB + N) at 41.5 °C ± 1 °C and then incubated for 3 h. Meanwhile, the TL initial intensity of FLFIA strip being recorded using a portable LF reader. Then a 100 μL of the incubated sample broth is added onto the sample pad. Wait for 10 min to allow sample flow. Subsequently, a 100 μL of washing buffer, followed by a 100 μL of GO solution are added. After strip dryness, record the TL final intensity. If the R_{TL} is < 0.4 indicates a negative sample, while if it is ≥ 0.4 indicates a positive sample. Though, CL should be quenched in both positive and negative samples to confirm the successful flow of solutions through the strip pads. Accordingly, the total assay time of FLFIA is only 5 h, including 3 h of sample enrichment.

On the other hand, in order to detect *E. coli* O157 in food samples, using the traditional horizontal method stated by the International Organization for Standardization (ISO 4:1665, 2001) more than 60 h of sample examination were required to confirm the presence of this pathogen. The detection of *E. coli* O157 by ISO's method necessitates four successive stages: a) enrichment, b) separation and concentration, c) isolation and d) confirmation. Briefly, the sample was enriched in nine times the weight in mTSB + N for 6 h and subsequently for a further 12–18 h. Then *E. coli* O157 were separated and concentrated using immunomagnetic beads coated with anti-*E. coli* O157 antibodies after 6 h and again, if necessary, after a further 12–18 h incubation. Afterwards, *E. coli* O157 captured with immunomagnetic particles were subcultured onto cefixime tellurite sorbitol MacConkey agar (CT-SMAC) and the agar plates were incubated at 37 °C/18–24 h. Subsequently, typical *E. coli* O157 colonies (sorbitol negative) were streaked onto nutrient agar (NA) and incubated at 37 °C/18–24 h. Eventually, *E.*

Table 1
Spike and recovery experiment in minced beef and river water.

Real samples (n ≥ 3)	Initial level of *Ec* O157:H7 (CFU mL^{-1} or g^{-1})	Spiked value of *Ec* O157:H7 (CFU mL^{-1} or g^{-1})	R_{TL} in standard buffer	R_{TL} in real samples	Recovery (%)
River water	0.0	10^3	0.419	0.411	97.98
	0.0	10^4	0.559	0.532	95.11
Minced beef	0.0	10^3	0.419	0.398	95.02
	0.0	10^4	0.559	0.501	92.86

Where, n, number of replicates. R_{TL}, Ratio of test line intensity = final intensity/initial intensity of test line. *Ec* O157:H7, *E. coli* O157:H7. CFU, colony forming units.

coli O157 on NA was confirmed by indole production and agglutination with *E. coli* O157 antiserum. Thus, the traditional method is laborious, time consuming and of high cost, as well as, it requires well-trained operators and highly equipped facilities. That confirms the advantages of FLFIA over standard traditional methods.

4. Conclusions

In conclusion, we exclusively developed a fluorescent lateral flow immunoassay based on quantum dots as donors of non-radiative energy and graphene oxide as an acceptor for such energy. We used only a single antibody on the test line to capture the target pathogen, which reduced the total assay cost per strip to be 60% less than the conventional LF. This study is the first report of using that principle for *E. coli* O157:H7 detection in minced beef and river water. FLFIA achieved outstanding LODs of *E. coli* O157:H7 (≈ 133 and $178\,CFU\,mL^{-1}$ or g^{-1} in river water and mined beef, respectively). Theoretically, this indicates the possibility of detecting as low as one $CFU\,mL^{-1}$ or g^{-1} of *E. coli* O157:H7 after about 3 h of food sample enrichment in a suitable broth. The detection of *E. coli* O157:H7 by FLFIA in beef complex matrix designates the ability of their using for other food commodities, as well as for other similar bacterial species with changing the antibody. A portable lateral flow reader was used for reading and quantifying the results. Alongside, analysing the images with ImageJ software was proved to be an alternative way for reading the results with smartphones. FLFIA showed numerous advantages in comparing with the standard traditional method of *E. coli* O157 detection, as well as against other previously reported rapid methods.

Declaration of Competing Interest

The authors declare that there is no any conflict of interest in this work.

Acknowledgements

References

Arbault, P., Buecher, V., Poumerol, S., & Sorin, M. L. (2000). Study of an ELISA method for the detection of *E. coli* O157 in food. *Progress in biotechnology: Vol. 17*, (pp. 359–368). Elsevier https://doi.org/10.1016/S0921-0423(00)80093-3.

Aydin, M., Herzig, G. P., Jeong, K. C., Dunigan, S., Shah, P., & Ahn, S. (2014). Rapid and sensitive detection of *Escherichia coli* O157: H7 in milk and ground beef using magnetic bead-based immunoassay coupled with tyramide signal amplification. *Journal of Food Protection, 77*(1), 100–105. https://doi.org/10.4315/0362-028X.JFP-13-274.

Berg, B., Cortazar, B., Tseng, D., Ozkan, H., Feng, S., Wei, Q., ... Di Carlo, D. (2015). Cellphone-based hand-held microplate reader for point-of-care testing of enzyme-linked immunosorbent assays. *ACS Nano, 9*, 7857–7866. https://doi.org/10.1021/acsnano.5b03203.

Buchanan, R. L., & Klawitter, L. A. (1992). The effect of incubation temperature, initial pH, and sodium chloride on the growth kinetics of *Escherichia coli* O157:H7. *Food Microbiology, 9*, 185–196. https://doi.org/10.1016/0740-0020(92)80046-7.

CDC, Centers for Disease Control and Prevention (2009). Reports of E. coli Outbreak Investigations from 2006-2009, CDC, USA. URL https://www.cdc.gov/ecoli/2006-2009-outbreaks.html. Accessed 03.06.2019.

Cheeveewattanagul, N., Morales-Narváez, E., Hassan, A.-R. H., Bergua, J. F., Surareungchai, W., Somasundrum, M., & Merkoçi, A. (2017). Straightforward immunosensing platform based on graphene oxide-decorated nanopaper: A highly sensitive and fast biosensing approach. *Advanced Functional Materials, 27*(38), 1702741. https://doi.org/10.1002/adfm.201702741.

Findlay, J. W. A., Smith, W. C., Lee, J. W., Nordblom, G. D., Das, I., DeSilva, B. S., & Bowsher, R. R. (2000). Validation of immunoassays for bioanalysis: A pharmaceutical industry perspective. *Journal of pharmaceutical and biomedical analysis, 21*(6),

1249–1273. https://doi.org/10.1016/S0731-7085(99)00244-7.

Food and Agriculture Organization of the United Nations/World Health Organization (FAO/WHO, 2008). Shiga toxin-producing Escherichia coli (STEC) and food: attribution, characterization, and monitoring (Report). Microbiological risk assessment series 31, Rome. Available on: www.fao.org/publications. Accessed 03.06.2019.

Gaudreau, L., Tielrooij, K. J., Prawiroatmodjo, G. E. D. K., Osmond, J., de Abajo, F. G., & Koppens, F. H. L. (2013). Universal distance-scaling of nonradiative energy transfer to graphene. *Nano Letters, 13*(5), 2030–2035. https://doi.org/10.1021/nl400176b.

Han, J., Zhang, L., Hu, L., Xing, K., Lu, X., Huang, Y., ... Chen, T. (2018). Nanozyme-based lateral flow assay for the sensitive detection of *Escherichia coli* O157: H7 in milk. *Journal of Dairy Science, 101*, 5570–5779. https://doi.org/10.3168/jds.2018-14429.

Hassan, A.-R. H. A.-A., de la Escosura-Muñiz, A., & Merkoçi, A. (2015). Highly sensitive and rapid determination of *Escherichia coli* O157: H7 in minced beef and water using electrocatalytic gold nanoparticle tags. *Biosensors and Bioelectronics, 67*, 511–515. https://doi.org/10.1016/j.bios.2014.09.019.

Islam, M., Doyle, M. P., Phatak, S. C., Millner, P., & Jiang, X. (2004). Persistence of enterohemorrhagic *Escherichia coli* O157:H7 in soil and on leaf lettuce and parsley grown in fields treated with contaminated manure composts or irrigation water. *Journal of Food Protection, 67*, 1365–1370.

ISO 16654:2001. Microbiology of food and animal feeding stuffs – Horizontal method for the detection of Escherichia coli O157. URL https://www.iso.org/standard/29821.html. Accessed 03.06.2019.

Jay, J. (2000). *Microorganisms in foodsModern food microbiology* (6 ed.). New York: Van Nostrand Reinhold.

Johnson, J., Brooke, C., & Fritschel, S. (1998). Comparison of the BAX for screening/*E. coli* O157: H7 method with conventional methods for detection of extremely low levels of Escherichia coli O157: H7 in ground beef. *Applied Environmental Microbiology, 64*, 4390–4395.

Karakus, C., & Salih, B. A. J. (2013). Comparison of lateral flow immunoassays (LFIA) for the diagnosis of Helicobacter pylori infection. *Journal of Immunological Methods, 396*, 8–14. https://doi.org/10.1016/j.jim.2013.08.010.

Kim, S. U., Jo, E.-J., Mun, H., Noh, Y., & Kim, M.-G. (2018). Ultrasensitive detection of *Escherichia coli* O157:H7 by immunomagnetic separation and selective filtration with nitroblue tetrazolium/5-bromo-4-chloro-3-indolyl phosphate signal amplification. *Journal of Agricultural and Food Chemistry, 66*, 4941–4947. https://doi.org/10.1021/acs.jafc.8b00973.

Lin, T. N., Huang, L. T., Shu, G. W., Yuan, C. T., Shen, J. L., Lin, C. A. J., ... Kuo, H. C. (2013). Distance dependence of energy transfer from InGaN quantum wells to graphene oxide. *Optics letters, 38*(15), 2897–2899. https://doi.org/10.1364/OL.38.002897.

Lorusso, V., Dambrosio, A., Quaglia, N. C., Parisi, A., Lasalandra, G., Mula, G., ... Normanno, G. (2011). Development of a multiplex PCR for rapid detection of verocytotoxin-producing *Escherichia coli* O26 in raw milk and ground beef. *Journal of Food Protection, 74*, 13–17. https://doi.org/10.4315/0362-028X.JFP-10-201.

Luo, K., Hu, L., Guo, Q., Wu, C., Wu, S., Liu, D., ... Lai, W. (2017). Comparison of 4 label-based immunochromatographic assays for the detection of *Escherichia coli* O157: H7 in milk. *Journal of Dairy Science, 100*, 5176–5187. https://doi.org/10.3168/jds.2017-12554.

McFarland, J. (1907). Nephelometer: An instrument for estimating the number of bacteria in suspensions used for calculating the opsonic index and for vaccines. *Journal of American Medical Association, 14*, 1176–1178. https://doi.org/10.1001/jama.1907.25320140022001f.

Merkoçi, A., & Morales-Narváez, E. (2015). Sensitive qualitative bioassay using graphene oxide as analyte revealing agent. European Patent No. EP13188693.9.

Morales-Narváez, E., & Merkoçi, A. (2012). Graphene oxide as an optical biosensing platform. *Advanced Materials, 24*, 3298–3308. https://doi.org/10.1002/adma.201200373.

Morales-Narváez, E., Hassan, A. R., & Merkoçi, A. (2013). Graphene oxide as a pathogen-revealing agent: Sensing with a digital-like response. *Angewandte Chemie International Edition, 52*(51), 13779–13783. https://doi.org/10.1002/anie.201307740.

Morales-Narváez, E., Naghdi, T., Zor, E., & Merkoçi, A. (2015). Photoluminescent lateral-flow immunoassay revealed by graphene oxide: Highly sensitive paper-based pathogen detection. *Analytical Chemistry, 87*(16), 8573–8577. https://doi.org/10.1021/acs.analchem.5b02383.

Ngwa, G. A., Schop, R., Weir, S., León-Velarde, C. G., & Odumeru, J. A. (2013). Detection and enumeration of *E. coli* O157:H7 in water samples by culture and molecular methods. *Journal of Microbiological Methods, 355*(92), 164–172. https://doi.org/10.1016/j.mimet.2012.11.018.

Olsen, S. J., Miller, G., Kennedy, M., Higgins, C., Walford, J., McKee, G., ... Mead, P. (2002). A waterborne outbreak of *Escherichia coli* O157:H7 infections and hemolytic uremic syndrome: Implications for rural water systems. *Emerging Infectious Diseases, 8*, 370–375. https://doi.org/10.3201/eid0804.000218.

Scallan, E., Hoekstra, R. M., Angulo, F. J., Tauxe, R. V., Widdowson, M. A., Roy, S. L., ... Griffin, P. M. (2011). Foodbome illness acquired in the United States – Major pathogens. *Emerging Infectious Diseases, 17*, 7–15. https://doi.org/10.3201/eid1701.P11101.

Shen, Z., Hou, N., Jin, M., Qiu, Z., Wang, J., Zhang, B., ... Li, J. (2014). A novel enzyme-linked immunosorbent assay for detection of *Escherichia coli* O157:H7 using immunomagnetic and beacon gold nanoparticles. *Gut Pathogens, 6*, 14. https://doi.org/10.1186/1757-4749-6-14.

Shi, X., Meng, X., Sun, L., Liu, J., Zheng, J., Gai, H., ... Yeung, E. S. (2010). Observing photophysical properties of quantum dots in air at the single molecule level: Advantages in microarray applications. *Lab on a Chip, 10*(21), 2844–2847. https://doi.org/10.1039/c005258b.

Song, C., Li, J., Liu, J., & Liu, Q. (2016). Simple sensitive rapid detection of *Escherichia coli* O157: H7 in food samples by label-free immunofluorescence strip sensor. *Talanta,*

156, 42–47. https://doi.org/10.1016/j.talanta.2016.04.054.

Tsiraki, M. I., Yehia, H. M., Elobeid, T., Osaili, T., Sakkas, H., & Savvaidis, I. N. (2018). Viability of and *Escherichia coli* O157: H7 and *Listeria monocytogenes* in a delicatessen appetizer (yogurt-based) salad as affected by citrus extract (Citrox©) and storage temperature. *Food Microbiology, 69*, 11–17. https://doi.org/10.1016/j.fm.2017.07.014.

Zamora-Gálvez, A., Morales-Narváez, E., Romero, J., & Merkoçi, A. (2018). Photoluminescent lateral flow based on non-radiative energy transfer for protein detection in human serum. *Biosensors and Bioelectronics, 100*, 208–213. https://doi.org/10.1016/j.bios.2017.09.013.

Zhang, L., Huang, Y., Wang, J., Rong, Y., Lai, W., Zhang, J., & Chen, T. (2015).

Hierarchical flowerlike gold nanoparticles labeled immunochromatography test strip for highly sensitive detection of *Escherichia coli* O157: H7. *Langmuir, 31*, 5537–5544. https://doi.org/10.1021/acs.langmuir.5b00592.

Zhaohui, Q., Chunyang, L., Yingchun, Fu., & Yanbin, L. (2017). Rapid and sensitive detection of *E. coli* O157:H7 based on antimicrobial peptide functionalized magnetic nanoparticles and urease catalyzed signal amplification. *Analytical Methods, 9*, 5204–5210. https://doi.org/10.1039/c7ay01643c.

Zhou, C., Zou, H., Li, M., Sun, C., Ren, D., & Li, Y. (2018). Fiber optic surface plasmon resonance sensor for detection of *E. coli* O157: H7 based on antimicrobial peptides and AgNPs-rGO. *Biosensors and Bioelectronics, 117*, 347–353. https://doi.org/10.1016/j.bios.2018.06.005.

Low-Cost Strategy for the Development of a Rapid Electrochemical Assay for Bacteria Detection Based on AuAg Nanoshells

Lorenzo Russo,[†,‡] Juan Leva Bueno,[†] Jose Francisco Bergua,[†,‡] Monica Costantini,[§] Marco Giannetto,[§] Victor Puntes,[†,∥,⊥] Alfredo de la Escosura-Muñiz,[†] and Arben Merkoçi*,[†,‡,∥]

[†]Catalan Institute of Nanoscience and Nanotechnology (ICN2), CSIC and The Barcelona Institute of Science and Technology, Campus UAB, Bellaterra, 08193 Barcelona, Spain

[‡]Universitat Autònoma de Barcelona (UAB), Campus UAB, Bellaterra, 08193 Barcelona, Spain

[§]Department of Chemistry, Life Sciences and Environmental Sustainability, University of Parma, Parco Area delle Scienze 17/A, 43124 Parma, Italy

[∥]Vall d'Hebron Institut de Recerca (VHIR), 08035 Barcelona, Spain

[⊥]Institució Catalana de Recerca i Estudis Avançats (ICREA), P. Lluís Companys 23, 08010 Barcelona, Spain

Ⓢ Supporting Information

ABSTRACT: A low-cost strategy for the simple and rapid detection of bacterial cells in biological matrixes is presented herein. *Escherichia coli* and *Salmonella typhimurium* were chosen as model bacteria for the development of an electrochemical assay based on hollow AuAg nanoshells (NSs). By taking advantage of their electrocatalytic properties for the in situ generation of the electrochemical signal without the need of any other kind of reagent, substrate, or redox enzyme, high sensitivities (down to 10^2 CFU/mL) were achieved. Moreover, the recognition and discrimination of the model bacterial cells in the sample matrix was possible by relying solely on nonspecific affinity interactions between their cell walls and AuAg NSs surface, avoiding the use of expensive and fragile biological receptor. Compared to traditional, laboratory-based analytical tests available, this assay provides a promising proof-of-concept alternative that allows to obtain good sensitivities and selectivity in very short times in addition to the low cost.
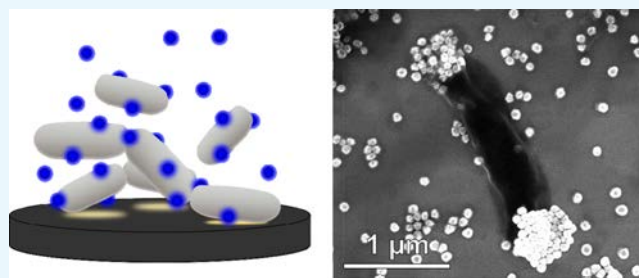
INTRODUCTION

Bacterial resistance to antimicrobials is considered widely the most urgent health issue the world is facing in the coming years.[1] Nowadays, the choice to prescribe antibiotics is rarely based on definitive diagnoses, which generally require laboratory-based analytical test (i.e., polymerase chain reaction (PCR), traditional plate counting), often consisting of days-long procedure characterized by high costs and the need for highly trained and skilled personnel. Effective, rapid, low-cost diagnostic tools are needed for guiding optimal use of antibiotics in human and animal medicine and, also in the form of point-of-care (POC) devices. Such tools should be easily integrated into clinical, pharmacy, and veterinary practices as high-throughput screening methods for the early discrimination between bacterial and viral infections.[2] In this context, nanotechnology has proven to be extremely successful in providing innovative and advantageous solutions to overcome the conventional in vitro diagnostic intrinsic limitations through the rational design of advanced nanomaterials with suitable properties and functionalities.[3−6] Among them, nanomaterials with unique electrochemical and electrocatalytic properties have been introduced as signal-amplification carriers or direct signal-generating elements to increase sensitivities and enhance analytic performances.[7−9]

The cost of diagnostics technologies is on the other hand one of the fundamental global health aspects to be considered for accessing the market with competitive and sustainable products.[10] Indeed, recognition elements found on the few POC electrochemical biosensors available consist fundamentally of biomolecules (i.e., enzymes, nucleic acids, antibodies), which represent one of the largest fraction of the total production cost.[11] Besides their unmatched specificity and selectivity, several drawbacks, such as high production cost and high susceptibility to environmental conditions (i.e., pH, temperature, metal cations, fouling agents, metabolites) can limit their applicability, especially when integrated into POC devices.[12] Exploiting instead the catalytic properties of electroactive nanomaterials presents a number of advantages, such as a lower production cost and engineering, ease of mass production, and a higher stability both in working conditions and long-term storage.[13−15]

The aim of this work is therefore to employ the unique electrocatalytic properties of AuAg nanoshells (NSs)[16] for the quantitative detection of two model bacteria, *Escherichia coli* and *Salmonella typhimurium* (*Salmonella*). The ability to tune precisely their morphology and metal composition grants AuAg NSs with increased resistance to chemical oxidation while allowing them to generate a strong electrochemical signal. These unique features, together with high colloidal stability and large surface area, make AuAg NSs extremely promising materials to be employed as electrochemical labels in biosensors applications. Although AuAg NSs have been applied previously as nanostructured carriers for intracellular drug delivery and as surface enhanced Raman scattering labels for optical detection,[17,18] to the best of our knowledge, no similar reports of the use of this class of particles as electrochemical reporters have been published yet. Moreover, in our system, the detection of bacterial cells is achieved without the use of any biological receptor, basing it instead on nonspecific interactions between the AuAg NSs and the intrinsically highly differentiated bacterial cell surfaces. This approach, also experimented elsewhere,[19,20] provides a promising proof of concept for the development of a low-cost, robust electrochemical assay reaching high sensitivities (down to 10^2 CFU/mL) in very short times (within 10 min) compared to the available commercial *E. coli* POC assays and recently reported nanoparticles-based electrochemical detection techniques.[21]

RESULTS AND DISCUSSION

Electrochemical Properties of AuAg NSs. AuAg nanoshells consist of a hollow structure composed of a gold–silver alloy shell, which encloses an inner cavity. Their synthesis, based on a modified galvanic replacement reaction (GRR) reported previously by our group,[22] allows to precisely control both the morphology and the relative amount of the two noble metals. Figure 1A shows the transmission electron microscopy (TEM) micrographs of the product of the GRR displaying highly monodisperse hollow AuAg NSs of ca. 60 nm diameter, with a thin outer shell of ca. 10 nm thickness. The hollow particles bear a poly(vinyl pyrrolidone) (PVP) layer adsorbed on their surface during their synthesis, a hydrosoluble polymer, which provides enhanced colloidal stability without compromising their electrochemical properties.

Conventionally, noble-metal and semiconductor nanoparticles applied so far as electrochemical labels require strong oxidants or acids to generate their corresponding cationic species through corrosion, which can then be detected electrochemically through common voltammetric techniques.[23] Translating these technologies into electrochemical diagnostic platforms for commercial use becomes therefore extremely difficult due to the danger implied in handling these corrosive reagents. Although Ag NPs are instead prone to corrosion, they have found limited practical use due to severe susceptibility to oxidation,[24] resulting in limited durability and reproducibility in many biorelated applications. Thus, AuAg NSs were chosen as electrochemical signaling tool, thanks to their ability to generate an electrochemical signal in the presence of mild oxidizing agents, as demonstrated recently by our group.[16] The exposure of AuAg NSs to relatively high concentrations of nucleophilic halides and dissolved oxygen, typically found in most biological matrixes, is sufficient for activating their electrochemical properties: thanks to the residual Ag atoms contained in AuAg NSs cores, whose
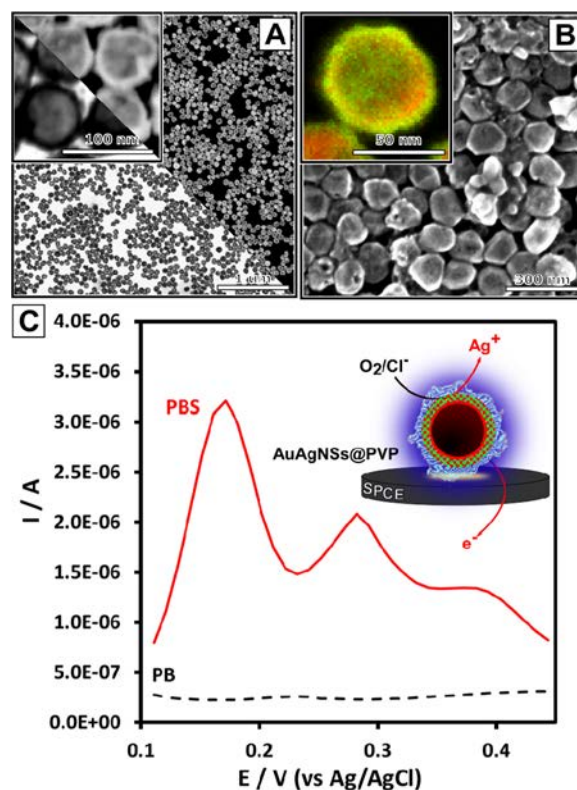
Figure 1. (A) TEM and high-angle annular dark-field scanning transmission electron microscopy (HAADF-STEM) micrographs of highly monodisperse 60.0 ± 4.4 nm AuAg NSs composed of a thin (≈10 nm) shell with a smooth surface and a large (≈40 nm) internal void. (B) Scanning electron microscopy (SEM) AuAg NSs surface characterization and HAADF-STEM elemental distribution micrographs of a single AuAg NS (inset; Au: green, Ag: red). At the final stage of GRR, Ag is found both in the Au-rich alloy outer thin shell and the inner particle surface in its metallic form. (C) Comparison of differential pulsed voltammetries (DPVs) of AuAg NSs in different buffers. The potential scan run in phosphate buffer saline (PBS) (red curve) causes the anodic stripping signal of Ag to appear at +0.16 V vs Ag/AgCl. When instead AuAg NSs are measured in phosphate buffer (PB) 10 mM pH 7.5 (black dashed curve), no relevant anodic current is observed. In the absence of chlorides in the matrix, no Ag corrosion is possible and therefore no stripping detection can be carried out.

amount can be precisely controlled during synthesis[22] (Figure 1B), Ag⁺ cations are generated by corrosion without compromising the particles' structural stability, and anodic stripping analysis can be carried out for their detection.[16] Figure 1C shows the DPVs of AuAg NSs in PBS (red curve), showing a relatively strong and defined anodic peak at +0.16 V vs Ag/AgCl, completely absent instead when the same measurement is performed in PB (black dashed curve), that is, without chlorides in solution. A secondary oxidation peak is also observed at more positive potentials (+0.28 V vs Ag/AgCl), corresponding to the oxidation of alloyed Ag found in the outer shell of the particles.[16] These findings not only confirm the electrochemical mechanism of the current generation described above but also make AuAg NSs a promising substitute of natural redox enzymes as electrochemical labels for sensing applications.

We investigated systematically the different experimental parameters involved in the DPV measurement for optimizing the sensitivity of the system. First, Ag corrosion was monitored during this time to maximize the amount of Ag⁺ cations
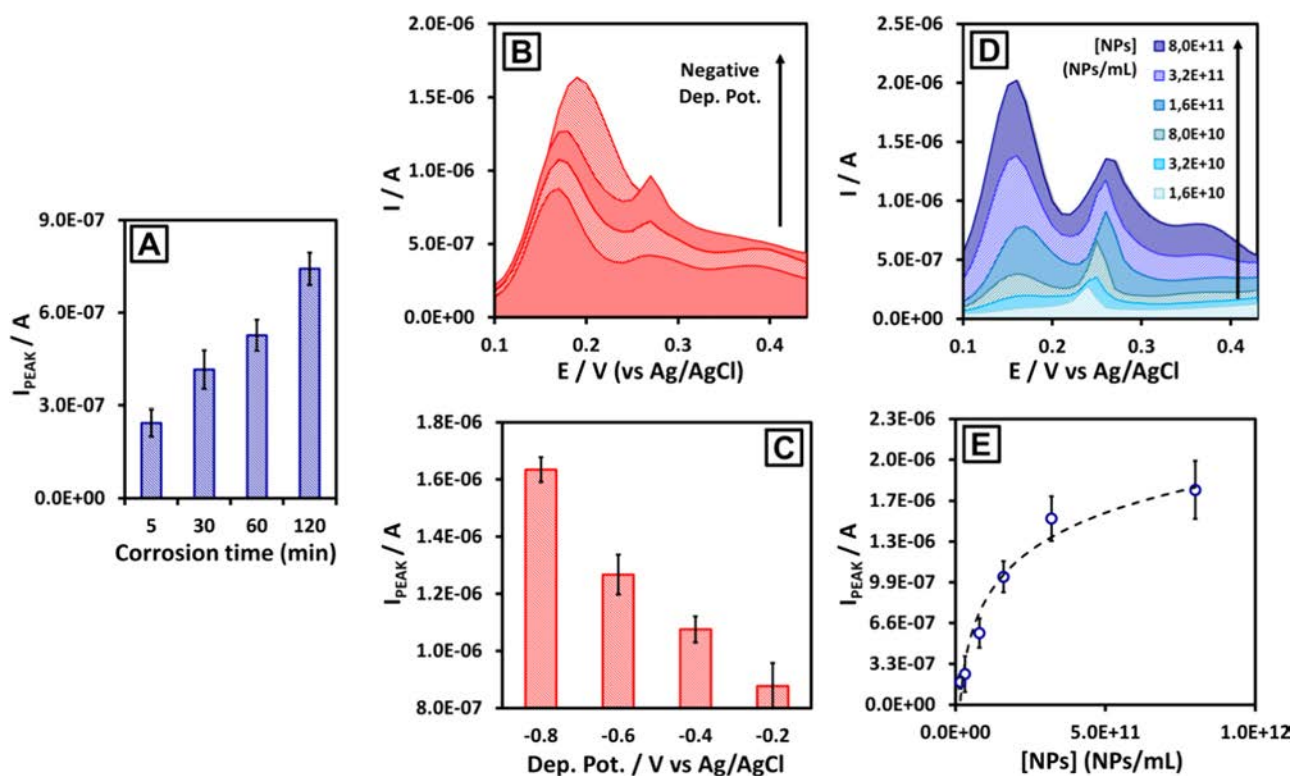
Figure 2. A) Time of residence of AuAg NSs in the oxidant matrix affects the anodic stripping current of Ag. Five minutes after mixing the hollow nanocrystal solution with PBS 10 mM pH 7.5, a relatively intense DPV current is obtained. Higher corrosion times allow to further enhance the current signal up to 4-fold for 120 min. (B, C) Effect of DPVs' initial deposition potential on the anodic stripping wave of Ag on screen printed carbon electrodes (SPCEs). (D, E) The dependency of the anodic stripping current on AuAg NSs' concentration is analyzed by running the DPVs of solution of increasing particles concentrations. The analytic peak (+0.16 V vs Ag/AgCl) intensity correlates positively with the increasing particles concentration (ranging from 1.6×10^{10} to 8.0×10^{11} NPs/mL), showing a logarithmic trend due to diffusion toward the electrode surface.

generated and, therefore, the corresponding anodic stripping current produced for a fixed amount of AuAg NSs (Figure 2A).

As expected, a higher residence time of the particles in the saline buffer before measurement causes a greater degree of Ag corrosion and therefore produces a stronger anodic current. Although the strongest signal was obtained for longer times (2 h), a 5 min long corrosion in the sample matrix was considered enough for generating the necessary signal intensity for the development of a rapid assay able to compete with traditional ones. This parameter could in theory be further optimized by increasing the total surface area available for chloride corrosion, for instance, by tuning the particles synthesis so to obtain a porous alloys shell.[22] It is worth mentioning that, despite the high salinity of the medium, no AuAg NSs aggregation is observed, thanks to the steric stabilization provided by the PVP coating (study of AuAg NSs colloidal stability can be found in Figure S1).

Second, the effect of the deposition potential, which is the negative potential applied at the beginning of the measurement needed for reducing Ag+ onto the electrode surface,[25] was also analyzed. The DPVs of AuAg NSs solutions at a fixed concentration were therefore run by applying different deposition potentials before the measurement, namely, −0.2, −0.4, −0.6, and −0.8 V vs Ag/AgCl.

As shown in Figure 2B, varying the applied reduction potential does not seem to affect relevantly the oxidation peak's shape, apart from a slight shift in the peak position. On the contrary, a clear positive correlation between the applied deposition potential and the anodic current recorded at 0.16 V

vs Ag/AgCl is observed (Figure 2C), resulting in increased current intensities up to 2-fold for −0.8 V vs Ag/AgCl. Remarkably, the possibility to reduce Ag+ by applying more positive deposition potentials than silver's formal reduction one (Ag+ reduction potentials = 0.7996 V)[26] depends on the ability of AuAg NSs to catalyze the underpotential deposition of Ag+ on their surfaces, as recently discovered by our group.[16] This electrocatalytic effect is directly dependent on the particles' composition and morphology and can be tuned by modifying their synthesis.[22] Even though the highest signal obtained through this mechanism was found when using a deposition potential of −0.8 V vs Ag/AgCl, using less negative ones led to an improvement in the overall reproducibility of the measurement. In these conditions, in fact, Ag/AgCl pseudoreferences electrodes, known to display stability issues in electrolytes containing high chlorides concentrations,[27] showed a higher reproducibility. Figure S2 shows the behavior of the pseudoreference Ag/AgCl electrode vs the initial deposition potentials used. Besides the expected reference oxidation peak (≈0.0 V vs Ag/AgCl), the appearance of a satellite one when applying more negative deposition potentials (−0.4, −0.6, −0.8, and −1.0 V vs Ag/AgCl) was considered a probable cause of the reproducibility problems encountered. Using milder reduction potentials during the DPV measurement (−0.2 V vs Ag/AgCl) allows instead to completely avoid this effect. Moreover, the possibility to use AuAg NSs as electrochemical labels without the need to apply highly negative reduction potentials during the deposition step represents a further advantage because it eliminates the risk of
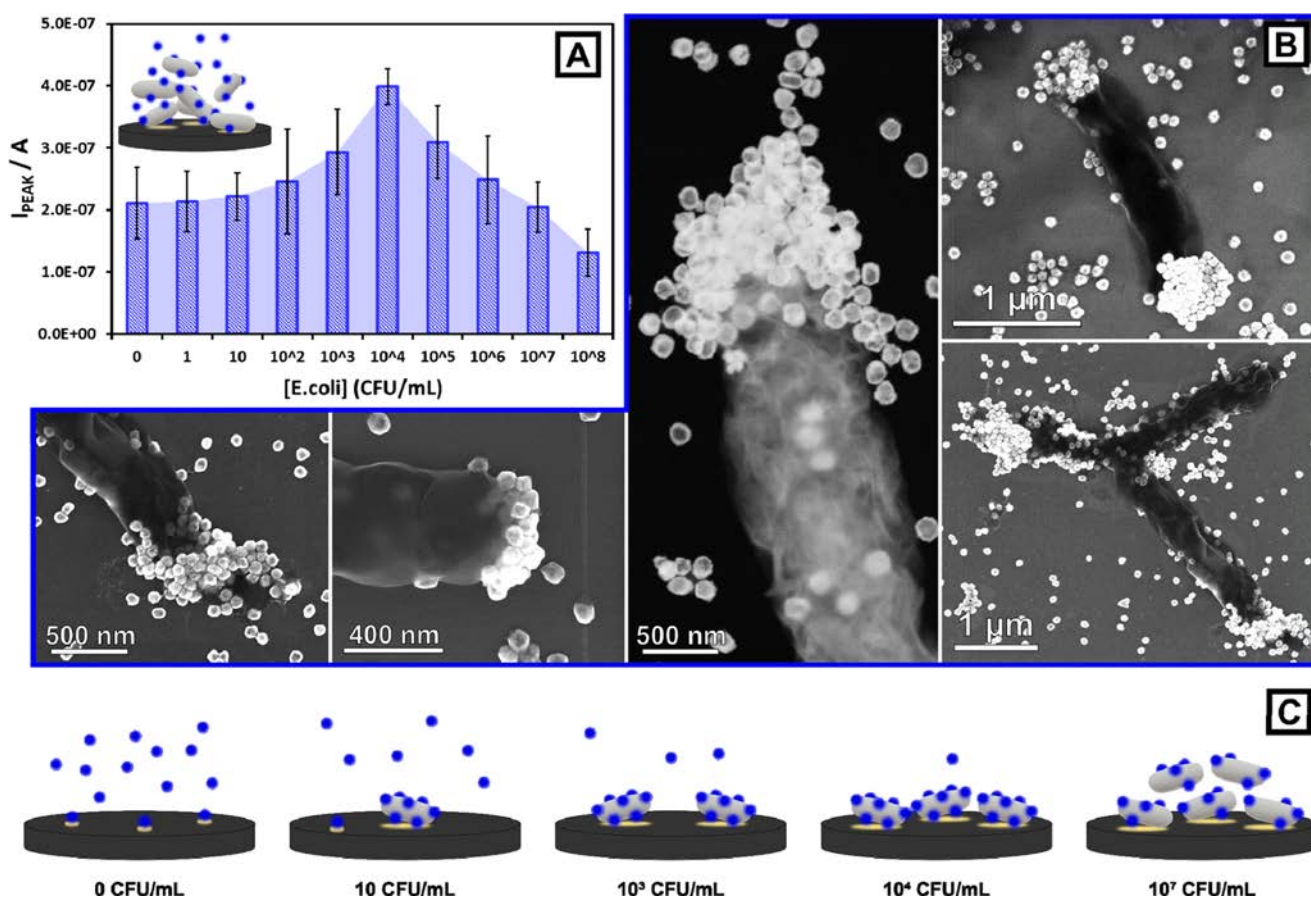
Figure 3. (A) *E. coli* detection through incubation with AuAg NSs and DPV measurement (bacteria cells concentration ranging from 10^1 to 10^8 CFU/mL). Error bars represent measurement standard deviation ($n = 5$), whose relatively high value are a result of the bacteria quantification (OD_{600}) high error. (B) STEM images (dark field and SEM) of *E. coli* cells decorated with AuAg NSs after incubation and differential centrifugation. (C) Affinity-based detection mechanism, depicting AuAg NSs (blue) and *E. coli* cells (gray) coming into contact with the electrode surface.

interference from redox-active species easily found in biological matrixes.

Finally, the correlation between AuAg NSs concentration and the measured electrochemical signal was studied by recording the anodic stripping peak intensity at +0.16 V while varying particles' concentration up to a 5-fold increase. As shown in Figure 2D,E, the electrochemical signal follows an increasing trend for the lower range of concentrations, after which it reaches a saturation plateau. This behavior is reasonably compatible with the electrochemical mechanism described above, considering that because no NSs immobilization over the electrode surface is carried out before the measurement, the diffusion rate of NSs toward the electrode surface will set an upper limit for the electron transfer and only the fraction of particles found in close proximity of the electrode surface will provide a detectable signal.[28] This setup allows detection of AuAg NSs down to a limit of detection of 5.6×10^{10} NPs/mL, but further improvement in sensitivity could be achieved by implementing longer deposition or corrosion steps.

Bacteria Detection. Conventional methods for specific quantification and differentiation of microbial cells use either selective culturing media, which can take up to several days to distinguish a positive from a negative sample, or molecular biology techniques, which instead target mainly intracellular biomarkers (i.e., proteins, nucleic acids) and therefore require

complex and time-consuming procedures for extraction, amplification, and revelation (i.e., immunolabeling, PCR).[29] A less explored strategy for cell sensing focuses instead on the extracellular complex array of macro/biomolecules expressed on bacterial cell walls (i.e., phospholipids, lipopolysaccharides). Such sensing strategy takes advantage of the chemical fingerprint of these complex moieties to generate a nonspecific but selective response relying on the differential binding affinities between different nanoprobes and bacterial cells, thus without the need of costly biological receptors (i.e., antibodies, peptides, and nucleic acids).[20,30,31] This approach has been shown already to be a viable and promising one for their rapid detection and identification with minimal processing.[19,32]

The general protocol herein adopted for bacteria detection consists in mixing a solution of a model bacterial strain of *E. coli* at a given concentration (ranging from 10^1 to 10^8 CFU/mL) with PVP-coated AuAg NSs at a final concentration of 1.6×10^{11} NPs/mL, incubating the mixture for 5 min in PBS 10 mM pH 7.4 and then rapidly depositing it onto SPCEs to run a DPV, as described in the Experimental Section. The variation in anodic stripping current at +0.16 V, generated by the controlled corrosion of AuAg NPs in PBS, was then correlated with the concentration of *E. coli* cells (Figure 3A), revealing an initial increase in intensity up to a concentration of 10^4 CFU/mL, followed by a steep decrease in the peak current for higher ones. For *E. coli* concentrations higher than 10^6 CFU/mL, the
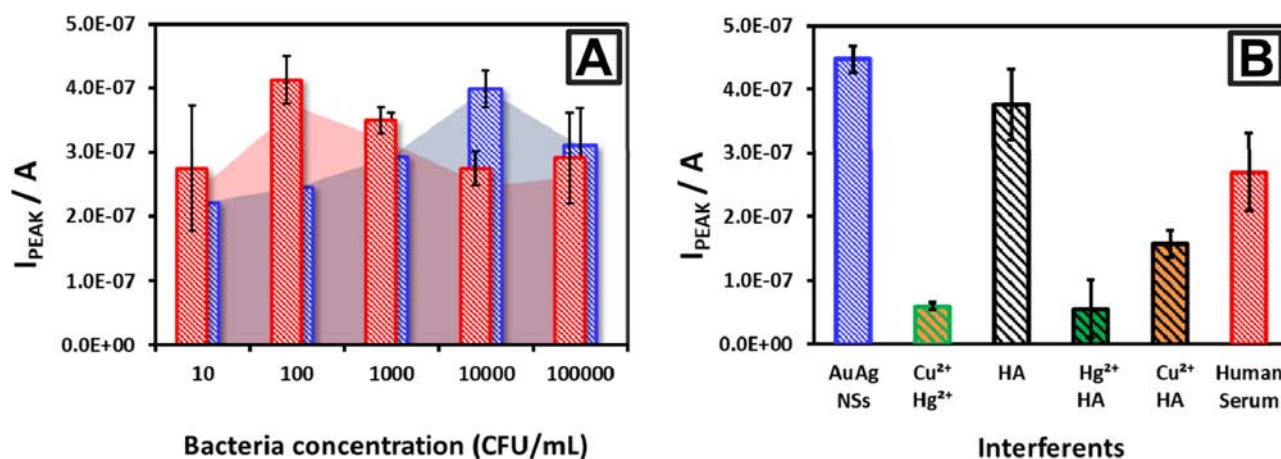
Figure 4. (A) Peak current profiles for different concentrations of *E. coli* (blue) and *Salmonella* (red): without the use of any specific receptor, affinity-based interactions between PVP-coated AuAg NSs and bacteria cell walls allow to selectively discriminate between the two species. (B) Peak currents recorded for assays run on samples containing *E. coli* suspension of 10^4 CFU/mL in the presence of different interfering species, namely, humic acid (HA), mercury (Hg^{2+}) and copper (Cu^{2+}) ions, and human serum.

voltammetric signal displays values lower than the blank ones. This peculiar current profile, encountered also in a previous work,[33] can be explained considering the bacteria's ability to "capture" the electroactive NPs in a solution through the nonspecific affinity interactions between PVP-coated AuAg NSs and the microorganisms' cell walls. As confirmed by the ζ-potential measured at three different pHs (Table S1), AuAg NSs colloidal stabilization is electrosteric, which is caused both by the electrostatic repulsion due to the negative surface charge (-24.5 ± 0.31 mV at pH = 7.5) and the steric interaction provided by the PVP adsorbed layer. Interestingly, this same layer appears to be also responsible for the nonspecific interaction between AuAg NSs in a solution and *E. coli* cell wall: as shown in the STEM micrographs of *E. coli* cells incubated with PVP-coated AuAg NSs (Figure 3B), the hollow nanocrystals seem to stick and accumulate on the bacterial cell wall extremities, probably thanks to the weak but additive interactions between the coating polymer and the extracellular macromolecules (i.e., phospholipids, lipopolysaccharides, and flagellar proteins). This kind of nonspecific interactions has been showed to be favored by the relatively hydrophobic character of both the extracellular macromolecules expressed and PVP, which is somehow able to screen the electrostatic repulsion between the negatively charged objects.[34−36] This attachment is not permanent, given the reversible nature of the weak interactions involved, but it is sufficient to label the bacterial cells with electrochemical reporters: after incubation of bacteria suspension with AuAg NSs, all the samples were purified through differential centrifugation[37] to separate the bacteria−particles complexes formed from the unattached ones (the presence in Figure 3B STEM images of free particles is likely caused by the later detachment during solvent evaporation upon sample preparation).

During the electrochemical assay, once the suspension of AuAg NSs-decorated bacteria in PBS is deposited on the electrode, cells quickly start to sediment, bringing the captured particles in contact with the electrode surface. For bacterial concentration ranging from 10^1 to 10^4 CFU/mL, the number of active electrochemical reporters found at the electrode surface is increased compared to the blank sample (Figure 3C, "0 CFU/mL") (in the absence of any cell, only the NPs in close proximity or contact with the electrode surface are able

to provide an electrochemical signal). By increasing the concentration of cells, more particles can attach to the bacteria cell walls and thus reach the vicinity of the electrode surface, increasing the anodic stripping current of silver generated from the NSs (Figure 3C, "$10^1−10^4$ CFU/mL"). The electrochemical signal though reaches a maximum and then starts to decrease again for higher *E. coli* concentrations due to the depletion of free NPs in solution. In this second regime, the bacterial cells compete for capturing the limited amount of AuAg NSs, which are now distributed over a larger surface area, and hinder this way the electron transfers to the electrode surface (Figure 3C, "10^7 CFU/mL"). This particular electroanalytical response could be further improved for developing a more robust and reliable method for bacteria detection by performing a set of serial dilutions of the sample, where observing an increase rather than a decrease in current would correspond to a precise range of microbial concentrations, as demonstrated in Figure S3.

To test the selectivity of this detection strategy, a second model bacterial strain, *S. typhimurium*, was submitted to the same detection methodology. The current-vs-concentration profile obtained by incubating *Salmonella* cells with AuAg NSs (Figure 4, red bars) resulted in substantial similarity to the one observed with *E. coli* (Figure 4, blue bars), although reaching the maximum current intensity for lower bacteria concentrations. This differentiation between the two electrochemical responses can be explained by taking into account that the two bacterial species possess analogous but dissimilar variety and type of surface functional macromolecules expressed on their cell walls.[20] Their distinct functionalities will determine the degree of interaction with the functional macromolecules present on the particles surface, depending for instance on the intrinsic availability of hydrogen bonds donors or their hydrophobic character. As a consequence, the average ratio between the number of electrochemical reporters per bacterial cell will vary between different species. When incubating *Salmonella* cells with AuAg NSs, the overall sum of weak, nonspecific affinity interactions with the PVP-coated NPs corresponds to a distinct capture efficiency and NPs/bacteria ratio compared to the *E. coli* characteristic one, shifting, in other words, the bacteria concentration at which the capture effect reaches its maximum. This behavior, already reported

previously for PVP-coated AgNPs,[33,36,32] not only confirms the signal modulation mechanism proposed (Figure 3A,C) but also demonstrates the proof of concept for the feasibility of a semispecific assay able to discriminate between different pathogenic organisms without recurring to highly specific but also costly and fragile biological receptors. It is worth mentioning that this intrinsic affinity is obtained without the help (and notably the cost) of any kind of antibody or other bioreceptor, and that it could be in theory improved significantly by screening the nonspecific affinity of different coating polymers toward a particular bacterial cell species.[30,38]

For further testing the capability of this assay to distinguish and quantify different bacterial strains in complex mixtures containing both *E. coli* and *Salmonella*, a set of experiments were run (Figure S4). The results obtained show clearly that the assay in its current proof-of-concept format is not able to distinguish univocally between different compositions of the two model bacterial strains without constructing the whole concentrations profile. Nevertheless, it seems that the influence of *Salmonella* on the current generation mechanism, which is the capture of AuAg NSs in a solution through their nonspecific adsorption onto bacterial cells, is stronger than that of *E. coli*. This behavior gives additional clues about the different affinities of bacterial cell walls for AuAg NSs and could be used to further tune the hydrophobicity of the coating polymer toward a better selectivity of the assay.

To test the specificity in complex samples, we performed the assay over a suspension of 10^4 CFU/mL *E. coli* in the presence of two different kinds of interfering species. To check the specificity in the presence of large bio-macromolecules, the assay was run first in a duplicate experiment in human serum (Figure 4B, human serum), given the potential applicability of this assay in biological samples, and in the presence of humic acid (4 mg/L) (Figure 4B, HA), the major component of river waters' total organic carbon,[39] for application in environmental sensing. In the first case, the oxidation current peak at +0.16 V vs Ag/AgCl decreased in comparison to the control sample (Figure 4B, AuAg NSs), probably due to the formation of a protein corona around AuAg NSs,[40] which could either hinder the electron transfer to the electrode or directly lower the hollow nanocrystals' affinity for the macromolecules expressed onto the bacteria cell wall. Because the electrochemical quenching was not complete, this issue could be easily overcome by tuning the amount of AuAg NSs used in the assay to obtain a stronger current. In the case of humic acid instead, even though a slight decrease in the average intensity is observed, AuAg NSs seem to preserve their electrochemical properties, possibly due to the different chemical nature of humic substances, which makes them more stable in a solution and less prone to adsorption.[39] A second set of experiment was run to test the resilience of the assay to the presence of heavy metals, a common contaminant in river waters. Copper and mercury (2 and 0.006 mg/L, respectively)[41] salts were therefore chosen as interfering species because their oxidation potentials fall well within the potential window used in the assay. The electrochemical properties of AuAg NSs were this time completely quenched, both in the presence of metals and when either of them was used. Hg^{2+} was shown to quench the redox behavior completely, whereas Cu^{2+} resulted in a milder suppression. This effect can be easily explained taking into account the formation of amalgams between these cations and the noble metals, Au and Ag, constituting of the hollow nanostructures, as well as other deposition effects.[42,43]

CONCLUSIONS

In this work, we propose a low-cost strategy for the simple and rapid detection of bacterial cells in biological matrixes based on the use of hollow AuAg NSs as novel electrochemical reporters. Through a rapid electrochemical test (<10 min), the model bacterial strain *E. coli* was quantified down to a concentration of 10^2 CFU/mL using low-cost, one-use SCPEs as the sensing platform. The protocol developed does not need any additional reagent, substrate, or redox enzyme for generating the electrochemical signal, which is provided in situ by the controlled corrosion of AuAg NSs caused by the matrix salinity. Moreover, discrimination between *E. coli* and *S. typhimurium* was achieved without the use of any biological receptor but through nonspecific affinity interactions between the microorganism cell wall and AuAg NSs' surface, providing selectivity at a minimal operative and reagents cost. This work provides a promising proof of concept for the development of low-cost, rapid electrochemical assay for bacteria quantification able to compete with conventional costly and time-consuming laboratory analyses.

EXPERIMENTAL SECTION

Silver nitrate ($AgNO_3$), trisodium citrate ($Na_3C_6H_5O_7$), tannic acid ($C_{76}H_{52}O_{46}$), $HAuCl_4 \cdot 3H_2O$ (99%), poly(vinyl pyrrolidone) $(C_6H_9NO)_n$ $M_w \approx 55\,000$ (PVP), human serum, and humic acid were purchased from Sigma-Aldrich. Copper nitrate trihydrate and mercury nitrate standard solutions were purchased from Panreac. All the chemicals were used as received without further purification. Distilled water passed through a Millipore system ($\rho = 18.2$ MΩ) was used in all the experiments. All the glassware were first rinsed with acetone and then with Millipore water before use. Buffers solutions were prepared in Milli-Q water obtained from a Millipore system Vent Filter MPK01. Both buffers, phosphate buffer (PB) and phosphate buffer saline (PBS), were prepared at a concentration of 0.01 M and at pH 7.4. PB was prepared by mixing sodium-phosphate monobasic hydrogen along with sodium-phosphate dibasic hydrogen in the desired proportion; PBS was purchased from Sigma-Aldrich in tablets.

Screen printed carbon electrodes (SPCEs) were fabricated with a semiautomatic screen-printing machine DEK248 (DEK International, Switzerland). Electrodes were printed over Autostat HT5 polyester sheets (McDermid Autotype, U.K.) using Carbon Sensor Paste C2030519P4 for working and counter electrodes, Gray Dielectric Paste D2070423P5 silver/silver chloride ink for reference electrode, and Minico 7000 Blue insulating ink (Acheson Industries, The Netherlands) to insulate the contacts and define the sample interaction area.

All the nanoparticles were characterized by UV−vis spectroscopy (Perkin-Elmer "Lambda25"), dynamic light scattering (Malvern Zetasizer), transmission electron microscopy (TEM), and scanning electron microscopy (SEM) (FEI Magellan 400L). The high-resolution TEM images were obtained using a FEI Tecnai F20 field-emission gun microscope with a 0.19 nm point-to-point resolution operated at 200 keV.

The electrochemical experiments were performed by AUTOLAB PGSTAT302N (Echo Chemie, The Netherlands) potentiostat/galvanostat, which was connected to a computer and monitored by GPES software. All the experiments were performed at room temperature. The SCPEs were connected with the potentiostat through a homemade connector. The

general protocol for the electrochemical measurements of nanoparticles (NPs)-containing samples is as follows: 10 μL of AuAg NSs suspension at a nominal concentration of 1.6×10^{11} NPs/mL, unless specified otherwise, were transferred into a plastic 1.5 mL Eppendorf tube containing 50 μL of a bacteria suspension in PBS 10 mM pH 7.4 with a given bacteria colony forming units (CFU)/mL. After incubation in the saline matrix for a given time and under stirring at 600 rpm in a thermoshaker at 25 °C, 50 μL of the mixture was displaced onto the SPCE so as to cover the three electrodes. Differential pulsed voltammetry (DPV) was run: after applying a fixed deposition negative potential for 60 s, voltage was scanned between −0.05 and +0.4 V with 0.01 V step potential. Cyclic voltammetries were recorded in the same conditions scanning from −0.8 to +0.3 V at 100 mV/s scan rate with 0.005 V step potential.

E. coli O157:H7 (CECT 4783) and *Salmonella enterica* subsp. *enterica* serovar Typhimurium LT2 (CECT 722 T) strains were obtained from "Colección Española de Cultivos Tipo" (CECT). *E. coli* stock cultures were kept in trypticase soy agar (TSA) sloped tubes at 4 °C and stored in these conditions no longer than 2 months. To start up the culture, some *E. coli* colonies were transferred from TSA to trypticase soy broth tubes at 37 °C for 24 h for bacterial growth. Next day, a small fraction of the new grown bacterial culture was taken with a loop ($\approx$1 μL) and carried to a TSA plate. Again, bacteria were allowed to grow at 37 °C for 24 h. Finally, a glass tube was filled up with 0.01 M PBS and some colonies were introduced into the tube. Bacteria solution was vortexed and OD was measured using McFarland standards: a value of 0.5 indicated a bacterial density of around 1.5×10^8 CFU/mL. *E. coli* living cells were eventually subjected to a sharp temperature increase (80 °C) for 20 min to kill without compromising the outer cell wall structure. The same process was carried out for *Salmonella* strain.

ASSOCIATED CONTENT

Ⓢ Supporting Information

The Supporting Information is available free of charge on the ACS Publications website at DOI: 10.1021/acsomega.8b02458.

Stability study for AuAg NSs; stability study for Ag/AgCl pseudoreference electrode; Z-potential of AuAg NSs; dilution method for electrochemical assay; multi-component samples analysis (PDF)

AUTHOR INFORMATION

Corresponding Author
*E-mail: arben.merkoci@icn2.cat.

ORCID Ⓘ
Arben Merkoçi: 0000-0003-2486-8085

Notes
The authors declare no competing financial interest.

ACKNOWLEDGMENTS

REFERENCES

(1) World Health Organization. *Global Action Plan on Antimicrobial Resistance*; WHO Press, 2015; pp 1−28.

(2) Drain, P. K.; Hyle, E. P.; Noubary, F.; Freedberg, K. A.; Wilson, D.; Bishai, W. R.; Rodriguez, W.; Bassett, I. V. Diagnostic Point-of-Care Tests in Resource-Limited Settings. *Lancet Infect. Dis.* 2014, 14, 239−249.

(3) Huang, X.; Liu, Y.; Yung, B.; Xiong, Y.; Chen, X. Nanotechnology-Enhanced No-Wash Biosensors for In Vitro Diagnostics of Cancer. *ACS Nano* 2017, 11, 5238−5292.

(4) Lee, W. G.; Kim, Y.-G.; Chung, B. G.; Demirci, U.; Khademhosseini, A. Nano/Microfluidics for Diagnosis of Infectious Diseases in Developing Countries. *Adv. Drug Delivery Rev.* 2010, 62, 449−457.

(5) Polavarapu, L.; Liz-Marzán, L. M. Towards Low-Cost Flexible Substrates for Nanoplasmonic Sensing. *Phys. Chem. Chem. Phys.* 2013, 15, 5288−5300.

(6) Bülbül, G.; Hayat, A.; Andreescu, S. Portable Nanoparticle-Based Sensors for Food Safety Assessment. *Sensors* 2015, 15, 30736−30758.

(7) Qiu, H.-J.; Li, X.; Xu, H.-T.; Zhang, H.-J.; Wang, Y. Nanoporous Metal as a Platform for Electrochemical and Optical Sensing. *J. Mater. Chem. C* 2014, 2, 9788−9799.

(8) Ambrosi, A.; Merkoçi, A.; de la Escosura-Muñiz, A. Electrochemical Analysis with Nanoparticle-Based Biosystems. *TrAC, Trends Anal. Chem.* 2008, 27, 568−584.

(9) Kelley, S. O.; Mirkin, C. A.; Walt, D. R.; Ismagilov, R. F.; Toner, M.; Sargent, E. H. Advancing the Speed, Sensitivity and Accuracy of Biomolecular Detection Using Multi-Length-Scale Engineering. *Nat. Nanotechnol.* 2014, 9, 969−980.

(10) Huckle, D. Point-of-Care Diagnostics: Will the Hurdles Be Overcome This Time? *Expert Rev. Med. Devices* 2006, 3, 421−426.

(11) El Harrad, L.; Bourais, I.; Mohammadi, H.; Amine, A. Recent Advances in Electrochemical Biosensors Based on Enzyme Inhibition for Clinical and Pharmaceutical Applications. *Sensors* 2018, 18, 164.

(12) Rocchitta, G.; Spanu, A.; Babudieri, S.; Latte, G.; Madeddu, G.; Galleri, G.; Nuvoli, S.; Bagella, P.; Demartis, M. I.; Fiore, V.; et al. Enzyme Biosensors for Biomedical Applications: Strategies for Safeguarding Analytical Performances in Biological Fluids. *Sensors* 2016, 16, 780.

(13) Kotov, N. A. Inorganic Nanoparticles as Protein Mimics. *Science* 2010, 330, 188−189.

(14) Cheng, H.; Lin, S.; Muhammad, F.; Lin, Y. W.; Wei, H. Rationally Modulate the Oxidase-like Activity of Nanoceria for Self-Regulated Bioassays. *ACS Sens.* 2016, 1, 1336−1343.

(15) Wang, C.; Chen, W.; Chang, H. Enzyme Mimics of Au/Ag Nanoparticles for Fluorescent Detection of Acetylcholine. *Anal. Chem.* 2012, 84, 9706−9712.

(16) Russo, L.; Puntes, V.; Merkoçi, A. Tunable Electrochemistry of Gold-Silver Alloy Nanoshells. *Nano Res.* 2018, 6336.

(17) Wang, Y.; Salehi, M.; Schütz, M.; Schlücker, S. Femtogram Detection of Cytokines in a Direct Dot-Blot Assay Using SERS Microspectroscopy and Hydrophilically Stabilized Au-Ag Nanoshells. *Chem. Commun.* 2014, 50, 2711−2714.

(18) Jang, H.; Kim, D. E.; Min, D. H. Self-Assembled Monolayer Mediated Surface Environment Modification of Poly-(Vinylpyrrolidone)-Coated Hollow Au-Ag Nanoshells for Enhanced Loading of Hydrophobic Drug and Efficient Multimodal Therapy. *ACS Appl. Mater. Interfaces* 2015, 7, 12789−12796.

(19) Miranda, O. R.; Li, X.; Garcia-Gonzalez, L.; Zhu, Z. J.; Yan, B.; Bunz, U. H. F.; Rotello, V. M. Colorimetric Bacteria Sensing Using a Supramolecular Enzyme-Nanoparticle Biosensor. *J. Am. Chem. Soc.* 2011, 133, 9650−9653.

(20) Chen, J.; Andler, S. M.; Goddard, J. M.; Nugen, S. R.; Rotello, V. M. Integrating Recognition Elements with Nanomaterials for Bacteria Sensing. *Chem. Soc. Rev.* **2017**, *46*, 1272−1283.

(21) Chen, J.; Jiang, Z.; Ackerman, J. D.; Yazdani, M.; Hou, S.; Nugen, S. R.; Rotello, V. M. Electrochemical Nanoparticle−enzyme Sensors for Screening Bacterial Contamination in Drinking Water. *Analyst* **2015**, *140*, 4991−4996.

(22) Russo, L.; Merkoçi, F.; Patarroyo, J.; Piella, J.; Merkoçi, A.; Bastús, N. G.; Puntes, V. Time- and Size-Resolved Plasmonic Evolution with Nm Resolution of Galvanic Replacement Reaction in AuAg Nanoshells Synthesis. *Chem. Mater.* **2018**, *30*, 5098−5107.

(23) Wan, Y.; Zhou, Y.-G.; Poudineh, M.; Safaei, T. S.; Mohamadi, R. M.; Sargent, E. H.; Kelley, S. O. Highly Specific Electrochemical Analysis of Cancer Cells Using Multi-Nanoparticle Labeling. *Angew. Chem., Int. Ed.* **2014**, *53*, 13145−13149.

(24) Zheng, Y.; Zeng, J.; Ruditskiy, A.; Liu, M.; Xia, Y. Oxidative Etching and Its Role in Manipulating the Nucleation and Growth of Noble-Metal Nanocrystals. *Chem. Mater.* **2014**, *26*, 22−33.

(25) Cloake, S. J.; Toh, H. S.; Lee, P. T.; Salter, C.; Johnston, C.; Compton, R. G. Anodic Stripping Voltammetry of Silver Nanoparticles: Aggregation Leads to Incomplete Stripping. *ChemistryOpen* **2015**, *4*, 22−26.

(26) Douglas, F.; Yañez, R.; Ros, J.; Marín, S.; De La Escosura-Muñiz, A.; Alegret, S.; Merkoçi, A. Silver, Gold and the Corresponding Core Shell Nanoparticles: Synthesis and Characterization. *J. Nanopart. Res.* **2008**, *10*, 97−106.

(27) Toh, H. S.; Batchelor-McAuley, C.; Tschulik, K.; Compton, R. G. Electrochemical Detection of Chloride Levels in Sweat Using Silver Nanoparticles: A Basis for the Preliminary Screening for Cystic Fibrosis. *Analyst* **2013**, *138*, 4292−4297.

(28) Kleijn, S. E. F.; Lai, S. C. S.; Koper, M. T. M.; Unwin, P. R. Electrochemistry of Nanoparticles. *Angew. Chem., Int. Ed.* **2014**, *53*, 3558−3586.

(29) Tamerat, N.; Muktar, Y. Application of Molecular Diagnostic Techniques for the Detection of *E. coli* O157:H7: A Review. *J. Vet. Sci. Technol.* **2016**, *7*, 362.

(30) Jiang, Z.; Le, N. D. B.; Gupta, A.; Rotello, V. M. Cell Surface-Based Sensing with Metallic Nanoparticles. *Chem. Soc. Rev.* **2015**, *44*, 4264−4274.

(31) Feng, Z. V.; Gunsolus, I. L.; Qiu, T. A.; Hurley, K. R.; Nyberg, L. H.; Frew, H.; Johnson, K. P.; Vartanian, A. M.; Jacob, L. M.; Lohse, S. E.; et al. Impacts of Gold Nanoparticle Charge and Ligand Type on Surface Binding and Toxicity to Gram-Negative and Gram-Positive Bacteria. *Chem. Sci.* **2015**, *6*, 5186−5196.

(32) Sepunaru, L.; Tschulik, K.; Batchelor-McAuley, C.; Gavish, R.; Compton, R. G. Electrochemical Detection of Single *E. coli* Bacteria Labeled with Silver Nanoparticles. *Biomater. Sci.* **2015**, *3*, 816−820.

(33) Hassan, A. R. H. A. A.; de la Escosura-Muñiz, A.; Merkoçi, A. Highly Sensitive and Rapid Determination of *Escherichia coli* O157: H7 in Minced Beef and Water Using Electrocatalytic Gold Nanoparticle Tags. *Biosens. Bioelectron.* **2015**, *67*, 511−515.

(34) El Badawy, A. M.; Silva, R. G.; Morris, B.; Scheckel, K. G.; Suidan, M. T.; Tolaymat, T. M. Surface Charge-Dependent Toxicity of Silver Nanoparticles. *Environ. Sci. Technol.* **2011**, *45*, 283−287.

(35) Song, J. E.; Phenrat, T.; Marinakos, S.; Xiao, Y.; Liu, J.; Wiesner, M. R.; Tilton, R. D.; Lowry, G. V. Hydrophobic Interactions Increase Attachment of Gum Arabic- and PVP-Coated Ag Nanoparticles to Hydrophobic Surfaces. *Environ. Sci. Technol.* **2011**, *45*, 5988−5995.

(36) Bondarenko, O.; Ivask, A.; Käkinen, A.; Kurvet, I.; Kahru, A. Particle-Cell Contact Enhances Antibacterial Activity of Silver Nanoparticles. *PLoS One* **2013**, *8*, No. e64060.

(37) Sousa, C.; Sequeira, D.; Kolen'Ko, Y. V.; Pinto, I. M.; Petrovykh, D. Y. Analytical Protocols for Separation and Electron Microscopy of Nanoparticles Interacting with Bacterial Cells. *Anal. Chem.* **2015**, *87*, 4641−4648.

(38) MacKenzie, D. A.; Sherratt, A. R.; Chigrinova, M.; Kell, A. J.; Pezacki, J. P. Bioorthogonal Labelling of Living Bacteria Using Unnatural Amino Acids Containing Nitrones and a Nitrone Derivative of Vancomycin. *Chem. Commun.* **2015**, *51*, 12501−12504.

(39) Frimmel, F. Aquatic Humic Substances. In *Biopolymers, Volume 1: Lignin, Humic Substances and Coal*; Wiley-VCH, 2001; pp 301−310.

(40) Barbero, F.; Russo, L.; Vitali, M.; Piella, J.; Salvo, I.; Borrajo, M. L.; Busquets-Fité, M.; Grandori, R.; Bastús, N. G.; Casals, E.; et al. Formation of the Protein Corona: The Interface between Nanoparticles and the Immune System. *Semin. Immunol.* **2017**, *34*, 52−60.

(41) Gorchev, H. G.; Ozolins, G. WHO Guidelines for Drinking-Water Quality. *WHO Chron.* **1984**, *38*, 104−108.

(42) Li, L.; Feng, D.; Fang, X.; Han, X.; Zhang, Y. Visual Sensing of Hg2+ Using Unmodified Au@Ag Core−shell Nanoparticles. *J. Nanostructure Chem.* **2014**, *4*, 117.

(43) Price, S. W. T.; Speed, J. D.; Kannan, P.; Russell, A. E. *Exploring the First Steps in Core − Shell Electrocatalyst Preparation: In Situ Characterization of Cu and Pd Shells on Supported Au Nanoparticles* **2011**, *133*, 19448−19458.

Straightforward Immunosensing Platform Based on Graphene Oxide-Decorated Nanopaper: A Highly Sensitive and Fast Biosensing Approach

Nopchulee Cheeveewattanagul, Eden Morales-Narváez, Abdel-Rahim H. A. Hassan, José Francisco Bergua, Werasak Surareungchai, Mithran Somasundrum, and Arben Merkoçi*

Immunoassays are nowadays a crucial tool for diagnostics and drug development. However, they often involve time-consuming procedures and need at least two antibodies in charge of the capture and detection processes, respectively. This study reports a nanocomposite based on graphene oxide-coated nanopaper (GONAP) facilitating an advantageous immunosensing platform using a single antibody and without the need for washing steps. The hydrophilic, porous, and photoluminescence-quenching character of GONAP allows for the adsorption and quenching of photoluminescent quantum dots nanocrystals complexed with antibodies (Ab-QDs), enabling a ready-to-use immunosensing platform. The photoluminescence is recovered upon immuno-complex (antibody-antigen) formation which embraces a series of interactions (hydrogen bonding, electrostatic, hydrophobic, and Van der Waals interactions) that trigger desorption of the antigen-Ab-QD complex from GONAP surface. However, the antigen is then attached onto the GONAP surface by electrostatic interactions leading to a spacer (greater than ≈20 nm) between Ab-QDs and GONAP and thus hindering nonradiative energy transfer. It is demonstrated that this simple—yet highly sensitive—platform represents a virtually universal immunosensing approach by using small-sized and big-sized targets as model analytes, those are, human-IgG protein and *Escherichia coli* bacteria. In addition, the assay is proved effective in real matrices analysis, including human serum, poultry meat, and river water. GONAP opens the way to conceptually new paper-based devices for immunosensing, which are amenable to point of care applications and automated diagnostics.

1. Introduction

Immunoassays capitalize on the selectivity and sensitivity of antibody–antigen interactions so as to capture and detect analytes in biological or environmental samples.[1] Being highly specific techniques, immunoassays are the most extensively used detection approaches for the analytical determination of clinically relevant biomarkers.[2,3] They are also important drug screening platforms and prominent proteomic tools.[4,5] Consequently, they are a corner-stone in diagnostics and biological research. In fact, there are different configurations (direct, indirect, sandwich, competitive) and various technologies exploiting immunoassays such as microarray, lateral flow, and enzyme-linked immunosorbent assay.[1] Nevertheless, they often require time-consuming labors (e.g., multiple washing steps) and/or at least two antibodies in charge of the capture and detection of the analyte, respectively. In addition, most of them are not particularly easy-to-use or amenable to portability.[6] Given this paucity,

N. Cheeveewattanagul, Dr. E. Morales-Narváez, Dr. A.-R. H. A. Hassan, J. F. Bergua, Prof. A. Merkoçi
Nanobioelectronics and Biosensor Group
Catalan Institute of Nanoscience and Nanotechnology (ICN2)
CSIC and BIST
Campus UAB, Bellaterra, 08193 Barcelona, Spain
E-mail: arben.merkoci@icn2.cat

N. Cheeveewattanagul, Dr. W. Surareungchai
Division of Biotechnology
School of Bioresources and Technology
King Mongkut's University of Technology Thonburi
Bangkhuntien Campus, Bangkok 10150, Thailand

Dr. E. Morales-Narváez
Biophotonic Nanosensors Laboratory
Centro de Investigaciones en Óptica A. C
Loma del Bosque 115, Lomas del Campestre
León, Guanajuato 37150, Mexico

Dr. A.-R. H. A. Hassan
Food Hygiene Department
Faculty of Veterinary Medicine
Beni-Suef University
Beni-Suef 62511, Egypt

Dr. W. Surareungchai
Nanoscience & Nanotechnology Graduate Program
King Mongkut's University of Technology Thonburi
Bangkhuntien Campus, Bangkok 10150, Thailand

Dr. M. Somasundrum
Biochemical Engineering and Pilot Plant Research
and Development Unit
National Center for Genetic Engineering and Biotechnology
National Science and Technology Development Agency
at King Mongkut's University of Technology Thonburi
(Bangkhuntien Campus)
Bangkok 10150, Thailand

Prof. A. Merkoçi
ICREA – Institució Catalana de Recerca i Estudis Avancats
Barcelona 08010, Spain

The ORCID identification number(s) for the author(s) of this article can be found under https://doi.org/10.1002/adfm.201702741.

ADVANCED
SCIENCE NEWS
www.advancedsciencenews.com

**ADVANCED
FUNCTIONAL
MATERIALS**
www.afm-journal.de

the technological and scientific community is actively working on the development of cost-efficient and simple approaches facilitating innovative immunosensing approaches.[7–15]

We have previously reported bacterial cellulose nanopaper as an advantageous biosensing platform, since it offers a myriad of outstanding properties,[16,17] including environmental sustainability, biodegradability, excellent chemical-modification capabilities (so as to be functionalized), optical transparency, and several other physicochemical properties (low density, hydrophilicity, high porosity, high flexibility, high surface area, and high crystallinity).[18,19] Moreover, we have been studying the interaction between photoexcited quantum dots and graphene oxide (GO), offering innovative approaches in biosensing based on nonradiative energy transfer, which is highly efficient due to the high surface area and excellent photoluminescence-quenching nature exhibited by GO,[20] even when compared with other carbon forms.[21] Herein, we engineered a hydrophilic, porous, and photoluminescence-quenching nanohybrid material made of graphene oxide-coated nanopaper (GONAP). Although the optical properties of GO have been exploited in several immunosensing systems, they often require both, a capture antibody and a detection antibody.[22,23] GONAP represents an advantageous immunosensing platform that uses a single antibody and requires no-washing steps. This nanocomposite facilitates adsorption and quenching of photoluminecent quantum dots nanocrystals conjugated with antibodies (Ab-QDs), allowing a ready-to-use immunosensing platform. As the immunocomplex creation involves hydrogen bonding, electrostatic, hydrophobic, and Van der Waals interactions, the complex antigen-Ab-QDs undergo a desorption from GONAP surface upon immunocomplex formation and the photoluminescence is then recovered given that the antigen is anchored onto the GONAP surface by electrostatic, π–π stacking and hydrogen bonding interactions. Specifically, given the moieties of GO, such as hydroxyl and carboxyl groups, and the hydroxyl groups of nanopaper, hydrogen bonding between GONAP and hydroxyl and amino groups present in the analytes (or Ab-QDs) is also able to occur. These phenomena lead to a spacer (greater than $\approx$20 nm) between Ab-QDs and GONAP, which avoids highly efficient nonradiative energy transfer. Thus, the fluorescence recovery is proportional to the analyte concentration. The operational concept of this immunosensing platform is depicted in **Figure 1**. To demonstrate that this immunosensing platform is technically sound for small-sized and big-sized targets detection, we employed human-IgG protein and *Escherichia coli* (*E. coli*) bacteria as model analytes, respectively. Additionally, we performed a series of assays in real matrices such as human serum, poultry meat, and river water to prove the potential effectiveness of the approach in real sample analysis.
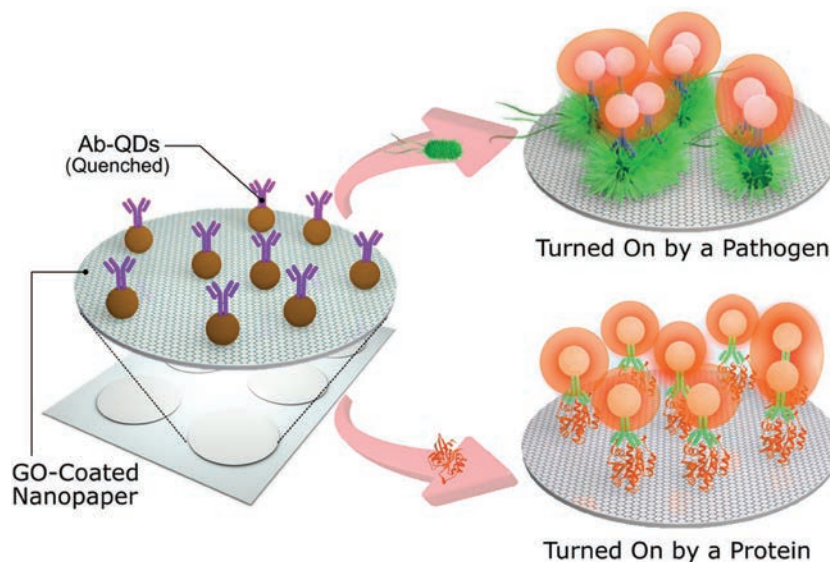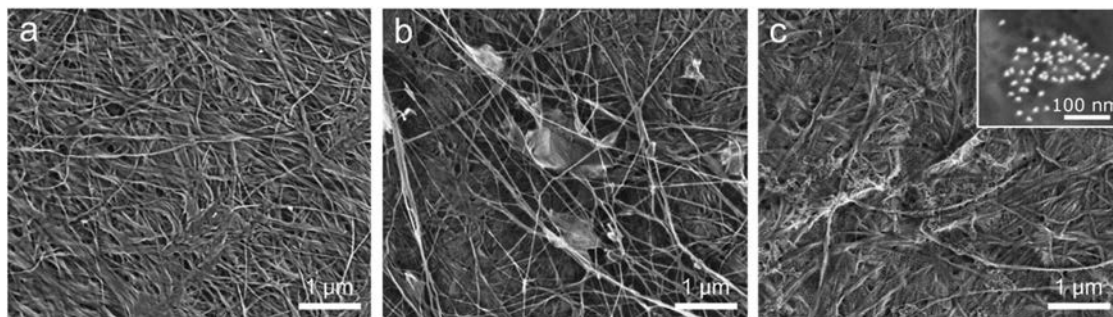

Figure 1. Operational concept of the immunosening approach (schematic representation, not to scale). The hydrophilic, porous, and photoluminescence-quenching character of GONAP allows for the adsorption and quenching of Ab-QDs, whereas photoluminescence recovery is triggered by the immunocomplex formation phenomenon, which involves a series of forces and interactions detaching the antigen-Ab-QD complex. Nevertheless, the antigen is then attached onto GONAP surface working as spacer between GONAP and Ab-QDs and hindering highly efficient nonradiative energy transfer. The immunosensing platform can be turned "On" by either big-sized analytes (pathogens) or small-sized analytes (proteins).

2. GONAP Biosensing Platform

Bacterial cellulose nanopaper (BC, a film of nanocellulose) synthesized by *Acetobacter xylinum* was employed in the proposed immunosensing platform. BC has been previously characterized in terms of average fiber diameter ($\approx$45 $\pm$ 10 nm), fiber length (>10 µm), crystallinity ($\approx$82%), crystallite size ($\approx$6.3 nm), average tensile strength ($\approx$345 MPa), Young's modulus ($\approx$17.3 GPa), and strain-at-break ($\approx$7%).[16] A water-based dispersion of single layer GO sheets with average lateral dimension range of $\approx$500 nm and C/O ratio about one unit (supplier's data) was exploited to build the GONAP nanocomposite. As BC exhibits hydroxyl groups onto the surface and GO also has hydroxyl groups onto the basal plane, they can be easily coupled via hydrogen bonding (see the Experimental Section). Streptavidin-decorated CdSe@ZnS QDs with an average size $\approx$14 $\pm$ 2 nm and a maximum emission wavelength at $\approx$665 nm were employed as photoluminecent agents in the proposed immunosensing platform. Scanning electron microscopy (SEM) micrographs of bare BC, GONAP, and Ab-QDs-GONAP are shown in **Figure 2**, respectively.

Various concentrations of GO decorating BC were evaluated and compared with bare BC in order to select the most efficient photoluminescence-quenching concentration judiciously. Herein, 150 µg mL^{-1} of GO in milliQ water was selected as the optimum concentration and the most appropriate for the immunosensing platform (see Figures S1 and S2 in the Supporting Information), which achieved the maximum quenching efficiency (around 50%) when compared with bare BC. Additionally, the concentration of QDs and anti-*E. coli* antibody

**ADVANCED
SCIENCE NEWS**

www.advancedsciencenews.com

**ADVANCED
FUNCTIONAL
MATERIALS**

www.afm-journal.de

Figure 2. Scanning-electron micrographs of GONAP platform. a) Bare bacterial cellulose nanopaper. b) GONAP. c) Ab-QDs on GONAP.

and the incubation time for the immunoreaction were carefully selected based on the most sensitive response, taking the analysis of the blank sample as reference. It was found that the optimum concentrations of QDs and Ab are 100×10^{-9} M and 0.9 mg mL^{-1}, respectively. Consequently, [GO] $\approx$ 150 µg mL^{-1}, [QDs] $\approx 100 \times 10^{-9}$ M, and [anti-*E. coli* Ab] $\approx$ 0.9 mg mL^{-1} were employed for sensitive detection of foodborne pathogen (*E. coli* O157:H7). Moreover, the optimum incubation time was 30 min for capturing the target bacteria by the specific Ab. The same aforementioned optimization procedures were carried out for protein detection, whereas the optimum concentrations were $\approx$100 µg mL^{-1}, 100×10^{-9} M, and 0.2 mg mL^{-1} for GO, QDs, and antihuman IgG Ab, respectively, for protein detection, while an optimum incubation period of 2 h was found the most appropriate for protein detection (see Figure S5 in the Supporting Information). It is well known that the suitable incubation time for any immunoreaction strongly depends on the analyte size,[24] thus there is a significant difference between *E. coli* and protein detection in this parameter (*E. coli* size $\approx 0.5 \times 1.5$ µm, human IgG size $\approx$ 12 nm). Although the size of these analytes is completely different, the biosensing mechanism is driven by the same aforementioned principle that eventually leads to a spacer between photoexcited QDs and GONAP (greater than $\approx$20 nm), hindering a highly efficient nonradiative energy transfer phenomenon. Thus, the proposed biosensing system is able to detect both small-sized and big-sized analytes as demonstrated below.

2.1. GONAP for Pathogen Detection

The performance of the proposed immunosensing platform as a pathogen detection device was evaluated by using tenfold serial concentrations of *E. coli* O157:H7 (10–10^6 Colony Forming Unit "CFU" mL^{-1}) in a standard buffer. Blank sample (buffer containing zero bacteria) was studied to distinguish between the presence and the absence of the target analyte. The photoluminescence intensity ratios (F_1/F_0) of the test and the blank spots were estimated in dimensionless units by dividing the final photoluminescence intensity (F_1) into the initial photoluminescence intensity (F_0) of the same GONAP spot, which determine the presence or absence of the target pathogen. Furthermore, the F_1/F_0 ratio allows for the measurement of tiny amounts of the analyte circumventing analytical problems due to the original intensity of F_0, which can be considered the
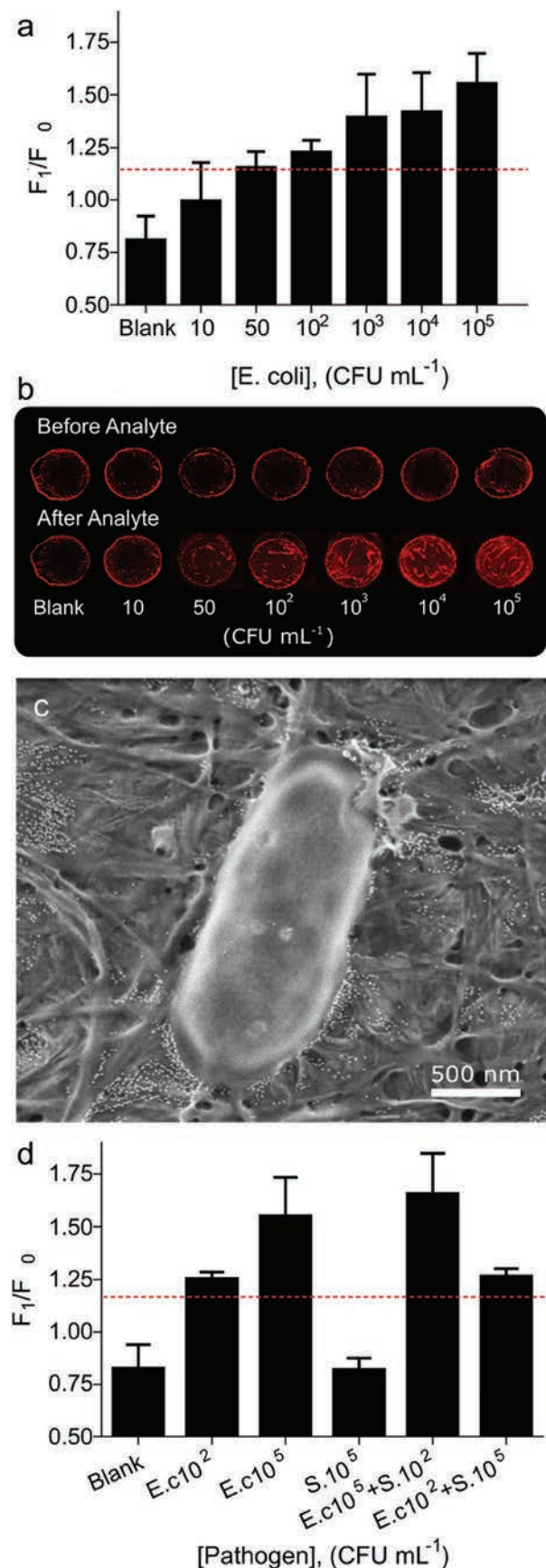
background signal. Given the operational concept of the immunosensing platform, the photoluminescence of the test spots is expected to increase upon addition of the pathogen, whereas that of the blank spots is expected to be relatively constant or decrease slightly due to the removal of the excess of some Ab-QD complexes after the contact with the liquid sample. **Figure 3**a shows how the F_1/F_0 ratio of the analyzed blank sample was around 0.8, while serial dilutions of *E. coli* obtained a F_1/F_0 ratio greater than this value. The proposed immunosensing platform showed a highly sensitive response to the presence of the target bacteria with a wide detection range, from 10 to 10^6 CFU mL^{-1}, where the F_1/F_0 ratio increased gradually with *E. coli* concentration at the range from 10 to 10^5 CFU mL^{-1} with a full saturation of the system at 10^6 CFU mL^{-1}. As experimental evidences, Figure 3b shows images of the photoluminescent performance of GONAP immunosensing platform targeting *E. coli* and Figure 3c displays a SEM micrograph of the platform after adding the target bacteria. Moreover, from that logarithmic response, the estimated detection limit of *E. coli* in standard buffer was about 55 CFU mL^{-1}, which has been calculated by the mean value F_1/F_0 ratio of the blank plus three times its standard deviation, see Figure S10A in the Supporting Information (threshold line).

In order to investigate the effect of washing steps on GONAP immunosensing platform, a series of assays was carried out via GONAP immunosensing platform and washing steps were performed using 100 µL of PBST followed by 100 µL milli-Q water. After discarding the washing solution, a fluctuating response in the F_1/F_0 ratio with serial *E. coli* concentrations has been observed. This could be attributed to the weak attaching forces between GONAP and the complex antigen-Ab-QDs.[25] This fluctuating response is shown in Figure S4 in the Supporting Information. Importantly, we discovered that the overall optimal performance of the proposed immunosensing platform does not require washing steps.

2.1.1. GONAP Specificity in Pathogen Detection

We also explored the specificity of GONAP immunosensing platform targeting *E. coli* in the presence of another nontarget bacterial strain form the same "*Enterobacteriaceae* family." *Salmonella typhimurium* was selected as a nonspecific pathogen for conducting this experiment. Different concentrations of the target and nontarget bacteria were simultaneously analyzed in standard

Figure 3. GONAP immunosensing platform for pathogen detection. a) Overall performance of *E. coli* detection in standard buffer. b) Photoluminescence images of GONAP immunosensing platform (before and after adding different concentrations of pathogen). c) Scanning-electron micrographs of *E. coli* captured by GONAP immunosensing platform. d) Study of the specificity of GONAP immunosensing platform targeting a model pathogen (*E. coli*, *E.c*) in the presence of a nontarget pathogen (*S. typhimurium*, *S.*). The threshold in red (a, d) represents the limit of detection of the proposed device, which was estimated as the mean value of the blank samples plus three times their standard deviation. The error bars represent the standard deviation of at least three replicates.

buffer in order to assess the specificity of the developed assay as follows: (a) blank standard buffer, (b) low concentration of *E. coli* (10^2 CFU mL^{-1}), (c) high concentration of *E. coli* (10^5 CFU mL^{-1}), (d) high concentration of *S. typhimurium* (10^5 CFU mL^{-1}), (e) a mixture of high concentration of *E. coli* (10^5 CFU mL^{-1}) and low concentration of *S. typhimurium* (10^2 CFU mL^{-1}), and (f) a mixture of high concentration of *S. typhimurium* (10^5 CFU mL^{-1}) and low concentration of *E. coli* (10^2 CFU mL^{-1}). It was found, as illustrated in Figure 3d, that the F_1/F_0 ratio of the nontarget pathogen (*S. typhimurium*) even at high concentration was below the threshold of the limit of detection limit (LOD) and very similar to blank one. Additionally, the presence of the nontarget pathogen in the same media with the target one (*E. coli*) does not affect the response of the immunoassay; since the response produced by a mixture of [*E. coli* (10^2 CFU mL^{-1}) + *S. typhimurium* (10^5 CFU mL^{-1})] was very similar to that of *E. coli* (10^2 CFU mL^{-1}) alone, likewise, the response of a mixture [*E. coli* (10^5 CFU mL^{-1}) + *S. typhimurium* (10^2 CFU mL^{-1})] was very close to that of *E. coli* (10^5 CFU mL^{-1}) alone. These results indicate the high specificity and selectivity of the developed immunoassay even in the presence of other competing nonspecific bacteria.

2.1.2. GONAP for Pathogen Detection in Real Samples

Although the application of any developed assay in buffer solution is very important for optimization, the analysis in real samples with minimal sample preparation is crucial in emergent biosensing platforms.[7] Therefore, serial concentrations of *E. coli* O157:H7 were inoculated in poultry meat and river water to be assayed by the proposed GONAP-based pathogen detection platform. Blank solutions of both poultry meat extract and river water were used as a negative control in this experiment. As shown in Figure S5 in the Supporting Information, the F_1/F_0 ratios of the blank solutions of poultry meat extract and river water were around 0.7 and 0.8, respectively. While the presence of the target bacteria increases the F_1/F_0 ratio to higher values. The obtained results illustrated in Figure S5A,B in the Supporting Information show that the proposed pathogen detection platform has a highly sensitive response to the presence of *E. coli* in complex matrices of poultry meat and river water at wide detection ranges accounted for 50–1.5×10^5 CFU g^{-1} and 50–10^5 CFU mL^{-1}, respectively. Whereas, the F_1/F_0 ratios raised gradually with increasing bacterial concentrations with logarithmic responses at the ranges 50–1.5×10^4 CFU g^{-1} and 50–10^4 CFU mL^{-1} in poultry meat and river water, respectively (Figure S5 in the Supporting Information). From these logarithmic responses,

**ADVANCED
SCIENCE NEWS**

www.advancedsciencenews.com

**ADVANCED
FUNCTIONAL
MATERIALS**

www.afm-journal.de

Table 1. Spike and recovery assay results.

Real samples	Spiked bacteria [CFU mL^{-1} or CFU g^{-1}]	F_1/F_0[a] in standard buffer	F_1/F_0[b] in real matrices	Recovery [%]
Poultry meat	10^2	1.145	1.118	97.60
	10^3	1.205	1.184	98.30
	10^4	1.396	1.305	93.47
River water	10^2	1.101	1.061	96.35
	10^3	1.231	1.201	97.60
	10^4	1.359	1.323	97.30

[a]Performed in standard buffer; [b]Performed in real matrices. The experiment was done by spiking 10^2, 10^3, and 10^4 CFU mL^{-1} of *E. coli* in standard buffer, poultry meat, and river water ($n = 3$ for each sample), and the recovery percentages of bacteria from real samples were estimated by comparing with standard buffer.

it was estimated that the limits of detection of *E. coli* in poultry meat and river water are 65 and 70 CFU g or mL^{-1}, respectively. These relatively low limits of detection in real samples without broth enrichment indicate the capability of *E. coli* detection in real food and water samples at levels <1 CFU g^{-1} and 1 CFU mL^{-1}, respectively, after ≈2 h of broth incubation. Although there was a slight influence by the matrix of real samples due to the effect of the microenvironment changes (the local viscosity, pH, ionic strength, polarity, and hydrogen-bonding capability of the matrix) on the photoluminescence of QDs,[26] it does not affect the feasibility of the assay in real samples and confirms the possibility of using this novel immunoassay for pathogen detection in other complex real samples. As detailed in the Supporting Information, recovery tests were performed in order to investigate the accuracy and the performance of the developed immunoassay in complex matrices and standard buffer. These results confirming an acceptable accuracy level of the proposed system are shown in **Table 1**.
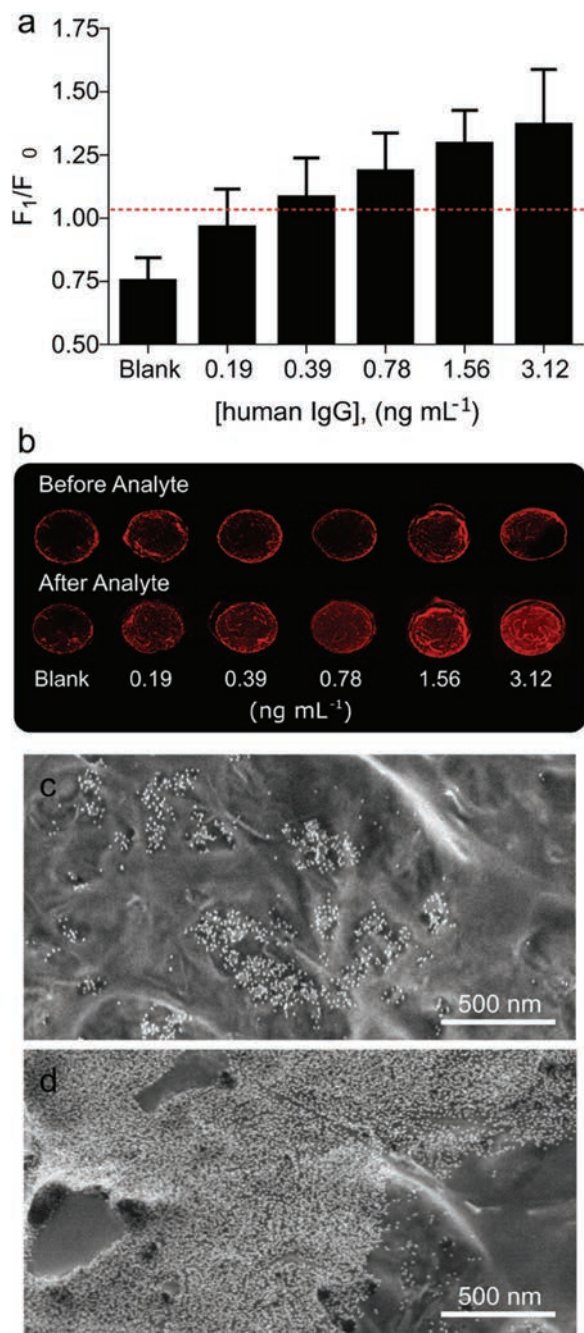
2.2. GONAP for Protein Detection

In addition, we explored the overall performance of GONAP immunosensing platform for the detection of a human protein. Human IgG has been employed as a model protein. First, a polyclonal antihuman IgG antibody (pAb) was used for the immunoassay. Several concentrations of human IgG ranging from 3.125 to 50 ng mL^{-1} in standard buffer were investigated (under optimized condition, Figure S3 in the Supporting Information). As shown in Figure S9 in the Supporting Information, the F_1/F_0 ratio of the blank buffer was around 0.9 units, while the presence of the target analyte (IgG) obtained greater values due to the aforementioned operational principle of the proposed immunosensing system. A detection range from 3.125 to 25 ng mL^{-1} was obtained (Figure S9A in the Supporting Information). A scanned photo of GONAP before and after various amounts of IgG (from top and downward: 3.125, 6.25, 12.5, and 25 ng mL^{-1}) presented that the photoluminescent intensity is correlational with the amount of protein, see Figure S9B in the Supporting Information. From that logarithmic relation, a limit of detection accounted for 1.91 ng mL^{-1} was obtained (Figure S11A in the Supporting Information).

To investigate whether this innovative immunoassay can only be accomplished by integrating polyclonal antibodies or not, a monoclonal antibody targeting human IgG (mAb) was also employed. Interestingly, it was found that GONAP immunosensing platform is also able to operate using monoclonal antibodies. In fact, mAb provided greater fluorescence intensities than those obtained using polyclonal antibodies when both were compared using human IgG concentration of 3.125 ng mL^{-1} (Figure S11D in the Supporting Information). For human IgG detection using mAb, the detection range was 195 pg mL^{-1}–3.125 ng mL^{-1} (**Figure 4**a), and provided a lower limit of detection than that of pAb, accounted for 1.60 ng mL^{-1}, as calculated from the logarithmic response in Figure S11B in the Supporting Information. Importantly, pAb are expected to perform a sandwich-like immunocomplex due to its ability to bind multiple sites of the antigen, whereas mAb cannot perform a sandwich-like configuration due to its ability to bind a single site of the antigen. Hence, these results suggest both, that the complex antigen-Ab-QD is likely to be anchored by the antigen side and that GONAP is also able to anchor sandwich-like immunocomplexes (Figure S6 in the Supporting Information), enforcing the virtually universal operational principle of GONAP immunosensing platform. Moreover, scanning electron microcopy revealed that mAb promotes a higher population density of complexes antigen-Ab-QD upon analyte addition (Figure 4d) when compared to that promoted by using pAb (Figure 4c). This observation clarifies the high sensitivity obtained by using mAb.

The selectivity study of the proposed GONAP-based immunoassay for protein detection was also investigated in the presence of nonspecific immunoglobulin type and using pAb (it should be remarked that polyclonal antibodies are often less specific than monoclonal antibodies). These experiments are described in the Supporting Information, whose results indicate the high specificity of the developed immunoassay using pAb even in the presence of other competing nonspecific type of immunoglobulin (Figure S7 in the Supporting Information). Likewise, we successfully explored the efficiency of the protein sensing platform in complex matrixes by screening different concentrations of human IgG (HIgG) in human serum (Figure S8 in the Supporting Information).

2.2.1. GONAP for Protein Detection in Real Samples

Moreover, in order to compare the performance of the developed immunoassay in real samples and standard buffer, spike and recovery tests were done using human immunoglobulin-depleted serum as a real matrix. Three concentrations of human IgG within the respective detection range were spiked in human immunoglobulin depleted serum samples, and then the recovery percentages from human serum were estimated and compared with those of standard buffer. It was found that the recoveries of human IgG from human serum ranged from 93 to 98%, as listed in **Table 2**. These recovery percentages

**ADVANCED
SCIENCE NEWS**
www.advancedsciencenews.com

**ADVANCED
FUNCTIONAL
MATERIALS**
www.afm-journal.de

Figure 4. GONAP immunosensing platform for protein detection. a) Photoluminescent response for protein detection in standard buffer using monnoclonal antihuman IgG antibody (mAb). b) Experimental evidence (scanned photo) of the photoluminescent intensity on GONAP before and after adding different concentrations of protein. c) Scanning-electron micrograph of human IgG at a concentration of 25 ng mL^{-1} in standard buffer. The target is captured by the protein sensing platform using a polyclonal antibody. d) Scanning-electron micrographs of human IgG at a concentration of 3.12 ng mL^{-1} in standard buffer. The target is captured by the protein sensing platform using a monoclonal antibody.

indicate that the complex matrix of human serum does not affect the reliability of the proposed immunoassay and confirm the possibility of its application in real sample analysis.

Table 2. Spike and recovery assay results in human immunoglobulin (IgG/IgA/IgM/IgE) depleted serum.

Spiked protein (ng mL^{-1})	F_1/F_0 [a]	F_1/F_0 [b]	Recovery [%]
6.25 (pAb)	1.30	1.23	94.35
12.5 (pAb)	1.41	1.36	96.76
25 (pAb)	1.62	1.59	98.46
0.39 (mAb)	1.08	1.01	93.75
0.78 (mAb)	1.18	1.10	93.08
1.56 (mAb)	1.29	1.27	98.66

[a] Performed in standard buffer; [b] Performed in human serum samples. The experiment was done by spiking 6.25, 12.5, and 25 ng mL^{-1} of HIgG in standard buffer and human immunoglobulin IgG/IgA/IgM/IgE depleted serum ($n = 9$ for each sample), and the recovery percentages of protein from human serum depleted immunoglobulin samples were estimated by comparing with standard buffer. (pAb) Performed using a polyclonal antibody. (mAb) Performed using a monoclonal antibody.

3. Conclusion

Taking advantage of the hydrophilic, porous, and photoluminescence-quenching character of GONAP, we developed an advantageous and highly transformative immunosensing platform requiring no-washing steps and exploiting a single antibody. The immonosensing mechanism is triggered by an immunoreaction leading to both desorption of previously anchored Ab-QDs and attachment of the complex antigen-Ab-QD. This configures a spacer (> ~20 nm) between GONAP and the Ab-QDs, disrupting highly efficient nonradiative energy transfer. Fast (30 min), highly sensitive, and selective detection and quantification of a pathogen (*E. coli*) have been recorded at limits of detection accounted for ≈55, 65, and 70 CFU mL^{-1} or g^{-1} in standard buffer, poultry meat, and river water, respectively, without previous broth enrichment. This result indicates the ability to detect <1 CFU mL^{-1} or g^{-1} of *E. coli* after ≈2 h of sample-broth enrichment. Moreover, the proposed device showed a quick (120 min) and sensitive detection of human protein at a detection limit of for 1.60 ng mL^{-1}. In addition, this innovative immunosensing platform is able to show an acceptable level of accuracy (recovery values between 93 and 98%). Although the specificity and sensitivity (in terms of percentage of false positive/negatives, respectively) of this approach has not been determined in the present stage of this research, the successful application of this immunoassay in real matrices analysis opens up innovative capabilities in food, environmental, and biological samples analysis. Additionally, this paper-based platform is easy-to-use, cost-effective, and suitable for portability, point of care applications, automated devices, and multianalyte detection as well.

4. Experimental Section

All commercial reagents were of analytical grade and handled according to the material safety data sheets suggested by the suppliers. BC nanopaper was purchased from Nanonovin Polymer Co. (Mazandaran, Iran). GO was purchased from Angstron Materials (Dayton, OH, U.S.A.). Poly-L-lysine coated glass slides (Cat.No. 22247-1) were purchased from

Polysciences Europe GmbH (Hirschberg an der Bergstrasse, Germany). Anti-*E. coli* antibody (biotin) (pAb, ab68451), sheep antihuman IgG H&L (biotin), and mouse monoclonal H2 antihuman IgG Fc (biotin) (mAb, ab99766) were obtained from Abcam (Cambridge, U.K.), and streptavidin-quantum dot 655 was from Life Technologies (Carlsbad, CA, USA). Phosphate buffered saline (PBS) tablet (P4417), bovine serum albumin (BSA), and Tween-20 were purchased from Sigma-Aldrich (Madrid, Spain). *E. coli* O157:H7 (CECT 4783, *E. coli*) and *Salmonella* enterica subsp. enterica serovar typhimurium LT2 (CECT 722T, *S. typhimurium*) strains were obtained from the Colección Española de Cultivos Tipo (CECT, Valencia, Spain). IgG and IgA from human serum were purchased from Sigma-Aldrich (Madrid, Spain). Human immunoglobulin IgG/IgA/IgM/IgE depleted serum was purchased from Celprogen (Torrance, CA, USA). PBS (10×10^{-3} M, pH 7.4) with 0.5% (v/v) Tween-20 (PBST) containing 1% of BSA fraction V (w/v) was employed as standard buffer. All aqueous solutions were freshly prepared in ultrapure water produced using a Milli-Q system (>18.2 MΩ cm^{-1}) purchased from Millipore. TS-100 Thermo-Shaker (Biosan, Riga, Latvia) was used as the stirrer for modification of QDs with antibodies. An AlphaScan 3.0 microarray scanner (San Leandro, CA, USA) was used to record the photoluminescence images on GONAP surface. A JP Selecta 2000210 oven (JP Selecta s.a., Barcelona, Spain) was used for drying graphene oxide nanocomposites. SEM was performed through a Magellan 400L SEM High Resolution SEM (FEI, Hillsboro, OR, USA).

Synthesis of GONAP: GO was integrated into the BC nanonetwork via hydrogen bonding by taking advantage of the presence of hydroxyl groups exhibited by both BC and GO. To this end, nine pieces of previously sterilized wet BC (size ≈$0.25 \times 0.25 \times 0.1$ cm^3) were washed in 100 mL of hot milliQ water at 60 °C for 30 min under vigorous stirring. Consequently, the water was discarded and 100 mL of graphene oxide suspension (150 µg mL^{-1}) was added to the cellulose nanopaper (see detailed optimization procedure of GO concentration in the Supporting Information) and incubated at 90 °C for 2 h with vigorous stirring. After that, GONAP was separated from the GO suspension and washed five times with milliQ water, which removes unbound GO and ensures a homogeneous distribution of the GO embedded in BC. Finally, the composites were kept to dry in a hot air oven at 50 °C for 30 min. The color change of BC from colorless to dark brown confirms the synthesis of GONAP. Then, the dried composites were kept at room temperature under dark conditions before being used in the immunoassay. SEM was used to characterize and confirm the successful synthesis of the composite.

Conjugation of QDs with Antibodies (Ab): For pathogen detection, QDs were mixed with anti-*E. coli* Ab in a standard buffer to form final concentrations of 100×10^{-9} M for QDs and 900 µg mL^{-1} for Ab. While for protein detection, QDs were mixed with antihuman IgG Ab in the standard buffer to reach final concentrations of 100×10^{-9} M for QDs and 200 µg mL^{-1} for Ab. Subsequently, the conjugation process was carried out by continuous shaking at 650 rpm, and 4 °C for 30 min (see detailed optimization procedure of QDs concentration and the conjugation process in Figures S1–S3 in the Supporting Information).

Bacterial Strains and Inocula Preparation: Freeze-dried cultures of *E. coli* O157:H7 and *S. typhimurium* were revived in Tryptone Soy Broth (Oxoid Ltd., UK) and incubated for 24 h at 37 °C, then transferred onto Tryptone Soy Agar plates (Oxoid Ltd., UK). Stock cultures of both strains were prepared on Tryptone Soy Agar slopes for future use. Afterward, bacterial cell suspensions were prepared directly in sterile PBST and river water, using bacterial colonies from the plates, during the logarithmic phase, to obtain a bacterial load of 1.5×10^8 CFU mL^{-1} according to McFarland standards[27] using Densimat densitometer (Biomerieux, Brazil). Subsequently, tenfold decimal bacterial dilutions ($10–10^8$ CFU mL^{-1}) were prepared from the original one. Finally, heat killing of the inocula was performed by placing the inoculated tubes in a water bath at 90 °C for 15 min to stop bacterial replication. While in case of poultry meat, a tube of heat-killed bacteria (1.5×10^8 CFU mL^{-1}) in sterile PBST was used to prepare tenfold decimal dilutions in poultry extract. The prepared inocula were stored at 4 °C until being used.

Preparation of Poultry Meat Extract: Chicken meat fillets were obtained from a local retail market in Barcelona and analyzed by standard culturing method for the presence of *E. coli*,[28] and only negative samples were selected to be inoculated with bacteria. Twenty-five grams of *E. coli*-free poultry meat was homogenized with 225 mL of sterile PBS in a sterile bag using a stomacher (Lab Blender 400, Seward, UK) for 3 min. Then the homogenate was clarified by filtration using Whatman filter paper, grade 41 (pore size: 20–25 µm) to remove large particles, and finally the filtrate was used as a diluent for preparation of different bacterial inocula.

Preparation of GONAP Immunosensing Platform: A punching tool was used to cut the dried GO–BC composites into small rounded spots (diameter ≈ 0.6 cm), and then these spots were placed onto a poly-L-lysine slide. Consequently, 1.5 µL of the previously prepared QDs-Ab conjugate was dropped on each GONAP spot, and left to dry at room temperature. The initial photoluminescence intensity (F_0) of these spots was measured using a microarray scanner. A silicone gasket was used per each slide to separate each spot/assay.

Using GONAP Immunosensing Platform for E. coli Detection in a Standard Buffer: 100 µL of each dilution of the previously prepared suspensions of *E. coli* O157:H7 in standard buffer ($10–10^6$ CFU mL^{-1}) was pipetted onto each spot of GONAP immunosensing platform, which were placed on the poly-L-lysine slide masked with silicone gasket. In parallel, control spots were prepared using standard buffer free of *E. coli*. Three parallel experiments analyzing the same sample were carried out to ensure repeatability. Then the mixture was incubated at room temperature for 30 min. Afterward, bacterial suspensions were discarded and the test and control spots were left to dry at room temperature before reading the final intensity of the photoluminescence (F_1) using the microarray scanner. ImageJ 1.50i (Wayne Rasband, National Institutes of Health, Maryland, USA) was used to analyze both initial and final photoluminescence intensities to calculate the intensity ratio (F_1/F_0). LOD of the developed immunoassay was estimated by calculating the average F_1/F_0 of blank samples plus three times the standard deviation. The specificity of the assay was evaluated using *S. typhimurium* as nonspecific bacteria (separately and in the presence of *E. coli* O157:H7).

Validating GONAP Immunosensing Platform for E. coli Detection in Real Matrices: The performance of the developed immunosensing platform in bacteria detection was evaluated in complex matrices using poultry meat and river water as model samples. The same aforementioned procedure carried out for *E. coli* inoculated in standard buffer was applied for previously prepared tenfold serial concentrations of *E. coli* O157:H7 inocula in poultry meat and river water; however, the concentration of QDs was increased to 120×10^{-9} M in case of river water. LOD in real samples was estimated by the same above mentioned method in standard buffer.

To assure whether the performance is affected by the difference between the buffer used to prepare the standard curve and the real sample matrix or not, spike and recovery experiment was conducted to assess the precision of the developed immunosensing platform in complex sample types. This experiment was conducted by spiking 10^2, 10^3, and 10^4 CFU mL^{-1} or g of *E. coli* O157:H7 in standard buffer, poultry meat, and river water (three replicates for each bacterial concentration in each sample), and the recovery percentages of the bacteria from real samples (poultry meat and river water) were calculated as compared with the standard buffer.

Using GONAP Immunosensing Platform for Protein Detection in Standard Buffer: The aforementioned procedure of *E. coli* detection was adapted in case of protein (human IgG) detection. Briefly, human IgG was prepared at different concentrations in the standard buffer (3.125–100 ng mL^{-1}) and stored in the fridge at 4 °C until use. 100 µL of the analyte suspensions were added on the previously prepared spots of GONAP immunosensing platform for human IgG. After incubation for 2 h at room temperature, the analyte suspension was discarded and the spots were left to dry at room temperature before reading the final photoluminescence intensity using a microarray scanner. Afterward, the analysis of the images and calculation of the LOD of IgG were done by the same above-mentioned methods used in *E. coli* detection. The

ADVANCED
SCIENCE NEWS
www.advancedsciencenews.com

ADVANCED
FUNCTIONAL
MATERIALS
www.afm-journal.de

specificity of the assay was evaluated using human IgA as a nontarget protein (separately and in a mixture with human IgG).

Validating GONAP Immunosensing Platform for Protein Detection in Human Serum: The performance of the developed immunosensing platform for protein detection was evaluated in complex real matrices using human immunoglobulin-depleted serum as a real matrix. The same aforementioned procedure carried out with human IgG inoculated in standard buffer was conducted for various concentrations of human IgG (7–700 ng mL^{-1}) in human immunoglobulin-depleted serum. The LOD of human IgG in human serum was estimated by the same abovementioned method in *E. coli* detection. Similar to *E. coli* detection procedures, a spike and recovery test was conducted for IgG by spiking 6.25, 12.5, and 25 ng mL^{-1} of IgG in both standard buffer and human immunoglobulin-depleted serum (at least three replicates for each protein concentration) and the recovery percentages of protein from human serum were calculated as compared with standard buffer.

Supporting Information

Supporting Information is available from the Wiley Online Library or from the author.

Acknowledgements

Conflict of Interest

The authors declare no conflict of interest.

Keywords

[1] D. Wild, in *The Immunoassay Handbook*, 4th ed., Elsevier, Oxford, **2013**, pp. 7–10.

[2] M. C. Brown, in *Lateral Flow Immunoassay* (Eds: R. Wong, H. Tse), Humana Press, Totowa, NJ, **2009**, pp. 1–16.

[3] Y. Wang, R. Vaidyanathan, M. J. A. Shiddiky, M. Trau, *ACS Nano* **2015**, *9*, 6354.

[4] I. Wright, J. E. Van Eyk, *Clin. Chem.* **2016**, *63*, 245.

[5] A. G. Paulovich, J. R. Whiteaker, *Nat. Biotechnol.* **2016**, *34*, 1033.

[6] B. Berg, B. Cortazar, D. Tseng, H. Ozkan, S. Feng, Q. Wei, R. Y.-L. Chan, J. Burbano, Q. Farooqui, M. Lewinski, D. Di Carlo, O. B. Garner, A. Ozcan, *ACS Nano* **2015**, *9*, 7857.

[7] A. P. F. Turner, *Chem. Soc. Rev.* **2013**, *42*, 3184.

[8] R. de la Rica, M. M. Stevens, *Nat. Nanotechnol.* **2012**, *7*, 821.

[9] Y. Song, W. Wei, X. Qu, *Adv. Mater.* **2011**, *23*, 4215.

[10] Y. Zhang, Y. Guo, Y. Xianyu, W. Chen, Y. Zhao, X. Jiang, *Adv. Mater.* **2013**, *25*, 3802.

[11] E. Morales-Narváez, L. Baptista-Pires, A. Zamora-Gálvez, A. Merkoçi, *Adv. Mater.* **2017**, *29*, 1604905.

[12] E. Waltz, *Nat. Biotechnol.* **2017**, *35*, 11.

[13] K. Yamada, T. G. Henares, K. Suzuki, D. Citterio, *Angew. Chem. Int. Ed.* **2015**, *54*, 5294.

[14] C. S. Jeon, I. Hwang, T. D. Chung, *Adv. Funct. Mater.* **2013**, *23*, 1484.

[15] Y. Zhu, K. Kekalo, C. NDong, Y.-Y. Huang, F. Shubitidze, K. E. Griswold, I. Baker, J. X. J. Zhang, *Adv. Funct. Mater.* **2016**, *26*, 3953.

[16] E. Morales-Narváez, H. Golmohammadi, T. Naghdi, H. Yousefi, U. Kostiv, D. Horák, N. Pourreza, A. Merkoçi, *ACS Nano* **2015**, *9*, 7296.

[17] B. Heli, E. Morales-Narváez, H. Golmohammadi, A. Ajji, A. Merkoçi, *Nanoscale* **2016**, *8*, 7984.

[18] D. Klemm, F. Kramer, S. Moritz, T. Lindström, M. Ankerfors, D. Gray, A. Dorris, *Angew. Chem. Int. Ed.* **2011**, *50*, 5438.

[19] H. Golmohammadi, E. Morales-Narváez, T. Naghdi, A. Merkoçi, *Chem. Mater.* **2017**, *29*, 5426.

[20] E. Morales-Narváez, A.-R. Hassan, A. Merkoçi, *Angew. Chem. Int. Ed.* **2013**, *52*, 13779.

[21] E. Morales-Narváez, B. Pérez-López, L. B. Pires, A. Merkoçi, *Carbon* **2012**, *50*, 2987.

[22] M. Liu, H. Zhao, X. Quan, S. Chen, X. Fan, *Chem. Commun.* **2010**, *46*, 7909.

[23] J. H. T. Luong, S. K. Vashist, *Biosens. Bioelectron.* **2017**, *89*, 293.

[24] E. P. Diamandis, T. K. Christopoulos, *Immunoassay*, Academic Press, San Deigo, **1996**.

[25] J.-L. Chen, X.-P. Yan, K. Meng, S.-F. Wang, *Anal. Chem.* **2011**, *83*, 8787.

[26] U. Resch-Genger, M. Grabolle, S. Cavaliere-Jaricot, R. Nitschke, T. Nann, *Nat. Methods* **2008**, *5*, 763.

[27] J. McFarland, *JAMA, J. Am. Med. Assoc.* **1907**, *XLIX*, 1176.

[28] ISO 7251:2005: Microbiology of food and animal feeding stuffs—Horizontal method for the detection and enumeration of presumptive *Escherichia coli*—Most probable number technique.

1702741 (8 of 8)

Fast Screening of Toxic Substances using Bioluminiscent Nanopaper

Jie Liu[1,2], José Francisco Bergua[1], Eden Morales-Narváez[1], Jahir Orozco[1], Ruslan Álvarez-Diduk[1], Teresa Vincent[3], Guohua Zhong[2], Arben Merkoçi[1,4]

[1] Catalan Institute of Nanoscience and Nanotechnology (ICN2), CSIC and The Barcelona Institute of Science and Technology, Campus UAB, Bellaterra, 08193 Barcelona, Spain

[2] Laboratory of Insect Toxicology, Key Laboratory of Pesticide and Chemical Biology, Ministry of Education, South China Agricultural University, Guangzhou 510642, P. R. China

[3] Departament d'Enginyeria Química, Universitat Autònoma de Barcelona, Bellaterra, Barcelona 08193, Spain

[4] ICREA, Institució Catalana de Recerca i Estudis Avançats, Barcelona, Spain

E-mail: arben.merkoci@icn2.cat

ABSTRACT

Chemical pollution is widely spread in environment nowadays. Particularly, the uncontrolled use of pesticides in agriculture leads to high-levels of these chemical compounds in water resources. INTCATCH H2020 European project aims to monitor and manage water quality in EU countries through the use of biosensors [1].

In this context, a biosensor for pesticides monitoring has been developed using the luminiscent bacteria *Aliivibrio fischeri* in combination with a nanopaper-based platform [2]. *A. fischeri* had previously been used in the ready-to-use kit Microtox ® since 1978 as a bioindicator of toxicity of water samples [3]. However, this methodology requires high-trained personal and expensive laboratory equipment. The use of nanopaper offers several advantages such as biocompatibility, low cost and simple procedure, increasing the sensitivity of the biosensor at the same time [4]. To study its applicability three common-used pesticides were chosen as model analytes: diuron, tributyltin (TBT) and polybrominated diphenyl ethers (PBDE). Results obtained so far as well as some future plans in applying such nanopaper platform combined with mobile phone for simple in-field pesticides monitoring will be presented.
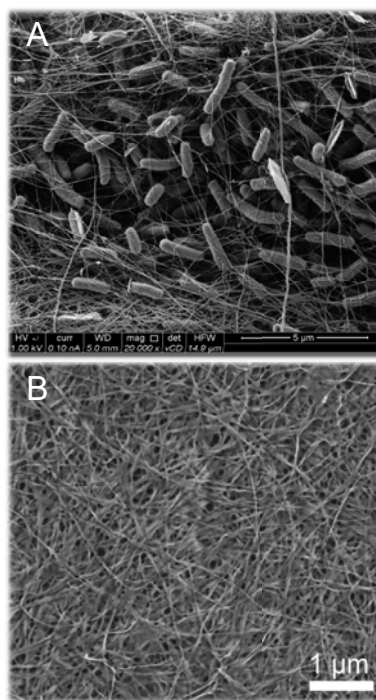
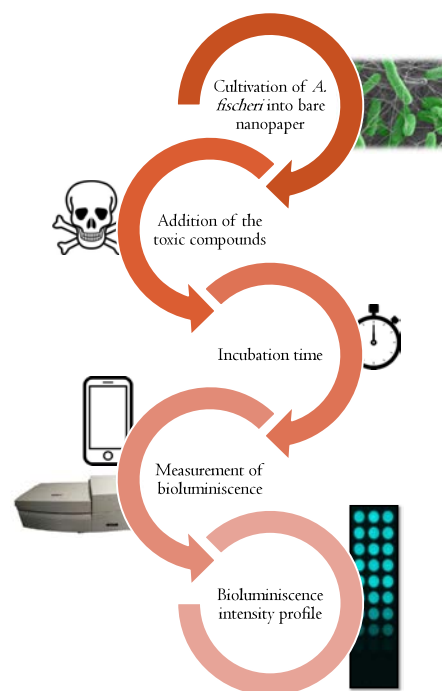Figure 1: A) *Aliivibrio fischeri*; B) Bare nanocellullose

Figure 2: Toxicity assay with *A. fischeri* embedded into nanopaper

RESULTS

Bacteria-nanopaper supports *A. fischeri* immobilization within the fibers for an optimal assay due to its biocompatible characteristics. Toxicity assays were carried out with this platform using three different pesticides: diuron, TBT and PBDE. Obtained results show that bacteria bioluminescence intensity decreases after 5 and 15 minutes of incubation when increasing concentrations of toxic compounds are applied. Besides, effectiveness of this platform was studied in real samples: lake water and sea water.

Reusability of the nanopaper scraps was achieved after 10 cycles of washing with 70% ethanol and milliQ water to be subsequently inoculated with *A. fischeri*. Finally, storability of the nanocomposites is reached using a 5% glycine solution keeping them at -20ºC.

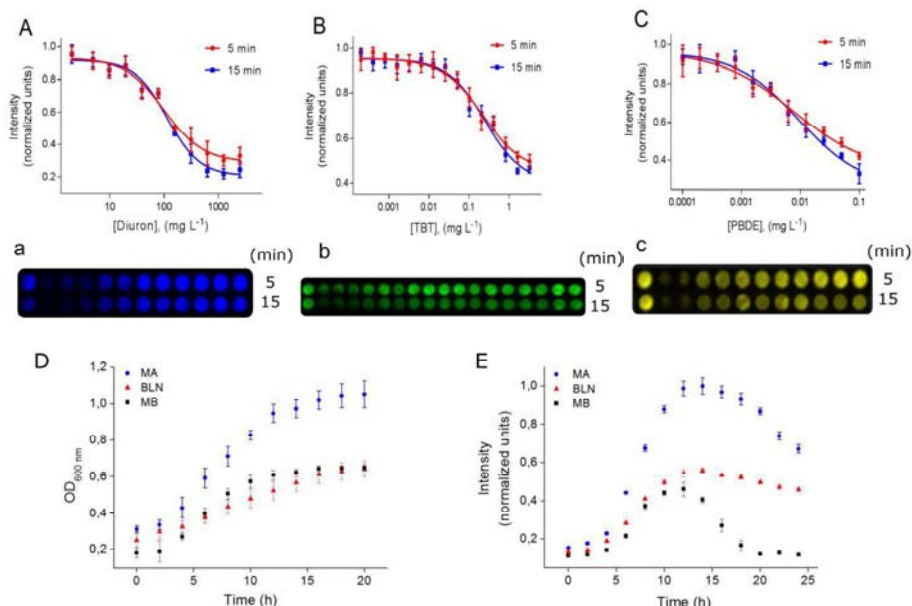Figure 4: Bioluminescence intensity of recycled bacteria-nanopaper

Figure 3: A) Diuron inhibition profile, B) TBT inhibition profile, C) PBDE inhibition profile, D) Cellular growth tendency, E) Cellular bioluminescence tendency
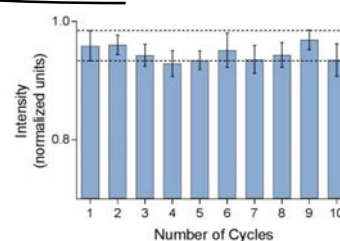
CONCLUSIONS

Combination of nanopaper embedded with *A. fischeri* showed outstanding biocompatibility, sensitivity, stability and reusability for the detection of toxic compounds. In addition, it defines not only a low-cost but also a suitable platform for real water samples analysis.

REFERENCES

[1] http://intcatch.eu/index.php/the-project

[2] J. Liu, E. Morales-Narváez, J. Orozco, T. Vincent, G. Zhong, A. Merkoçi. *NanoResearch*. **2017**. DOI: 10.1007/s12274-017.1610-7

[3] E. Argese, C. Bettiol, A. V. Ghirardini, M. Fasolo, G. Giurin, P. F. Ghetti, *Environ. Toxicol. Chem.* **1998**, *17,* 1005.

[4] E. Morales-Narváez, H. Golmohammadi, T. Naghdi, H. Yousefi, U. Kostiv, D. Horák, N. Pourreza, A. Merkoçi. *ACS Nano.* **2015**, 9, *7*, 7296-7305.

IMPROVEMENT OF LATERAL FLOW STRIPS PERFORMANCE FOR BACTERIA DETECTION

MSc. José Francisco Bergua, Prof. Chun-Jen Huang

CONTEXT & OBJECTIVES

Water quality is one the most important aspects to assess life quality and healthcare worldwide. Natural water sources can be polluted by a great variety of contaminants such as chemical products or biological microorganisms. In this context, biosensors provide a useful tool to monitor water quality previous to human water intake. More specifically, lateral flow strips (LFS) are simple devices that allow detection of several analytes such as proteins or pathogens. The most well-known LFS kit is the pregnancy test.

During this stay in Taiwan, I have worked trying to modify LFS design in order to improve the performance of the assay to detect *Escherichia coli*, the most common bacteria found in humans and animals that provides a reliable information of water fecal contamination.

RESULTS & DISCUSSION

Poly(2-methacryloyloxyethyl- phosphorylcholine) (PMPC) was chosen as the zwitterionic polymer to modify nitrocellulose pad. Dip-coating was the procedure used to impregnate nitrocellulose with PMPC. After UV light exposure, the polymer gets attached to the nitrocellulose pad, making it more hydrophilic and hampering bacteria unspecific adsorption.

Indeed, water flow was faster in the treated nitrocellulose pad (22 seconds) compared to the control one (non-treated, 25 seconds).

CONCLUSIONS & FUTURE PERSPECTIVES

- PMPC dip-coating procedure worked properly on nitrocellulose material.
- Water flow was faster in the PMPC-modified LFS than in the non-treated LFS, indicating nitrocellulose has become more hydrophilic.
- Fluorescent bacteria can be seen on the nitrocellulose pad in order to check their flow across this pad.

MATERIALS & METHODS

Lateral flow strips are made of 4 different parts, called pads, made of cellulose, glass fibre and nitrocellulose. In this study, nitrocellulose pad has been treated with a zwitterionic polymer (polymer with at least two functional groups, one positively and another negatively charged, but with a net neutral charge) so as to promote bacteria flow through the LFS.
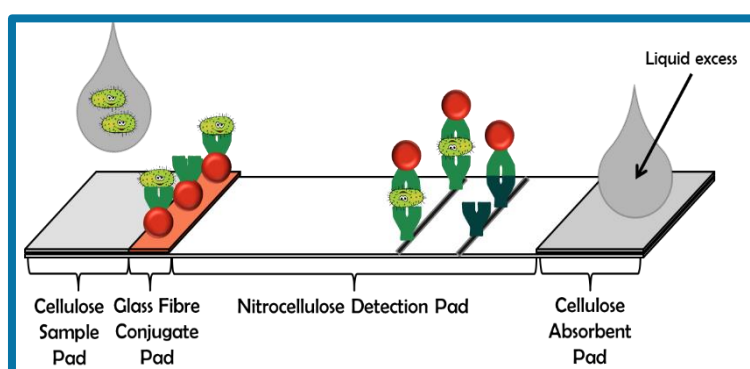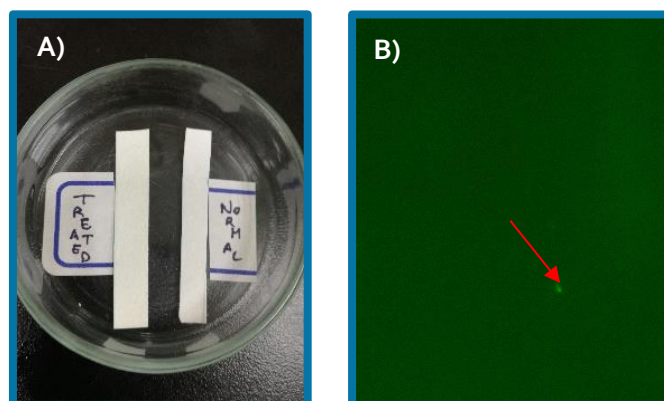

Figure 1. Lateral flow strip design.

Figure 2. A) Nitrocellulose pad modified (left) and non-treated (right). B) Fluorescent bacteria onto nitrocellulose pad (green point indicated by a red arrow).

ACKNOWLEDGMENTS